LixCoO -based thin films and devices for potential application to nonvolatile resistive memories

Van-Son Nguyen

université PARIS-SACLAY

NNT : 2017SACLS344

Thèse de doctorat

UNIVERSITÉ PARIS SUD
Comprendre le monde, construire l'avenir

FILMS MINCES ET DISPOSITIFS À BASE DE Li_xCoO_2 POUR APPLICATION POTENTIELLE AUX MÉMOIRES RÉSISTIVES NON VOLATILES

Thèse de doctorat de l'Université Paris-Saclay
préparée à l'Université Paris-Sud

École doctorale n°575 : Electrical, optical, bio : physics and engineering (EOBE)
Spécialité de doctorat: Électronique et Optoélectronique, Nano- et Microtechnologies

Thèse présentée et soutenue à GIF-SUR-YVETTE, le 20 Octobre 2017, par

Mr Van-Son NGUYEN

Composition du Jury :

Mme Agnès BARTHÉLÉMY Professeur, Université Paris-Sud, UmPhy CNRS/Thales	Présidente
Mr Brice GAUTIER Professeur, INSA Lyon, Laboratoire INL	Rapporteur
Mr Jean-Christophe LACROIX Professeur, Université Paris-Diderot , Laboratoire ITODYS	Rapporteur
Mr Raphaël SALOT Ingénieur de Recherche, CEA-LETI, Laboratoire LMBE	Examinateur
Mr Olivier SCHNEEGANS Chargé de Recherche Hdr, CNRS, Laboratoire GeePs	Directeur de thèse
Mr Philippe LECOEUR Professeur, Université Paris-Sud, Laboratoire C2N-Orsay	Co-Directeur de thèse
Mr Claude PASQUIER Professeur, Université Paris-Sud, Laboratoire LPS	Invité

Université Paris-Saclay
Espace Technologique / Immeuble Discovery
Route de l'Orme aux Merisiers RD 128 / 91190 Saint-Aubin, France

Dedicated to: Ba Bắc mẹ Phê
các em Thúy, Hùng, Dũng

và Trần Thị Thương Hoài.

Université Paris-Saclay
Espace Technologique / Immeuble Discovery
Route de l'Orme aux Merisiers RD 128 / 91190 Saint-Aubin, France

Université Paris-Saclay
Espace Technologique / Immeuble Discovery
Route de l'Orme aux Merisiers RD 128 / 91190 Saint-Aubin, France

ACKNOWLEDMENTS

Here, I would like to acknowledge the following organizations and individuals who encouraged, inspired, supported and assisted me during my thesis.

First of all, I am grateful for the financial support from the “Electrical, optical, bio: physics and engineering (EOBE)” Doctoral School, as well as from the “Labex NanoSaclay” and “Cnano Idf” centers.

I would like to express my deepest gratitude to my supervisor Dr. Olivier Schneegans, for his unceasing patience, guidance, extremely valuable and always intellectually challenging comments. He was very kind to take me under his wing, to respond to all my queries. Also, I would like to especially thank my co-supervisor Prof. Philippe Lecoeur for his invaluable help with technical knowledge and feedback on physical points of the results. Thank you both for trying hard to make me accept that it is possible to know more, and at the same time, that it is not possible to know everything.

I’m also very grateful to Prof. Brice Gautier and Prof. Jean-Christophe Lacroix, who accepted with enthusiasm to be reviewers of my thesis, for their helpful comments and questions. I would also like to thank the members of committee, Prof. Agnès Barthélémy, Dr. Raphaël Salot and Prof. Claude Pasquier, for their helpful questions and suggestions.

I would like to express my special thanks to the OXIDE team (including PhDs, Masters) at the C2N-Orsay lab: without their help and support, this thesis would not have been possible. First, I would like to thank Thomas Maroutian for all his great help concerning result discussions and advices. I would also like to thank Guillaume Agnus and Sylvia Matzen for their guidance in micro nano fabrication and processing, and Pascal Aubert for helping me with finite elements simulation. The EIS measurements would not have been done without the help of Etienne Thiebaut. And for creating the best working condition and facility for students in cleanroom, I would like to thank all the CTU staff.

At LPS lab, I am also very grateful for their cooperation, contribution, and valuable time spent for discussion: Pascale Auban-Senzier for the numerous deposits of gold electrodes by thermal evaporation, Kang Wang for etching by FIB, Pierre-Antoine Albouy for structural analyses by XRD, Nathalie Brun and Katia March for measurements by STEM.

At the GEMaC lab, I would like to express special thanks to François Jomard for his valuable time spent for discussions and measurements by SIMS.

At GeePs lab, I would like to thank David Alamarguy for his analyses by XPS, Frédéric Houzé and Pascal Chrétien for their advices in the preparation of conferences. Thank you also to Sylvain Franger from the ICMMO lab, concerning knowledge on intercalation materials. Thank you also to Pavan Nukala from CentraleSupelec, for TEM charaterizations, and to Van Huy Mai from Le Quy Don Technical University, for useful discussions and suggestions.

Last, but certainly not least, I thank all my family in Vietnam for their unending love, understanding and support, without which this thesis would not have been possible.

Université Paris-Saclay
Espace Technologique / Immeuble Discovery
Route de l'Orme aux Merisiers RD 128 / 91190 Saint-Aubin, France

TABLE OF CONTENTS

INTRODUCTION

Since its initial commercial development around 1988, Flash memory has been extensively used as *non-volatile memory* for digital data storage in most mobile electronic devices (laptop, mobile phone, tablet...). However, with the extreme development of information technology (IT) in the era of the Internet of Things (IoT), the need of fast and high capacity data storage increases in an exponential way. Hence the current limits of Flash memory (e.g. low information density, low endurance and slow speed) must be overcome to follow the information storage requirements.

Towards this objective, many researches recently developed around the concept of resistive memories based on the switching between different resistance levels by applying appropriate bias voltages. Memories whose resistance variations depend on electrochemical reactions (ReRAM) are potentially good candidates towards next-generation non-volatile memories. The underlying redox mechanisms observed are often based on the formation/rupture of conducting filaments, involving migration of cations of metal elements (coming from the electrodes), or oxygen vacancies. This filamentary character makes it challenging to attain extreme downscaling towards the nanometric scale.

In order to overcome this latter limitation, a particular class of layered materials - used in the field of energy storage – has begun to be studied since 2011. Interesting preliminary results have already been obtained on Li_xCoO_2 thin films, but deeper understanding is still needed concerning the nature of the underlying mechanisms, as well as further studies concerning the potential applicability of these materials towards nonvolatile resistive memories (ReRAM) : this is the goal of my dissertation. In my thesis, the work has been carried out in the Laboratoire Génie Électrique et Électronique de Paris (GeePs) and the Centre de Nanosciences et de Nanotechnologies (C2N-Orsay) in collaboration with the Laboratoire de Physique des Solides (LPS), the Institut de Chimie Moléculaire et des Matériaux d'Orsay (ICMMO), the Groupe d'Étude de la Matière Condensée (GEMaC), the LITEN-CEA de Grenoble, the University of Cyprus, and the "Le Quy Don" Technical University at Hanoï, Vietnam.

This document is subdivided into five chapters. In chapter 1, we present a brief overview of different types of nonvolatile memories and introduce the notion of Redox Resistive Switching (RS) phenomenon, including the overall related common mechanisms. Moreover, the structural and electrical properties of Li_xCoO_2 will be recalled, and work done so far on this material in the field of RS will be briefly presented.

Chapter 2 presents fabrication methods and characterization techniques which have been used to elaborate Li_xCoO_2 thin films and devices therefrom. The structure of the Li_xCoO_2 thin films we studied and the behavior of the devices have been investigated using various methods and techniques.

The main results of my thesis concerning the involved mechanisms are then presented in chapter 3 and 4. In chapter 3, we investigate the electrochemical mechanisms which are at the origin of resistive switching, in the micrometric electrode/film/electrode configuration. We try to determine the validity of a formerly proposed mechanism which was however not yet demonstrated before. In chapter 4, we study the experimental switching kinetics of devices, and propose a numerical model to explain the results observed. The stability of information over time has also been examined at this stage.

In the fifth and last chapter, we examine the potential applicability of Li_xCoO_2-based devices to Re-RAM memories through the study of their performances in terms of endurance (i.e. maximum number of write/erase cycles). Specifically, the influence of several parameters (such as voltage pulses, chemical nature of the electrodes, temperature etc.) on these performances is investigated.

CHAPTER 1

INTRODUCTION AND STATE OF THE ART

TABLE OF CONTENTS

INTRODUCTION

This chapter is subdivided in four parts. In the first part, we present a brief overview of different types of nonvolatile memories (NVMs): Flash memories, as well as emerging memories such as Ferroelectric memories (FRAM), Magnetic memories (MRAM), Phase Change Memories (PCRAM). The main structure, working principle and major performance parameters of each type of memory will be addressed.

In the second part, we present in more detail emerging memories whose information (the resistance value) depends on electrochemical (redox) reactions: they are thus referred as Redox RAMs (ReRAMs). These memories are often classified into three main classes, depending on the specific mechanisms involved: Electrochemical Metallization Memories (ECM), Valence Change Memories (VCM) and Thermochemical memories (TCM). Each class will be presented and some examples given.

The third part introduces Li_xCoO_2 thin film which has been extensively studied in this thesis. The structural and electrical properties of this layered material will be recalled, which are useful for the following chapters. Specifically, the electrical conductivity of Li_xCoO_2 can vary over 4-5 order of magnitude as a function of the (x) stoichiometry. This is the main reason why this material has been studied for potential applicability towards nanoscale information storage.

Several international research groups have begun since 2013 to study experimentally Li_xCoO_2-based resistive switching towards memories and neuromorphic circuits. These works will be discussed in this last part. Besides, work carried out on Li_xCoO_2 since 2011 at the GeePs and collaboration labs will be recalled. Specifically, the main results of the former thesis (V.H. Mai, 2014) will be mentioned, which are the starting point of my own thesis work.

1 THE ROADMAP OF NONVOLATILE MEMORIES

1.1 Introduction

Over the past 20 years, a variety of different memory technologies have been successfully researched and developed. These technologies have been bringing a mass of memory productions to the commercial market, becoming one of the most developing technologies in the modern daily life and the future. These memories can be classified into two large categories, volatile and nonvolatile memories. The main difference is that the latter have an ability of retaining data when the power is switched off. Therefore, they are considered as the secondary storage.

An overview of the most important and developed memories is summarized in **Fig. 1.1** below. Concerning non-volatile memories, Flash memories dominate the computing industry nowadays. Nevertheless, due to limitations of this kind of memories (low switching speed, density, endurance) new technologies of memories are required to replace Flash [1].

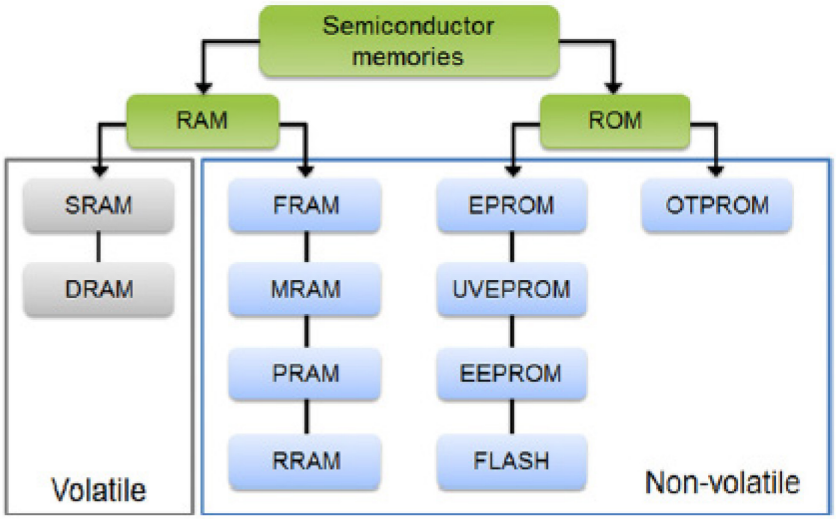

Figure 1.1: General overview of some categories of memories [2].

In terms of nonvolatile memory performances, the five most important parameters must be considered are:

- The write/read speed;
- The endurance (the maximum write/erase cycles);
- The density (the minimum feature size of cells);
- The energy required for write/read operation;

- The data retention;

After briefly recalling the main characteristics of the Flash, FeRAM, M-RAM and PC-RAM memories, we will discuss Redox-RAM (which will be hereinafter referred to Re-RAM, for simplicity).

1.2 Flash memory

Being developed since the late 1990s, Flash memory is a mature member of nonvolatile memory family with a huge market all over the world. The main characteristics of the Flash memory are a high retention time of over 10 years, a typical access time of 0.1ms (vs ~10ms for a HDD), and an endurance of 10^3-10^5 [3].

The structure and principle of the flash memory is basically depicted in **Fig. 1.2**. In a Flash memory cell, there is a specific location called conductive electrode (or floating gate) surrounded by an insulator, creating a charge trapping layer [3]. By controlling the conductance of the channel (with a V_{CG} voltage applied between the control gate and the substrate), two distinguishable logical states "0" and "1" can be stored. The source-drain current control is due to three main physical mechanisms: channel hot electron mechanism, photoelectric effect and the Fowler-Nordheim electron tunneling which are reported in [4].

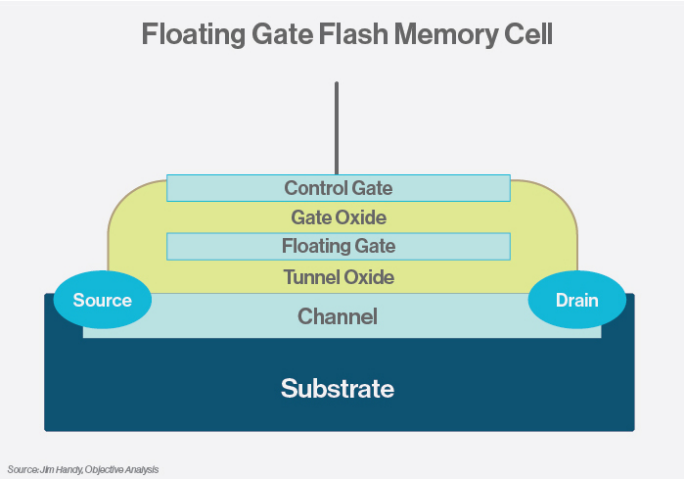

Figure 1.2: Schematic of flash memory [5]

However, the flash memory has also some drawbacks. During the write operation, since the floating gate is isolated from external contact by two barriers, the total writing voltage required is relatively high (minimum 6V) in the case of a SiO_2 barrier, as shown in ref. [3], and even higher (10-12V) for a faster operation. Such high voltage leads to progressive destruction of the writing zones, yielding rather low average endurance (typically 10^3 to 10^5). Therefore, ongoing researches attempt to overcome this endurance drawback. Low memory density is also a

shortcoming of the flash memory. The typical size of the memory cell is relatively high (about 40 nm) [6]. Besides, another limitation of Flash memory is the slow writing speed (1ms/0.1ms order of magnitude [7]). Therefore, other types of non-volatiles memories (called emergent memories) have been then investigated to increase speed and density. Some types of such memories are described below.

1.3 Fe-RAM, M-RAM and PC-RAM

1.3.1 Ferroelectric Random-Access Memory (FeRAM)

The ferroelectric RAM (FeRAM or FRAM) is composed by a ferroelectric layer sandwiched between two electrodes (instead of a dielectric layer) to achieve non-volatility. Such layers consist of ferroelectric materials such as $BaTiO_3$, $BiFeO_3$ or PZTO *etc.* [8-10].

When an external electric field is applied across the stack, the electric dipoles tend to align themselves to the field direction, produced by small shifts in the positions of atoms and shifts in the distributions of electronic charge in the crystal structure. After the electric field is removed, the dipoles retain their polarization states. As a result, two possible states ON and OFF can be stored, as shown in **Fig. 1.3** [9].

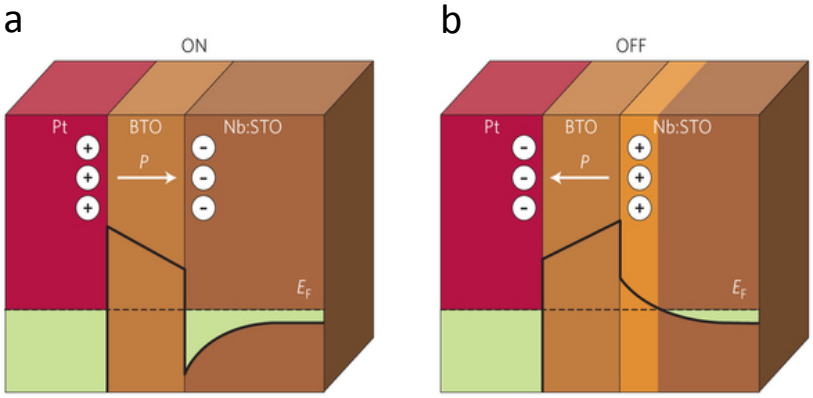

Figure 1.3: Structure and principle of a FeRAM {Pt-BTO-Nb:STO} cell. **a)** The ON state and **b)** the OFF state corresponds to different ferroelectric polarization [10]

The key advantages of FeRAM today are high speed, low-power consumption and long endurance. In particular, Chanthbouala *et al.* showed that the write voltage is as low as few volts and the read voltage is extremely low (100mV [11]). Several recent researches have shown that Ferroelectric Tunneling Junctions (FTJs) provide surprisingly fast write/read speed of 100ns, largely reproducible endurance of 4×10^6 cycles with OFF/ON ratios of four-orders-of-magnitude difference, as reported in ref. [12]. The same ratio but shorter endurance (2000

cycles) was exhibited by Yamada *et al.* [13]. However, FeRAM must challenge some limitations such as low storage densities (thus storage capacity limitation), destructive readout and high cost [14].

1.3.2 Magnetic Random-Access Memory (MRAM)

Magnetic Random Access Memories (MRAM) based on Tunneling Magnetoresistance Effect (TMR) have gained a very significant attention since 1990s [15]. The main idea is to utilize ferromagnetic materials whose resistivity depends on their magnetic polarizations [16]. The magnetic orientation of one layer is fixed, the other one can be programmed to specific stable magneto-resistance states (example shown in **Fig. 1.4**). A small sense current is then used to read out the resistance of the device. When two magnetizations are oriented to be parallel, the current flowing through the device is higher than in the case of anti-parallel magnetizations.

Figure 1.4: The Magnetoresistance Junction device has **a)** low- and **b)** high- resistance corresponding to the orientations of magnetization in two ferromagnetic layers: parallel and anti-parallel, respectively.

The main advantages of the MRAM are a high endurance (>10^{12} cycles), and an extremely fast speed of 10ns. These memories have also a very small cell leakage and low degradation during write/read operation. However, MRAM suffers from some limitations such as high write current/energy, low integration density and low scalability [17]. The present scale limit MRAM reaches therefore around 130 nm.

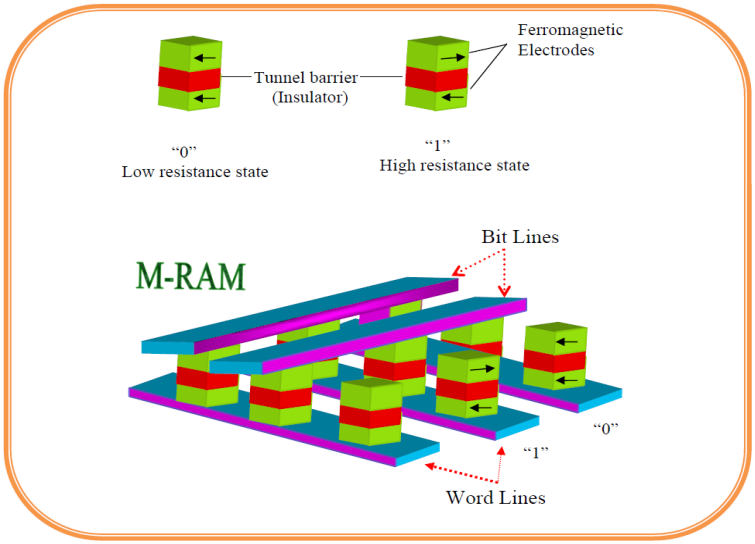

Figure 1.4: Simplified crossbar structure of a MRAM cell [18]

1.3.3 Phase Change Random Access Memory (PC-RAM)

Phase change memory (PCM) is an emerging technology that exploits the large resistance contrast between the amorphous and crystalline states in so-called phase change materials. The amorphous phase tends to have high electrical resistivity, while the crystalline phases exhibit a low resistivity (typically 3 or 4 orders of magnitude lower). These phases are easily exchanged because of the heating induction through optical or electrical approaches [19]. The simplified structure of PCM is shown in **Fig. 1.5**. The phase change material is sandwiched between the top electrode and the heater. By alternating the temperature of the heater, the crystallized mushroom cell volume increases, resulting in the low resistive switching in the SET process [20]. The RESET process (using a very fast temperature increase beyond the melting point) leads a switch back to an amorphous state.

Non-volatile PCM exhibits many advantages such as fast switching performance (<10ns) and long endurance (>10^{12} cycles) [19], [21]. The minimum cell size is up-to-date 22nm. However, the greatest challenge of the PCM is the requirement of a high programming current density. Due to high temperature, leaking currents might easily appear in the dielectric material. In addition, the long-term resistance and threshold voltage drift probably limit the multilevel operation possibilities of PCM [22].

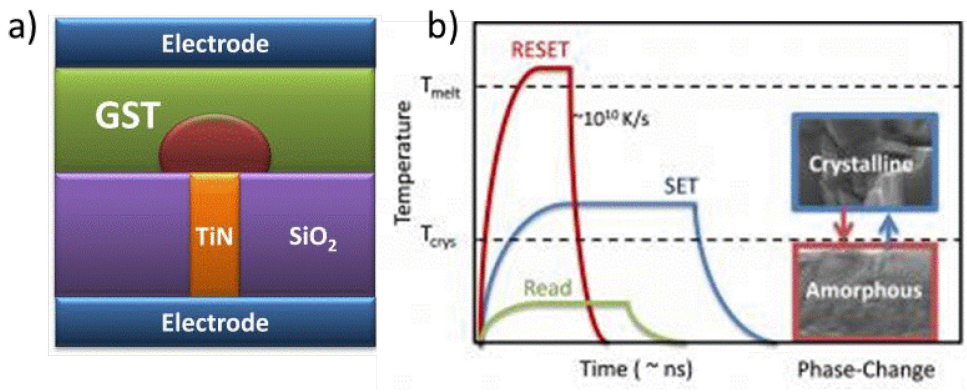

Figure 1.5: a) Cross-sectional schematics of PCM, **b)** The dependence on temperature of PCM [23].

1.4 Conclusion

As shown in the **table 1.1**, Fe-RAM, MRAM and PC-RAM are much faster than flash memory, and show a much better endurance. However, the cell density of these storage devices is lower in comparison to flash memory. Also, the programming current density (thus the write energy) is still high, which leads to high-power consumption.

Criteria	**FLASH**	**Fe-RAM**	**M-RAM**	**PC-RAM**
Write time	0.1 ms	10 ns	10 ns	100ns
Endurance	10^{3-5}	$> 10^{14}$	$> 10^{12}$	$> 10^{9}$
Minimal size	20 nm	180 nm	130 nm	65 nm
Write energy	10 fJ	30 fJ	100 pJ	10 pJ

Table 1.1: Summary of some specifications of non-volatile memories.

A recent survey from Stanford Electronics Lab [24] has clearly shown the present trend of non-volatile memories in the applicability point of view. The flash memory has nowadays dominated in the branch of storage capacity (see **Fig. 1.6**). The other NVMs (Fe-RAM, MRAM, PC-RAM) have many advanced features, however their storage capacity increase appears to slow down progressively year by year.

This is why researches also develop exponentially on the concept of redox resistive memory (Redox-RAM or ReRAM), which appear as potential good candidates in terms of density, storage capacity (see **Fig. 1.6** ReRAM) and low-energy consumption. The next section will thus be devoted to Re-RAM memories and their related mechanisms. This will be useful in

the following chapters, in order to compare these mechanisms to those proposed in the framework of my thesis.

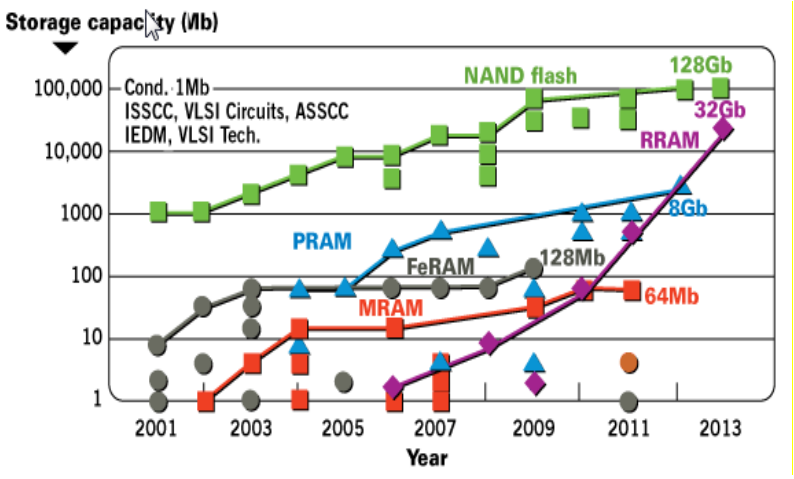

Figure 1.6: Evolution of storage capacity of nonvolatile memories (by Stanford Memories Trend) [24].

2 REDOX-BASED RESISTIVE SWITCHING PHENOMENA

2.1 Basic principle of redox-based resistive switching

A general ReRAM cell consists of a capacitor-like structure in which an insulating or semiconducting oxide is sandwiched between two metal electrodes (see **Fig. 1.7** [25]). The conductivity of the oxide is modified by applying a bias voltage pulse: this resistive switching phenomenon occurs as a result of electric fields applying to the oxide. The determination of the underlying processes is an important issue to better control the performances of such ReRAM cells. In literature, attempts have been made to classify ReRAM in different categories, depending on the mechanisms involved (almost related to redox reactions).

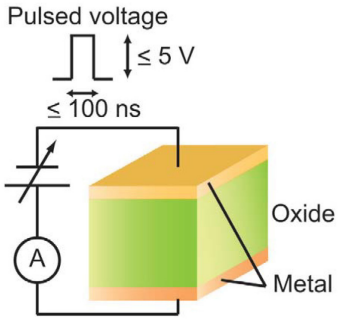

Figure 1.7: Diagram of a ReRAM memory cell with a capacitor-like structure in which an insulating or semiconducting oxide is sandwiched between two metal electrodes. [25].

2.2 Classifications of Redox-based Resistive Switching

2.2.1 Switching polarities

The resistance of the material can switch between at least two values: OFF (high resistance) and ON (low resistance). To classify the different types of Re-RAM, a distinction is often made between two regimes, called Unipolar Switching and Bipolar Switching [26]. Switching is called unipolar when switching from one state to another (OFF → ON or ON → OFF) does not depend on the polarity of the voltage signal, as shown in **Fig. 1.9a**. On the other hand, switching is called bipolar when the OFF → ON transition occurs for one polarity of voltage, and ON → OFF for the reverse polarity (**Fig. 1.9b**).

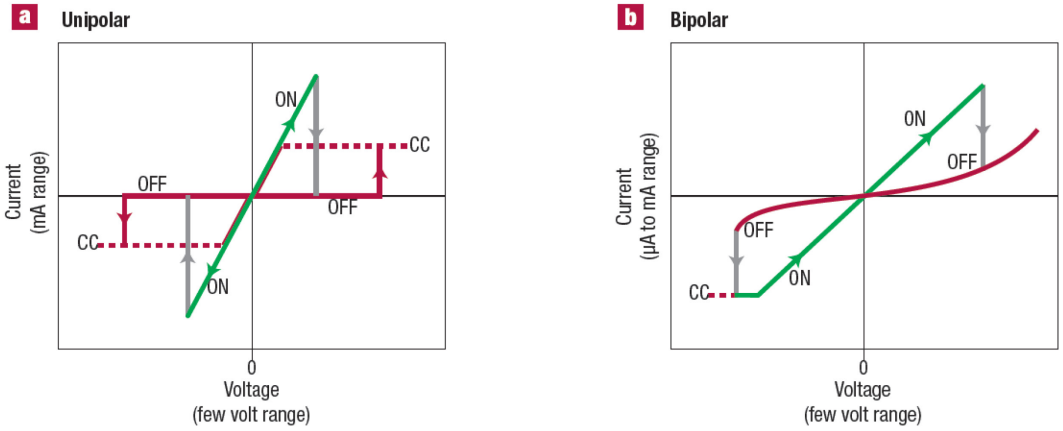

Figure 1.9: Schematic view of **a)** Unipolar switching and **b)** Bipolar switching proposed by Waser [26].

Waser *et al.* proposed to classify the redox reactions in three main categories [27],

- Electrochemical Metallization mechanism (ECM)
- Valence Change Mechanism (VCM)
- Thermochemical Mechanism (TCM)

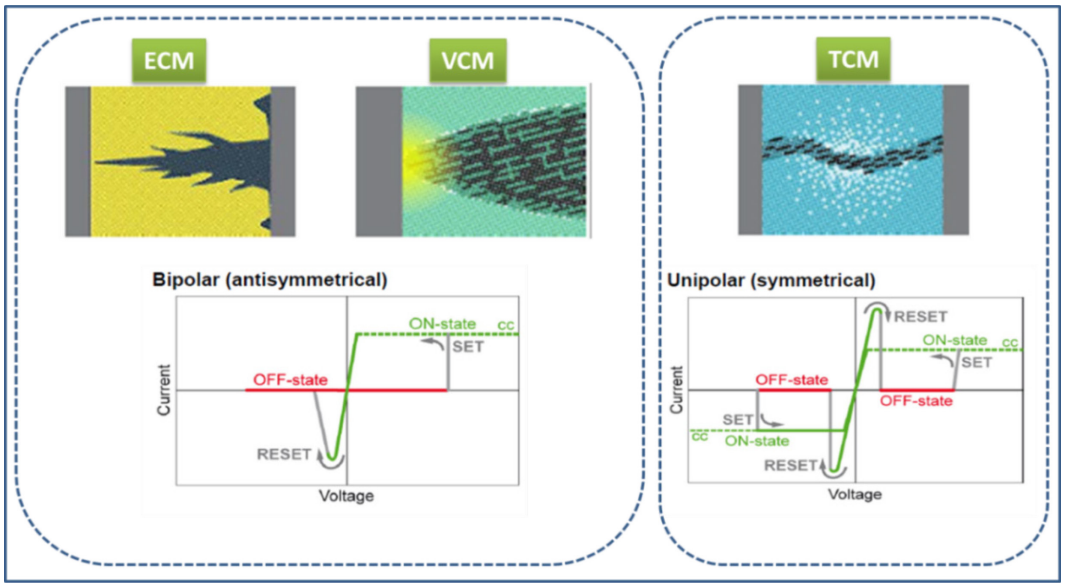

Figure 1.10: Three mechanisms of Redox-based Resistive Switching: ECM, VCM and TCM. Adapted from [27].

ECM and VCM mechanisms typically show a Bipolar Resistive Switching in which the SET and RESET operations occur on opposite bias polarity, whereas TCM show a unipolar switching, as illustrated in the schematic view (**Fig. 1.10**). The specific characteristics of ECM, VCM and TCM will be emphasized in detail in the followings.

2.2.2 Electrochemical Metallization (ECM)

The MIM (Metal-Insulator-Metal) structure of an ECM cell is composed of a top active electrode (AE, such as for example Cu, Ag, Ti, Ta or Ni), a bottom inert counter electrode (CE, such as Au, Pt or W) and a thin film of a solid electrolyte "I" sandwiched between two electrodes. The solid electrolyte thin film is often made from oxide, mixed conductors, ion electrolytes, selenide, sulfide, chalcogenide or halide materials such as Cu-doped TiO_2, NiO_x [28], SiO_2, ZrO_2, HfO_2, Ta_2O_5, SrTiO3, Ag_2S, Cu_2S, AgI, Ag-GeS_x, $GeSe_x$ etc. [29]. The ECM cells operates due to the formation and dissolution (rupture) of metallic filaments in the insulator matrices, as proposed by Waser [30] and Sawa [25].

Among various models of ECM, a typical example is reported by Valov *et al.* [29]. **Fig 1.11** shows the whole filament forming/disrupting processes of a {Cu/Cu^{2+}-doped oxide thin film/Pt}MIM cell. First, when the CE is negatively polarized, the Cu metal of AE is dissolved into Cu^{2+} ions according to the half-cell oxidation reaction $Cu \rightarrow Cu^{2+} + 2e^-$ and these ions begin to migrate towards the cathode (**Fig. 1.11a**) across the electrolyte under the effect of electric field. These ions located near the CE surface are reduced due to the reaction $Cu^{2+} + 2e^- \rightarrow Cu$ (**Fig. 1.11b).** A conducting bridge made of Cu atoms will be formed and lengthened until it

reaches the AE, which corresponds to a RS from HRS to LRS (**Fig. 1.11c**). As the memory cell is reversely biased, this forming metallic filament is dissolved into Cu^{2+} because of the oxidation reaction $Cu \rightarrow Cu^{2+} + 2e^-$ at the interface of the AE. The conducting bridge is therefore disrupted (RESET switch from LRS to HRS reversibly: **Fig. 1.11d**). After that, reversible RS occur between HRS and LRS by applying opposite polarized bias voltages.

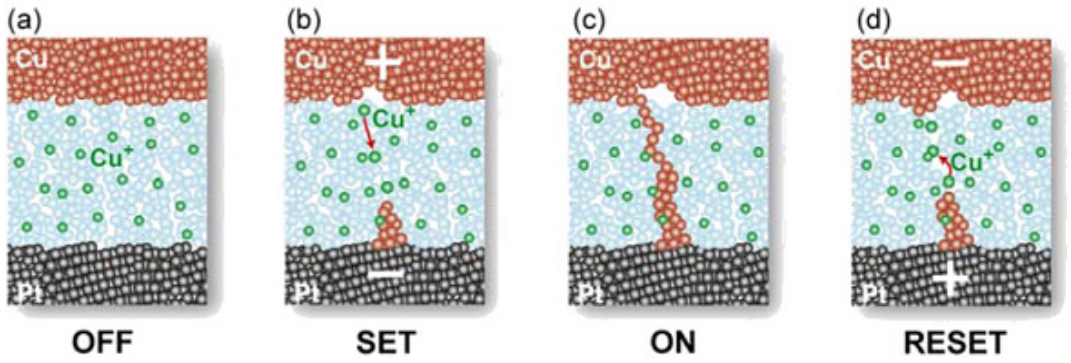

Figure 1.11: Process of electrochemical metallization: **a)** initial OFF state, Electroforming step: **b)** Electrode dissolution and migration of cations towards the cathode and **c)** conducting bridge between two electrodes switches the cell to ON state. **d)** RESET: Dissolution of the conducting filament due to the reverse bias, switch of the cell to OFF state [29].

Transmission Electron Microscopy (TEM) is a useful method to observe the mechanism of ECM resistive switching. For example, in Ag/SiO_2/Pt cell (as shown in **Fig. 1.12**), TEM images reveal dendrite-like multifilament which are formed and disrupted in the insulating matrix of SiO_2 layer.

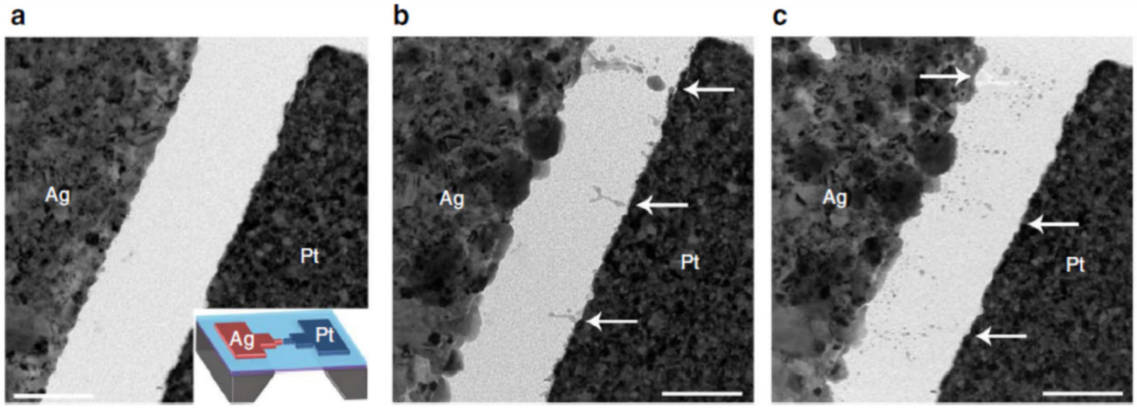

Figure 1.12: Observation by TEM of conductive filament in a SiO_2 dielectric layer sandwiched between two electrodes made of Ag and Pt [31]. **(a)** The as-made MIM structure before applying the biased voltage. **(b)** The conductive filaments of Ag atoms are electroformed in the SiO_2 layer. The arrows indicate the multifilament growth and extension [27]. **(c)** The filaments are dissolved by applying a reverse bias.

Moreover, it is important to note that ECM requires an electroforming SET process at the initial state to create the conductive bridges between the electrodes. At a constant bias sweeping rate, the applied voltage of electroforming process is significantly higher than that of SET process as shown in **Fig. 1.13a**. In some cases, the maximum electroforming voltage could reach few tens volts. Moreover, the electroforming step is a very slow process, taking from few milliseconds to thousands seconds [27]. Therefore, the electroforming step in ECM cells can be considered as a drawback due to its energy consumption and time-consuming process. Another reason is that the power dissipation is out of control during the electroforming step [2]. Fortunately, a limit compliance current can be set to avoid an electrical breakdown.

Besides, another limitation comes from the lateral size of the conductive filaments. In the literature, this lateral size is found to reach about 20nm near the tip of the filament (near AE) and approximately 70nm at the base (near CE) [31]. Similar results could be found in ref. [32]–[35]. Apparently, this limitation can lead to a difficulty in miniaturization of the MIM cells because it is almost impossible to reduce the ECM cell below the lateral size of the filaments.

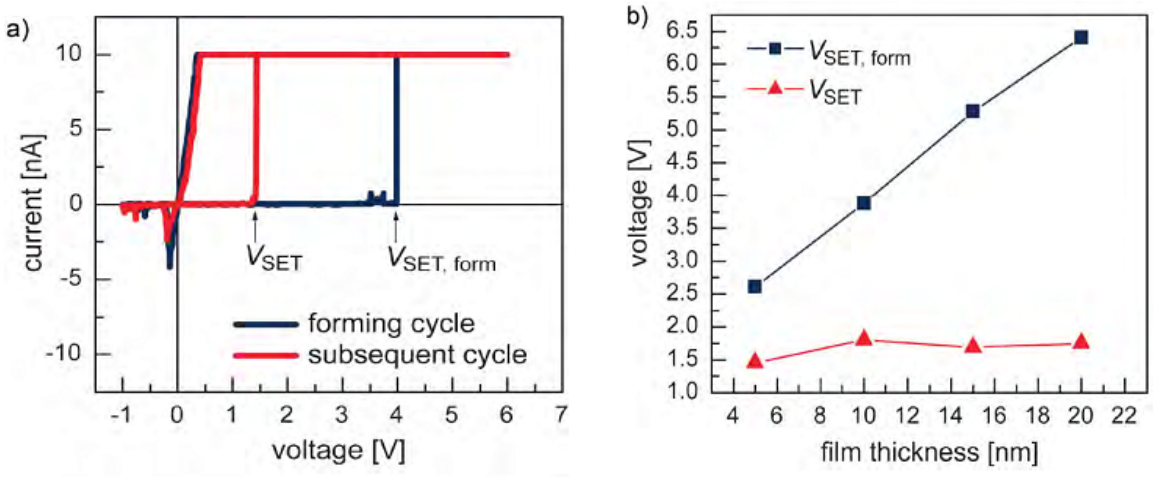

Figure 1.13: a) I-V characteristics of ECM switching shows the required electroforming voltage $V_{SET,form}$ (+4V) which is much higher than subsequent SET voltage (V_{SET}=+1.5V), **b)** Strong dependence of the electroforming voltage on the film thickness [30].

2.2.3 Valence Change Mechanism (VCM)

The term "valence change" indicates the changes of the valence state of the metal element of the oxide located between the electrodes. RS based on valence change mechanism occurs in materials such as $SrTiO_3$, TiO_x, HfO_x, TaO_x, ZrO_x *etc.* [36]. In such materials, it has been observed that RS involves the migration of oxygen vacancies. These migrations modify the oxidation state of the metal cations (which remain immobile), which results in the local conductivity modifications of the oxide films.

Fig. 1.14 shows a sketch of RS process of a simple MIM cell composed by an oxide film such as TiO_2 (nearly insulating) sandwiched between two electrodes: Pt as active electrode (AE) and a Pt inert counter electrode (CE) [37]. O^{2-} anions migrate from the cathode to the anode (in blue in the figure), where they are oxidized to O_2. To this migration of O^{2-} anions corresponds the formation of oxygen vacancies ($V_{\ddot{O}}$), along conductive paths, where the reduced TiO_x material becomes locally more conductive (red in the figure). These paths finally reach the anode (**Fig 1.14c**). After this step, for each new switching cycle, these conductive paths will subsequently disrupt/reconnect.

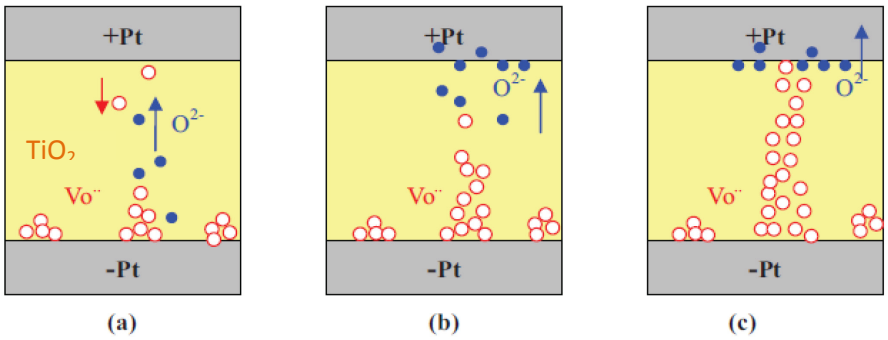

Figure 1.14: Simplified sketch of the electroforming step of TiO_x, belonging to VCM. Adapted from [37].

The electroforming process in VCM is dominated by the modified valence of the metal cations during switching. Below are shown two examples of MIM cells : $Au/SrTiO_3/Nb:SrTiO_3$ and $Pt/Ta_2O_{5-x}/Ta/Si$ (studies of Beaumer *et al.* [38] and Skaja *et al.* [39], respectively). Both cells behave like VCM because the redox reactions which occur in the film leading to a change of the valence state of metallic ions (Ti, and Ta respectively). In the first case ($Au/SrTiO_3/Nb:SrTiO_3$), a single filament of reduced Ti^{3+} has been mapped by XPEEM (X Ray Photoemission Electron Microscopy) imaging method, as Ti^{3+} exhibits its main contribution to the conductivity of the cell, in contrast to the Ti^{+4} at surroundings, as shown in **Fig. 1.15a, b**. In the second case ($Pt/Ta_2O_{5-x}/Ta/Si$), dendrite-like filament and multifilament structure are observed by PEEM (Photoelectron Microscopy), as shown in **Fig. 1.15 c, d** [39].

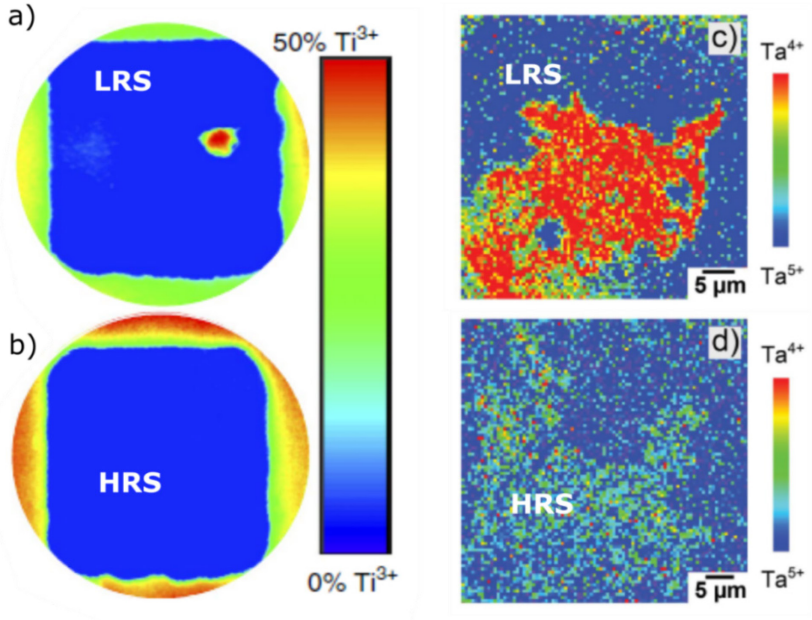

Figure 1.15: False color map of Ti^{3+} spectral distribution: **a)** Ti^{3+} distribution in the spot (in red), showing one single filament (cell in LRS) **b)** cell at HRS : the filament has disappeared (in blue), adapted from [38]; PEEM analysis of Ta^{4+} : **c)** Ta^{4+} distribution in red spectrum (cell at LRS) **d)** cell at HRS, adapted from [39].

2.2.4 Thermochemical mechanism (TCM)

In this type of mechanism, thermal effects are predominant over the electrochemical processes, so the mechanism is unipolar. The application of a voltage between the electrodes leads to some kinds of breakdown, which yields a considerable heating, and thus causes a reduction at high temperature of the oxide towards the metallic element, in the form of a filament (**Fig. 1.16B**). The voltage at the terminals of the electrodes drops then, due to the existence of a resistance compliance (or current compliance) with the considered cell. The local temperature drops. The reaction is stopped, then the ON state remains stable [3].

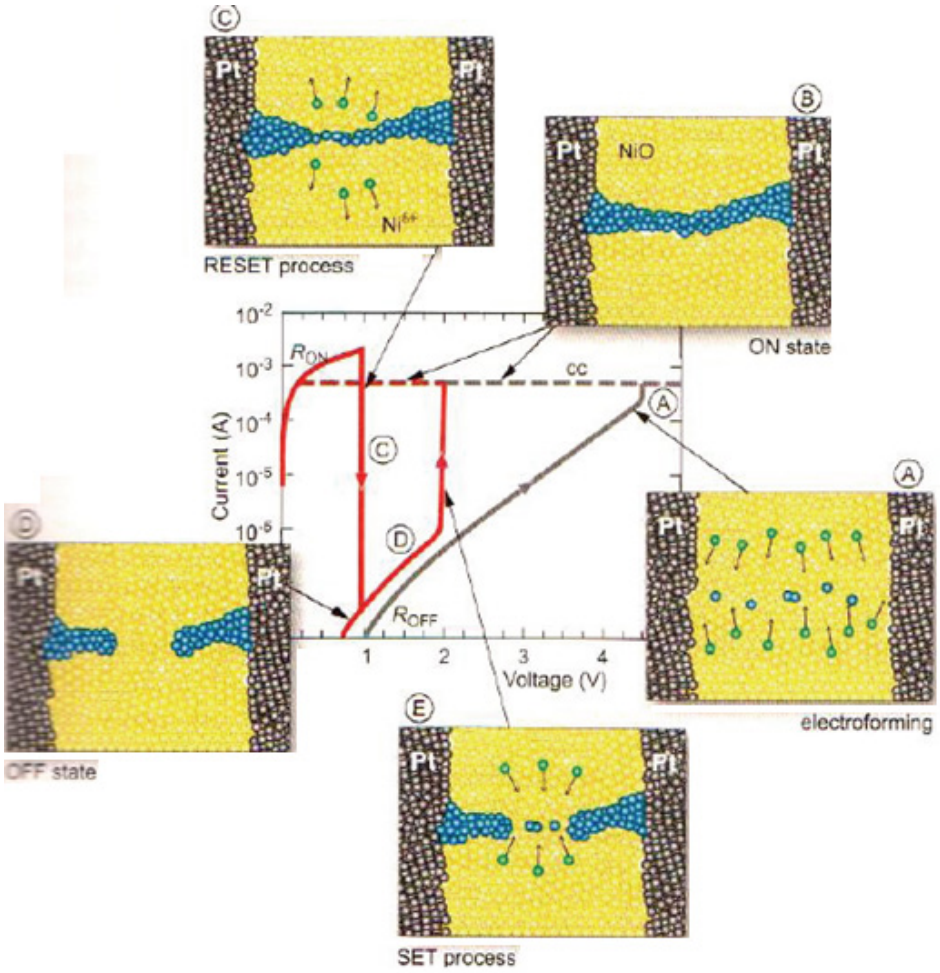

Figure 1.16: Example of forming process of unipolar resistive switching in TCM cell: **(A)** initial state, **(B)** electroforming of the conducting filament (ON state) due to thermic effects **(C)** & **(D)** rupture of conducting filament (OFF state), **(E)** SET process [3].

One of the ways to observe TCM mechanism is exhibited in **Fig. 1.17**. The methodology is shown and the surface of the film is electrically scanned using Conducting Probe AFM (CP-AFM) after removal of the TE. As the film is at HRS, most of the conducting filaments are disconnected. When the LRS is thermally SET, the filaments are formed, as shown in white colors.

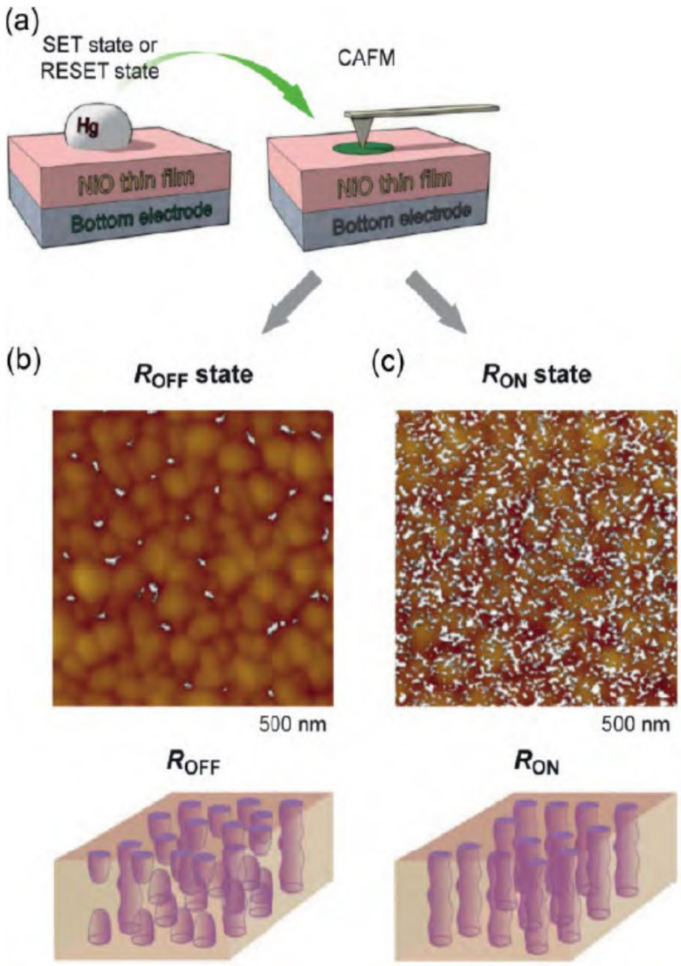

Figure 1.17: Multifilament scenario of a NiO TCM cell: **a)** CP-AFM is used to investigate the surface change due to switching, **b)** multifilament are disconnected (corresponding to OFF state) and **c)** connected (corresponding to ON state) [27].

3 FUNDAMENTAL PROPERTIES OF Li_xCoO_2

3.1 Introduction

This section provides a deeper understanding basis of structural and electrical behavior of Li_xCoO_2. This will help us to explain some electrical processes such as Resistive Switching in the Li_xCoO_2 memristive device afterwards.

3.2 Structural and electrical properties of Li_xCoO_2

3.2.1 Structural properties

$LiCoO_2$ (x=1) is a member of the Li_xMO_2 family (M=Cr, Co, Ni, Mn …) which crystallizes in layered closed-pack-oxygen-anions structure [40]–[43]. $LiCoO_2$ possesses two crystalline structures: Low-Temperature (LT) $LiCoO_2$ and High-Temperature (HT) $LiCoO_2$.

LT-$LiCoO_2$, which is usually fabricated at low temperature from 300°C to 600°C, typically exhibits a spinel cubic structure $Fd3m$ with a lattice constant of 8 Å and the ratio between lattice constants c/a = 4.90 Å [44]. On the other hand, HT-$LiCoO_2$ is synthesized by heating a mixture of lithium carbonate and cobalt oxide at high temperature (>600°C) in air [40], [45]. HT-$LiCoO_2$ indexes to a hexagonal structure belonging to the space group $R\bar{3}m$ with ratio $c/a = 4.99$ which significantly differs from the case of LT-$LiCoO_2$. Furthermore, the similar results with indexed lattice parameters $a = b = 2.8138$ Å and $c = 14.0516$ Å are found in ref. [46], with a tremendous observation of layered structure of HT-$LiCoO_2$ using HRTEM (High Resolution Transmission Electron Microscopy).

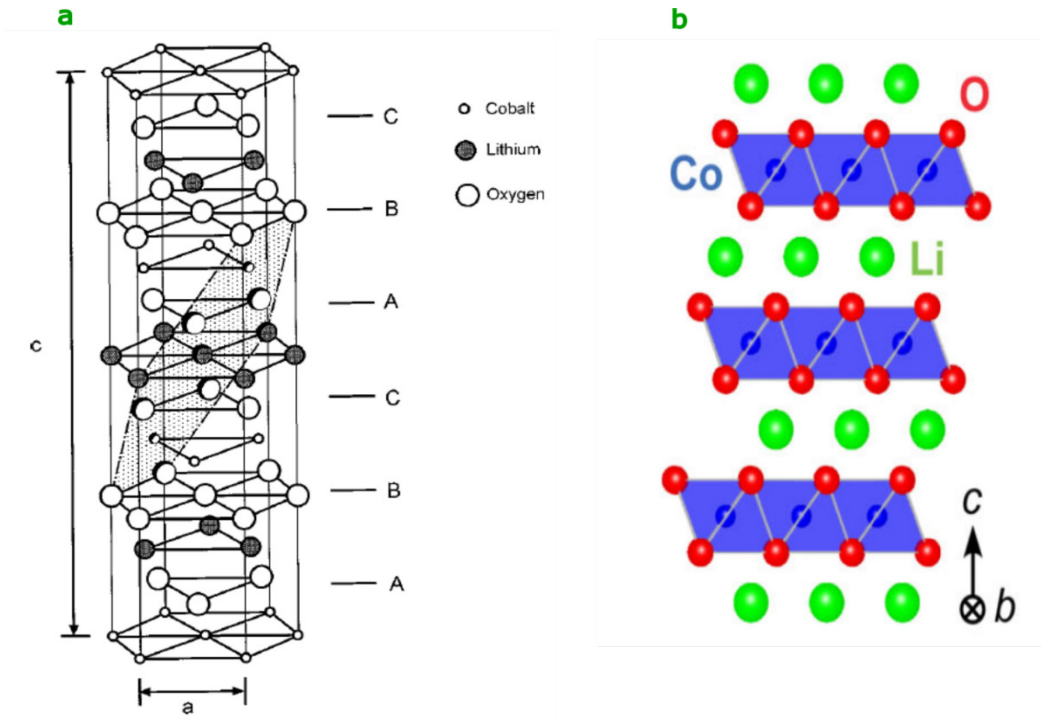

Figure 1.18: a) 3D - hexagonal structure of HT-$LiCoO_2$ with lithium ions alternated between the Oxygen close-packed planes in sequence ABCABC, adapted from [47], **b)** simple 2D view: lithium ions sandwich between CoO_2 layers resulting in a ABAB stack, adapted from [48].

In fact, the layered structure of $LiCoO_2$ enables Li^+ ions to reversibly insert into and to extract from the lattice by electrochemical means and these two processes strongly depend on the crystalline structure of $LiCoO_2$, and the lattice parameters. In contrast to LT-$LiCoO_2$, HT-$LiCoO_2$ possesses a hexagonal structure that allows faster Lithium lithiation/delithiation. It has indeed been reported that the large lattice parameter c/a = 4.99 in the case of HT-$LiCoO_2$ phase indicates a small binding energy of lithium to others [41], resulting in a high mobility of lithium transport.

Furthermore, as shown in **Fig. 1.18**, layers of lithium ion alternate between oxygen layers, or more precisely, between CoO_2 layers if we take into account the strong Van de Waals force in O-Co-O bonding [47]. The functionality of this CoO_2 sub-lattice is twofold. First, it creates the ideal two-dimension pathway for lithium transportation. Second, it prevents a decomposition in close packing structure to enhance the reversibility of lithium intercalation/deintercalation [49].

We can see the lattice parameters evolution as a function of the lithium stoichiometry. As shown in **Fig. 1.19**, the a-parameter is nearly constant as the stoichiometry x varies for both HT- and LT-Li_xCoO_2. On the other hand, the c-parameter of HT-Li_xCoO_2 varies from 14.25 to 14.05 in the interval $0.6 \le x \le 1.0$ whereas the c-parameter of LT-Li_xCoO_2 stays nearly constant.

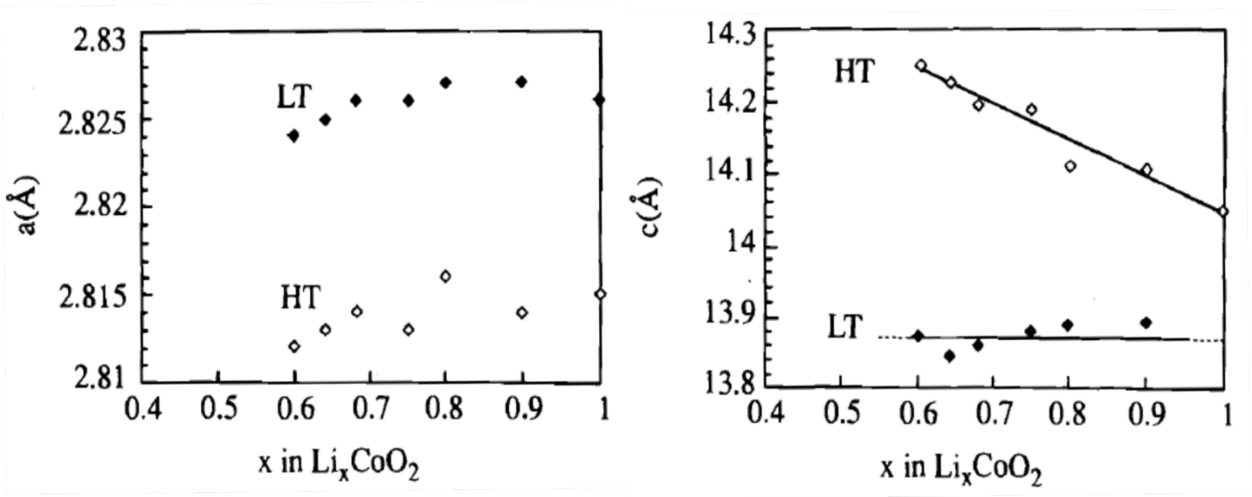

Figure 1.19: Variation of the lattice parameters a and c of HT-Li_xCoO_2 and LT-Li_xCoO_2 as the function of lithium stoichiometry x [43].

The following graph from Ménétrier et al. [50] (**Fig. 1.20**) allows better observing the relation between the c-parameter and the stoichiometry of HT-$LixCoO_2$.

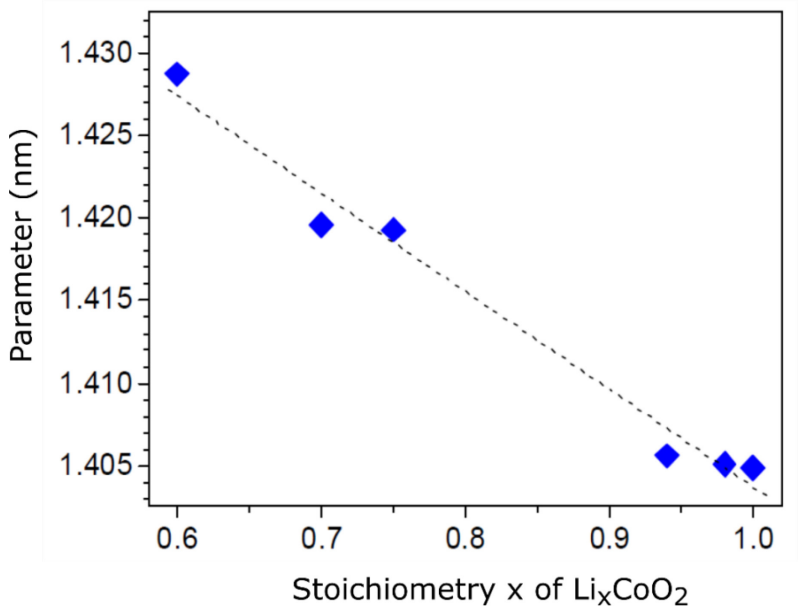

Figure 1.20: Evolution of c-parameter as a function of stoichiometry x, extracted from the table of values from the study of Ménétrier *et al.* [50].

HT-Li_xCoO_2 can be prepared by different elaboration means such as RF-sputtering or Pulsed Laser Deposition (PLD). As schematically drawn in **Fig. 1.21**, the orientation of c-parameter is along with the surface of the substrate in the case of RF sputtering deposition, and is normal to the substrate in the case of PLD deposition. This difference relates to the nature of the substrate and growth conditions. In the case of RF-sputtering the deposition is done on Si/SiO_2 at room temperature while deposition with PLD is obtained in-situ on crystalline surface at 300°C. The texture obtained with RF-sputtering is the consequence of the post-annealing step of the full film, while the obtained texture by PLD is the consequence of surface minimization during in-situ growth. The detailed characterization of the c-parameter orientation of Li_xCoO_2 thin film obtained by RF sputtering (method used in this thesis) will be discussed in the next chapter.

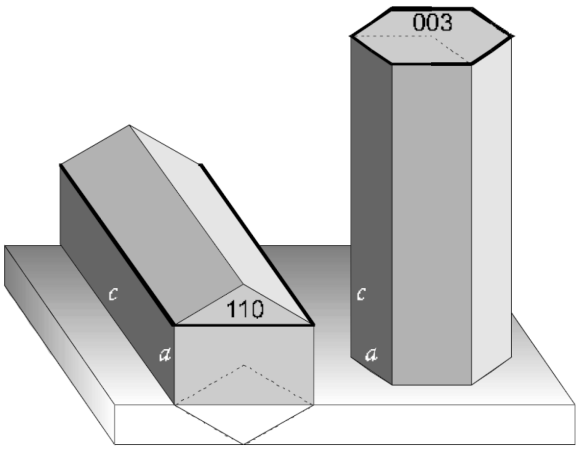

Figure 1.21: The c-parameter orients (left) parallel to the substrate by RF sputtering and normal to the substrate by PLD [51].

3.2.2 Electrical properties

The study of electrical behavior of Li_xCoO_2 dates back to 1980s when Molenda *et al.* observed a conductivity dependence as a function of temperature and stoichiometry (x) of lithium [45]. Following researches published more precise results, as shown in **Fig. 1.22** (Li_xCoO_2 conductivity for several x stoichiometry, as a function of reciprocal temperature [52], [53]).

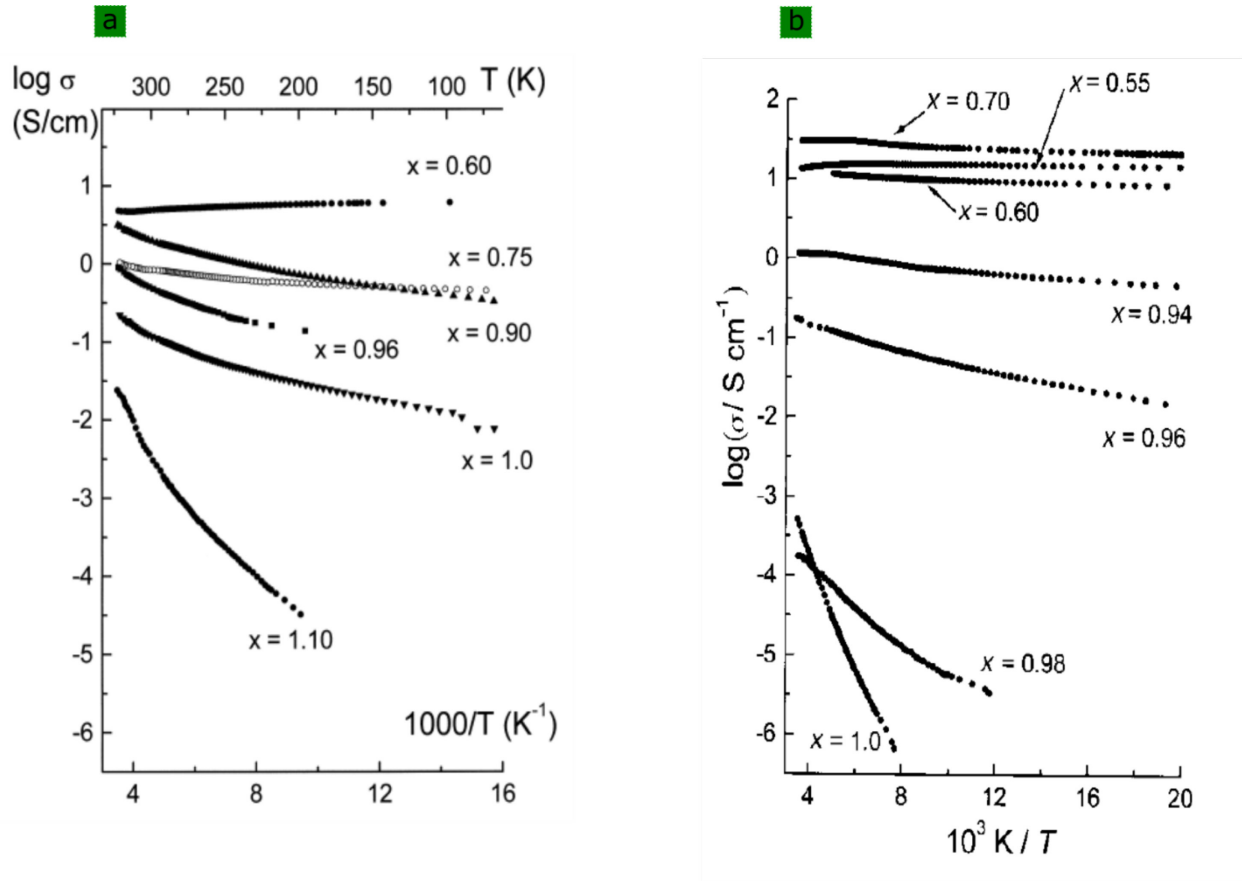

Figure 1.22: Variation of the electronic conductivity as the function of the stoichiometry and the reciprocal temperature in the interval of (a) $0.6 \leq x \leq 1.1$ [53] and (b) $0.55 \leq x \leq 1.0$ [52].

From the conductivity data of **Fig. 1.22**, we plotted the evolution of the conductivity of Li_xCoO_2 as a function of x at ambient temperature. **Fig. 1.23** illustrates the very high variation of the conductivity over a restricted range of $x = [0.8 - 1.0]$ over 5 orders of magnitude.

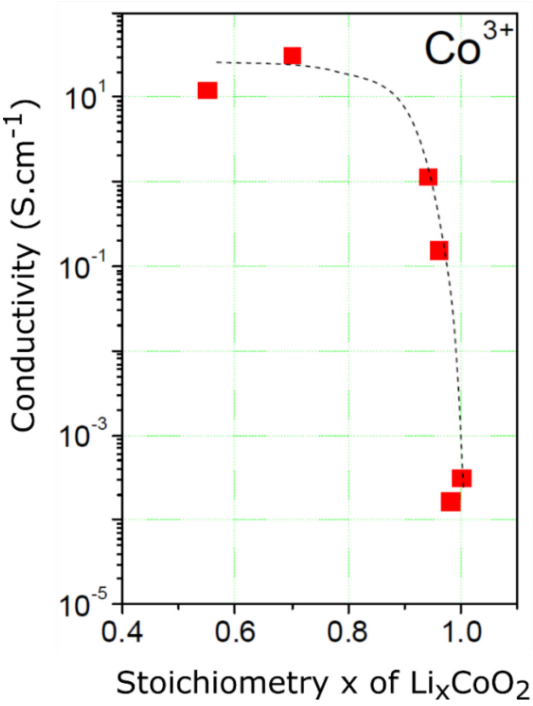

Figure 1.23: Evolution of the conductivity at ambient temperature as a function of the stoichiometry x of Li_xCoO_2, from the data of ref. [54].

Furthermore, it is worth noting that for x ≥0.94, Li_xCoO_2 has a single semiconducting phase and for $x \leq 0.75$, Li_xCoO_2 is in a single metallic phase. In the $0.75 \leq x \leq 0.94$ interval, both phases coexist [56]. Thus, the transition (by intercalation/deintercalation) from $x = 0.94$ to $x = 0.75$ is obtained by the continuously proportional evolution of both phases.

The nature of semiconducting-metallic transition has been studied by researchers using several means. For example, based on 7Li MAS NMR spectra, Menetrier *et al.* [52] conclude that the insulator-metal transition (from $0.94 \leq x \leq 1.0$ to $x \leq 0.75$) originates from a gradual change in the electronic properties from localized to delocalized electrons upon lithium deintercalation. Furthermore, Milewska *et al.* [55] experimentally performed NEXAFS spectroscopy confirming the variation of the electrons state (localized/delocalized).

On the other hand, using density functional theory (DFT) calculations, Marianetti *et al.* [56] state that the semiconducting-metallic transition is due to a Mott transition. The binding of holes (associated to Li ion vacancies) in $LiCoO_2$ structure creates an impurity band. The resulting impurity potential may localize holes, which leads to an insulating phase. For a larger number of Li ion vacancies (thus a larger number of holes), the decomposition of impurity band occurs, hence holes become delocalized, yielding a metallic character. Thus, if we see variation of the electronic properties of films (in Chapter 3), these above mechanisms would account for the resistive switching phenomenon observed in our Li_xCoO_2-based devices.

4 RESEARCHES ON RESISTIVE SWITCHING OF LITHIUM-BASED DEVICES

4.1 Work of Greenlee et al. on Li_xCoO_2 and Li_xNbO_2

In 2013, Greenlee *et al.* simulated (by finite element method) the resistance variation of parallel electrodes cells containing $LiNbO_2$ and $LiCoO_2$ [57], and found that ionic motion of Li^+ inside the films can lead to small resistance changes (less than an order of magnitude). The behavior of such simulated devices appears volatile: indeed, the resistance goes back to its initial value after some while (a few seconds depending on the configuration).

But when considering ion extraction (Li^+ ions go outside the film), they asserted that behavior becomes nonvolatile, and results in a much more significant and *stable* change (several orders of magnitude), as can be seen in **Fig. 1.24** below.

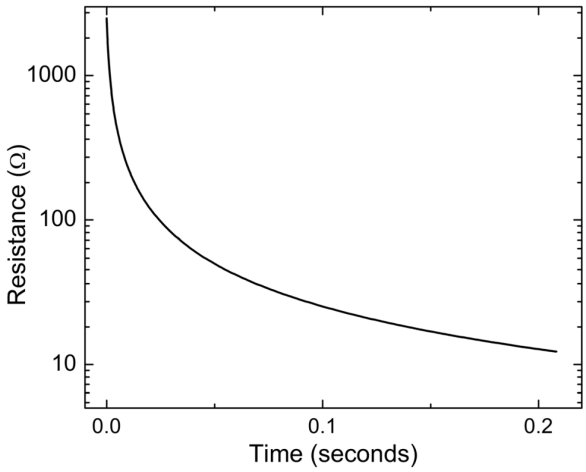

Figure 1.24: Example of transient resistance response. Over 2 orders of magnitude resistance change is achieved in this simulation example.

Greenlee *et al.* attempted to apply their simulation conclusions to experimental devices: $LiCoO_2$ – based transistors have been elaborated [58], using liquid electrolyte (see **Fig. 1.25** left). In this configuration, they observed resistance changes, however the temporal response was very slow (in the 10^5 (seconds) timescale, see **Fig. 1.25** right), which could hardly lead to any memory applicability.

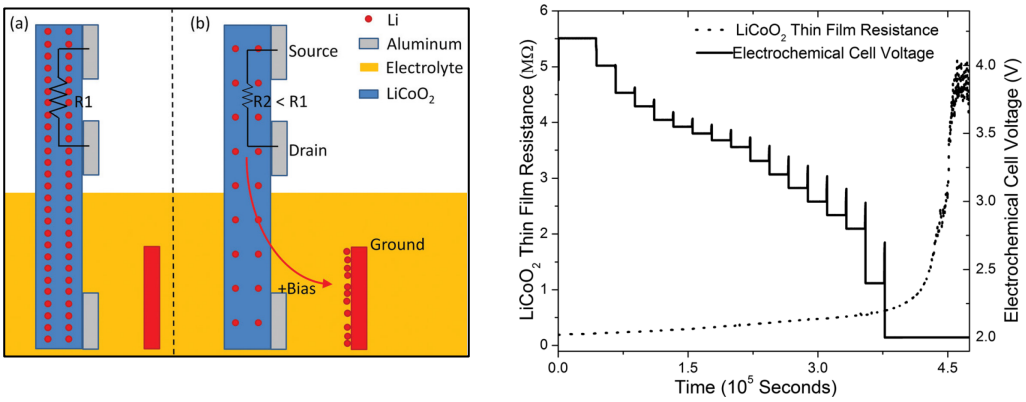

Figure 1.25: (left) Schematic illustration of LixCoO2-based transistor from Greenlee *et al.*, **(right)** temporal response as a function of electrochemical cell voltage, in the 10^5s timescale.

They also studied $LiNbO_2$ crystals [59] and demonstrated a slight memristive behavior by I-V characteristics, due to Li^+ motion inside $LiNbO_2$ (thus, volatile behavior), as can be seen in **Fig. 1.26**.

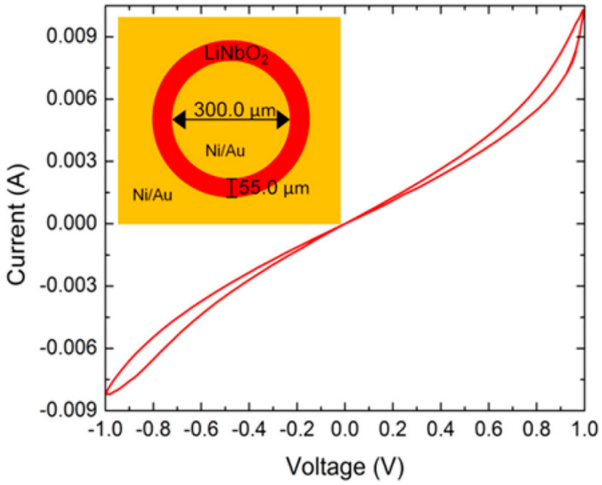

Figure 1.26: I-V loop for a $LiNbO_2$ memristor (inset: schematic view of the annular geometry), showing a memristive effect.

4.2 Work of Fuller et al. on Li_xCoO_2

In 2016, Fuller *et al.* [60] utilized Li_xCoO_2 to elaborate Li-ion cells in planar FET (Field Effect Transistor) configuration, as shown in **Fig. 1.27**. The electrolyte is composed by a LIPON (lithium phosphorous oxynitride) layer of 400nm (the Li_xCoO_2 film is 120nm). The time response is in the order of seconds: hence, this configuration appears attractive for neuromorphic

computation, which does not require fast modifications. Towards memory applicability however, faster switching would be needed. Besides, cycling endurance results shown reach 40 cycles (much higher endurance is however expected).

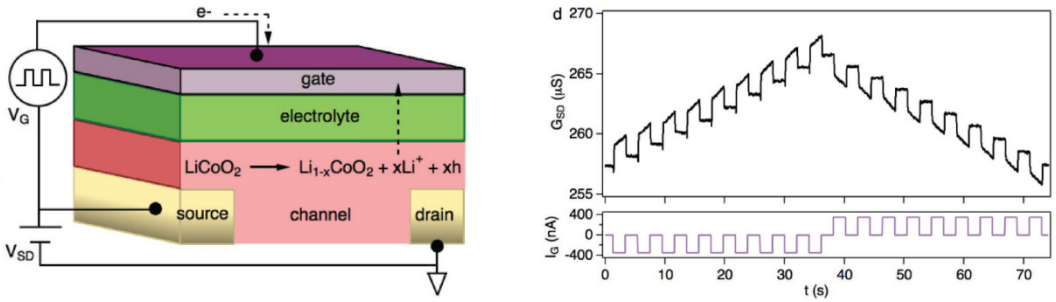

Figure 1.27: (Left) Schematic illustration of Li_xCoO_2-based transistor from Fuller *et al.,* **(right)** conductivity change as a function of current pulsing

4.3 Work of Zhu et al. on Li_xFeO_5

In 2016, Zhu *et al.* [61] succeeded in modifying the electrical and magnetic properties of Li_xFeO_8 film surfaces, as shown in **Fig. 1.28** left. The modifications have been attributed to the intercalation/deintercalation of Li^+ ions in $SrRuO_3$ and to the redox modifications of Fe ions (Fe^{2+} and Fe^{3+} ions have different magnetic moments, which leads to modifications observed on MFM images -not shown here-, and to resistance switching, **Fig. 1.28** right). After a forming process, the HRS/LRS ratio reaches 200.

Zhu *et al.* noted however that additional studies were needed to fully reveal the filament formation processes involving the Li-ion storage mechanism.

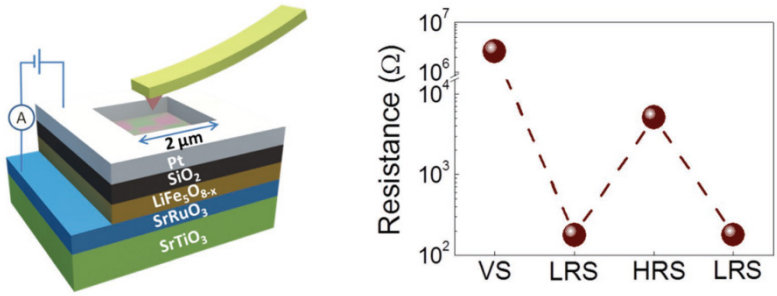

Figure 1.28: (Left) Schematic illustration of Li_xFeO_5 modification from Zhu *et al.,* **(right)** resistance change as a function of voltage application

4.4 Research on Resistive Switching of Li_xCoO_2 at GeePs and collaboration labs

In 2007, electrical properties of layered cobalt oxide such as Na_xCoO_2 were initially studied using Conducting Probe Atomic Force Microscopy (CP-AFM). Schneegans *et al.* [62] have carried out probe-mediated local surface modifications allowing reversible modifications of the surface resistivity of monocrystalline Na_xCoO_2 by applying adequate tip/sample voltage (> 2V to modify the surface conductivity, and +1V to read the modifications). These results were promising towards high density information storage. As illustrated in **Fig. 1.29**, at least three states could be written on the *ab* face of Na_xCoO_2 single crystal using the bias voltage [63].

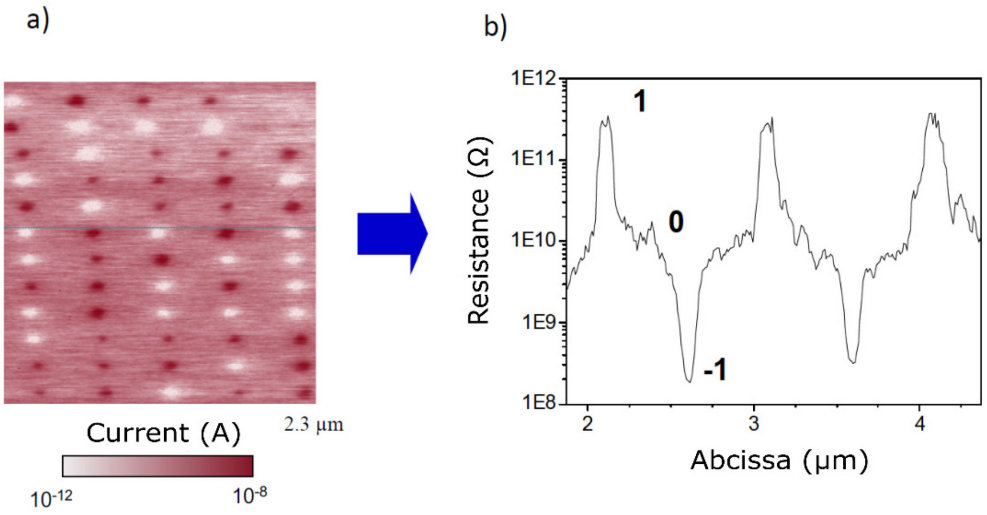

Figure 1.29: a) Conducting (in red) and insulating spots (in white) were obtained using positive bias (+4V) and negative bias (-3V) under nitrogen atmosphere, respectively (then read at +1V). **b)** At least three states of resistance could be randomly "stored" on Na_xCoO_2.

Inspired from this work, another member of layered cobalt oxide such as Li_xCoO_2 (in the form of films) has been studied in collaboration with C2N, LITEN-CEA and the University of Cyprus. As shown in **Fig 1.30**, local electrochemical modifications can also be achieved by application of bias voltage between a Li_xCoO_2/doped-Si layer and a CP-AFM tip, while the tip scans the surface. The film becomes conducting if the sample/tip bias is positive and reversely, becomes insulating if the bias is negative.

The electrochemical nature of this local resistance modification of Li_xCoO_2 surfaces was studied in detail by V.H. Mai [50]. Although similar behavior has been observed in both materials, Li_xCoO_2 differs from Na_xCoO_2, as it is much more stable in ambient air. Indeed, the surface of Na_xCoO_2 is covered with carbonates in a few seconds (vs. a few days for Li_xCoO_2).

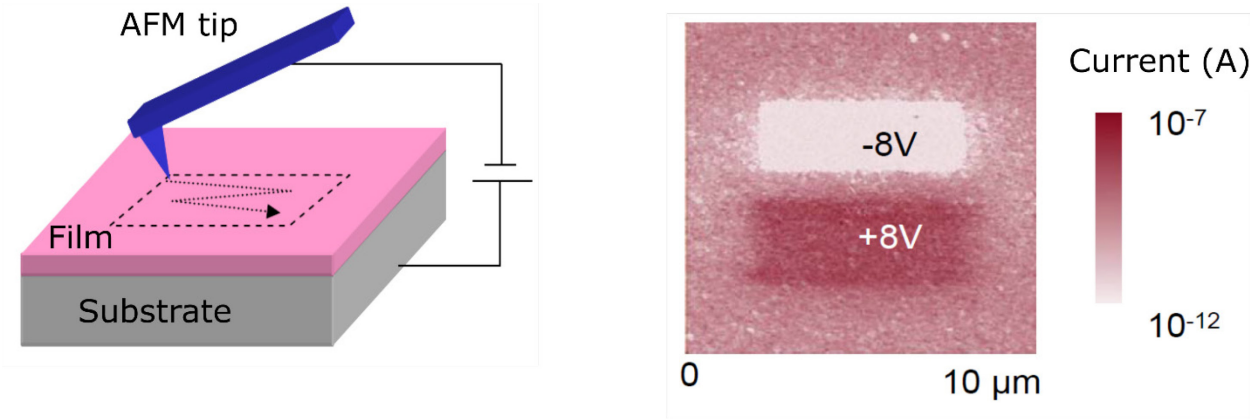

Figure 1.30: Schematic of experiment (left). CP-AFM electrical image (right): conducting (in red) and insulating zone (in white) were obtained using positive bias (+8V) and negative bias (-8V) under ambient atmosphere, respectively, then read at +1V.

Mouradpour *et al.* studied then the behavior of Li_xCoO_2 thin films in the MIM configuration, for which the electrodes lateral size is greater than the 100nm-thick films. They observed for the first time in 2011, a reversible resistive abrupt jump in resistance, as shown in **Fig. 1.31**.

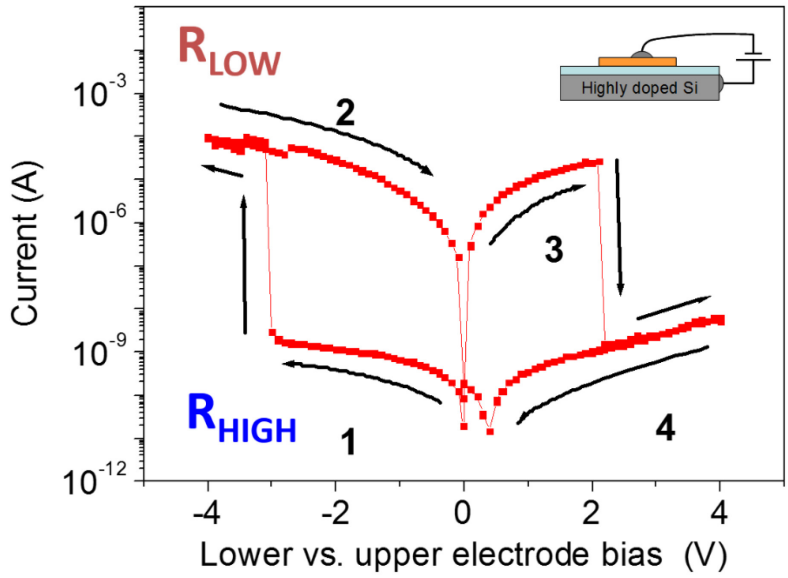

Figure 1.31: I-V characteristics of an MIM sub-millimetric cell (100x400 µm²) composed of a Li_xCoO_2 thin film: a bipolar resistive switching is observed, by using for ramp voltage (0V → -4V → +4V →0V, sweep rate $100\ mV.s^{-1}$). An abrupt resistance jump occurs at -3V (from a high to a low resistance state), and at +2.5V (from a low to a high resistance state). The resistance states are stable between these threshold voltages [63].

4.4.1 Study the involved mechanism

Two different configurations have been studied: {AFM tip/ film atomic contact} and Metal-Insulator-Metal (MIM) stacks in which the film is sandwiched between two electrodes as shown in **Fig. 1.32**. The film in the MIM stack configuration becomes more conducting (using read voltage +1V) after a negative bias (-8V 1s) is applied to the device (**Fig. 1.32a)**. Surprisingly, in the case of a tip-sample contact, the film becomes more insulating (using read voltage +1V) after scanning at -8V (**Fig 1.32b**). Hence two different mechanisms were proposed to explain this paradoxical difference.

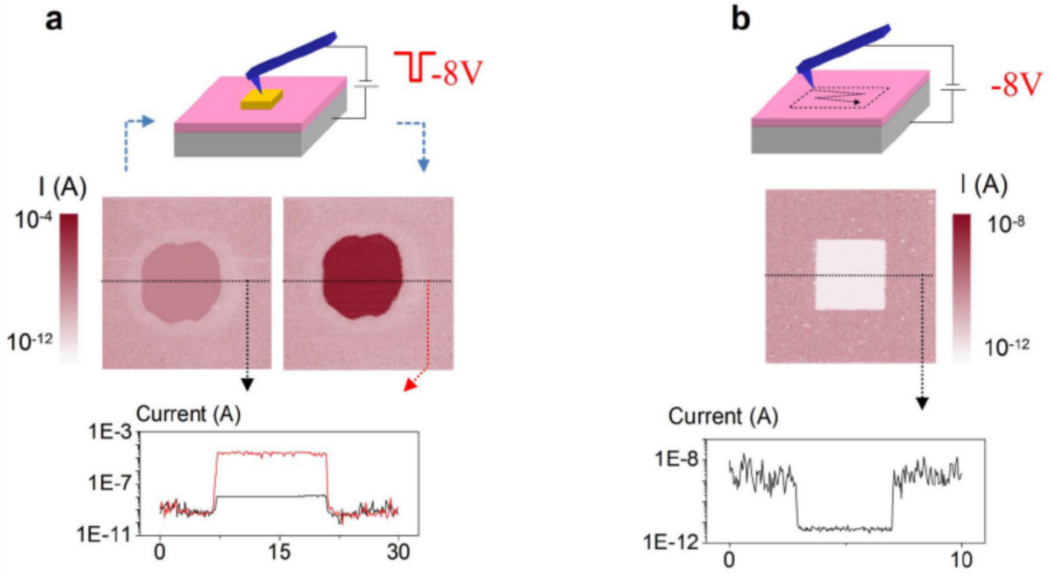

Figure 1.32: Two different configurations: **a)** MIM cell with 10x10 µm^2 top electrode, the resistance decreases four orders of magnitude after application of a bias -8V for 1s, **b)** tip/ Li_xCoO_2 sample nanocontact: the resistance increases more than three orders of magnitude when a -8V is applied [64].

In the tip-sample configuration, the cause of resistance modifications has been clarified. The electrical potential concentrated on the tip/sample nanocontact modifies the surface neighborhood (**Fig. 1.33**) [64]. If the substrate is negatively polarized, Co^{4+} is reduced to Co^{3+} and H_2O (from the meniscus) oxidized to O_2. This was established by studying the influence of ambient-water-vapor-pressure on the electrochemical modifications. The modification of the film surface could not be carried out at low pressure, implying a much lower water meniscus size.

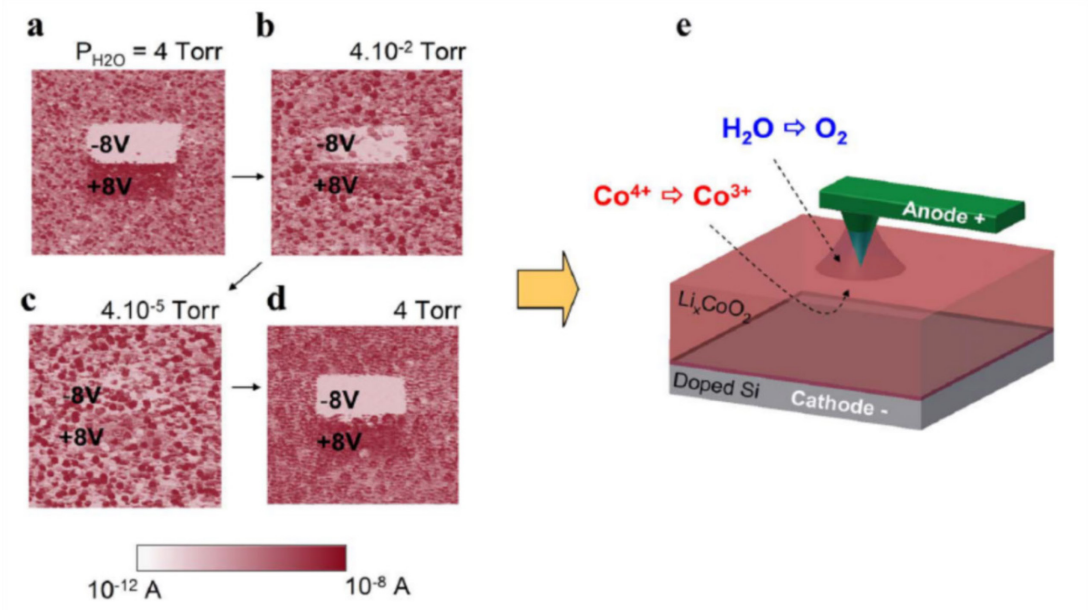

Figure 1.33: (a-d) electrical images showing a dependence of surface modification (of area of 10x10 μm^2) on the ambient water vapor pressure: the lower the pressure, the more difficult the modification; **(e)** Schematics of mechanism for tip/sample modification, based on the redox reactions of cobalt and water meniscus.

In the MIM configuration, on the other hand, the electrical potential is distributed over the whole volume between the top electrode and the bottom substrate. Hence, it is predicted that electrochemical reactions involve here cobalt and lithium in the film. Such a mechanism was proposed by V.H Mai *et al.* [50]. However, the direct evidence of the mechanism involving ion transport remained an unanswered question. Therefore, one of the objectives of this thesis is to study further the mechanism in the MIM configuration.

4.4.2 Preliminary results on kinetics and cycling endurance

Since another objective of this thesis is related to the applicability towards resistive Re-RAM memory, some preliminary results obtained by V.H. Mai (in the previous thesis) are presented here. First, the switching kinetics of MIM cell had been preliminary studied using bias pulses as shown in **Fig. 1.34**. The resistance of cells decreases progressively as a function of consecutive pulses applied.

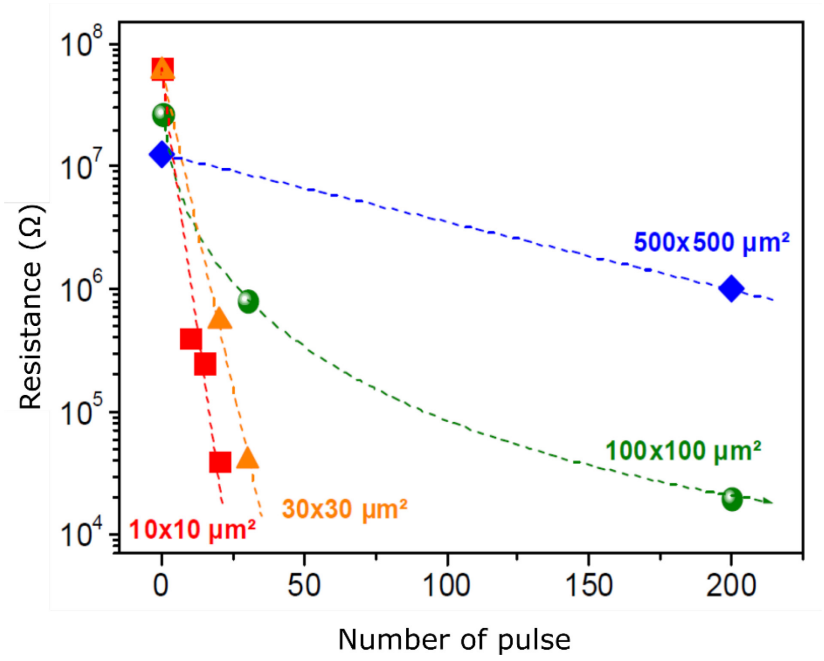

Figure 1.34: Resistance of Li_xCoO_2 MIM cells {Au/LixCoO2/p-doped Si} of different top electrode sizes (10x10 µm², 30x30 µm², 100x100µm² and 500x500 µm²), as a function of the number of applied pulses −8V ($\tau = 50ms, T = 150ms$). The smaller the top electrode sizes, the faster the switching kinetics [64].

A more detailed experimental study will be carried out and presented in the next chapters and a simple mathematic model will be proposed to account for the experimental results.

Moreover, preliminary endurance results have been obtained on cells, as shown in **Fig. 1.35**. The endurance of the device was obtained by *manually* switching from HRS to LRS and vice-versa (**Fig. 1.35a**). In **Fig. 1.35b**, the endurance was automatically obtained by a program, which will be afterwards developed and improved in my thesis. Nevertheless, the endurance had not yet been investigated as a function of different parameters (voltage pulse characteristic, nature of the top electrode…). This thesis will point out the influence of these parameters on the endurance of the Li_xCoO_2 devices.

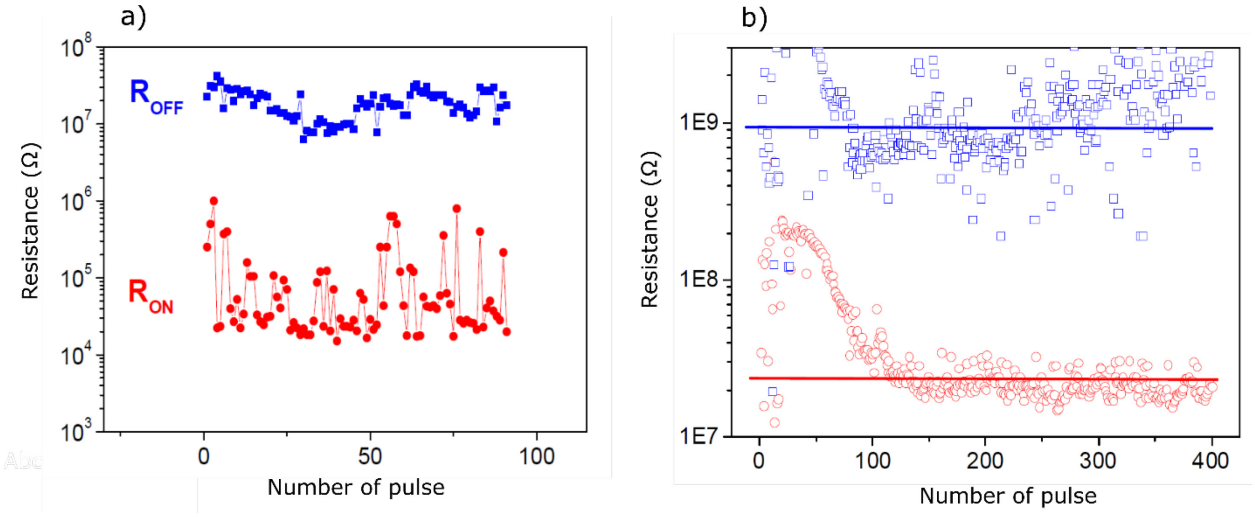

Figure 1.35: Preliminary results of the endurance of Li_xCoO_2 MIM cell were obtained: **a)** by manually applying the pulses and **b)** by an automatic program (on the small TE with 10x10µm^2 in size [50]). This result is promising towards long endurance with small MIM LixCoO2-based cells.

5 CONCLUSION

In this chapter, the state of the art has been presented on the main characteristics of Flash memories, as well as emerging nonvolatile memories, such as FeRAM, M-RAM, PC-RAM, and ReRAM. To overcome the limitations of Flash memories, Re-RAM memories seem promising in terms of switching energy and rapidity, but in-depth studies are recent, dating back to the early 2000s. They have not yet fully clarified all the mechanisms which can be involved in resistive switching.

Studies began at the GeePs in 2010-2011, on a particular class of materials, cobalt oxides. A switching phenomenon was observed on Li_xCoO_2 film-based sub-millimetric cells with a very high HRS/LRS ratio (over 4 orders of magnitude). In the case of an {AFM tip / Li_xCoO_2 film surface} contact of atomic size, the mechanism has already been clarified during V.H. Mai's thesis (redox reaction of Co, and water from the tip/sample meniscus). However, in the configuration of electrodes whose lateral size is greater than the thickness of the film, the mechanism appears however "inverted". In this latter case (MIM stacks), a mechanism has been proposed, which appears consistent with indirect observations. However, direct proof of the existence of such a mechanism has remained an unanswered question. The objective of my thesis is to clarify completely the chemical phenomenon (s) at the origin of the RS in the MIM configuration, and to evaluate more precisely the performance potentialities (kinetics, cycling endurance, stability …) of this class of materials for potential applicability towards submicron and nanometer scale Re-RAM.

6 REFERENCES

[1] F. Pan, C. Chen, Z. Wang, Y. Yang, J. Yang, and F. Zeng, "Nonvolatile resistive switching memories-characteristics, mechanisms and challenges," *Prog. Nat. Sci. Mater. Int.*, vol. 20, pp. 1–15, 2010.

[2] D. S. Jeong *et al.*, "Emerging memories: resistive switching mechanisms and current status," *Reports Prog. Phys.*, vol. 75, p. 76502, 2012.

[3] R. Waser, *Nanoelectronics and Information Technology, 3rd Edition*. Wiley, 2012.

[4] R. Bez, E. Camerlenghi, A. Modelli, and A. Visconti, "Introduction to flash memory," *Proc. IEEE*, vol. 91, no. 4, pp. 489–501, 2003.

[5] "What is flash memory? - Definition from WhatIs.com." [Online]. Available: http://searchstorage.techtarget.com/definition/flash-memory. [Accessed: 28-Feb-2016].

[6] "Samsung announces 40 nm Flash, predicts 20 nm devices | TG Daily," 2006. [Online]. Available: http://www.tgdaily.com/hardware-features/28504-samsung-announces-40-nm-flash-predicts-20-nm-devices. [Accessed: 15-Dec-2015].

[7] P. Misra, Y. Sharma, G. Khurana, and R. S. Katiyar, "Resistive switching characteristics of mixed oxides," *Emerg. Mater. Res.*, vol. 4, no. 1, pp. 18–31, 2015.

[8] D. Pantel, S. Goetze, D. Hesse, and M. Alexe, "Room-temperature ferroelectric resistive switching in ultrathin Pb(Zr 0.2 Ti 0.8)O3 films.," *ACS Nano*, vol. 5, no. 7, pp. 6032–6038, 2011.

[9] V. Garcia and M. Bibes, "Ferroelectric tunnel junctions for information storage and processing," *Nat. Commun.*, vol. 5, pp. 1–12, 2014.

[10] E. Y. Tsymbal and A. Gruverman, "Ferroelectric tunnel junctions: Beyond the barrier.," *Nat. Mater.*, vol. 12, no. 7, pp. 602–4, Jul. 2013.

[11] A. Chanthbouala *et al.*, "A ferroelectric memristor," *Nat. Mater.*, vol. 11, no. 10, pp. 860–864, 2012.

[12] S. Boyn *et al.*, "High-performance ferroelectric memory based on fully patterned tunnel junctions," *Appl. Phys. Lett.*, vol. 104, no. 5, pp. 1–4, 2014.

[13] H. Yamada *et al.*, "Giant electroresistance of super-tetragonal BiFeO3-based ferroelectric tunnel junctions," *ACS Nano*, vol. 7, no. 6, pp. 5385–5390, 2013.

[14] J. Meena, S. Sze, U. Chand, and T.-Y. Tseng, "Overview of emerging nonvolatile memory technologies," *Nanoscale Res. Lett.*, vol. 9, no. 1, p. 526, 2014.

[15] J. M. Slaughter, "Materials for Magnetoresistive Random Access Memory," *Annu. Rev. Mater. Res.*, vol. 39, no. 1, pp. 277–296, 2009.

[16] J. S. Moodera, L. R. Kinder, T. M. Wong, and R. Meservey, "Large magnetoresistance at room temperature in ferromagnetic thin film tunnel junctions," *Phys. Rev. Lett.*, vol. 74, no. 16, pp.

3273–3276, 1995.

[17] Y. Fujisaki, "Current status of nonvolatile semiconductor memory technology," *Jpn. J. Appl. Phys.*, vol. 49, pp. 1000011–1000014, 2010.

[18] E. Titus, M. K. Singh, R. Krishna, R. G. Dias, A. Ferreira, and J. Gracio, "Carbon Nanotube Based Magnetic Tunnel Junctions (MTJs) for Spintronics Application," 2011. [Online]. Available: http://www.intechopen.com/books/electronic-properties-of-carbon-nanotubes/carbon-nanotube-based-magnetic-tunnel-junctions-mtjs-for-spintronics-application. [Accessed: 01-Jan-2016].

[19] S. Raoux, F. Xiong, M. Wuttig, and E. Pop, "Phase change materials and phase change memory," *MRS Bull.*, vol. 39, no. 8, pp. 703–710, 2014.

[20] H. S. P. Wong *et al.*, "Phase Change Memory," *Proc. Ieee*, vol. 98, no. 12, pp. 2201–2227, 2010.

[21] G. W. Burr *et al.*, "Phase change memory technology," *J. Vac. Sci. Technol. B*, vol. 28, no. 2, pp. 223–262, 2010.

[22] I. V. Karpov, M. Mitra, D. Kau, G. Spadini, Y. A. Kryukov, and V. G. Karpov, "Fundamental drift of parameters in chalcogenide phase change memory," *J. Appl. Phys.*, vol. 102, no. 12, p. 124503, Dec. 2007.

[23] "Phase Change Memory and Electrothermal Transport in Chalcogenides | Stanford NanoHeat Lab." [Online]. Available: https://nanoheat.stanford.edu/projects/phase-change-memory-and-electrothermal-transport-chalcogenides. [Accessed: 07-Mar-2016].

[24] "Stanford Memory Trends | Stanford Nanoelectronics Lab." [Online]. Available: https://nano.stanford.edu/stanford-memory-trends. [Accessed: 16-Dec-2015].

[25] A. Sawa, "Resistive switching in Rapid advances in information technology rely on high-speed and," *Mater. Today*, vol. 11, no. 6, pp. 28–36, 2008.

[26] R. Waser and M. Aono, "Nanoionics-based resistive switching memories," *Nat. Mater.*, vol. 6, no. 11, pp. 833–840, 2007.

[27] R. Waser, R. Dittmann, G. Staikov, and K. Szot, "Redox-Based Resistive Switching Memories – Nanoionic Mechanisms , Prospects , and Challenges," *Adv. Mater.*, vol. 21, no. 25–26, pp. 2632–2663, 2009.

[28] K. Kinoshita *et al.*, "Reduction in the reset current in a resistive random access memory consisting of Ni Ox brought about by reducing a parasitic capacitance," *Appl. Phys. Lett.*, vol. 93, no. 3, pp. 2012–2015, 2008.

[29] I. Valov and M. N. Kozicki, "Cation-based resistance change memory," *J. Phys. D. Appl. Phys.*, vol. 46, no. 7, p. 74005, 2013.

[30] R. Waser, R. Dittmann, C. Staikov, and K. Szot, "Redox-based resistive switching memories nanoionic mechanisms, prospects, and challenges," *Adv. Mater.*, vol. 21, no. 25–26, pp. 2632–2663, 2009.

[31] Y. Yang, P. Gao, S. Gaba, T. Chang, X. Pan, and W. Lu, "Observation of conducting filament growth in nanoscale resistive memories," *Nat. Commun.*, vol. 3, p. 732, 2012.

[32] G. Niu *et al.*, "Geometric conductive filament confinement by nanotips for resistive switching of HfO2-RRAM devices with high performance," *Sci. Rep.*, vol. 6, no. April, p. 25757, 2016.

[33] H. Lv *et al.*, "Evolution of conductive filament and its impact on reliability issues in oxide-electrolyte based resistive random access memory.," *Sci. Rep.*, vol. 5, p. 7764, 2015.

[34] D.-H. Kwon *et al.*, "Atomic structure of conducting nanofilaments in TiO2 resistive switching memory.," *Nat. Nanotechnol.*, vol. 5, no. 2, pp. 148–153, 2010.

[35] D. De Young, and M. Sharma, "Letters To Nature," *Nature*, vol. 433, no. January, pp. 47–50, 2005.

[36] I. Valov *et al.*, "Nanobatteries in redox-based resistive switches require extension of memristor theory," *Nat. Commun.*, vol. 4, pp. 1771–1779, 2013.

[37] L. Yang, *Resistive Switching in TiO2 thin films*. Schriften des Forschungszentrums Jülich, 2011.

[38] C. Baeumer *et al.*, "Spectromicroscopic insights for rational design of redox-based memristive devices.," *Nat. Commun.*, vol. 6, p. 8610, 2015.

[39] K. Skaja *et al.*, "Avalanche-Discharge-Induced Electrical Forming in Tantalum Oxide-Based Metal–Insulator–Metal Structures," *Adv. Funct. Mater.*, no. Mim, pp. 7154–7162, 2015.

[40] K. Mizushima, P. C. Jones, P. J. Wiseman, and J. B. Goodenough, "LixCoO2 (0<x<-1): A new cathode material for batteries of high energy density," *Solid State Ionics*, vol. 3–4, no. C, pp. 171–174, 1981.

[41] R. Gummow, M. Thackeray, W. David, and S. Hull, "Structure and electrochemistry of lithium cobalt oxide synthesised at 400??C," *Mater. Res. Bull.*, vol. 27, no. 3, pp. 327–337, 1992.

[42] B. Garcia, P. Barboux, F. Ribot, A. Kahn-Harari, L. Mazerolles, and N. Baffier, "The structure of low temperature crystallized LiCoO2," *Solid State Ionics*, vol. 80, no. 1–2, pp. 111–118, 1995.

[43] B. Garcia, "Electrochemical Properties of Low Temperature Crystallized LiCoO2," *J. Electrochem. Soc.*, vol. 144, no. 4, p. 1179, 1997.

[44] E. Rossen, J. N. Reimers, and J. R. Dahn, "Synthesis and electrochemistry of spinel LT-LiCoO2," *Solid State Ionics*, vol. 62, no. 1–2, pp. 53–60, 1993.

[45] J. Molenda, A. Stoklosa, and T. Bak, "Modification in the electronic structure of cobalt bronze LixCoO2 and the resulting electrochemical properties," *Solid State Ionics*, vol. 36, no. 1–2, pp. 53–58, 1989.

[46] Y. Shao-Horn, L. Croguennec, C. Delmas, E. C. Nelson, and M. a O'Keefe, "Atomic resolution of lithium ions in LiCoO2.," *Nat. Mater.*, vol. 2, no. July, pp. 464–467, 2003.

[47] A. Van der Ven, M. Aydinol, G. Ceder, G. Kresse, and J. Hafner, "First-principles investigation of phase stability in LixCoO2," *Phys. Rev. B*, vol. 58, no. 6, pp. 2975–2987, 1998.

[48] K. Iwaya *et al.*, "Impact of lithium-ion ordering on surface electronic states of Li xCoO2," *Phys. Rev. Lett.*, vol. 111, no. 12, pp. 1–5, 2013.

[49] G. Amatucci, J. Tarascon, and L. Klein, "CoO2, The End Member of the LixCoO2 Solid Solution," *J. Electrochem. Soc.*, vol. 143, no. 3, pp. 1114–1123, 1996.

[50] V. H. Mai, "Etude de phenomenes de commutation de resistance de films minces de LixCoO2. Autre [cond-mat.other]. Universite Paris Sud - Paris XI, 2014. Fran ̧cais. < NNT : 2014PA112115 > . < tel-01164971 >," *Thesis Univ. Paris-Sud*, 2014.

[51] P. J. Bouwman, *Lithium Intercalation in preferentially oriented submicron LiCoO2 films*. 2002.

[52] M. Ménétrier, I. Saadoune, S. Levasseur, and C. Delmas, "The insulator–metal transition upon lithium deintercalation from LiCoO2: electronic properties and 7Li NMRstudy," *J. Mater. Chem.*, vol. 9, pp. 1135–1140, 1999.

[53] S. Levasseur, M. Menetrier, E. Suard, and C. Delmas, "Evidence for structural defects in non-stoichiometric HT-LiCoO2: electrochemical, electronic properties and Li-7 NMR studies," *Solid State Ionics*, vol. 128, no. 1–4, pp. 11–24, 2000.

[54] S. L. and C. D. M. Menetrier, I. Saadoune, "The insulator – metal transition upon lithium deintercalation from," *J. Mater. Chem.*, vol. 9, pp. 1135–1140, 1999.

[55] A. Milewska *et al.*, "The nature of the nonmetal–metal transition in LixCoO2 oxide," *Solid State Ionics*, vol. 263, pp. 110–118, 2014.

[56] C. a Marianetti, G. Kotliar, and G. Ceder, "A first-order Mott transition in LixCoO2.," *Nat. Mater.*, vol. 3, no. 9, pp. 627–31, 2004.

[57] J. D. Greenlee, J. C. Shank, M. Brooks Tellekamp, and W. Alan Doolittle, "Spatiotemporal drift-diffusion simulations of analog ionic memristors," *J. Appl. Phys.*, vol. 114, no. 3, pp. 1–10, 2013.

[58] J. D. Greenlee, C. F. Petersburg, W. G. Daly, F. M. Alamgir, and W. Alan Doolittle, "In situ investigation of the channel conductance of a Li 1-xCoO2 ($0 < x < 0.5$) ionic-electronic transistor," *Appl. Phys. Lett.*, vol. 102, no. 21, pp. 10–14, 2013.

[59] J. D. Greenlee, J. C. Shank, M. B. Tellekamp, B. P. Gunning, C. A. M. Fabien, and W. A. Doolittle, "Liquid phase electro-epitaxy of memristive LiNbO2 crystals," *Cryst. Growth Des.*, vol. 14, no. 5, pp. 2218–2222, 2014.

[60] E. J. Fuller *et al.*, "Li-Ion Synaptic Transistor for Low Power Analog Computing," *Adv. Mater.*, vol. 29, no. 4, pp. 1–8, 2017.

[61] X. Zhu *et al.*, "In Situ Nanoscale Electric Field Control of Magnetism by Nanoionics," *Adv. Mater.*, vol. 28, no. 35, pp. 7658–7665, 2016.

[62] O. Schneegans *et al.*, "NaxCoO2 : A New Opportunity for Rewritable Media ?," *J. Am. Chem. Soc.*, vol. 129, pp. 7482–7483, 2007.

[63] A. Moradpour *et al.*, "Resistive switching phenomena in Li xCoO 2 thin films," *Adv. Mater.*, vol. 23, no. 36, pp. 4141–4145, 2011.

[64] V. H. Mai *et al.*, "Memristive and neuromorphic behavior in a Li(x)CoO2 nanobattery.," *Sci. Rep.*, vol. 5, p. 7761, 2015.

CHAPTER 2

FABRICATION METHODS AND CHARACTERIZATIONS OF Li_xCoO_2 THIN FILMS AND DEVICES

TABLE OF CONTENTS

INTRODUCTION

Chapter 2 presents fabrication methods and characterization techniques of Li_xCoO_2 thin films and devices elaborated therefrom. It consists of 3 parts. In the first part, we recall the elaboration method of films (RF sputtering setup at the LITEN-CEA and the C2N-Orsay). The deposition techniques of upper electrodes (Au, Ti, Cr) on the films (to obtain electrode/film/electrode devices) will be presented: Joule heating thermal evaporation has been used at LPS, and I carried out deposition by e-beam evaporation at C2N-Orsay.

In the second part we study the structural properties of Li_xCoO_2 thin films (coming from the LITEN-CEA), by using different characterization techniques. The mean thickness has been determined by X ray Reflexion (XRR), and the crystalline parameters (c-parameter and grain size) have been obtained by X-ray Diffraction (XRD) at the LPS lab. The film structure and the {film/Si substrate} interface (SiOx layer) have been analyzed, also at the LPS lab, by Scanning Transmission Electron Microscopy (TEM). Depth profiles and 3D maps of chemical composition (Li, Co, O, Si elements) have been obtained by Secondary Ion Mass Spectroscopy (SIMS) at the GEMaC lab located at Versailles.

In the third and last part, we present 3 techniques to study the electrical properties of MIM fabricated devices. I frequently used Conducting Probe AFM (CP-AFM) during my thesis at GeePs lab to characterize the topographical/electrical properties of film surfaces and study the RS behavior of MIM cells (using bias ramps and bias pulses). The second technique (two-probe method at C2N-Orsay) allows investigation of the performances of macroscopic devices (100x100 µm² and beyond, due to the macroscopic probe size): specifically, I developed programs and used these towards endurance and I-V curves measurements. Finally, I also utilized Electrochemical Impedance Spectroscopy (EIS) at the C2N-Orsay lab to try to characterize the ionic transport process in the MIM cells.

1 ELABORATION OF Li_xCoO_2 THIN FILMS AND DEVICES

1.1 Radio Frequency Magnetron sputtering setup

To elaborate the Li_xCoO_2 films, a Radio Frequency Magnetron sputtering setup has been built up at the C2N-Orsay lab.

The basic principle of sputtering is as follows. An inert gas Argon in a vacuum chamber is ionized by a high DC voltage (10kV) applying to the anode and cathode where the substrate and the target are placed, respectively. This process creates plasma of positively charged ions Ar^+ and negatively charged electrons. Due to the high electric field, the Ar^+ ions are accelerated to the cathode and start bombarding the target. The bombardment is a transferring process of momentum of the heavy Ar^+ ions to the desired source material atoms and a yields an ejection of those atoms, which are condensed on the substrate to form a thin film. The principle of the sputtering technique is simply sketched in the **Fig. 2.1**.

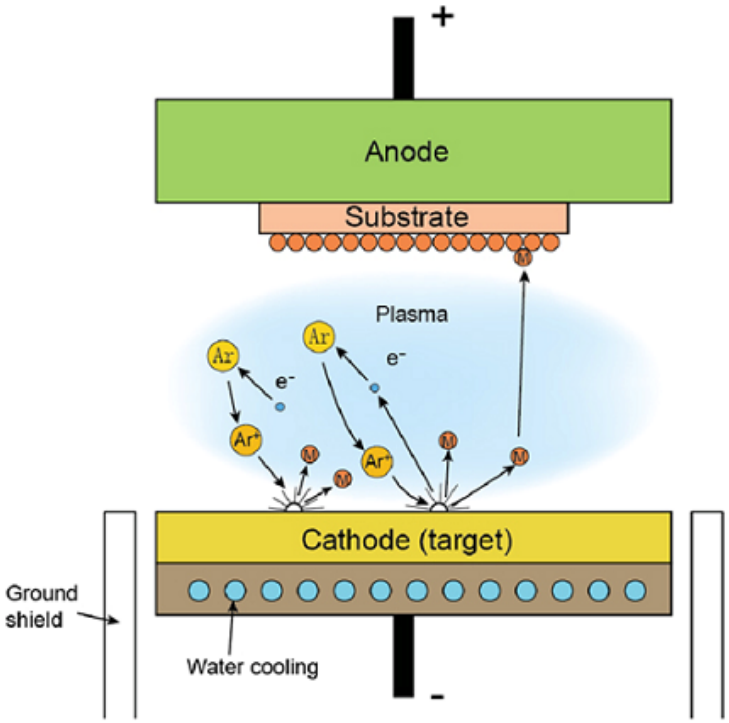

Figure 2.1: The principle of sputtering method [1].

RF magnetron sputtering is an extremely appropriate method to fabricate high quality and homogeneous Li_xCoO_2 thin films. At the C2N-Orsay Laboratory, the RF magnetron sputtering setup has being built up since the beginning of this thesis.

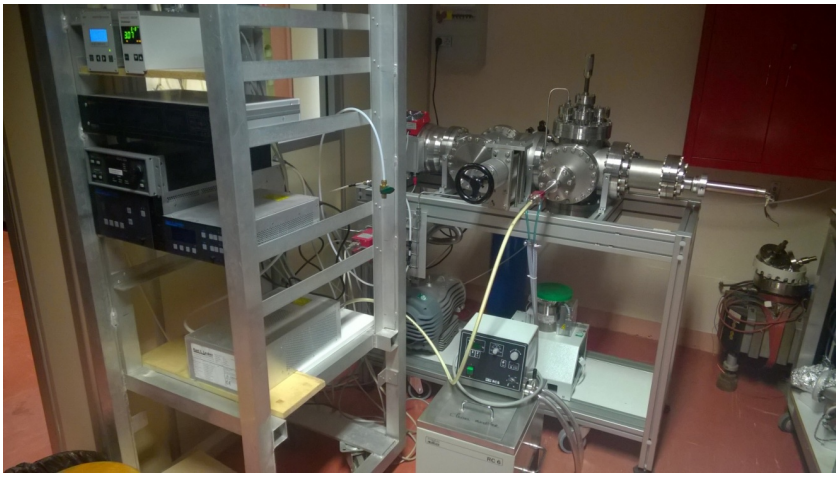

Figure 2.2: Photo of the Sputtering system which is being built at C2N-Orsay.

1.2 Elaboration of the Li_xCoO_2 thin films using RF Magnetron Sputtering

The building sputtering at C2N-Orsay is being finalized, but is currently not yet completely ready for Li_xCoO_2 films deposition. Hence the films have been deposited at CEA Grenoble using RF magnetron reactive sputtering (Alcatel SCM 600 apparatus) on p-doped Si (111) with an applied RF power of 500 W, and a stoichiometric target. The films were grown in a gas rate Ar/O_2: 3/1 atmosphere at pressure = 2.2 Pa and a bias voltage of 250 V was applied to the substrate. Thus, 4-inches wafers were obtained.

Subsequently, I carried out a post-annealing step to ~0.5x0.5cm² samples (cut from the 4-inch wafers): the samples (100nm Li_xCoO_2 film on Si substrate) were heated at 580°C for 1 hour in air (in an oven at LPS labs) to obtain the High-Temperature (HT) Li_xCoO_2 phase.

1.3 Microfabrication of upper electrodes by metallization methods

In this part, we present two common microfabrication methods used to deposit upper electrodes: Joule heating thermal evaporation and E-beam evaporation. The first method (Au deposition on Li_xCoO_2 films by using a solid mask) allows avoiding photoresists from lithography (which is the case in the 2nd method). Therefore, thermal evaporation has been

used towards study of the resistive switching mechanisms of Li_xCoO_2 thin films. The second method has been used for all the other experiments (studies of kinetics and performance).

1.3.1 Thermal evaporation for metal electrodes

Thermal evaporation involves two basic processes, evaporation and condensation of hot vapor of melting metals. The thermal evaporation (i.e. resistive evaporation) is a metallization method in which current flows through a crucible to heat a target material to its melting temperature. A gaseous phase of metal is condensed onto the substrate. At LPS lab, a current of 200A was applied to a tungsten crucible holding a gold wire. This gold wire is heated to its fusion temperature of 1063°C and begins to evaporate. The vapor of gold condenses on a Li_xCoO_2 thin film sample with a mask placed on the top of the chamber in a distance 20 cm from the crucible and under a 10^{-6} mbar vacuum. The deposition rate was measured by a varied-frequency quartz. A 60nm-thick Au layer was usually deposited at a speed of 10nm/min.

Fig. 2.3 shows the setup of the thermal evaporation at LPS and the TE (top electrodes) with different sizes obtained: $10x10\mu m^2$, $30x30\mu m^2$, $100x100\mu m^2$ and $500x500\mu m^2$. If smaller TE are required (<1µm), it is better to use lift-off process which will be discussed in the next part.

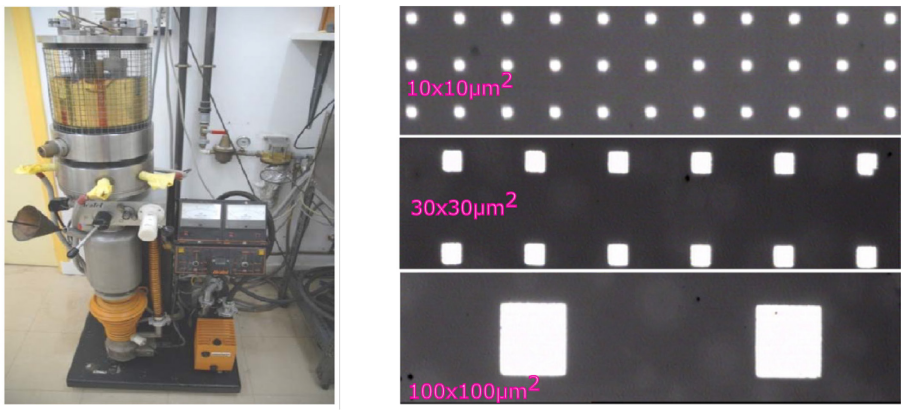

Figure 2.3: Thermal evaporation setup at LPS (left), optical images of different sizes of Au TE after thermal deposition (right).

1.3.2 E-beam Physical Vapor Deposition (EBPVD) of electrodes

To deposit Au/Ti electrodes on the Li_xCoO_2 films, we used EBPVD which is more complicated than Joule heating thermal deposition because it is required to perform a

microfabrication process in cleanroom. The overall process of this type of deposition can be illustrated in **Fig. 2.4**.

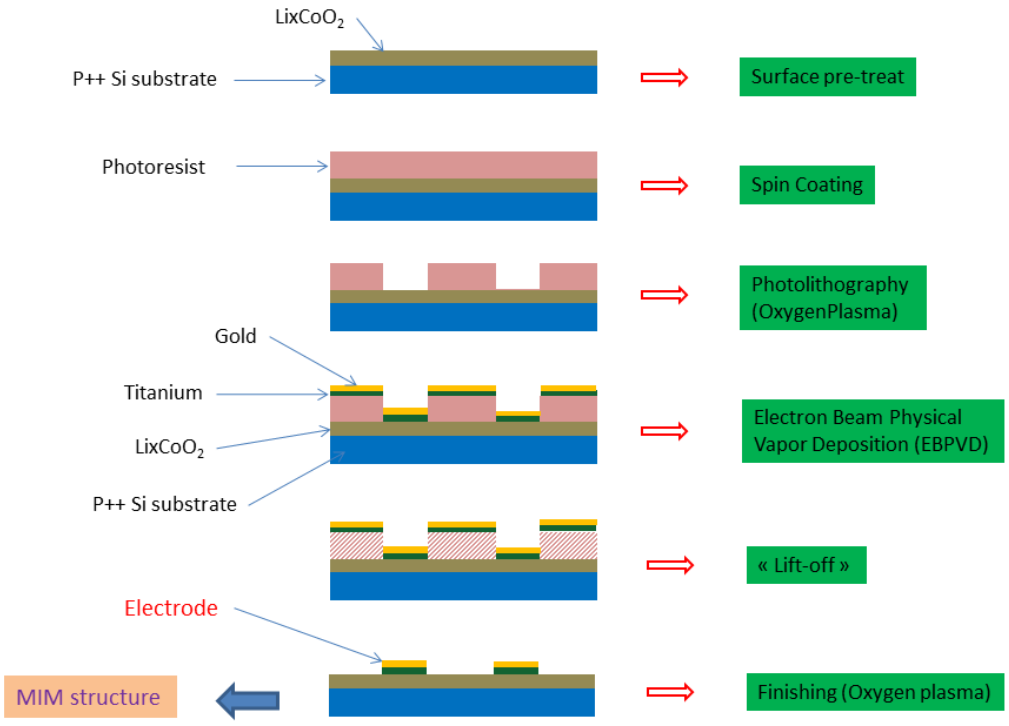

Figure 2.4: Lift-off process for making TE in cleanroom

The Li_xCoO_2 thin film substrate was pre-treated by IPA (isopropyl alcohol) before spin-coating a negative photoresist (AZ5214E). It was then soft-baked during 1min30" at 110°C. By an optical lithography step, we print desired microstructuring patterns of electrodes on the mask. The sample was then developed in a developer solution (AZ400K) and distilled H_2O (1:4). After lithography, Oxygen plasma cleaning was used to remove photoresist residues, to make a good contact between the future deposited electrodes and film. The patterns after lithography are shown in **Fig. 2.5a**.

However, the minimum size of patterns obtained by optical lithography is 5 µm. Using e-beam lithography, we can reach submicron sizes. In this latter case, the photoresist used is PMMA A6. After baking 15 min at 175°C, the sample is exposed using electron beam with a 200µC/cm^2 dose. Finally, we develop in a MIBK/IPA (1:3) solution. The patterns using e-beam lithography are shown in **Fig. 2.6**. We can see three kinds of pads with different lateral sizes: 1000nm, 800nm and 300 nm.

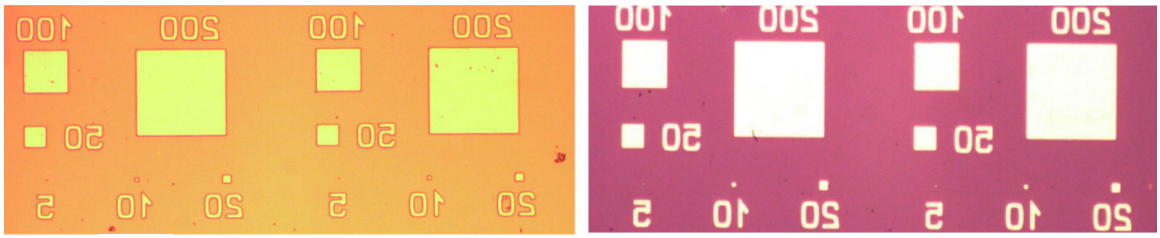

a) After Lithography b) After depostion

Figure 2.5: a) Microstructures printed by optical lithography and **b)** after deposition of top Au/Ti electrodes.

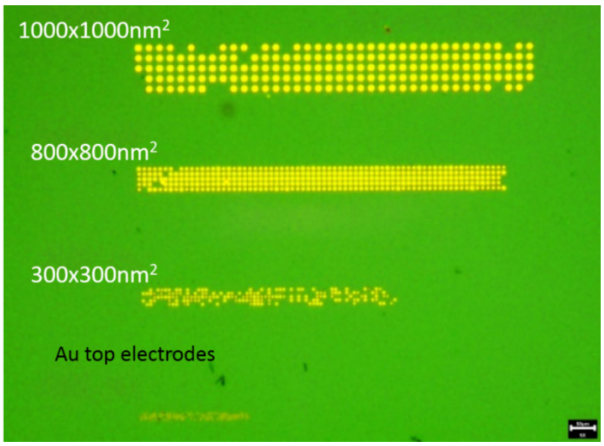

Figure 2.6: Submicron sized TEs using e-beam lithography

Au/Ti (or Au/Cr) is then deposited by using e-beam evaporation. The target metal is not heated like in thermal evaporation, but bombarded by a magnetic-controlled beam of electron generated from an electron gun. The electrons transfer their kinetic energy into thermal energy to vaporize the material. The gaseous phase of metals is condensed onto the film substrate. The overall process is executed in high vacuum (order of magnitude 10^{-8} Torr or better). The electrodes are deposited at a rate of 0.1 nm/s and 0.3 nm/s in the case of Ti (or Cr) and Au, respectively. The very low deposition rate and rotating substrate in EBPVD provide a very high quality of TE layers (because the step coverage is minimized as much compared to thermal evaporation). The sample is finally lift-offed in acetone solution for 3-4 hours. **Fig 2.5b** shows an example of TE (Au/Ti) after deposition by EBPVD. The MIM devices are then ready for electrical characterizations.

Other configurations of electrodes have also been fabricated, for example to study small cells (< 100x100 µm²) using macroscopic electrical characterization methods. In this case, we deposited an intermediate layer of Si_3N_4 (see Appendix A protocol 2). Another configuration of electrodes consisted in a deposition of a protection layer on top of the film surfaces (to avoid film-air contact), using positive lithography (see Appendix A protocol 3).

1.4 Film restriction of cells, by Focused Ion Beam (FIB) etching

The influence of lateral restriction of films has been studied (in Chapter 5). **Fig. 2.7a** represents the FIB technique process, carried out at the LPS lab, to obtain a delimited Li_xCoO_2 cell. The Li_xCoO_2/Si sample is first completely covered by Au (or Au/Ti). After that, a copper wire is approached to cover part of the film surface (see ① in **Fig 2.7a**). A focused Ga^+ beam is then used to bombard the film. The surrounding materials will be removed and only the covered part remains. After that, the copper wire is oriented perpendicular to the previous position (see ② in **Fig 2.7a**) and bombarding is carried out again. The resulting etching depth reaches around 300nm, creating a square-shaped MIM cell as shown in **Fig. 2.7b**. The square area depends on the diameter of copper wire. The minimum area we could obtain using FIB is $30 \times 30\mu m^2$. Towards studying endurance of 100x100µm² cells with two-probes method at C2N-Orsay, 100µm in diameter copper wires have been used.

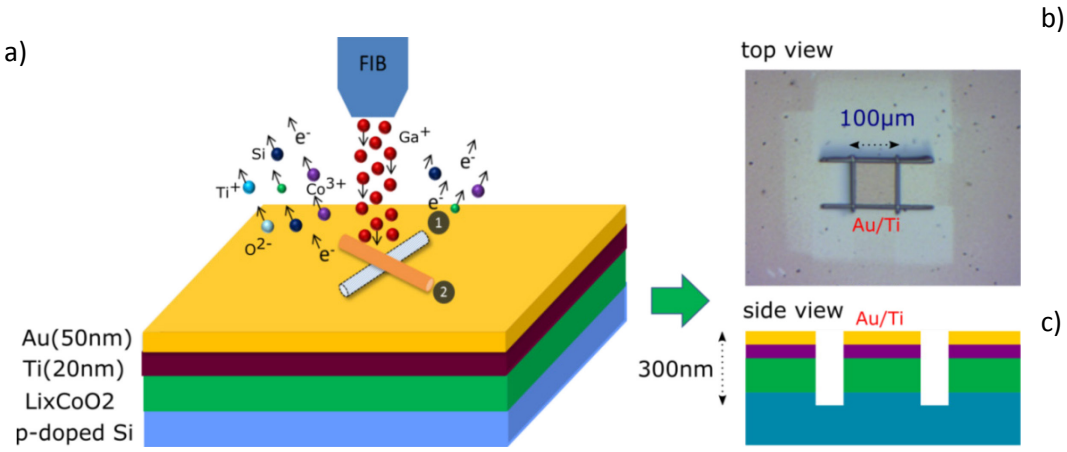

Figure 2.7: Schematic representation of FIB technique to construct area-restricted MIM cells: **a)** vertical bombarding of an MIM structure with copper wire coverage (at position 1) then bombarding again with copper wire at position 2. **b)** Top view optical image of an MIM cell and **c)** schematics of a cross-sectional view of such a resulting cell.

Optimizing the FIB parameters to obtain good devices was an important step. Etching depths beyond 450nm resulted in damaged cells which were already in a low resistance state ($\approx 10^4$ Ω, like being short circuited between top and bottom electrode), whereas for 200-300nm etching depths the cells were in usual high resistance state ($\approx 10^8$Ω - 10^9 Ω). Other parameters of FIB had to be optimized, for instance, the {wire/top surface} distance.

2 STRUCTURAL CHARACTERIZATIONS OF Li_xCoO_2 FILMS

In this section we present structural properties of Li_xCoO_2 thin films and MIM devices, by using different characterization techniques.

2.1 Mean film thickness by X-ray Reflectivity (XRR)

X-ray reflectivity (XRR) is a non-destructive technique to characterize thickness and roughness of films and multilayers. The incident light is reflected and refracted, not on planes of crystalline lattice, but on the flat interfaces of the films. Therefore, XRR works for both crystalline and amorphous films. **Fig. 2.8** shows a simple sketch of XRR. The incident X-ray beam, which strikes the interface air/film at angle larger than critical angle where the total internal reflection occurs, is partly reflected to the air medium and partly refracted to film medium with a different refractive index. The refracted beam is now considered as a new incident beam which is reflected on the second interface film/substrate and refracted to air medium again. After collecting those reflected and refracted beams, we can analyze the interference fringes of these beams if the path difference equals to an integer number of wavelengths. The thickness *t* of the film is then determined by the characteristics of all interference fringes.

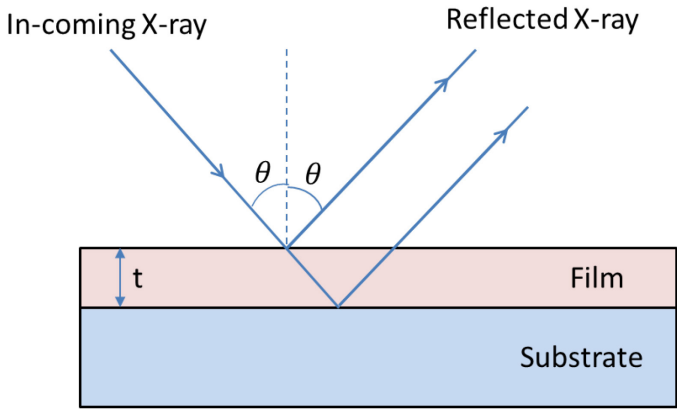

Figure 2.8: Schematic diagram of X-ray reflectivity

At the LPS lab, XRR has been used to determine the mean thickness of Li_xCoO_2 films. An example of XRR spectrum is shown in **Fig. 2.9a**. The film thickness (48.3 nm) was determined from the spectrum, and corresponds well to thickness (50nm) of the films elaborated at the LITEN-CEA.

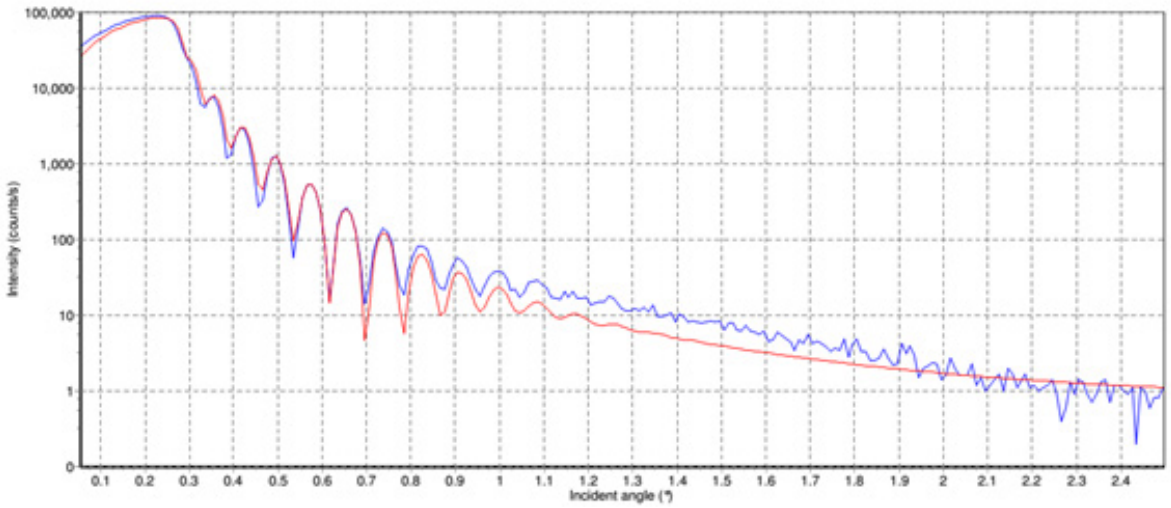

Figure 2.9a: XRR Fringe spectrum (blue curve) and software curve (red) to calculate the Li_xCoO_2 film thickness. The precise thickness of the film is 48.3nm (measured at LPS Lab).

Another example of XRR spectrum is shown in **Fig. 2.9b**. The film thickness (115.4 nm) determined corresponds well to thickness (100nm) of the films elaborated at the LITEN-CEA. Most studies (chapter 3 and 4) are carried out on 100nm thick films.

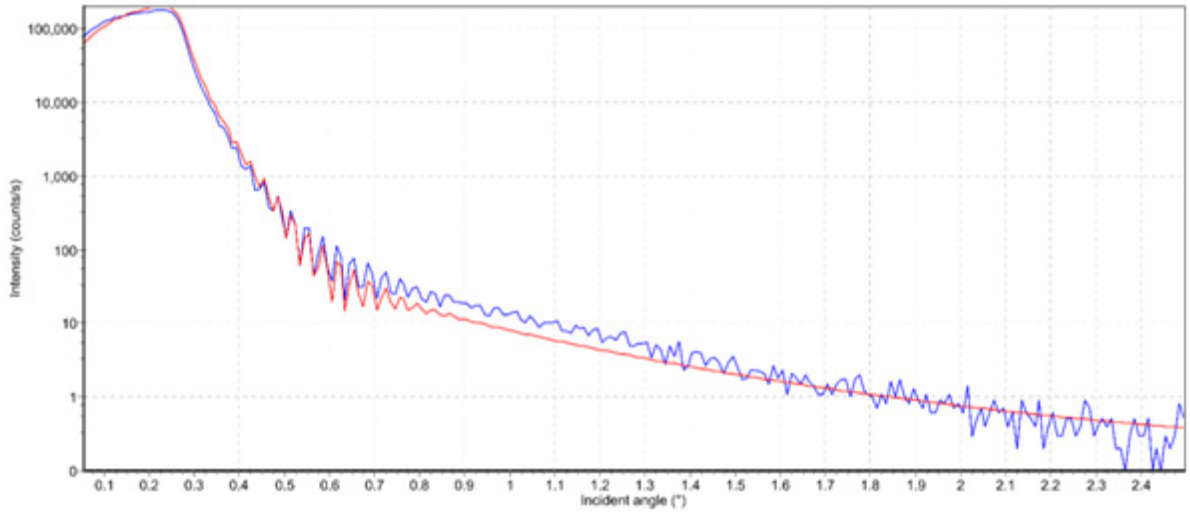

Figure 2.9b: XRR Fringe spectrum (blue curve) and software curve (red) to calculate the Li_xCoO_2 film thickness. The precise thickness of the film is 115.4nm.

2.2 Crystalline structure of the films by X-ray Diffraction (XRD) in transmission geometry

X-ray diffraction is one of the most common characterization tools used to study the crystalline structure of solid state materials. X-rays, which are generated by bombarding a metal target such as Cu or Mo, are exposed to the surface of sample. The atomic layers in crystalline structure of the sample cause the X-rays to diffract into many directions. Depending on the positions of the detectors, we can either detect scattered beams or transmitted beams which correspond to two XRD methods: reflection and transmission, respectively.

During V.H. Mai's thesis, analyses using XRD by reflection did not allow to observe diffraction peaks, this could be explained by the fact that the c-axis orientation is parallel to the horizontal plane, resulting in the absence of the (003) peaks in the diagrams. Thus XRD in transmission geometry (schematic sketch shown in **Fig. 2.10** below) had been used and allowed to obtain interesting preliminary results.

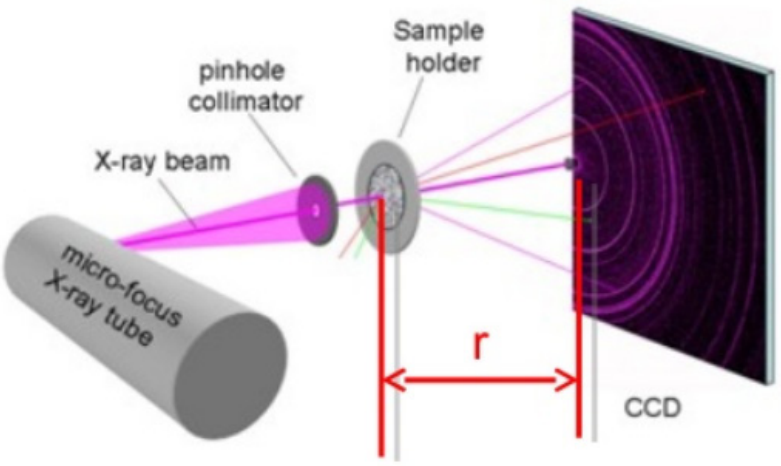

Figure 2.10: Schematics of XRD in transmission geometry [2].

The experimental protocol was the following: thin {Li_xCoO_2/p-doped Si (100µm)} samples were characterized by XRD transmission at LPS. The energy of X-rays beam (with selected Kα wavelength λ= 0,07107nm) of 18,4keV permits a transmission through the 100µm-thick Si substrate. The X-rays detector is a marked MAR345. An example was shown in **Fig. 2.11**: the dark ring appears on the detector sheet, and the corresponding peak at 2θ=8.7° on the diagram exhibits the crystallinity of the Li_xCoO_2 thin film.

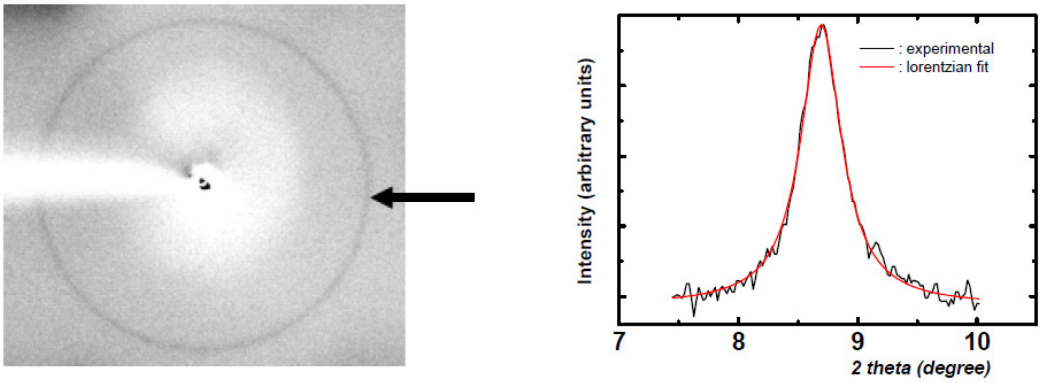

Figure 2.11: Example of XRD transmission ring pattern of a Li_xCoO_2 thin film [3]

Our objective here was to characterize further the c-parameter and the average grain size, as a function of annealing time of the films. Such values are exhibited in **Table 2.1**. The corresponding plots in **Fig 2.12** show that the c-parameter appears constant with annealing time. The grain size significantly increases the first few ten minutes before it becomes approximately constant.

Sample	***Annealing time (min)***	***c-parameter (nm)***	***Average size (nm)***
#37 (29.06)	01	1.4140	4.50
#38 (29.06)	15	1.4100	11.2
#18 (27.04)	60 (1h)	1.4088	-
#43 (06.07)	900 (15h)	1.4110	13.7

Table 2.1: Values of c-parameter and average grain size as a function of annealing time.

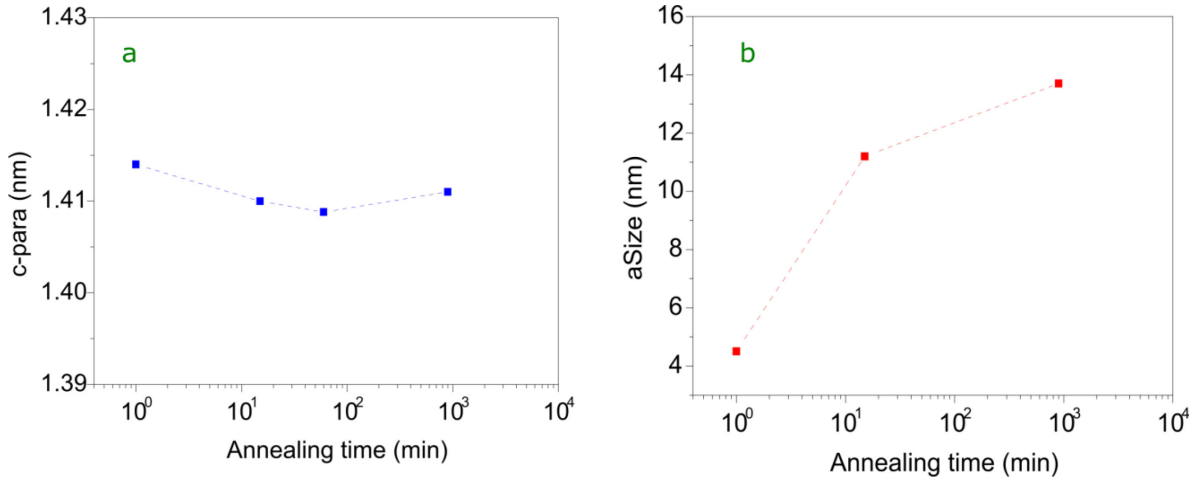

Figure 2.12: Evolution of **a)** c-parameter and **b)** grain size as the function of annealing time

2.3 Structure of Li_xCoO_2 thin films by Scanning Transmission Electron Microscopy (STEM)

One of very powerful tools being utilized for the structural characterization of the Li_xCoO_2 thin films is scanning transmission electron microscope (STEM). In TEM, also called conventional TEM (CTEM) the electrons in a parallel incident beam pass through the sample and are collected behind it. However, in a STEM the sample is raster-scanned by a convergent electron beam (probe) and transmitted electrons are collected with different types of detectors as High Angle Annular Dark Field (HAADF) detector which provides an image sensitive to mean Z and thickness of the sample. Energy loss of electrons during inelastic interactions can be measured using an electron spectrometer. The FWHM of zero-loss peak is about 0.35 eV in vacuum.

The schematics of STEM principle including imaging modes is shown in **Fig. 2.13a**. The probe is controlled to scan over a raster area using a couple of electromagnetic scan coils. After electron-electron interactions, the scattered electrons are then collected by different detectors depending on the angular distribution of secondary electron scattering, such as Bright Field Imaging, High-Angle Annular Dark-Field Imaging (HAADF-STEM) and Electron Energy Loss Spectroscopy (STEM-EELS). Here we introduce two high resolution imaging modes: HAADF-STEM and STEM-EELS.

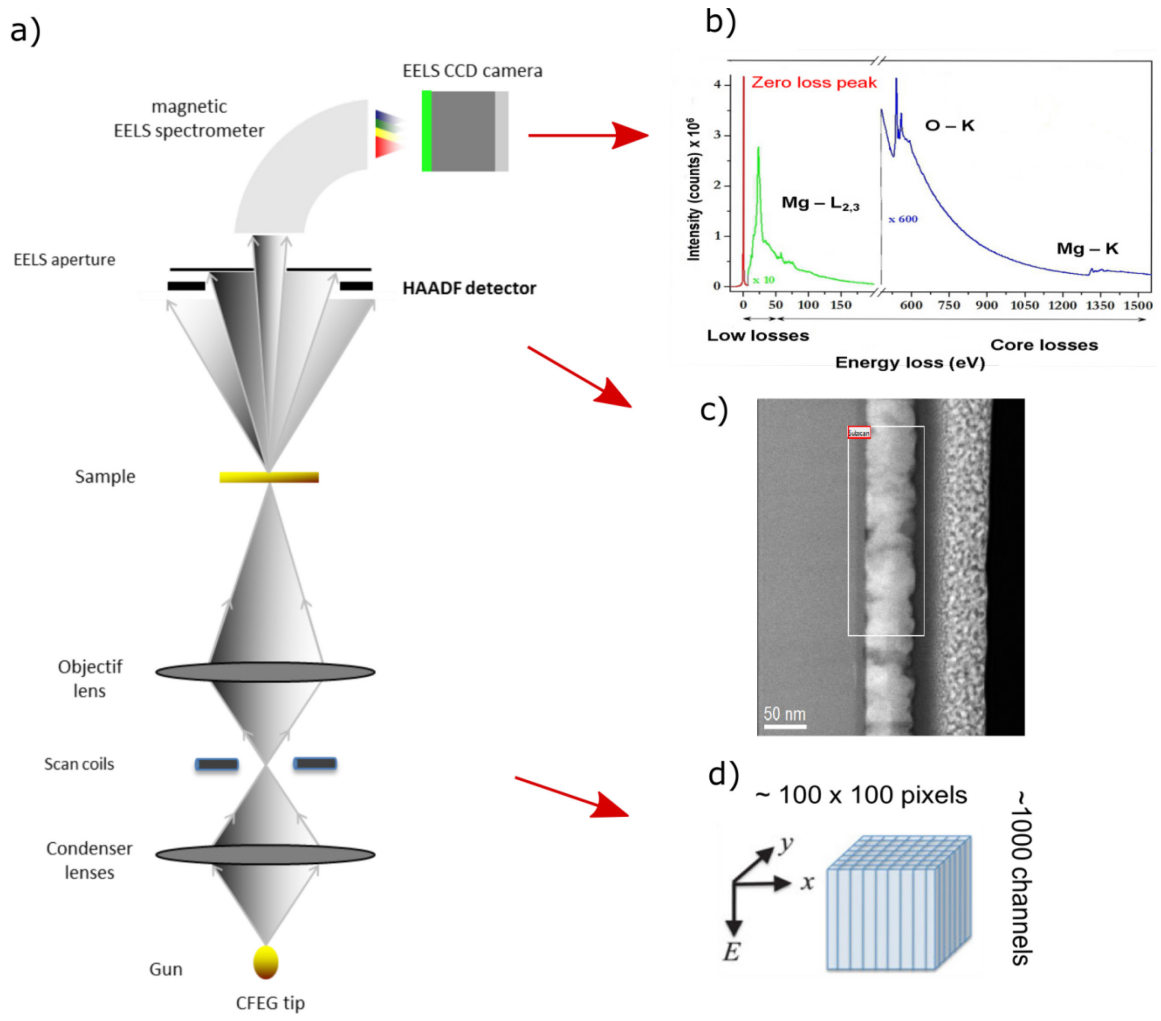

Figure 2.13: a) Schematics of STEM; **b)** EELS spectrum detected using EELS CCD Camera; **c)** HAADF image from HAADF detector and **d)** EELS datacube.

In a STEM, the high-angle annular dark-field image (HAADF) is collected from the HAADF detector, as shown in **Fig. 2.13c**. On the other hand, the Electron Energy Loss Spectrum (EELS) is collected on each area position corresponding to each pixel of the datacube as schematized in **Fig. 2.13d**. This 3-D dataset consists of about 100x100 pixels on two spatial dimensions (x & y) and 1000 channels on energy-loss dimension E. The EELS spectrum is divided into three main parts: Zero Loss peak, Low Losses and Core Losses, as shown in **Fig. 2.13b**. Each part of the spectrum represents the properties of material such as electronic band information, chemical composition, optical properties, etc. Hence, this advanced imaging technique is utilized to characterize our Li_xCoO_2 thin films with two aims: Observation of film structure using STEM-HAADF, and mapping of chemical components of the film using STEM-EELS. Detailed process is as following.

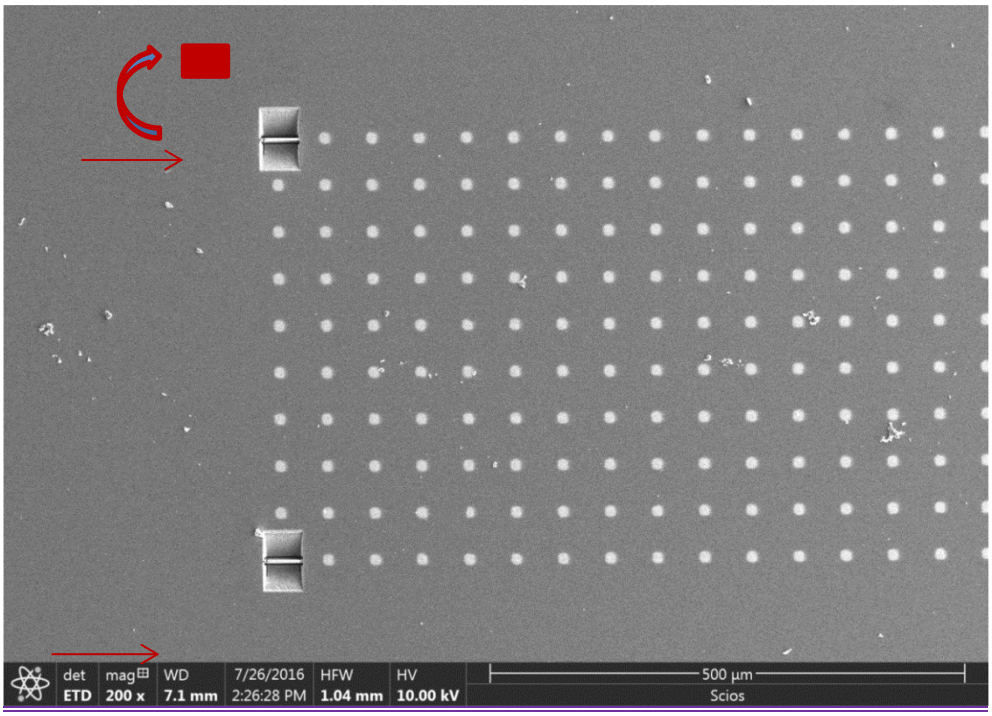

Figure 2.14: SEM image of a film surface on which gold pads have been deposited. Two TEM samples have been cut and are ready to be cut out and lifted.

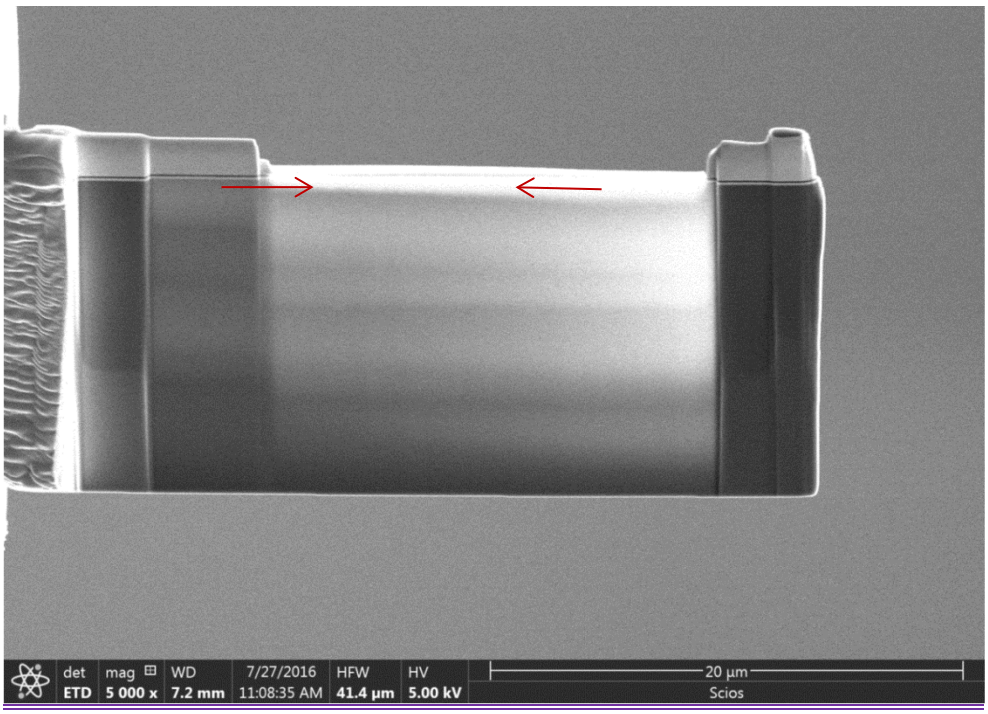

Figure 2.15: A TEM/STEM sample prepared by FIB. Red arrows indicate the position of the gold plot.

After top electrode deposition (Au by thermal Joule heating evaporation) on LixCoO2 thin films, the samples were then prepared by Field Ion Beam (FIB) method. One of the main advantages of this method is that the localization of the thin section can be precisely defined on the sample, due to the imaging system (built-in scanning electron microscope) of the FIB. This localization was essential to study the layers under the gold plot (constituting the switching device) after the commutation step.

First a line of platinum is deposited on the surface to protect the layers from the ion beam; then a piece about 20x10 µm is cut across the layer by "digging trenches" from the front and back of the region of interest, as shown in **Fig 2.14**. The resulting lamella (in **Fig. 2.15**) is then cut free, lifted out, then attached to a 3mm diameter microscopy grid. A final polishing step allows obtaining a sample transparent to electrons, ideally less than 40 nm thick for an EELS experiment at 60kV. Also, Li_xCoO_2 has to be observed at low voltage (60keV) in (S)TEM to minimize possible electron beam irradiation effects.

2.3.1 Comparison of a non-annealed film and a 7h annealed film

As shown in **Fig 2.16**, the Li_xCoO_2 film without annealing treatment is totally amorphous, thus it appears quite homogeneous and apparently non-oriented. After annealing of 7 hours at 580°C, the film is crystallized with c-axis [001] majority orienting in parallel to the substrate of the film which agrees to XRD results, as shown in **Fig 2.17a**. However, it exists some minority parts (<10%) of the film where the c-axis orients perpendicular to the substrate, as exhibited in **Fig 2.17b**.

Besides, before annealing, the thickness of SiO_2 layer is quite low ≈ 3nm. Nevertheless, STEM reveals that the SiO_2 layer of the 7h annealed film is much thicker, about 13nm. Finally, some defects in the film are observed, which may result from high-temperature annealing process. The important influences of characteristics such as crystal orientations, defects as well as SiO_2 layer on resistive switching of the MIM device will be covered in chapter 3.

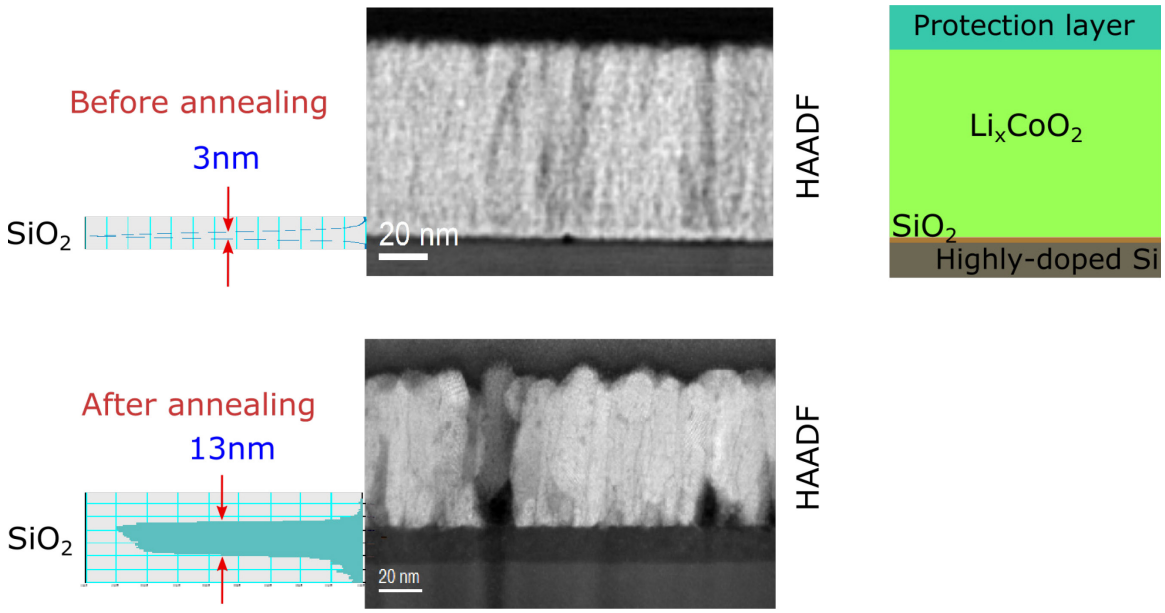

Figure 2.16: Characterization of the structure of a Li_xCoO_2 thin film by STEM: Sample (a) before annealing, (b) after annealing at 580°C for 7 hours.

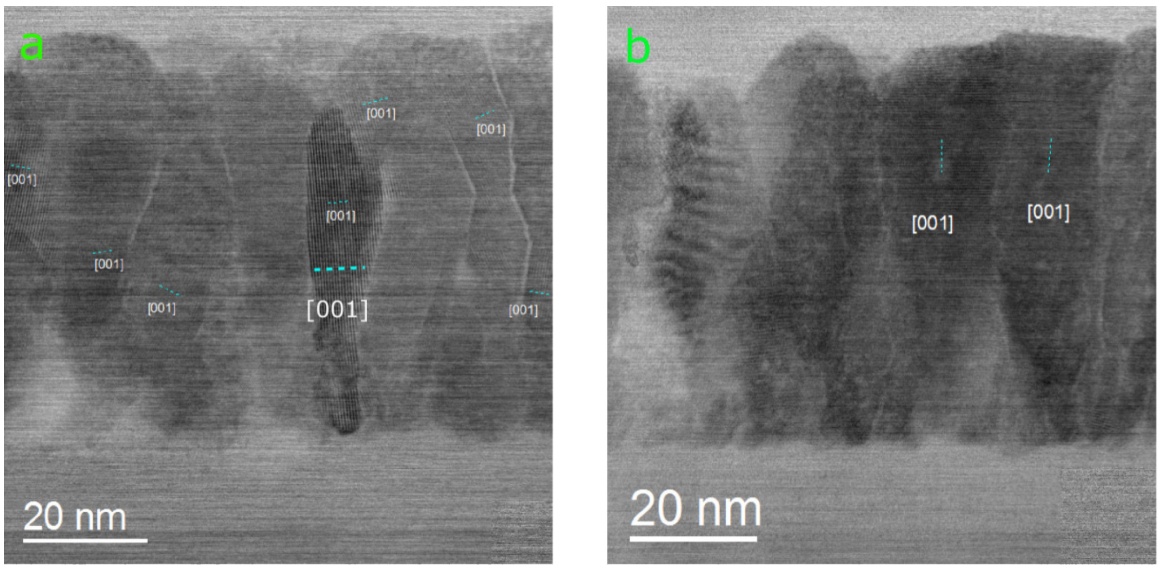

Figure 2.17: BF images showing the orientation of the grains: **(a)** Majority of c-axis orientation parallel to the substrate and **(b)** Minority of c-axis orientation perpendicular to the substrate.

2.3.2 Lithium detection in the annealed films

STEM is also capable to detect of Li ions and other components in the film using Electron Energy Loss Spectroscopy (EELS). **Fig. 2.18** shows energy loss spectrum of Li_xCoO_2 sample. Indeed, fine structures of Li-K, Si-$L_{2,3}$, Co-$M_{2,3}$ and Co-$L_{2,3}$ edges are very sensitive to oxidation state. For example, for Co-M2,3 edge, the fine structure of the edge depends on the oxidation state of the Cobalt [4].

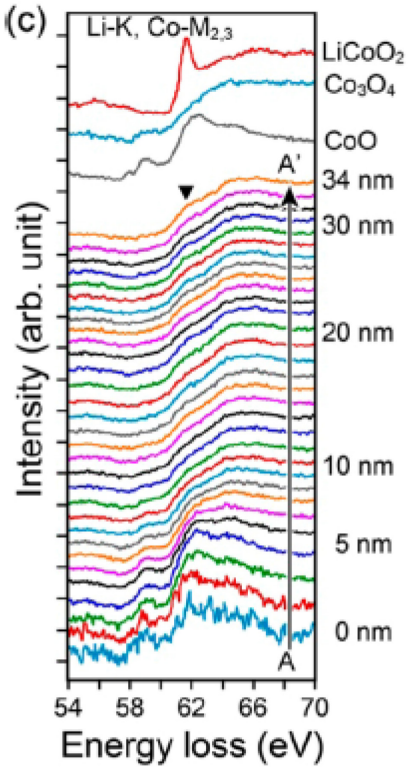

Figure 2.18: Energy Loss spectrum of a Li_xCoO_2 sample [4]

The energy dispersion in EELS was 0.05eV/ch. The result of STEM-EELS analysis is exhibited as follows. In **Fig. 2.19a**, the selected area shown in HAADF image was used to investigate the distribution of each component of the film. Thus a spectrum-image (data-cube) has been acquired on this area.

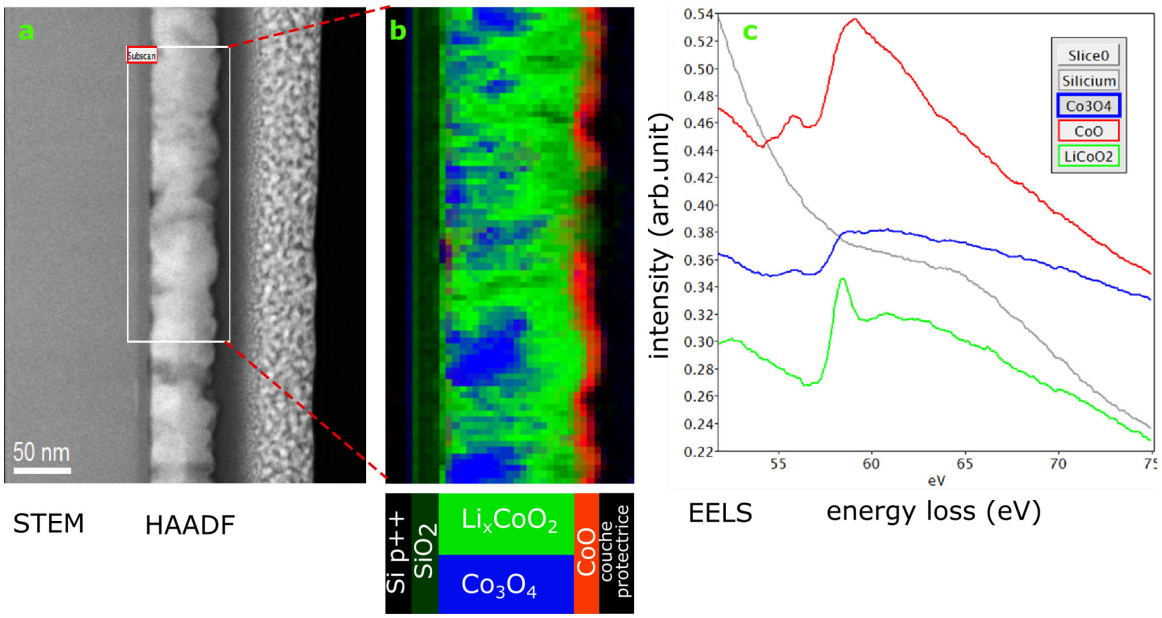

Figure 2.19: STEM-EELS analysis: **a)** HAADF image, **b)** abundances of the components extracted by VCA **c)** EELS components extracted by VCA.

As Li-K and Co $M_{2,3}$ edges are superimposed, it is not possible to use the classical quantification method with removing of background and edge intensity signal mapping. We chose then hyperspectral un-mixing methods [5]. These methods make the assumption that each individual spectra of the 10000 spectra data-cube is constituted by the linear combination of a few characteristic components. Thus, the procedure aims to decompose the measured pixel spectrum into a collection of constituent spectra, or *endmembers*, and a set of corresponding fractions, or *abundances*, that indicate the proportion of each endmember present in the pixel. We used one geometrical algorithm, Vertex Component Analysis (VCA) [XY], which is fast and easy to implement on usual data acquisition packages.

We found five characteristic components (shown in **Fig. 2.19c**) identified as Si, SiO_2, CoO, Co_3O_4 and Li_xCoO_2 by comparison with reference spectra which are found in the literature [5]. But the un-mixing is not perfect and there is a slight Li-K signal remaining in the Co components Co_3O_4 and CoO. Other algorithms have been tested without noticeable improvement [XZ]. We think that some difficulties in processing EELS data cube may arise from an excessive thickness, which reinforces nonlinear effects in the electron interaction with the sample. The abundances map for the characteristic CoO, Co_3O_4 and Li_xCoO_2 signals are combined in a false color image (see **Fig. 2.19b**) which shows inhomogeneity in the Li repartition and the presence of Li "puddles", the existence of which is hypothesized in [4]. The green color in SiO_2 layer may result from artifacts.

2.4 Chemical composition using Secondary Ion Mass Spectrometry (dynamic SIMS)

In many fields of material science and nanotechnology, Secondary Ion Mass Spectrometry (SIMS) has become a powerful tool to analyze chemical elements of solid surfaces.

The working principal of dynamic SIMS is the following: an accelerated continuous primary ion beam (ions such as O_2^+, O^-, Cs^+ are typically used) bombards the sample surface, which yields the ejection of atoms, ions, cluster ions, *etc.* The ejected ions (called secondary ions) are analyzed by a mass spectrometer. This allows obtaining various output data such as spectra, depth profiles of elements, 2D ion mapping, or 3D ion distributions, as shown in figure **Fig. 2.20a**.

At the GeMAC laboratory, the SIMS setup (shown in Fig **Fig. 2.20b**) is a IMS7f CAMECA with a very good depth resolution of few nanometers and a very fine mass resolution M/ΔM = 10000 [6].

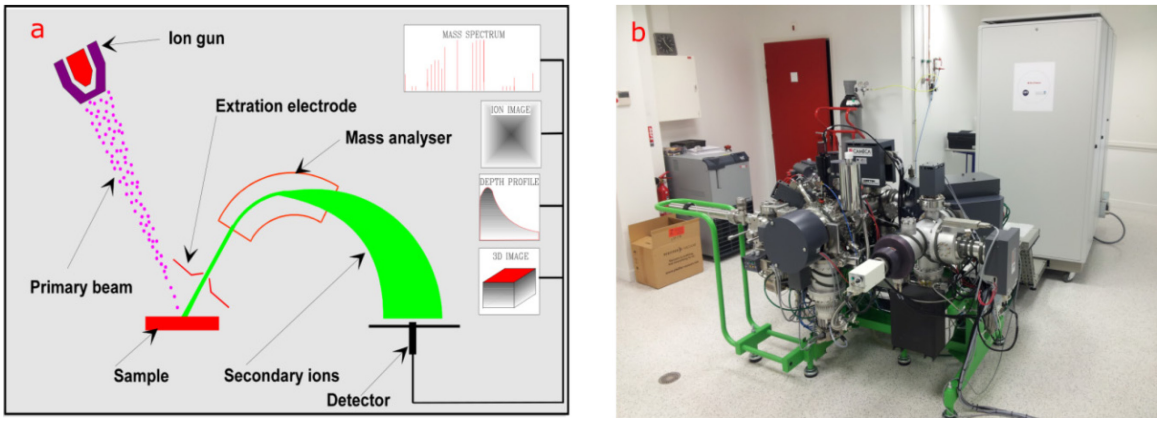

Figure 2.20: (a) the principle operation of SIMS, (b) SIMS setup at laboratory GeMAC.

Using this SIMS technique allows to characterize the chemical (element) composition of the Li_xCoO_2 films and devices (upper/electrode/substrate cells). Towards this goal, several questions had to be answered in order to obtain high quality SIMS characterizations, namely:

-what kind of primary ions is most appropriate for bombarding?

-what kind of ions are detected?

-is there an optimized primary beam impact energy for a better profile resolution?

These questions will be detailed below.

2.4.1 Influence of the primary ion source

Two kinds of primary ions can be used: O_2^+ (16O) and Cs^+ (133Cs). Normally, using O_2^+ (16O) allows a better sensitivity to elements detection.

Both O_2^+ (16O) and Cs^+ (133Cs) have been tried. Hereafter we can see examples of depth profiles of $LiCoO_2$/Si samples (having previously undergone a 5h annealing step). In **Fig 2.21a**, we can see that for a low etching time (< 400s), the Li intensity is high and nearly constant, and the Si detected intensity is very low: this corresponds to the Li_xCoO_2 film. After 400s etching time, the lithium detected decreases drastically and the Si intensity increases and becomes constant: this corresponds to the Si material.

However, using 16O source led to the following problems:

- the 16O intensity curve shape is difficult to understand (O is detected in the film, and also in Si): this can be explained by the fact that the O profile is a mixture of O coming from the analyzed material (Li_xCoO_2) and the source,

-the profile of other elements (in particular Co, green curve) exhibit a peculiar maximum (black arrow) near the film/substrate interface, which is not expected (however difficult to explain).

When using Cs^+ source, these problems were not encountered: the profiles of all elements (except O) are stable within the same material, as seen in **Fig 2.21b**. Besides, the O intensity maximum can be well explained by the existence of a SiO_x layer at the film/Si interface. Therefore in the following characterizations, Cs^+ ions have been used.

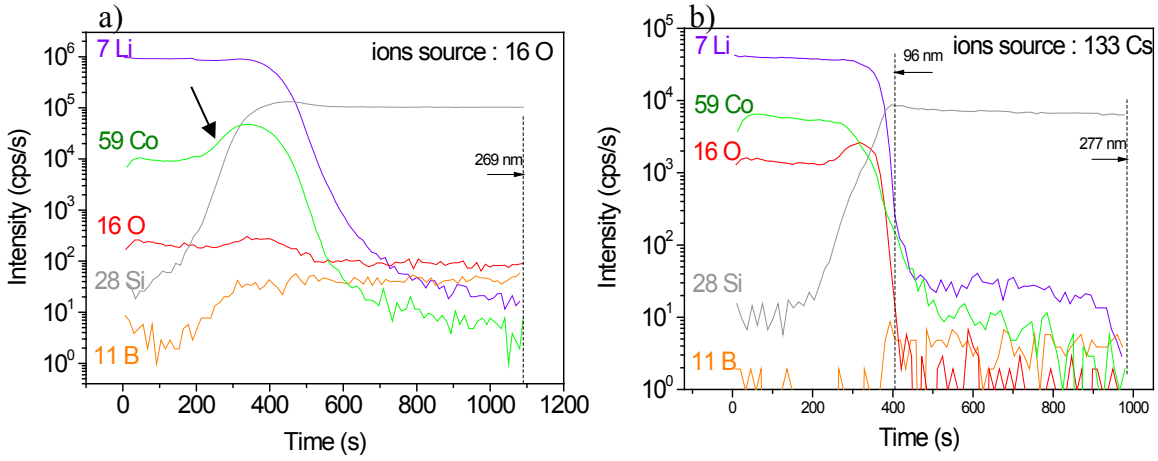

Figure 2.21: SIMS depth profiles of Li_xCoO_2 thin films (annealed 5h) in different situations: **a)** the primary ion source was composed by 16O ions **b)** the primary ion source was composed by 133Cs ions.

2.4.2 *Influence of detected ions: M^+ or CsM^+*

In order to detect an M element, it has been reported in literature that in some cases, a better depth profile resolution is obtained if CsM^+ ions are detected, rather than sole M^+ ions [7]. In **Fig 2.22** below, we can thus compare a typical example of depth profiles (of an non annealed sample) using both detection possibilities. Depth profiles for which M+ ions (M=Li, Co, O, Si, B) are detected, exhibit a surprising high maximum (corresponding to exaltation effects which could be due to an increase of the ionization rate of an element) (shown in **Fig 2.22a**). On the contrary, depth profiles for which CsM^+ ions are detected don't show such local maximum as shown in **Fig 2.22b**. Therefore in the following characterizations, the detection of CsM^+ ions has been privileged.

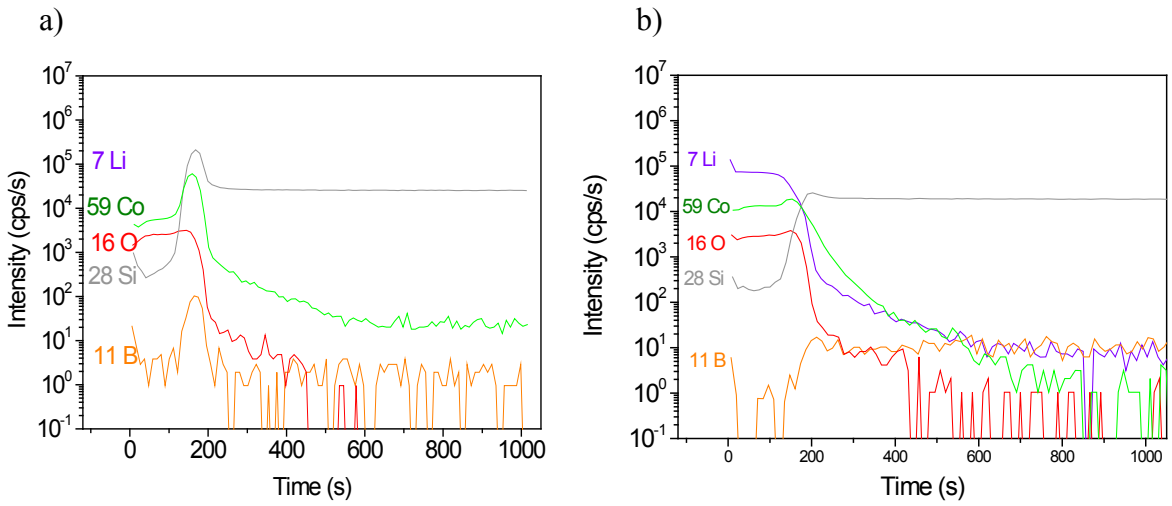

Figure 2.22: SIMS depth profiles of Li_xCoO_2 thin films in different situations: **a)** M^+ ions being detected (M = Li,Co, O, Si, B) **b)** CsM^+ ions being detected.

2.4.3 *Influence of primary ion energy impact*

Usually, lower impact energy allows a better resolution of detected elements at sharp interfaces. Hence, two impact energies have been tried: 5keV and 2keV. An example of results is shown in **Fig 2.23** below. Using 2 keV impact energy results in less stable profiles (**Fig. 2.23a**) within the film, compared to the case of5 keV impact energy (**Fig 2.23b**). This could be accounted for by a higher selective etching of elements in the film; a complete study of such phenomenon would however require efforts going beyond the frame of this thesis.

Therefore in the following characterizations, an impact energy of 5 keV will be privileged.

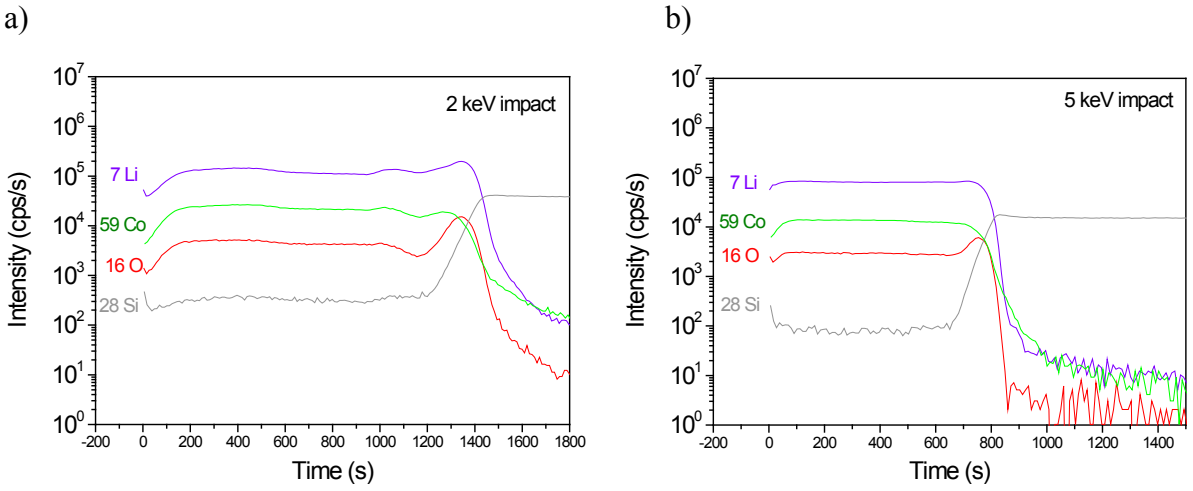

Figure 2.23: SIMS depth profiles of Li_xCoO_2 thin films (annealed 1h) in different situations: **(a)** 2keV energy impact **(b)** 5keV energy impact

2.4.4 Application to 3D view of the element composition of a virgin annealed sample

The optimized parameters allowed obtaining, not only depth profiles, but also 3D composition of the samples analyzed, as shown in **Fig 2.24** hereafter. Such characterizations will be used (in chapter 3) to analyze virgin cells and preswitched cells, in order to compare the spatial composition of the elements in the cells.

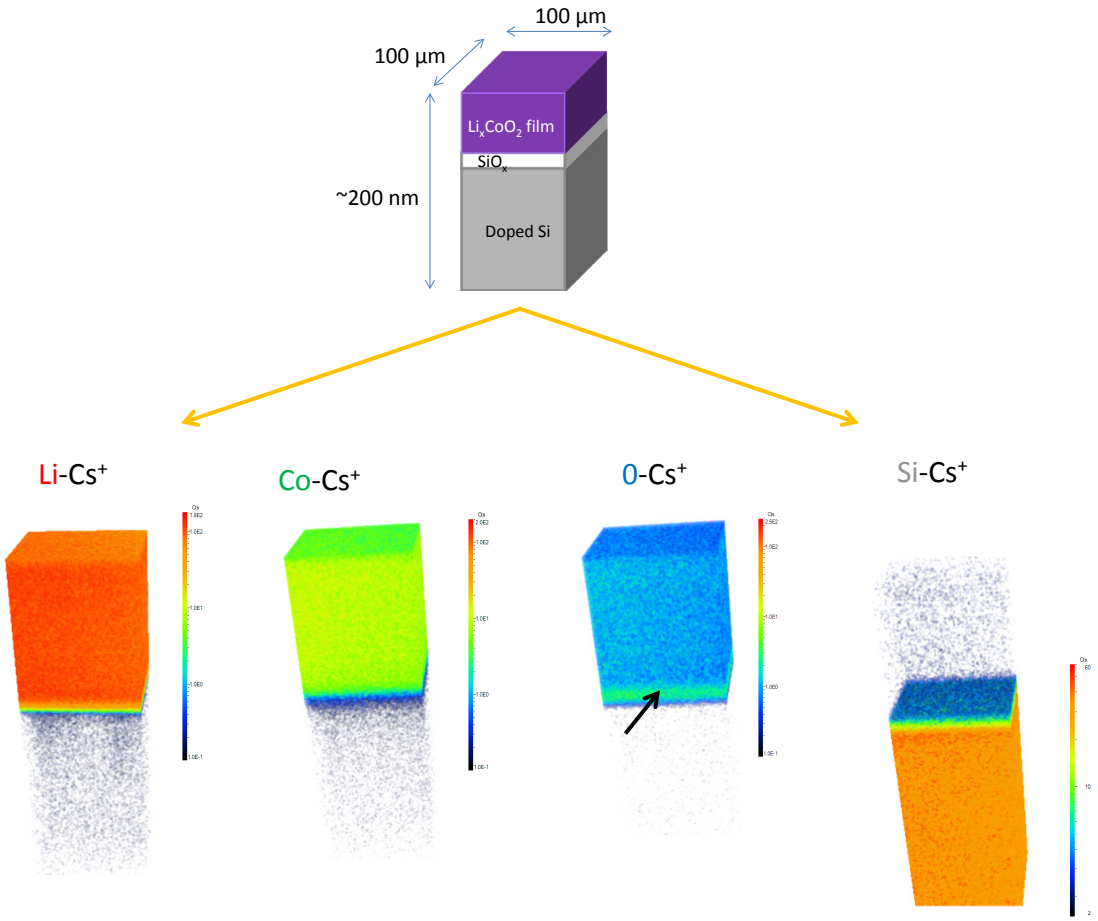

Figure 2.24: 3D Distribution of four elements (Li, Co, O and Si) of Li_xCoO_2 films deposited on Si, then annealed in air for 1 h To obtain these maps, Cs^+ ions have been used, and the signals recorded are Li-Cs^+, Co-Cs^+, O-Cs^+, and Si-Cs^+.

It is worth nothing that the SiO_x layer at the film/substrate is clearly seen on the O-Cs^+ 3D map (black arrow).

2.5 X-ray Photoelectron Spectroscopy (XPS)

The principle of XPS is schematized in **Fig. 2.25**. An X-ray source ($E_s = h\vartheta$) leads to the ejection of electrons, whose kinetic energies (E_{kin}) is measured by a photoelectron analyzer. If the work function W_f is known, then the binding energy (E_b) is determined ($E_b = h\vartheta - E_{kin} - W_f$). The binding energy spectrum allows characterizing the chemical nature of each element of a given sample.

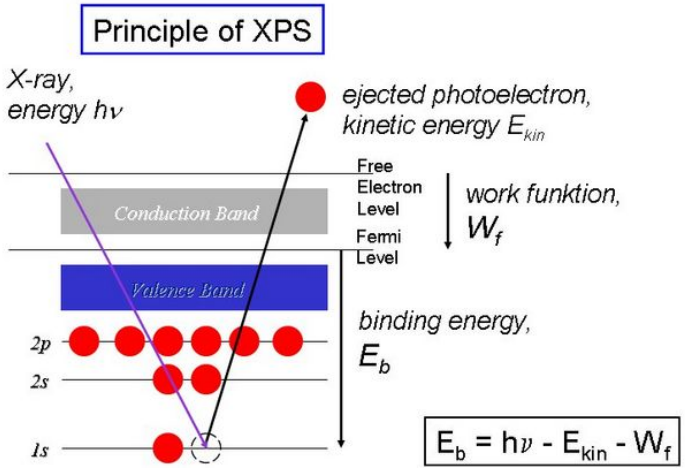

Figure 2.25: Principle of XPS technique [8].

At the GeePs laboratory, XPS technique has been used to obtain depth profiles of several elements (except Li) of Li_xCoO_2-based cells (by ionic etching with Ar^+ ions).

XPS measurements have been performed using a PHI 5000 VersaProbe spectrometer under 10^{-7} Pa vacuum. A monochromatized Aluminum Kα X-ray ($h\nu = 1486.6\,eV$) was emitted by applying high voltage (15kV). High resolution core level spectra were acquired with $23.5\,eV$ pass energy, an energy step of $0.1\,eV$ and time/step of 50ms. The Ar^+ ion beam conditions for depth profiling were the following: Ar^+ ion source was accelerated at 2 kV and the sputtered area was 2×2 mm^2. A dual beam charge neutralization was used during depth profiling.

3 ELECTRICAL CHARACTERIZATION TECHNIQUES OF MIM DEVICES

In this section, we present different electrical characterization techniques used to study the resistive switching behaviors of MIM cells: Conducting Probe Atomic Force Microscopy (CP-AFM) and two-probes method. These techniques will be discussed in detail thereafter. Electrical transport characterization method by the Electrochemical Impedance Spectroscopy (EIS) is also included at the end of this chapter.

3.1 Conducting Probe Atomic Force Microscopy (CP-AFM)

3.1.1 Basic principles of CP-AFM

Figure 2.26 illustrates the basic principle of the CP-AFM technique. It simultaneously allows topographical and electrical characterization of surfaces at nanometer scale [9].

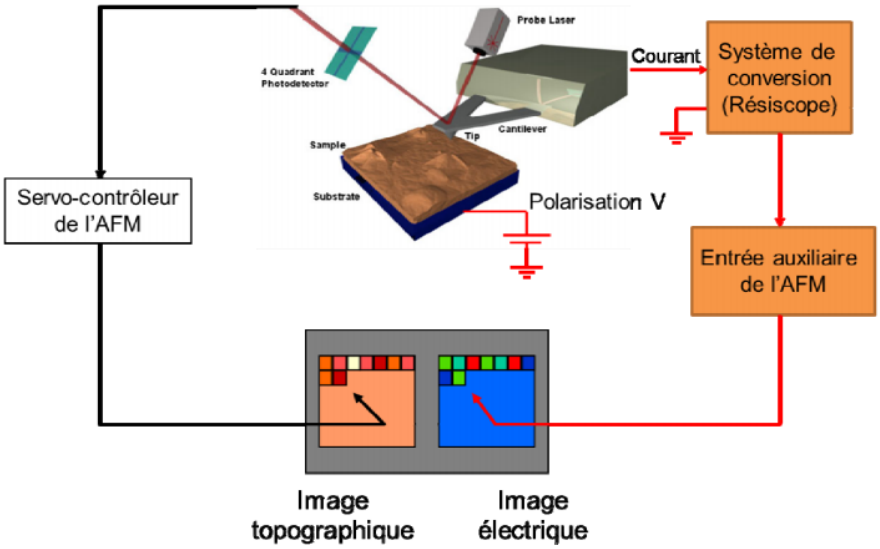

Figure 2.26: Schematic of CP-AFM and its principle of operation

The CP-AFM configuration which has been used is essentially similar to that of a conventional contact AFM. A tip (with a typical tip apex radius about 20-50nm) is located at the open end of a flexible cantilever. While the tip scans the surface (thanks to X-Y displacements of a piezoelectric device on which the sample is mounted), the deflection of the cantilever is detected though a laser beam reflected on the back top of the cantilever. A photodiode is used to analyze the laser beam deflection. A feedback loop allows the Z-displacement of the piezoelectric device to keep a constant cantilever deflection (in constant force mode). These Z-displacements allow the progressive elaboration of a topographical image.

At the GeePs laboratory, all the analyses in this thesis have been carried out in contact mode and constant deflection, using a Multimode IIIa apparatus from Bruker. The cantilevers are made by n-doped Si covered by p-doped diamond. A bias voltage V is applied to the sample, and the tip can be considered as grounded. The current i is then collected and converted into local resistance $R=V/i$ by a device called Resiscope (which has been developed at the GeePs lab and patented). The local resistance signals are finally used to construct the electrical image point by point. Measurable resistance values cover a wide range, from 10^2 to 10^{12} Ω for the setup we used.

3.1.2 Topographical and electrical resolution of CP-AFM

The nanocontact size a (supposed discoid, as shown on **Fig. 2.27**) between the tip and the surface depends on the tip apex radius Rt, the tip/surface force and the mechanical characteristics of the materials in contact (elastic modulus and Poisson coefficient). The relation is expressed in [11]. For a tip apex of 20-50nm and an average 100nN force, the nanocontact radius reaches maximum 2-3nm, for almost all materials.

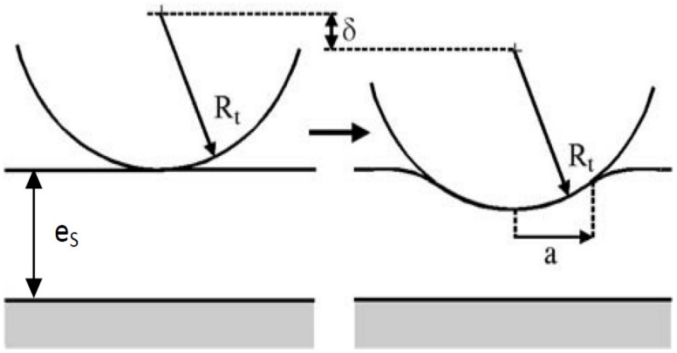

Figure 2.27: Schematic of nanocontact of radius a between the tip and the surface.

The topographical image resolution also depends on the surface roughness and the shape of the tip apex. Artifacts occur when the tip radius of curvature is higher than the local surface radius of curvature, as shown in **Fig. 2.28a**. Besides, the tip can be contaminated by some dusts or debris from the sample, as shown in **Fig. 2.28b**, which will also lead to artifacts. To remove contaminations, the best way is to scan the tip on a hard sample surface, while applying a higher force, until the tip becomes clean again.

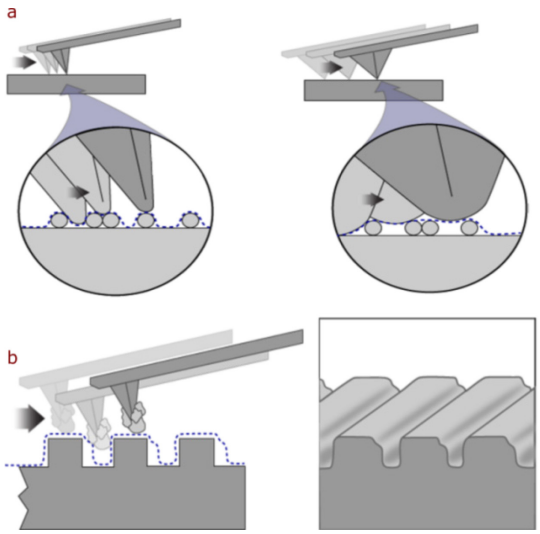

Figure 2.28: (a) high tip apex radius and **(b)** contaminations can reduce the resolution of the topographical image [10]

3.1.3 Electrical characterizations of thin films and MIM devices by CP-AFM

At GeePs laboratory, we characterize the electrical properties of surfaces in two configurations: Li_xCoO_2 thin films and MIM cells, as follows (**Fig. 2.29**).

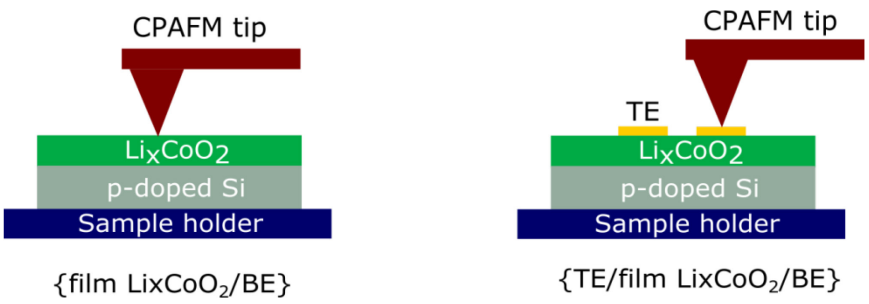

Figure 2.29: Two configurations used to characterize electrical properties of surfaces by CP-AFM

I usually characterized MIM {TE/film Li_xCoO_2/substrate} cells. The AFM tip is used to carry out two kinds of operations:

-characterizations without electrical modifications: a small bias is applied between the sample and the tip which is in contact with the top electrode (TE), in order to read the cell resistance value,

-modifications by application of a higher voltage, which will modify the film conductivity between the TE and the substrate.

An advantage of CP-AFM is the nanometric size of the tip apex. As a result, we are able to apply the biases on small TE areas (a few hundred nanometers). This is very useful to study the influence of downscaling on the behaviors of devices.

3.1.4 Example of characterization map using CP-AFM

Figure **2.30a** below shows an example of topographical/electrical images acquired using a +1V sample/tip voltage. The TE pads (1x1 µm²) have been deposited by e-beam lithography.

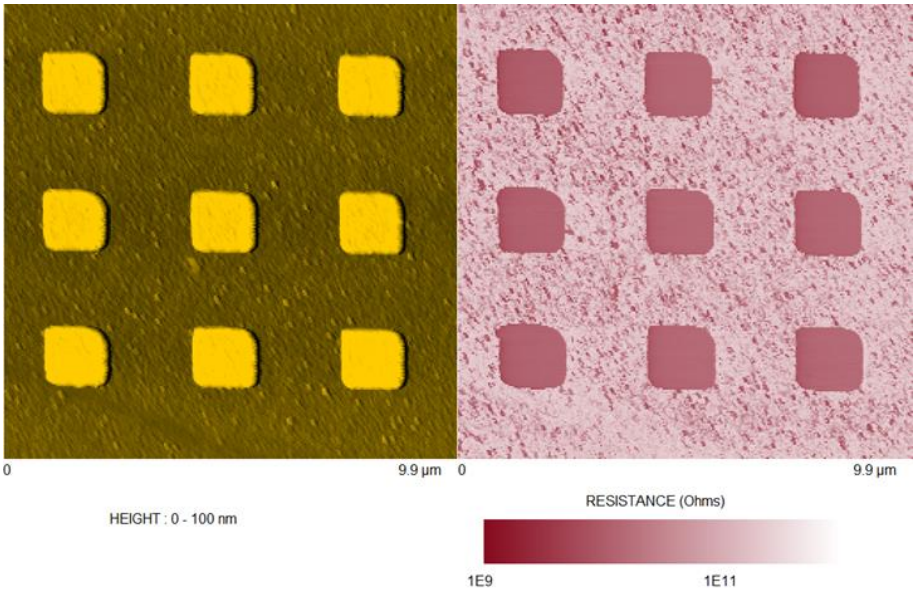

Figure 2.30a: topographical (left) and electrical (right) images of 1x1 µm² cells (recorded at +1V). Here, the cells resistance reach about 10^{10} Ω.

The electrical contrast of the previous electrical image can be explained the following way. In the case of a direct tip film surface, the resistance value measured by the Resiscope comes mainly from the tip/surface nanocontact (in **Fig. 2.31b-1**). On the contrary, the resistance measured when the tip touches the TE comes rather from the film resistance located between the TE and the substrate (in **Fig. 2.31b-2**), since the tip/TE resistance is low (~ a few kΩ).

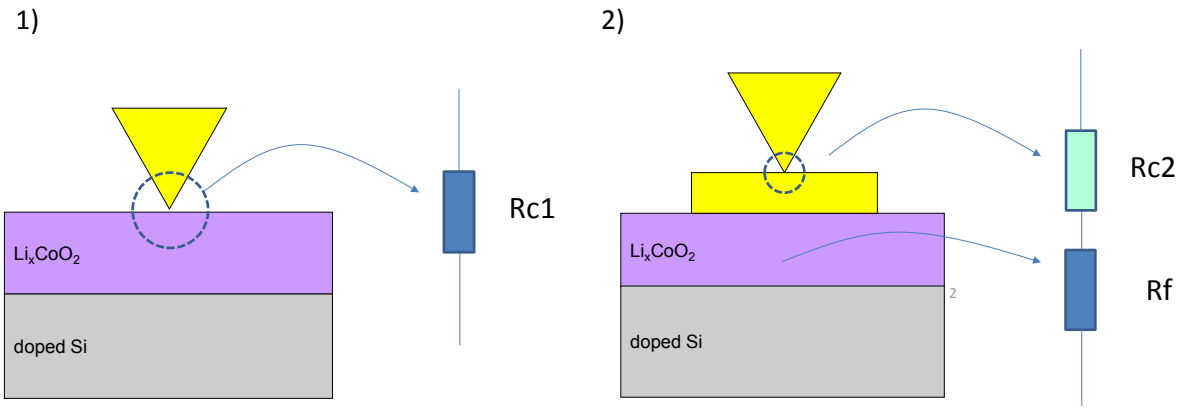

Figure 2.31b: 1) Rc1 corresponds to the tip/sample nanocontact.: Rc1 > 10^6 Ω **2)** Rc2 denotes the tip/TE contact : Rc2 reaches a few kΩ since the TE is made of Au, and Rf corresponds to the resistance of the film located between the TE and the doped Si substrate : Rf is typically in the range 10^6 -10^{12} Ω.

3.2 Two-probes method

The two-probes method is one of the standard and most-commonly used methods for resistivity measurement of devices. Two macroscopic probe tips (shown in **Fig. 2.32**) (usually made of Tungsten carbide) are mounted on the end of two separate arms which are fixed on two solid blocks. In these latter, three knobs allow tip displacements in X Y Z directions. As the probe is approaching to contact with sample surface, a kinematic bearing system eliminates lateral motion of the tip, providing a good contact without scratching electrode surface. The tips are usually shaped, so that the contact between them and surface of the sample is as small as few tens of microns.

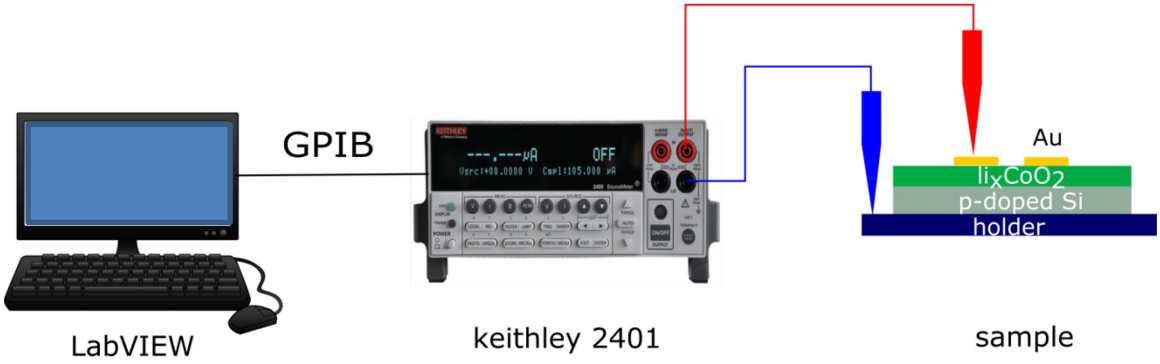

Figure 2.32: simple setup of two probes method

In our configuration, the two probes are connected to a Source Meter Keithley 2401 model as shown in **Fig. 2.32**. This electronical instrument provides precise voltage and current sourcing and measuring capabilities (1µV - 20V and 10 pA - 1A). The Keithley 2401 source meter has a 0.012% basic accuracy measurement and high reading speed (1700 readings/second). The source meter communicates with a computer via standard GPIB bus. The overall operation of this setup is controlled by a LabVIEW® program.

3.2.1 Pulses, ramps characteristics and read operation

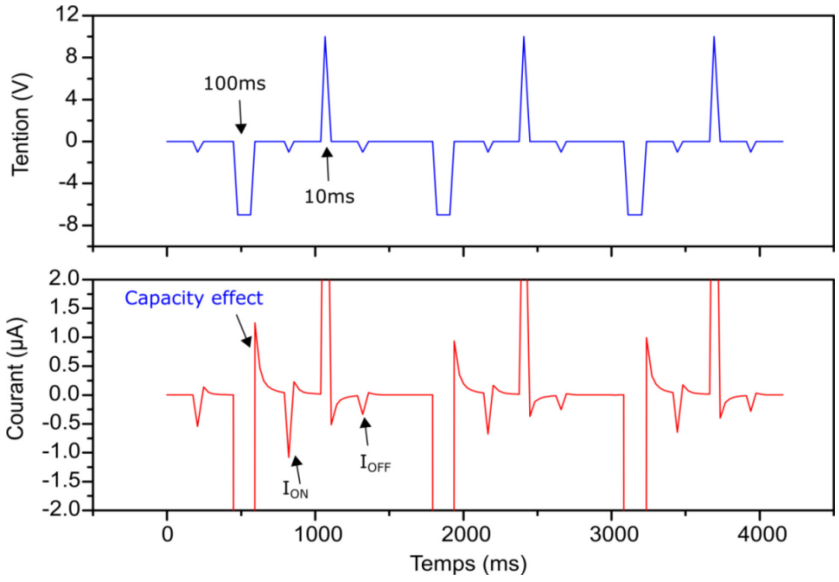

Figure 2.33: Voltage pulse characteristics and current response of Li_xCoO_2 MIM device

Towards endurance measurement experiments, I developed a LabVIEW® program to apply the bias pulses and measure the current flowing through the MIM studied device. If the applied pulse width is shorter than 50ms, the voltages have the shape of triangular spikes (for example in the case of 10ms pulses, as we can see in **Fig. 2.33**). This is because of the limitation of Keithley 2401 instrument. Therefore, the shortest pulse duration in our experiments was set to 50ms.

The read operation is always performed during application of low read voltages (≤1V) after a write voltage (higher voltage applied). During the read pulse, the current signals are measured after a delay set (>50ms) as sketched in **Fig. 2.34**. The read operation may take time depending on how many measurements must be recorded (green dots).

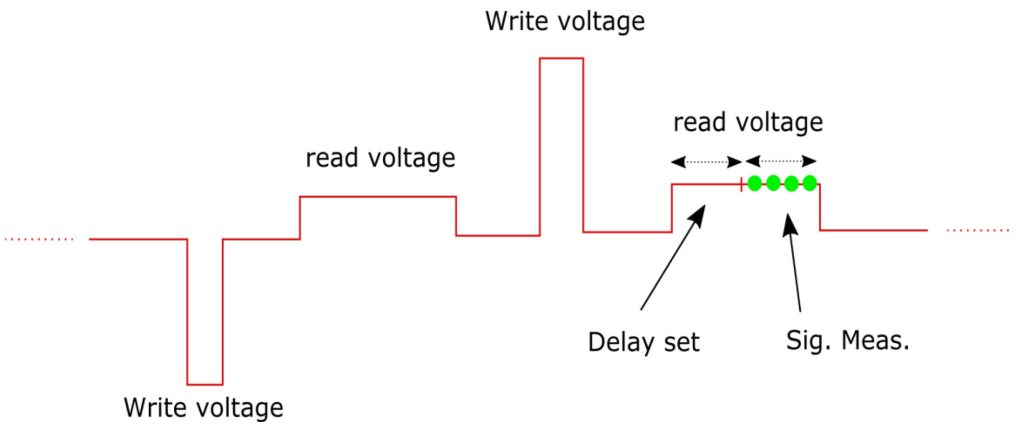

Figure 2.34: Sketch of read operation

3.2.2 Current compliance

Current compliance plays a crucial role for endurance measurements of such devices. If one wishes to record a high number of switching cycles, the applied power through the device must be limited in the low resistance state. As a result, current compliance limits the injected current in the device and therefore the Joule heating avoiding the breakdown of the device. When the output current exceeds a compliance value, the Source meter will immediately attempt to clamp that current.

With the Keithley 2410 model, we set the current compliance at 1mA for Li_xCoO_2 MIM device studies. The influence of current compliance on the performance on Li_xCoO_2 devices will be discussed in more detail in the next chapters.

3.2.3 Current-voltage curves

Towards I-V characteristics measurements, a ramped voltage has to be applied to the device. I thus developed another LabVIEW program. A typical I-V characteristic of a $100x100\mu m^2$ {Au/Li_xCoO_2/highly p-doped Si} cell is shown in **Fig. 2.35**. During the bias ramp, this sample switches from HRS to LRS at -6V then switches back to HRS at around +5V. A current compliance of 1mA is used to prevent the electrical breakdown.

In the thesis, two-probes method allowed to record I-V curves at different rates, in different environments such as low/high temperature, in vacuum...

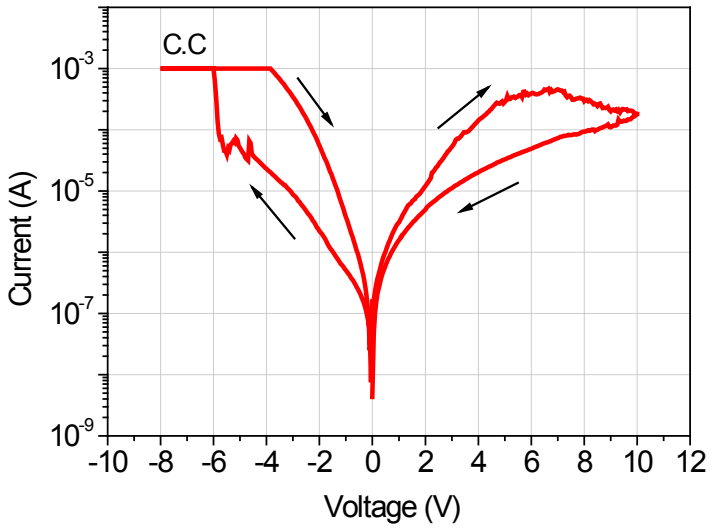

Figure 2.35: I-V characteristic of a 100x100µm^2 {Au/Li_xCoO_2/p-doped Si} cell, with a current compliance of 1mA (voltage sweep from 0→-8V→+8V→0 at a 0.1V/s rate)

3.3 Electrochemical Impedance Spectroscopy (EIS)

Electrochemical Impedance Spectroscopy (EIS) is a powerful diagnostic tool to characterize dynamics of electrochemical processes. It has been applied to study many physiochemical systems such as fuel cells, batteries, etc.

Electrochemical impedance is the response of an electrochemical cell to an alternative applied potential. To characterize this response, an AC voltage is applied to tune the cell at different frequencies.

For the Li_xCoO_2 MIM cells, EIS has been used to characterize the electrochemical reaction, conduction behaviors and diffusion of Li^+ ions through the cell before and after resistive switching. This may help to explain the RS mechanism of resistive switching.

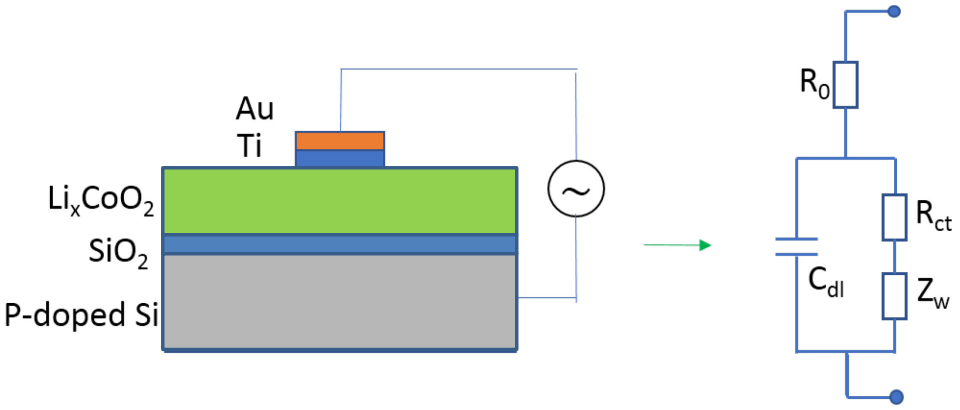

Figure 2.36: the Li_xCoO_2 based MIM structure (left) is represented by an electrical circuit (right)

The Li_xCoO_2-based memory structure is composed of a top electrode, the Li_xCoO_2 film, the bottom doped-Si substrate, and a thin SiO_2 layer (about 10nm thermally grown during annealing process for 1h @ 580°C) sandwiched between Li_xCoO_2 and Si. This structure can be modeled as an electrical circuit (called Randles model [11]) as shown in **Fig. 2.36**. The total impedance $Z\ (\omega)$ of the parallel RC circuit, which is frequency-dependent ($\omega = 2\pi f$), is given by:

$$Z(\omega) = Z' + jZ'' = R_0 + \frac{1}{\frac{1}{Z_W + R_{ct}} + j\omega C_{dl}}$$

where, R_0 quantifies the bulk resistance of the electrodes (Au/Ti and p-doped Si). This resistance is in series with the cell resistance, composed by:

- R_{ct} which is a charge transfer resistance. This resistance is due to a kinetically-controlled electrochemical reaction ($Red \leftrightarrow Ox + ne^-$). It depends on the reaction rate, temperature, concentration of the reaction products, and the applied voltage.
- Z_W, which is an impedance due to the ionic diffusion of reactants. This impedance is called Warburg diffusion impedance, and is defined as $Z_W = \sigma(\omega)^{-1/2}(1 - j)$ in which σ is the Warburg coefficient (depending on the temperature, diffusion coefficient, electrochemical reaction rate, *etc.*) [12].

In parallel to R_{ct} and Z_W, C_{dl} is a double-layer capacitance which depends mainly on the thickness of the SiO_2 layer e and the top electrode area S, defined as $C_{dl} = \rho(SiO_2) \times e/S$.

There are two ways to interpret the EIS data. First, the module of impedance $|Z|$ can be represented as a function of frequency f. This corresponds to the Bode plot. The interpretation using Bode plot clearly shows the influence of each element in the circuit as depicted in **Fig. 2.37a**. While the capacity effect appears important at high frequency, the ionic diffusion element (Z_W) has a particular low-frequency character (represented by a line with an overall $-45°$ slope). The charge transfer resistance (R_{ct}, due to resistance switching) is located in the intermediate frequency range.

In the second way to interpret the EIS data, the imaginary part of the Z impedance (its opposite: $-Z''$) is plotted versus the real part (Z') of the Z impedance, as illustrated in **Fig. 2.37b**. In this kind of plot, called Nyquist plot, the frequency is not explicit. The ionic diffusion element (Z_W) has a particular low-frequency character (represented by a line with an overall 45° slope).

At the C2N-Orsay lab, we developed an EIS measurement at low frequency and wide resistance range to try to detect Li^+ diffusion.

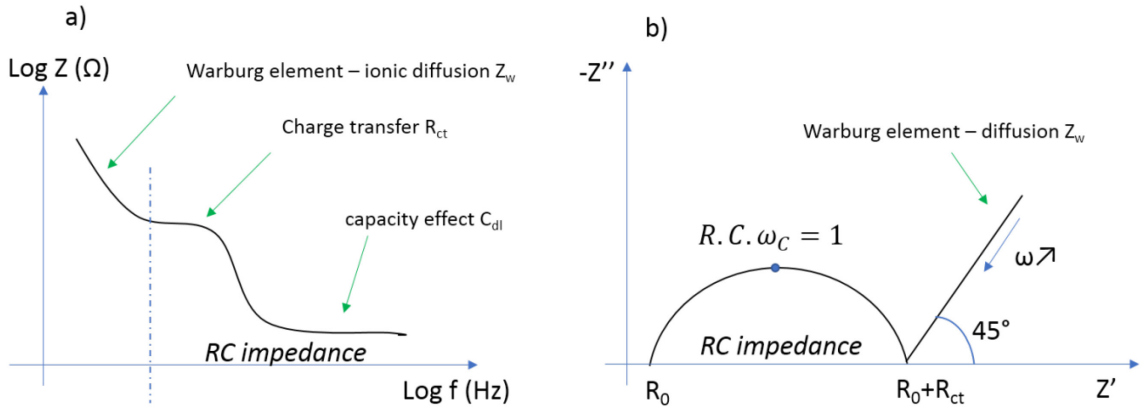

Figure 2.37: EIS data interpretation: **a)** The Bode plot, **b)** The Nyquist plot

4 CONCLUSIONS

The XRR technique allowed us to determine the mean thickness (~100nm) of most of the studied films. Moreover, XRD allowed us to obtain the average c-parameter value of the films, which is 1.41 nm (which corresponds to a stoichiometry of x=0.95): this parameter does not depend on the annealing time of the films. On the other hand, the average grain size of the films increases as a function of the post-annealing time, reaching approximately 10 nm for 1h annealing. More local analysis carried out by TEM (HAADF) showed that the c axis orientation of each grain is different, the mean c-axis being horizontally oriented. These analyzes also made it possible (by EELS) to detect the lithium element in these layers: apart from Li_xCoO_2, the films also contain Co_3O_4 and CoO (located in the neighborhood of the film surface). SIMS analyzes have enabled, after optimization of several parameters (ion source, impact energy, nature of the detected ions), to obtain nice depth profiles and 3D mappings of elements (Li, Co, O, Si): this will allow to compare pre-switched devices and virgin ones towards the determination of the RS mechanism (in Chapter 3).

The CP-AFM technique allowed us to obtain electrical images whose electrical contrast depends on whether the AFM tip directly contacts the film surface or the upper electrode surface. It is also a very simple tool for switching cells of any size: this will namely be used to study RS kinetics of devices in Chapter 4. The two-probes method is adequate for studying cells of 100x100µm surface (and beyond): it was used to carry out write/erase cycles, thanks to programs I was able to develop under LabVIEW. Such a technique will be used (in particular in chapter 5) to study the devices performances as a function of various parameters. Finally, an EIS technique has been developed in order to highlight the diffusion phenomenon which exists in the cells, which will be discussed in more details in Chapter 3.

5 REFERENCES

[1] "Magnetron Sputtering Technology." [Online]. Available: http://www.directvacuum.com/pdf/what_is_sputtering.pdf). [Accessed: 28-Jan-2017].

[2] "Comparing Olympus X-Ray Diffraction to conventional XRD." [Online]. Available: https://www.slideshare.net/OlympusIMS/comparing-olympus-xray-diffraction-to-conventional-xrd. [Accessed: 28-Jun-2017].

[3] V. H. Mai, "Etude de phenomenes de commutation de resistance de films minces de LixCoO2. Autre [cond-mat.other]. Universite Paris Sud - Paris XI, 2014. Fran ̧cais. < NNT : 2014PA112115 > . < tel-01164971 >," *Thesis Univ. Paris-Sud*, 2014.

[4] J. Kikkawa, S. Terada, A. Gunji, T. Nagai, K. Kurashima, and K. Kimoto, "Chemical States of Overcharged LiCoO 2 Particle Surfaces and Interiors Observed Using Electron Energy-Loss Spectroscopy," 2015.

[5] N. Dobigeon and N. Brun, "Ultramicroscopy Spectral mixture analysis of EELS spectrum-images," *Ultramicroscopy*, vol. 120, 2012.

[6] A. Fiori, F. Jomard, T. Teraji, G. Chicot, and E. Bustarret, "Improved depth resolution of secondary ion mass spectrometry pro fi les in diamond : A quantitative analysis of the delta-doping," *Thin Solid Films*, vol. 557, pp. 222–226, 2014.

[7] J. Sheng, L. Wang, G. E. Lux, and Y. Gao, "Improved determination of matrix compostion of Hg1−xCdxTe by SIMS," *J. Electron. Mater.*, vol. 26, no. 6, pp. 588–592, 1997.

[8] "X-ray Photoelectron Spectroscopy." [Online]. Available: https://www.ifw-dresden.de/institutes/ikm/research-teams-and-topics/micro-and-nanostructures/available-methods/xps/. [Accessed: 16-Aug-2017].

[9] T. W. Kelley, E. L. Granstrom, and C. D. Frisbie, "Conducting probe atomic force microscopy: A characterization tool for molecular electronics," *Adv. Mater.*, vol. 11, no. 3, p. 261–+, 1999.

[10] "AFM Image Quality." [Online]. Available: http://www.nanophys.kth.se/nanophys/facilities/nfl/afm/fast-scan/bruker-help/Content/Service and Apps/Troubleshooting/AFM Image Quality.htm. [Accessed: 21-Jun-2016].

[11] A. Lasia, "Electrochemical Impedance Spectroscopy and its Applications," *Mod. Asp. Electrochem.*, vol. 32, pp. 143–248, 1999.

[12] "Basics of Electrochemical Impedance Spectroscopy." [Online]. Available: https://www.gamry.com/application-notes/EIS/basics-of-electrochemical-impedance-spectroscopy/. [Accessed: 31-Jul-2017].

CHAPTER 3

MECHANISMS INVOLVED IN THE RESISTANCE SWITCHING PHENOMENON

TABLE OF CONTENTS

INTRODUCTION

In this chapter, {Au/Li_xCoO_2/Si} cells have been studied, using different means, in order to better understand the origin of the resistive switching phenomenon. This chapter is composed by three parts.

In the first part, we highlight the character (metallic or semiconducting) of the Li_xCoO_2-cells when these are in a high (resp. low) resistance state. To such an objective, the conductivity of these states has been recorded as a function of temperature. The obtained curves can be correlated to results from literature, to deduce in which way the films are modified (increase or decrease of x stoichiometry). Then, in order to confirm the hypothesis of ion migration, we quantitatively characterize the lithium distribution across the MIM cells in pristine and pre-switched cells, using Secondary Ion Mass Spectroscopy (SIMS).

In a second part, we study the resistive switching phenomenon, using a home-made setup which is being developed at C2N-IEF to characterize cells by Electrochemical Impedance Spectroscopy (EIS). The very first results obtained will be correlated to the semiconducting-metal transition.

Finally, in the third part, further discussion is done concerning the ionic and electronic conduction mechanisms involved. By examining I-V characteristics of cells, some more precise hypothesis can be put forward concerning the possible role of the SiO_2 thin layer which exists at the Li_xCoO_2/Si interface. Besides, the electronic conduction is also discussed and compared to a model of electron emission (Poole-Frenkel effect).

1 OBSERVATION OF NANOIONIC MIGRATION

1.1 Introduction: importance of film volume and bottom electrode, using finite element simulation

Resistive switching phenomenon was observed with two distinct experimental configurations. The first configuration corresponds to an AFM tip which applies the voltage directly on top of the Li_xCoO_2 surface. The second configuration is studied -in this thesis- using a deposited top metal electrode. An aim of this section is to provide some insight between these two configurations.

A finite elements simulation has been performed to estimate the difference in electric field distribution involving resistive switching inside these two distinct configurations: {AFM tip/ Li_xCoO_2/highly doped Si} and {Au/Li_xCoO_2/highly doped Si}. Results are given on figure in **Fig. 3.1**. In the simulation the electric field distribution is calculated on the finite elements of the MIM device using the following physical parameters: electrical conductivity of 10^9 S/m for the electrodes and 10^{-5} S/m for the film. A positive voltage of 8 volts is applied through the device from the top electrode while the bottom electrode is grounded.

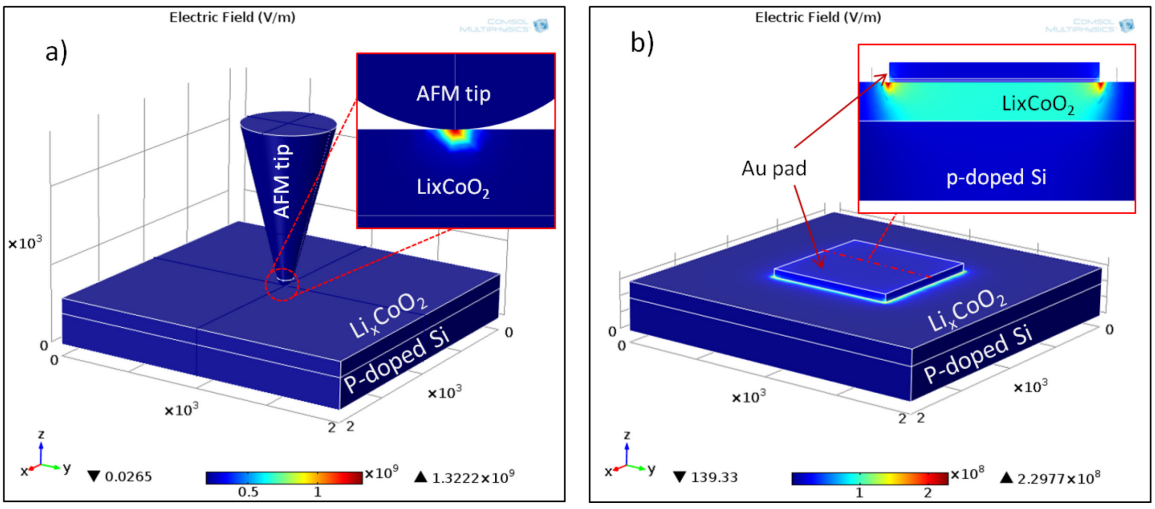

Figure 3.1: Finite element simulation of the electric field distribution in two configurations: a) {AFM Tip/ Li_xCoO_2/ highly doped Si} and b) {Au(50nm)/Li_xCoO_2/highly doped Si}. The voltage +8V is applied on the top of AFM tip and the bottom face of BE is grounded.

In the configuration described on **Fig. 3.1a**, the contact size between the AFM tip and the $LixCoO_2$ film is in the order of 1-2 nm (maximum), the electric field is thus concentrated at the tip/film interface. Therefore, the tip can only modify the film resistance at the immediate neighborhood of the surface (the main volume of the film and the bottom electrode are not involved in the modification). In opposite, the configuration described on **Fig. 3.1.b** is obviously completely different. The micrometric size of the gold electrode is much larger than the thickness of the film (~100 nm), resulting in a volumetric distribution of the electric field between the upper metallic electrode and the bottom {highly doped Si} electrode. We experimentally observed resistive switching phenomenon in this configuration. Thus the film volume and both electrodes could be involved in the switching process.

1.2 Indirect observation of Li^+ migration outward Li_xCoO_2 based devices: Temperature behavior of high resistance states and low resistance states

For over two decades, Lithium intercalation/de-intercalation from Li_xCoO_2 has been extensively studied [1]–[6] towards potential applicability in the field of energy storage (batteries).

Ménétrier *et al.* [7] showed that an *x* stoichiometry decrease leads to significant changes (also observed by *Molenda et al.* [8]) of the Li_xCoO_2 electrical conductivity, starting from a semiconducting state (from x = 1.0 to x = 0.74) to a metallic (or pseudo-metallic) state (from $x = 0.74$ to $x = 0.55$) (in between a mixture of both states exists). Hence, as shown in **Fig. 3.2a**, depending on the *x* stoichiometry, Li_xCoO_2 behaves differently with the absolute temperature. The electrical conductivity decreases rapidly with lowering temperature in the semiconducting regime, while it almost stable in metallic regime.

Hence in this section, our objective was to study the behavior (metallic or semiconducting?) of Li_xCoO_2 devices before/after resistance switching: to do so, we studied the overall conductivity of {Au/Li_xCoO_2/p-doped Si} devices as a function of temperature, to correlate them to the results of **Fig 3.2a**.

In our experiment, the resistance of an MIM cell has been measured (using a small bottom/top voltage of -0.1V) as a function of temperature (300K⇨77K⇨300K at 20K/min) for different successive resistance states: i) at the cell pristine state, ii) after a first SET1 switching pulse (**Fig 3.2b** inset) iii) after a second (SET2) switching pulse iv) after a third (SET3) switching pulse and finally v) after a RESET pulse (**Fig 3.2b** inset).

At a virgin state of the cell, the conductance decreases rapidly with decreasing temperature, then it fluctuates, due to the measurement limit of the Keithley source meter (see gray curve in **Fig 3.2b**). This can be correlated to **Fig 3.2a**: it corresponds to a lithium-rich phase ($x \approx 0.95$ in our film). After a SET1 pulse, the cell conductance (which has become higher at ambient temperature) decreases with 1000/T (blue curve) less rapidly than initial conductance does (gray curve). This can also be correlated to the results of *Ménétrier et al* [7]: it corresponds to a lower *x* stoichiometry and thereby a metallic phase. After the SET2 and SET3 pulses, the cell conductance is even higher, and the metallic character increases (orange and red curves). We did not apply further SET pulses, in order to avoid a breakdown of the cell. The final application of a RESET pulse led back to a more semiconducting character (green curve).

Therefore, the curves observed after SET1, SET2 and SET3 pulses can be reasonably explained by a modification of the Li_xCoO_2 film which is due to an *x* decrease in the film and a lithium de-intercalation from the film towards the bottom Si electrode (illustrated in **Fig 3.2c**). The RESET process can be attributed to a lithium reintercalation (not completely) from the Si towards the Li_xCoO_2 film (**Fig 3.2d**).

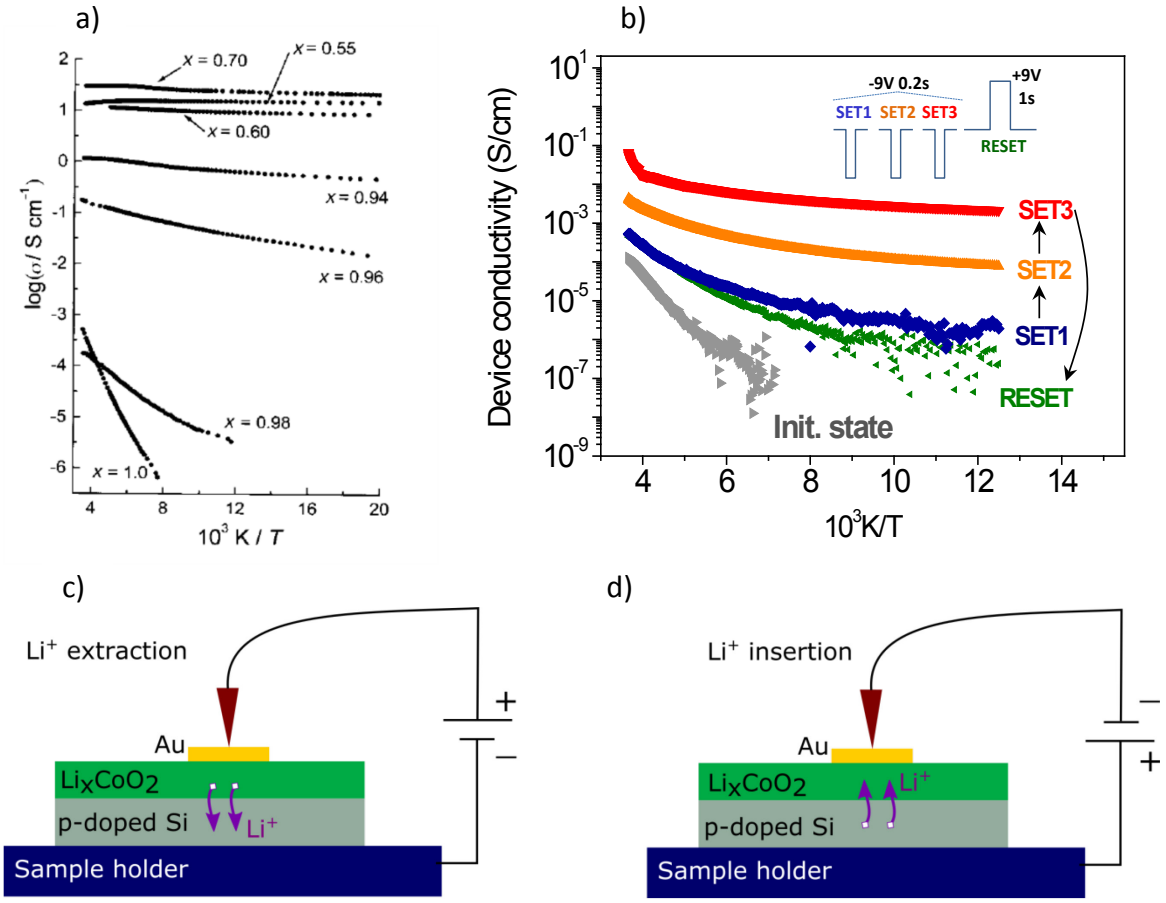

Figure 3.2: Evolution of electrical conductivity as the function of 1000/T by: **(a)** Ménétrier [7], **(b)** our experiment: 3 SET processes (Gray→blue→orange→red curves) using (-9V, 200ms) pulses, followed by a RESET process using one (+9V, 1sec) pulse **(c)** illustration of lithium deintercalation and **(d)** illustration of lithium re-intercalation back towards the Li_xCoO_2 thin film.

However several questions need to be addressed, in particular:

- Is it possible to observe directly the Li^+ migration outwards the film?
- Does this process involve homogeneous or filamentary changes?

The following experiments will help to better understand the origin of the resistive switching process.

1.3 Direct observation, using SIMS, of Li^+ diffusion into bottom electrode (silicon) in Li_xCoO_2 devices

Li ion intercalation/de-intercalation in solid state devices induces resistive switching and memory effects as well as changes in the magnetic properties of the layers. But as discussed in the first chapter, direct correlation with lithium distribution is still missing [9].

Here, we try to directly observe the presence of Li intercalated into Si inducing resistance switching effect. Using Secondary Ion Mass Spectrometry (SIMS) from the GeMAC Laboratory (Versailles) we quantitatively characterize the lithium distribution across the MIM cells.

To characterize Li distribution, three {Au/Li_xCoO_2/doped Si} cells have been characterized by SIMS as shown in **Fig. 3.3**. In a pristine cell, lithium content in Si appears very low (**Fig. 3.3a**) and its distribution appears fairly "uniform" (blue dots randomly distributed in the Si). This can correspond to a "noise" signal attributed to the lower detection limit of the SIMS technique for this element. The corresponding depth profile in **Fig. 3.3d**, reveals a similar (decreasing) evolution of lithium and cobalt intensities.

In pre-switched cells (6 devices studied, switched to a low resistance state $\leq 10^6\Omega$), one or more zones of greater Li concentration in the Si electrode are always recorded. These zones appear in the form of "carrots", measuring a few microns in diameter and a few hundred nanometers in depth. A typical example is illustrated in **Fig. 3.3b**. The Li composition found in these zones is over 20 times higher than the lower detection limit (surrounding zones of randomly distributed Li signal). Besides, the corresponding lithium profile in **Fig. 3.3e** shows a bump (see black arrow) which does not appear in **Fig. 3.3d** (pristine state cell).

Finally, in cells which had been pre-switched to a LRS and back to a HRS, it can be seen in **Fig. 3.3c** that nearly no lithium accumulation zone exists in Si. In addition, **Fig. 3.3f** shows no bump in the lithium profile inside Si (black arrow).

We can therefore conclude that lithium migration towards Si (after resistance switching to a cell low resistance state) has been clearly evidenced by SIMS.

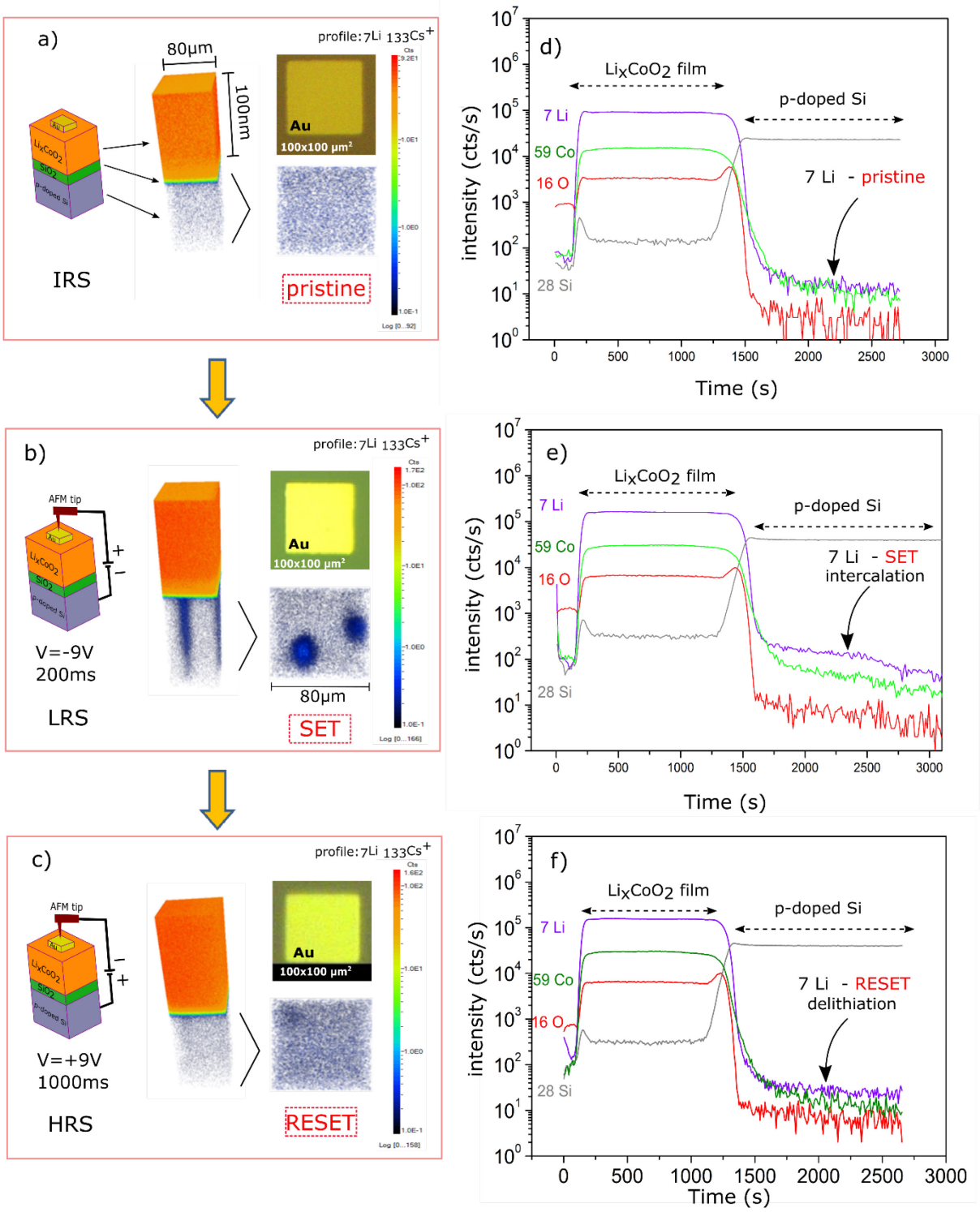

Figure 3.3: a) SIMS 3D distribution of 7Li in a pristine cell and **d)** SIMS depth profiles of Li, Co, O and Si of such a pristine cell **b)** SIMS 3D distribution of 7Li in a cell switched to a LRS and **e)** SIMS depth profiles of Li, Co, O and Si of such a LRS cell **c)** SIMS 3D distribution in a cell consecutively switched to LRS then HRS and **f)** SIMS depth profiles of Li, Co, O and Si of such cell.

To confirm that in 3D-SIMS distributions of 7Li, dark blue zones ("carrots") really correspond to a higher lithium concentration than in the surrounding zones, we selected two 30µm-side squared zones as illustrated in **Fig. 3.4a**: the red square corresponds a dark blue area observed (zone 1), and the blue square corresponds to an arbitrary zone (zone 2, different from zone 1). The red curve in **Fig. 3.4b** represents the 7Li depth profile in zone 1 while the blue curve represents the 7Li depth profile in zone 2. By comparing the intensity of two profiles, it emphasizes that the intensity i.e. the concentration of lithium in zone 1 is higher than in the surroundings (zone 2).

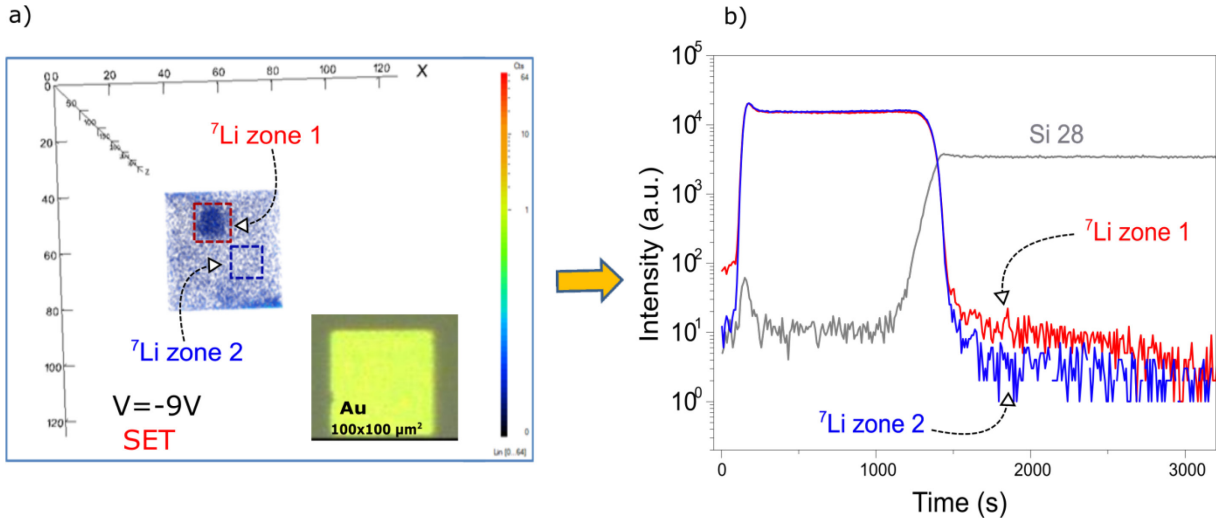

Figure 3.4: a) SIMS Characterization SIMS in two specific zones of a single cell (at LRS): Zone 1 marked in red corresponds to a higher Li concentration in Si compared to Zone 2 (marked in blue), by looking at the **b)** 7Li corresponding depth profiles.

1.4 Resistive switching mechanism deduced from previous observations: nanoionic-based mechanism

From indirect and direct observations reported in previous sections, the general mechanism of resistive switching in Li_xCoO_2 based MIM stack (**Fig. 3.5a**) can be therefore explained as follows. When the bottom electrode is negatively polarized, the electric field drives Li^+ ions to extract from the Li_xCoO_2 film and to intercalate into Si through the SiO_2 layer (SiO_2 acts as a solid electrolyte which allows Li^+ diffusion). Two redox reactions take place simultaneously in the cell:

- Li^+ ions are reduced to form Li_xSi complexes in Si (**Fig. 3.5b**: $Li^+ + e^- \rightarrow Li_xSi$ (presence of lithium observed by SIMS in Si, section 1.3). The x content in the Li_xCoO_2 film decreases (corresponding to an increased metallic character of the film: section 1.2).

- Co^{3+} is simultaneously oxidized in the film according to equation: $Co^{3+} \rightarrow Co^{4+} + e^-$.

In the reverse bias polarization shown on **Fig. 3.5c**, there is an oxidation of Li in Si according to equation: $Li_xSi \rightarrow Li^+ + e^-$. The opposite electric field drives Li^+ ions de-intercalate from the Si electrode (observed by SIMS, section 1.3) and insert into the Li_xCoO_2 film. The simultaneously reduced reaction of Co takes place in the film: $Co^{4+} + e^- \rightarrow Co^{3+}$. The stoichiometry x increases. The conductivity of the film decreases. The cell is switched back to a high resistance state.

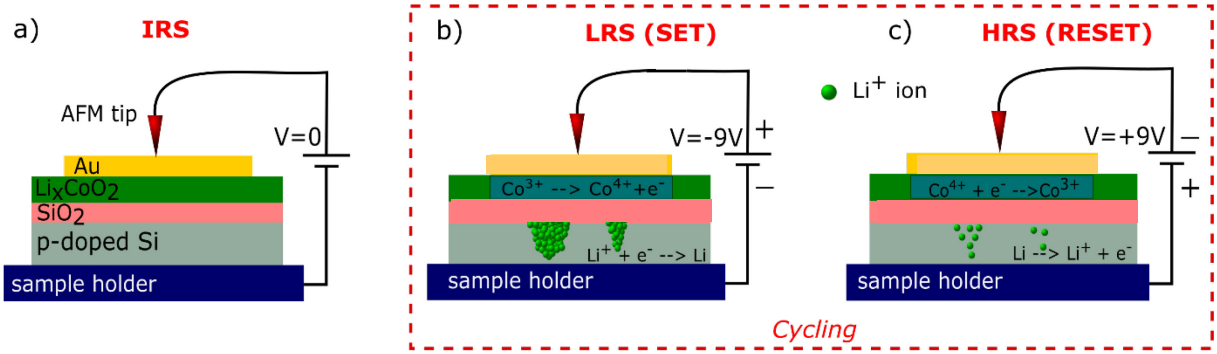

Figure 3.5: Mechanism of Redox Resistive Switching in Li_xCoO_2 based MIM cell: Schematics of MIM cell at three resistance states (a) IRS (no intercalation), (b) LRS (Li^+ intercalation: formation of conduction paths) and (c) HRS (Li^+ de-intercalation: disruption of conduction paths).

Hence, the modification of the Li_xCoO_2 film conductivity (insulator-metal transition) coupled with Li^+ intercalation/de-intercalation in Silicon appears as essential to nanoionic redox-based the resistive switching mechanism of Li_xCoO_2 MIM memristive devices.

Some questions remain however unanswered, for example: what is the exact role of the SiO_2 layer (~10-20 nm thick)? Does it only act as a solid electrolyte which allows Li^+ diffusion? We could think that, like in ECM cells (Chapter 1, part 2.2.2), metallic Li filaments grow inside SiO_2, starting from the bottom electrode (when negatively polarized) towards the Li_xCoO_2 film. Nevertheless, it remains only a hypothesis.

2 STUDY OF THE RESISTIVE SWITCHING MECHANISM USING ELECTROCHEMICAL IMPEDANCE SPECTROSCOPY

Electrochemical Impedance Spectroscopy (EIS), which was introduced in chapter 2, is used to study the resistive mechanism of Li_xCoO_2 thin film - based memory device. Since the mechanism is related to Li^+ diffusion (intercalation) and correlated insulating-metallic transition, the aim is to use EIS technique to study the response of the Li_xCoO_2 system to the application of a periodic AC signal, from which the EIS response may express the information of resistance/capacitive behavior of system, electrochemical reactions taking place at interfaces, electron transfer rate of reaction, diffusion control, *etc.*

The Li_xCoO_2 – based MIM cell structure can at first sight be represented by Randles circuits (section 3.3 Chapter 2). It must be kept in mind that our cells differ from such circuits (at low frequencies or DC, the Randle circuit has an "infinite" impedance which is not the case of our MIM cells). However this rough representation can give some hints towards comprehension.

We used a home-made setup which is being developed to characterize EIS at C2N laboratory. The EIS data of a {Au(50nm)/Ti(20nm)/Li_xCoO_2/p-doped Si} sample (annealed 1h at 580°C) responding to the AC signal with amplitude increasing from $0.142V$ to $8.5V$ is obtained. The frequencies measured are ranging from $4kHz$ to $1Hz$. The expected difference (HRS: Z_{OFF} and LRS : Z_{ON}) of the cell can be interpreted using Bode plot as shown in **Fig. 3.6a** and Nyquist plot (**Fig. 3.6b**). All elements of each resistance state such as capacitance, charge transfer resistance and Warburg diffusion could normally appear on the EIS spectrum.

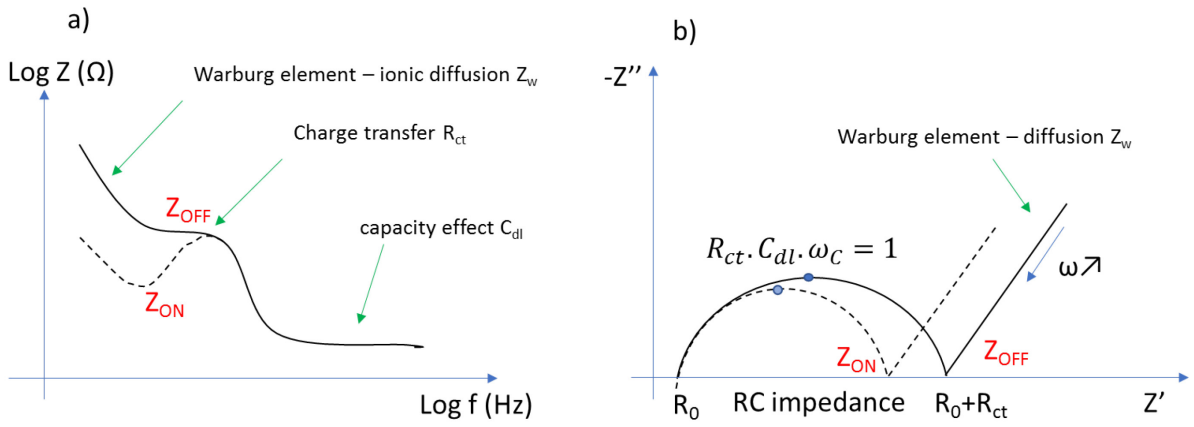

Figure 3.6: Sketch of the difference expected in EIS data of two resistance states of MIM cell: Z_{OFF} (before switching) by solid line and Z_{ON} (after switching) by dashed line interpreted using: **a)** The Bode plot, **b)** The Nyquist plot.

In regime A (AC voltage from 0.425V to 4.675V) on the Bode plot (**Fig. 3.7a**), the EIS curves exhibit a dramatic increase of cell impedance Z' as the frequency decreases from 4kHz down to 1Hz. Also, the Nyquist plot (**Fig. 3.7c**) confirms the existence of capacitive effect in this regime. The R_{OFF} (HRS) state remains during this regime. The not-well-defined semicircles become larger as the voltage increases in this regime. This can be accounted by a modification of the film properties (inside the film volume).

When the applied voltage becomes higher (over a threshold voltage), the cell switches from R_{OFF} to R_{ON}, and the EIS responses obtained from $4.675V$ to $6.685V$ illustrates many drops of impedance at low frequency, as shown in regime B (**Fig. 3.7a**). The i(v) curve in **Fig. 3.7b** also displays the HRS-to-LRS transition states occur in the voltage range from $3.9V$ to $6.2V$. In addition, a big jump from HRS to LRS at around $-6V$ in this i(v) curve can be correlated with EIS spectrum observation (on **Fig. 3.7a**). In **Fig 3.7d** we observed that the semi-circle becomes smaller when the AC voltage increases.

Finally, for higher voltages (regime C: from $6.685V \rightarrow 8.5V$), we can observe in **Fig. 3.7a**, that the cell stays now in its low resistance state (LRS). The fluctuation of EIS curves vanishes (observed by smooth curve in regime C, **Fig. 3.7b**). The semi-circle is very small as shown in **Fig 3.7d**.

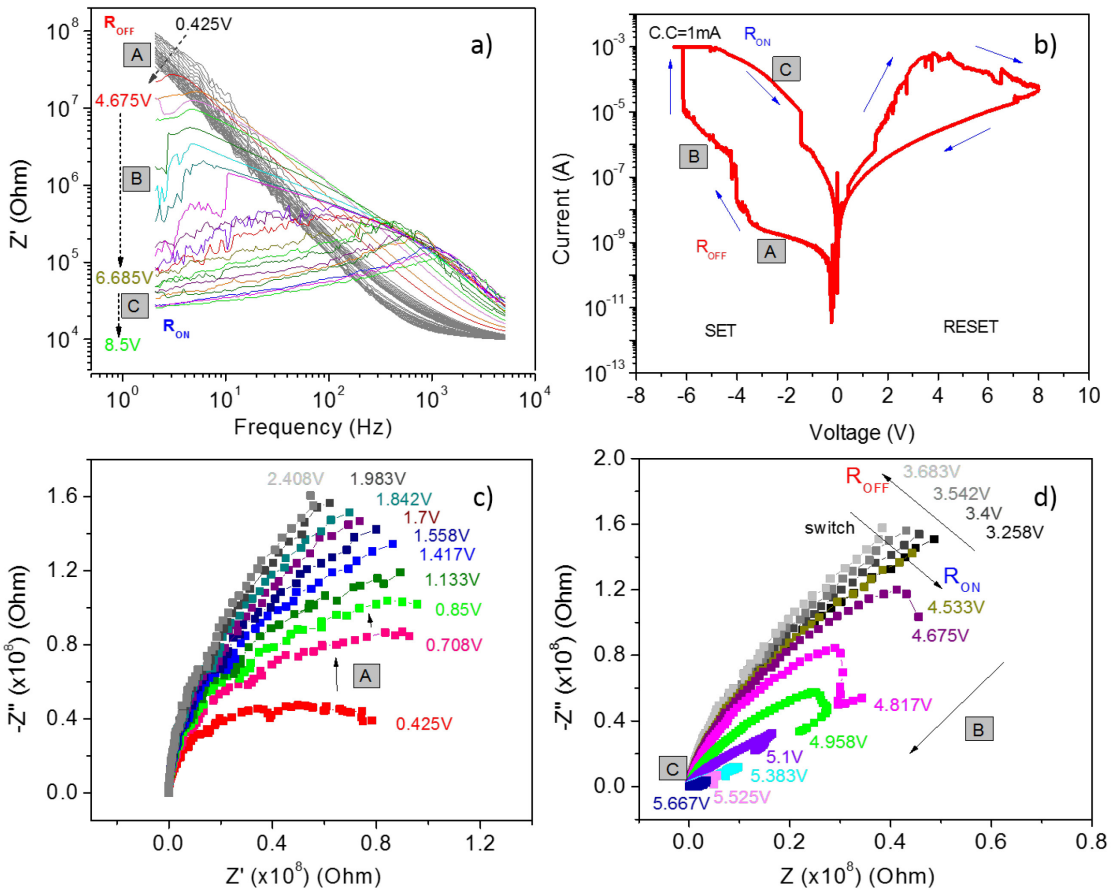

Figure 3.7: Interpretation of EIS data: **a)** Bode plots, **b)** i(v) characteristics of cell with slow sweeping rate of $0.005V.s^{-1}$ and current compliance of 1mA, **c)** & **d)** Nyquist plots. Regime A (AC voltage: 0.425V→4.675V) corresponds to capacitive effect. Regime B displays switching correlated to semiconductor-metal transition (AC input: 4.675V→6.685V). Regime C (AC input: 6.685V→8.5V) exhibits stable conduction. Frequency range of EIS measurement is from 4kHz to 1Hz. The amplitude of AC input is increased during EIS measurement with a step of few hundred mV.

The EIS results have also shown the resistance switching phenomenon of Li_xCoO_2 MIM device. However, the ionic (lithium) diffusion has not yet been observed by EIS, because we did not go below 1Hz. Further studies are needed to evidence lithium diffusion at lower frequencies.

3 ELECTRONIC AND IONIC CONDUCTION MECHANISMS

3.1 Introduction

Various models have been applied to explain conduction mechanisms for resistive switching [10]. **Table 3.1** shows two main contributions to electrical conduction which can occur at the interface and in bulk layers. Basically, the electrode-limited conduction mechanism is non-negligible if the system is highly thermally activated and the potential barrier is very small, which is not our case.

In the resistive switching mechanism of Li_xCoO_2 memory device we simply take into account two fundamentally bulk-limited conduction models: Ionic conduction (corresponding to ionic transport) and Poole-Frenkel conduction (corresponding to electronic transport), respectively.

Electrode-limited conduction mechanism	**Bulk-limited conduction mechanism**
1) Schottky emission	1) Poole-Frenkel emission
2) Fowler - Northeim tunneling	2) Hopping conduction
3) Direct tunneling	3) Ionic conduction
4) Thermionic - field emission	4) Ohmic conduction
	5) Space-charge-limited conduction
	6) Grain boundary limited conduction

Table 3.1: Summary of conduction mechanisms in general dielectric materials [10].

3.2 Ionic conduction

Here, we would like to put forward a possible role of the SiO_2 layer, apart from allowing the diffusion of Li^+ ions. Indeed, a possible generation (in SiO_2) of conducting paths made of metallic lithium might also exist, by comparison with the ECM model (presented in Chapter 1, section 2.2.2).

Ionic conduction corresponds to the Li^+ ion transport through a potential barrier under high electric field applied. As depicted in **Fig. 3.8**, in case there is no electric field E, Li^+ ions cannot overcome the high potential barrier Φ_B (due to SiO_2), thus nearly no ionic current is

possible. However, if $E \neq 0$, the potential barrier Φ_B is reduced by $qdE/2$. Li^+ now can migrate through SiO_2 layer. The ionic conductivity $\sigma_{(Li^+)}$ is given by [11]:

$$\sigma_{(Li^+)} = \sigma_0 . \exp\left[-\left(\frac{q\Phi_B}{kT} - \frac{qEd}{2kT}\right)\right] \quad (1)$$

Where σ_0 qualifies an exponential factor, q is the charge of carrier, d is the thickness of potential barrier (SiO_2), E is applied electric field, k is the Boltzmann constant ($= 1.38 \times 10^{-23} m^2.kg.s^{-2}.K^{-1}$) and T the absolute temperature (K).

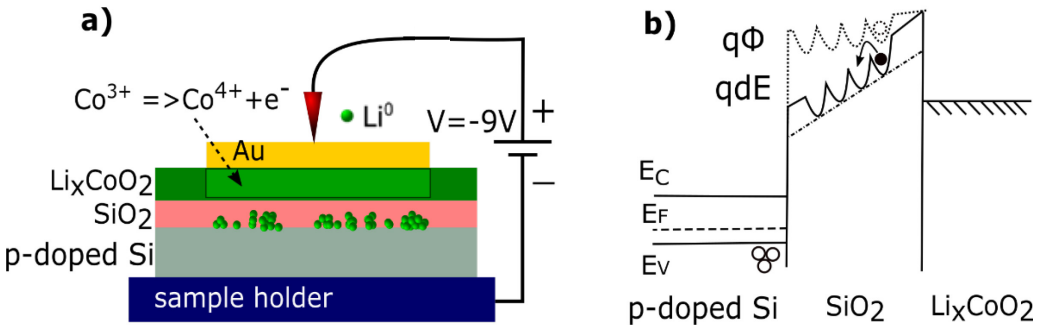

Figure 3.8: Ionic conduction model. **a)** Schematics of device with Li^+ diffusion into SiO_2 layer yielding possible conducting paths (in green) (Negative bias applied to bottom electrode); **b)** Schematics of energy diagram of ionic conduction model with (solid line) and without electric field (dashed line), adapted from [11].

To an {Au/Li_xCoO_2/Si} cell, we applied a negative bias ramp (0V→-7V→0V with sweeping rate of 0.05V/s in ambient air). In the I-V characteristics of the cell (shown in **Fig. 3.9**), we observe that the current response of the first voltage sweep (from 0V to $-4.5V$) is noisy. This might lead, as a hypothesis, to the formation of metallic conduction paths which start to grow from the bottom electrode. When the ramp voltage is further increased, the conduction paths may grow faster from the bottom electrode towards the film. At $-5V$ voltage, the conduction paths may be very close to the film, showing that the current fluctuates very much at this state. This state may be caused by the variation of nanoscale contact, as reported by N. Onofrio *et al.* for Cu/SiO_2 cells [12]. Finally, at a given threshold voltage ($-6V$), we observe a sudden switch from HRS to LRS. It could be interpreted the following way: a first conduction path reaches the film, making a conducting bridge in the cell (as schematics in inset of **Fig. 3.9**). The cell is set to LRS (the current compliance is set at 10mA to limit the joule heating effect and avoid electrical breakdown of the cell).

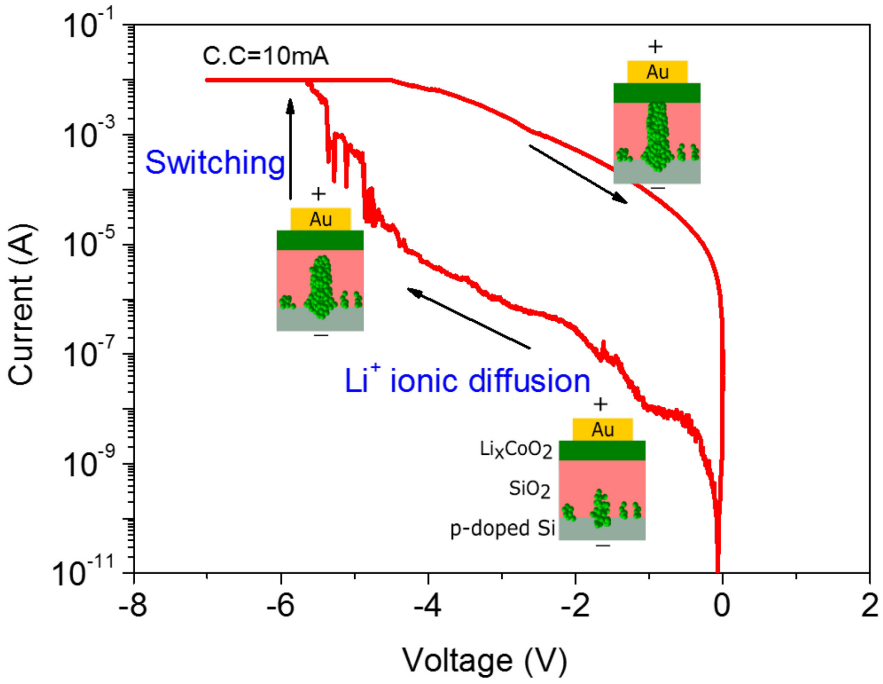

Figure 3.9: I-V characteristics of a {Au/Li_xCoO_2/p-doped Si} cell, showing ionic diffusion (metallic conduction paths appear in green) and switching mechanism hypothesis. Voltage is swept from 0V to -7V. Current compliance (or current limitation) is set to 10mA.

To some extents, this mechanism seems to be similar the ECM cell mechanism, for which the electroforming step yields a conducting filament, i.e. the ions migrate and are reduced in the electrolyte at nanoscale.

However, there are some differences. First, the ion source of an ECM cell is the product of redox reactions at the anode/electrolyte interface, leading to the dissolution of the anodic electrode. On the other hand, the Li^+ ions are de-intercalated from (and intercalated into) Li_xCoO_2 films. Second, the resistance state of the ECM cell depends on the conductivity of the filament, while the resistance state of Li_xCoO_2 MIM cell depends not only on the conduction paths but also on the Li_xCoO_2 film conductivity (which is modified due to the Li^+ migration).

3.3 Electronic conduction

Towards further discussion, we assume the hypothesis of metallic conduction paths formation, hypothesis which has been presented previously. Hence, when the Li metallic conduction paths are formed, the oxidation reaction of cobalt (which occurs simultaneously) produces more electrons as the equation: $Co^{3+} \rightarrow Co^{4+} + e^{-}$. On the other hand, the application of external electric field will reduce the Coulombic potential barrier. Thus the electrons are thermally activated to get out of the trap (by some probabilities) to the conduction band. This is called Poole-Frenkel (PF) emission of electrons. The illustration of PF model is shown in **Fig. 3.10**. The expression of PF model [13] is given by:

$$\sigma_{(elec)} = \sigma_0 . \exp\left(\frac{\beta E^{1/2}}{2kT}\right) \tag{2}$$

with:

$$\beta = e^{3/2}[\pi . \varepsilon . \varepsilon_0]^{-1/2}$$

Where σ_0 is an exponential factor, $\sigma_{(elec)}$ is the conductivity of the cell, E is the applied electric field, e is electrical charge of an electron, ε is dielectric constant of Li_xCoO_2 thin film, ε_0 vacuum permittivity, T is the absolute temperature, k the Boltzmann constant.

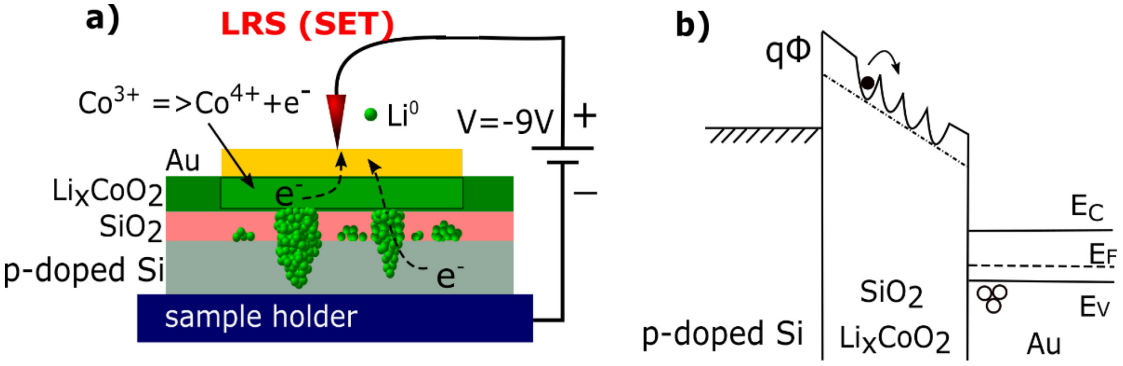

Figure 3.10: PF emission model. **a)** Schematics of an MIM device with Li+ diffusion into SiO_2 layer yielding possible metallic paths (Negative bias is applied to Bottom Electrode) and electron conduction in Li_xCoO_2 film and conduction path **b)** Schematics of energy diagram of ionic conduction model: electrons are de-trapped (delocalized) and jump to the conduction band through the potential barrier, providing current flow in the cell, adapted from [14].

Here, the aim is to compare the behavior of the R_{ON} state (low resistance state: LRS) of an MIM cell and the PF model of electronic conduction.

In the experiment, the I-V characteristics (0➔-12V➔+12V➔0V, sweeping rate $0.05V/s$) of an {Au/Ti/100nm thick Li_xCoO_2/p-doped Si} sample have been obtained at low temperature ($79K$, to avoid as much as possible the influence of temperature on switching cell, e.g. Joule heating etc.). Hence the sweep voltage from 0V to $12V$ in magnitude leads to a high electric field which varies from 0 to $1.5 \times 10^8\ V/m$.

For the PF model, the plot $Ln(\sigma)\ vs.\ E$ using equation (2) above is shown in **Fig. 3.11**. The exponential factor β depends on the dielectric constant ε of Li_xCoO_2. (we assumed $\varepsilon \approx 4$). As we can observe from **Fig 3.11**, after a sudden switch from HRS to LRS, the R_{ON} state behaves smoothly, and can be fitted (to some extent) with the PF model using the pre-exponential factor $\sigma_0 = \sigma_{ON} \approx 10^{-7}(S/cm)$ (green curve). This can be attributed to electronic conduction which takes place inside the Li_xCoO_2 film. We can however observe that in the negative voltage polarity, the experimental curve slightly deviates from the model (see blue arrow). Joule heating is high at this electric field regime, which can result in the higher curvature of the i(v) curve. But on the whole, after switching from HRS to LRS, the behavior seems to follow electronic conduction model.

During switching from LRS to HRS for positive voltages, we can observe that the I-V curve is noisy again, which can be attributed to the existence of ionic conduction (see black arrow on **Fig 3.11**). However, after LRS➔HRS complete switching, the curve behaves smoothly, and can be fitted also by the PF model, using the pre-exponential $\sigma_0 = \sigma_{OFF} \approx 10^{-9}(S/cm)$ (about 2 orders of magnitude lower than σ_{ON}) which is deduced from the Arrhenius relation of experimental $Log(\sigma)\ vs.\ 1000/K$ curve in some refs. [15],[16] (see blue curve).

This rough model is proposed to explain the electronic conduction mechanism, which is different from ionic conduction.

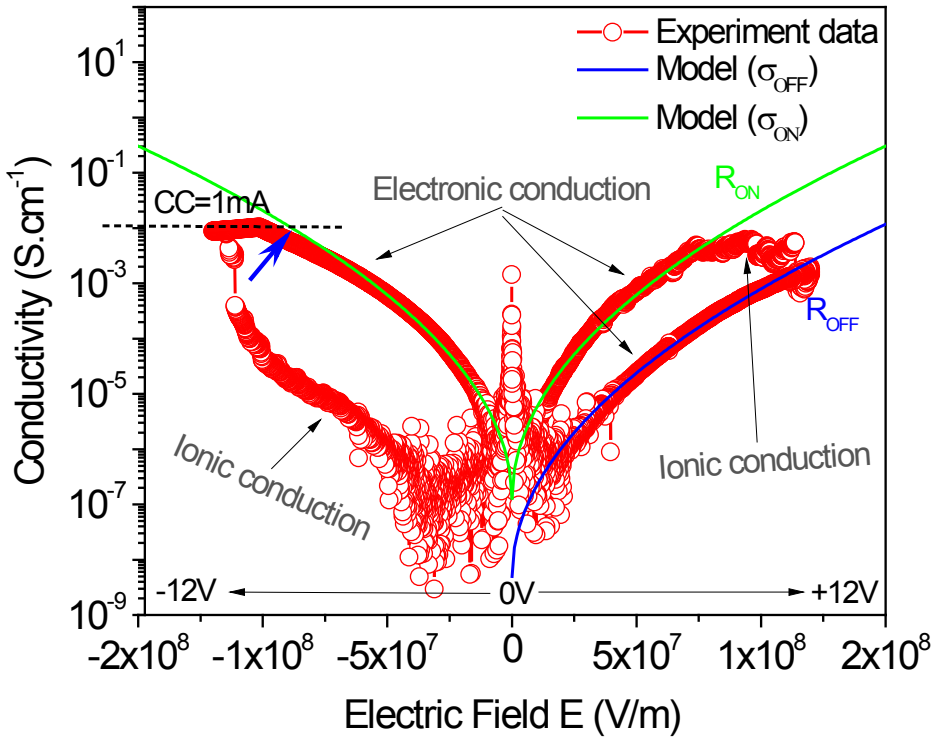

Figure 3.11: I-V characteristics of an {Au(50nm)/Ti(20nm)/Li_xCoO_2/p-doped Si} MIM cell at low temperature (79K). Sweep voltage is from $0V \rightarrow -12V \rightarrow +12V \rightarrow 0V$ (at 0.05V/s). The current compliance is set to 1mA. Experimental plot of $Ln(\sigma)\ vs.\ E$ is compared with PF model.

4 CONCLUSION

In this chapter, the nanoionic migration of lithium has been observed, first indirectly through the study of the character (metallic or semiconducting) of the Li_xCoO_2-cells when these are in a high (resp. low) resistance state (using conductivity measurements as a function of temperature). The cell high resistance state shows a semiconducting character which can be correlated to a high x stoichiometry ($x \geq 0.95$), whereas the low resistance state shows a much more metallic state which can be correlated to a lower x stoichiometry. Such observations already allow pointing out the intercalation/deintercalation of lithium ions from the films. Besides, Secondary Ion Mass Spectroscopy (SIMS) allowed characterizing the lithium distribution across cells, and clearly revealed the presence of Li in pre-switched cells (in a low resistance state), whereas no lithium is detected in pristine cells (in a high resistance state). These results confirm directly the importance of ionic migration outwards the films inside the bottom electrode, in the resistive switching process.

Furthermore, a home-made setup is being developed at C2N-IEF to characterize cells by Electrochemical Impedance Spectroscopy (EIS). In the preliminary results obtained, the resistance decrease is clearly observed on the Nyquist plots, and has been correlated to the semiconducting-metal transition. However, as lithium diffusion has not yet been detected, future studies will be carried out at lower frequencies (<1Hz).

Finally, by examining current-voltage curves, some more precise hypothesis can be put forward concerning the possible role of the SiO_2 thin layer: it acts as an electrolyte which allows Li^+ diffusion, but there might also be formation of metallic conduction paths which start to grow from the bottom electrode towards the film during the resistive switching process (from high towards low resistance state). Besides, the electronic conduction can be approached by a model of electron emission (Poole-Frenkel model).

5 REFERENCES

[1] J. Reimers and J. Dahn, "Electrochemical and In Situ X-Ray Diffraction Studies of Lithium Intercalation in Li x CoO2," *J. Electrochem. Soc.*, vol. 139, no. 8, pp. 2091–2097, 1992.

[2] Y. Uchimoto and H. Sawada, "materials science Changes in electronic structure by Li ion edge and oxygen K-edge XANES," pp. 872–873, 2001.

[3] B. Huang, Y. Jang, Y. Chiang, and D. R. Sadoway, "Electrochemical evaluation of LiCoO 2 synthesized by decomposition and intercalation of hydroxides for lithium-ion battery applications," vol. 28, no. 3, pp. 1365–1369, 1998.

[4] Y. Choi, "Electrochemical lithium intercalation into and de-intercalation from porous," vol. c, pp. 524–529, 1996.

[5] P. A. Albert, Z. Kovac, H. B. Lilienthal, T. B. Mcguire, C. Wolverton, and A. Zunger, "Prediction of Li Intercalation and Battery Voltages in Layered vs . Cubic LiCoO2," vol. 145, no. 7, pp. 2424–2431, 1998.

[6] A. Moradabadi and P. Kaghazchi, "Mechanism of Li intercalation/deintercalation into/from the surface of LiCoO2," *Phys. Chem. Chem. Phys.*, vol. 17, pp. 22917–22922, 2015.

[7] M. Ménétrier, I. Saadoune, S. Levasseur, and C. Delmas, "The insulator–metal transition upon lithium deintercalation from LiCoO2: electronic properties and 7Li NMRstudy," *J. Mater. Chem.*, vol. 9, pp. 1135–1140, 1999.

[8] A. Milewska *et al.*, "The nature of nonmetal – metal transition in," *Solid State Ionics*, vol. 263, pp. 110–118, 2014.

[9] X. Zhu *et al.*, "In Situ Nanoscale Electric Field Control of Magnetism by Nanoionics," *Adv. Mater.*, vol. 28, no. 35, pp. 7658–7665, 2016.

[10] E. W. Lim and R. Ismail, "Conduction Mechanism of Valence Change Resistive Switching Memory: A Survey," *Electronics*, vol. 4, no. 3, pp. 586–613, 2015.

[11] F.-C. Chiu, "Review Article: A Review on Conduction Mechanisms in Dielectric Films," *Adv. Mater. Sci. Eng.*, vol. 2014, p. 578168, 2014.

[12] N. Onofrio, D. Guzman, and A. Strachan, "Atomic origin of ultrafast resistance switching in nanoscale electrometallization cells," *Nat. Mater.*, vol. 14, no. 4, pp. 440–446, 2015.

[13] R. B. Hall, "The Poole-Frenkel effect," *Thin Solid Films*, vol. 8, no. 4, pp. 263–271, 1971.

[14] H. Schroeder, "Poole-Frenkel-effect as dominating current mechanism in thin oxide films - An illusion?!," *J. Appl. Phys.*, vol. 117, no. 21, 2015.

[15] S. L. and C. D. M. Menetrier, I. Saadoune, "The insulator – metal transition upon lithium deintercalation from," *J. Mater. Chem.*, vol. 9, pp. 1135–1140, 1999.

[16] A. Milewska *et al.*, "The nature of the nonmetal–metal transition in LixCoO2 oxide," *Solid*

State Ionics, vol. 263, pp. 110–118, 2014.

CHAPTER 4

SWITCHING KINETICS OF DEVICES AND TIME STABILITY OF RESISTANCE STATES

TABLE OF CONTENTS

INTRODUCTION

In this chapter, we studied the switching kinetics of devices, when Li_xCoO_2 films are modified under the application of adequate voltages. We also observed the stability of the cell resistance states with time, when no modifying voltage is applied.

Hence this chapter is composed by two parts. We first examined the switching kinetics: using voltage pulses allows indicating how fast the cell progressively switches between a high resistance state and low resistance states reversibly. The switching kinetics of a Li_xCoO_2-based cell is indeed believed to be dependent on the surface of the top electrodes (unlike purely filamentary switching which is independent from electrode surface). We also studied the influence of the chemical nature of top electrodes. We then propose a numerical model (which has been developed using a mathematical software) to account for the main observations. This model will be compared with the experimental results obtained.

In the second part, when no modifying voltage is applied to a Li_xCoO_2-based cell, we observe how long a cell remains in its resistance state (time stability). Specifically, the evolution of the initial resistance state will be studied under different environments (air and vacuum) by CP-AFM. As air seems to yield a resistance drift (which appears faster for the low resistance state), several protecting layers have been examined, in order to try to slow down such a drift.

1 SWITCHING KINETICS OF Li_xCoO_2 DEVICES

1.1 Introduction: method of study

Switching kinetics is an important performance parameter of memory devices. The objective of most studies ([1], [2]) is to determine the shortest time which allows switching between two extreme resistance values.

Here we chose a completely different way of study. Indeed, it had formerly been established that intermediate resistance states can be obtained. Hence, by recording the resistance evolution as a function of consecutive bias pulses, the measurements points allow to obtain a curve whose slope corresponds to a "kinetics" of modification (how fast the cell resistance is modified), which in its turn depends on the kinetics of the electrochemical processes involved. Using such an experimental protocol, we examined the experimental effect of various parameters (such as cell surface, chemical nature of the electrodes, et c…).

The principle of the experimental protocol used here is illustrated by **Fig. 4.1**. Starting from the initial resistance state of a cell, only negatively biased pulses lead to a resistance decrease. Thus consecutive negative pulses (-8V, 10ms or 30ms duration) are first applied to the {bottom electrode/top electrode} system. After each group of several pulses, the resistance state (which progressively decreases as a function of the pulses number) is measured using a small polarization (+1V). This allows obtaining the kinetics of the "SET process" (**Fig. 4.1** left, in red). Starting from this new resistance state (low resistance state), positive pulses (+8V) allow then obtaining the kinetics of the "RESET process" (**Fig. 4.1** right, blue) during which the cell resistance increases again.

In the following sections, the experimental influence of the cells area, as well as the chemical nature of the electrodes, will be studied.

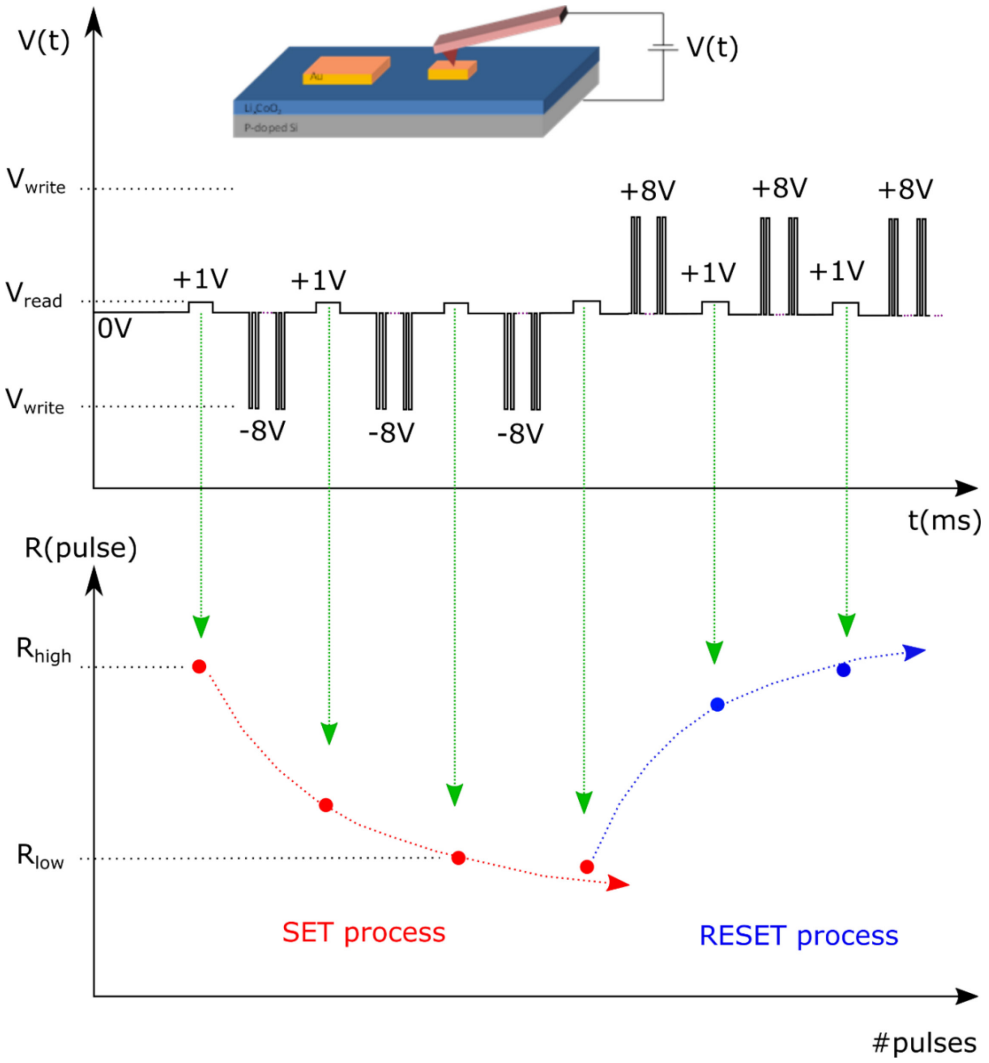

Figure 4.1: Schematics of the principle used to study the switching kinetics of Li_xCoO_2-based devices.

1.2 SET switching kinetics: observed influence of the top electrode area

In this experiment, 3 different sizes of Au top electrodes have been deposited (by thermal evaporation): 100x100µm², 30x30µm² and 10x10µm². The inset shows an optical image (top view) of the top electrodes.

The CP-AFM tip being in contact with a given top electrode, consecutive pulses (-8V 30ms, period 100ms) are applied (bottom electrode vs. tip). An example of cell resistance evolution recorded as a function of the number of pulses is illustrated in **Fig. 4.2**, for 3 cells of different top electrode areas.

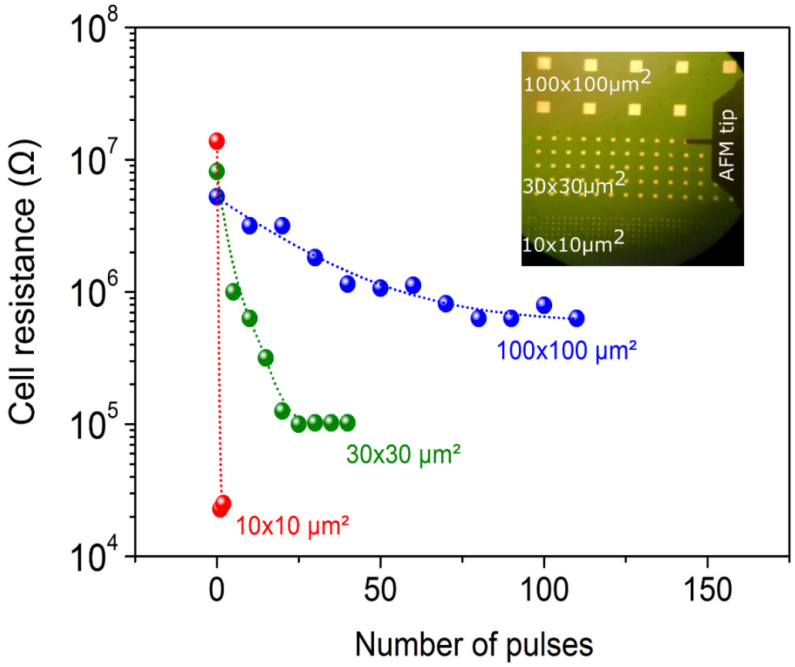

Figure 4.2: Resistance evolution of three different cells (10x10µm², 30x30µm², 100x100µm as the function of number of negative pulses (-8V, 30ms duration, 100ms period). The electrical measurement is characterized by CP-AFM. The cell resistance decrease behavior highly depends on the cell size.

We can observe that the resistances of the {Au/Li_xCoO_2/Si} cells decrease as a function of the number of negative pulses. Furthermore, the switching kinetics depends much on the top electrode area: a 10x10µm² cell switches completely to a low resistance state ($\leq 10^5$ Ω) after only 1-2 pulses. For 30x30µm² cells, the observed decrease is slower, and for 100x100µm² cells, even 100 pulses are not enough to reach a low resistance state. Hence, the smaller the electrode size, the faster the kinetics of the SET process.

The results also confirms that a high number of intermediate states can be obtained: this possibility of tuning the cells resistance is a key point towards the potential development of neuromorphic circuits [3] in the field of cognitive computing.

1.3 SET switching kinetics: observation of the influence of top electrode chemical nature

Here, the witching kinetics was compared between two configurations: cells composed by Au top electrodes and cells made of Ti top electrodes (+50nm Au on Ti, to make a good tip/electrode electrical contact) on a same sample (to facilitate comparison).

As we can see on **Fig. 4.3**, the switching kinetics of an {Au/film/Si} cell is much faster than an {Ti/film/Si} cell (for the same 200x200µm² surface). Hence the chemical nature of the top electrode has a great influence on the switching kinetics of the cells.

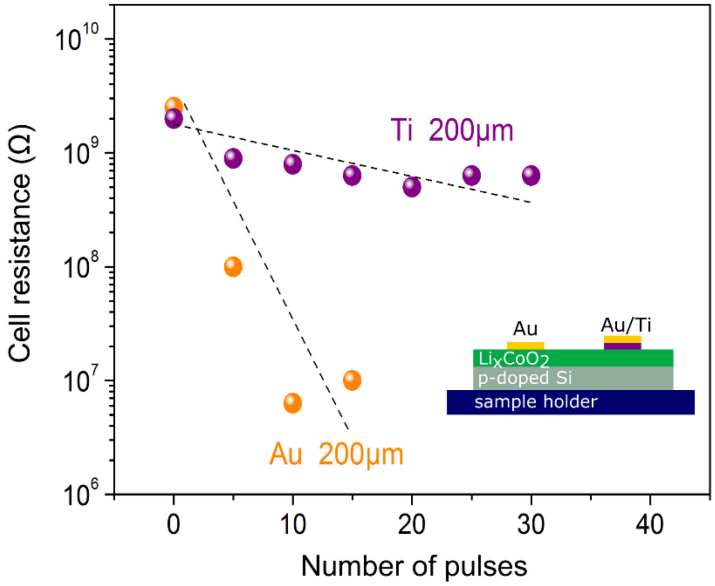

Figure 4.3: TE dependence of the switching kinetics: Comparison of the switching kinetics of electrodes made of Au and Au/Ti with same size ($200 \times 200\mu m^2$). The switching kinetics of Au/Li_xCoO_2/Si is much faster than the one of Ti/Li_xCoO_2/Si.

To account for this observation, a possible hypothesis is that a small oxide layer (TiO_x) exists at the Ti/Li_xCoO_2 interface after deposition, which leads to a voltage drop in this region. The remaining bias required to switch the Li_xCoO_2 volume cell would therefore be lower than in the case of a gold top electrode, hence yielding a slower switching kinetics. The existence of such a layer has indeed been evidenced by X-ray Photolectron Spectroscopy (XPS) analyses (not shown here).

1.4 RESET switching kinetics

Here, the witching kinetics was studied to compare the kinetics of the SET process to the kinetics of the RESET process.

For {Au/film/Si} cells, an example of result is shown in **Fig 4.4**: we can see that 15 pulses (-8V 10ms) are needed to switch a 100x100µm² cell to a low resistance state, but after only 5 positive pulses (+8V 10ms), the cell is already switched back to a high resistance state (black points). For {Ti/film/Si} cells in the same experiment, this phenomenon has not been observed clearly, due to the slower SET kinetics (already observed in the previous section) (**Fig. 4.4** blue points), but it has been observed for smaller Ti electrodes (20x20µm², not shown here).

Hence, the RESET process kinetics appears always higher than the SET process, and is not linked to the chemical nature of the top electrodes. Further studies have to be carried out to account for this behavior.

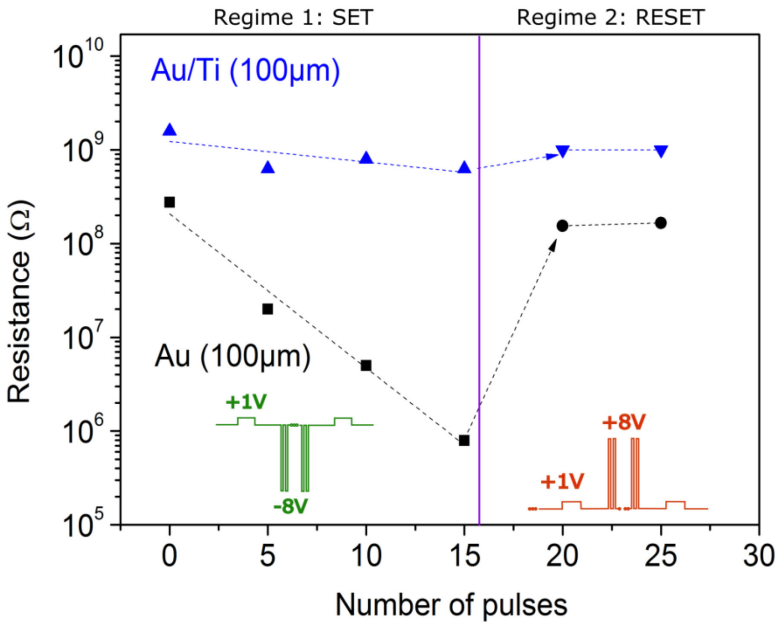

Figure 4.4: Switching kinetics of a {Au/film/Si} cell (black points): the RESET process appears much faster than the SET process. For a {Ti/film/Si} cell (blue points), the phenomenon does not appear clearly due to the 100x100µm² cell size (more pulses should have been applied to see it). During the SET process, -8V (τ=10ms, T= 100ms) have been applied; and during the RESET process, +8V (τ=10ms, T= 100ms) have been applied.

1.5 Tentative model of the SET switching kinetics

To better understand the important influence of the cell surface on the SET process kinetics, we tried to develop in simple mathematical model.

We represented the {AFM tip + MIM cell} structure by a simple electrical circuit, as shown in **Fig. 4.5**. An external voltage source $V_s(t)$ (delivering pulses) is applied to the whole circuit. The positive direction of the current i flowing in the circuit is depicted by an arrow in **Fig. 4.5b**. R_0 denotes the total resistance composed by {tip and lever resistance of the CP-AFM probe, the tip/electrode contact resistance, and the internal protection resistance of the Resiscope device} This resistance reaches about 10-20kΩ, which is small compared to initial the resistance of the cells. The MIM cell itself is represented by a resistance R (film resistance between the top and bottom electrodes; R will change, depending on the electrochemical reaction) in parallel to a double-layer capacitance C (considered roughly as the capacity between the top and bottom electrodes). The blue-colored circuit corresponds to an electrochemical cell whose current i_{ch} leads to the modification of the R value.

This equivalent MIM cell circuit with two main components R and C in parallel looks like a Randle's cell model which is commonly used in Electrochemical Impedance Spectroscopy (EIS) [4]–[6]. However, in our model, we mainly focus on the modification of R due to the redox reaction in a very simplified way, thus the C value is assumed constant during the modification of R. Besides, no temperature influence has been taken into account.

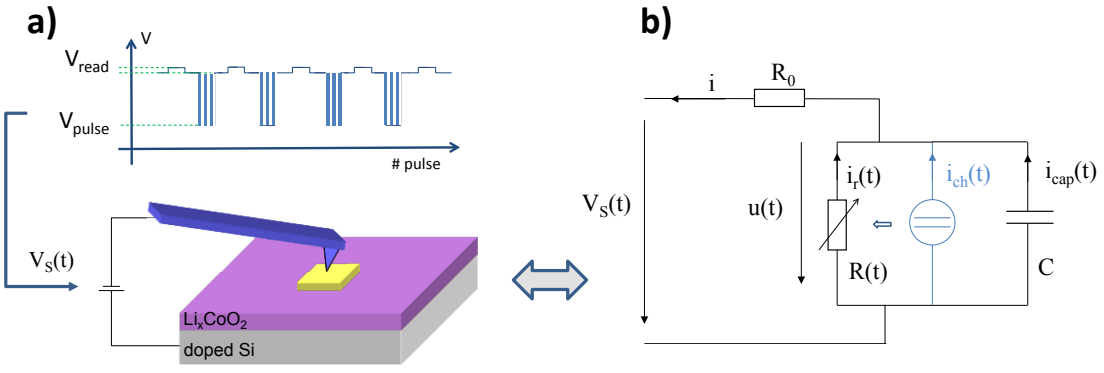

Figure 4.5: a) Schematics of a {AFM tip + MIM cell} structure, **b)** Representation of this structure by an equivalent electrical circuit

In order to obtain the evolution *R(t)* as a function of time, some further assumptions have to be done concerning the behavior of the MIM cell. As shown in **Fig. 4.6** below: the film modification is only considered in the volume located between the top electrode and the substrate (further extension of the film modification will be neglected for simplification).

Figure 4.6: The film modification is only considered in the {(top electrode surface) x (film thickness)} volume

Thus, inside volume $V = S \times e$ (S being the surface of top electrode and e the film thickness), a small modification (decrease) dx of film stoichiometry can be considered as proportional to $i_{ch} . dt$, with i_{ch} being a very small electrochemical current, and dt the application time. This results in the following expression, using a proportionality constant K_1:

$$V.dx = -K_1.i_{ch}.dt \quad (1)$$

which can be rewritten in the following way:

$$dx = -\frac{K_1.i_{ch}.dt}{V} = \frac{K_1.i_{ch}.dt}{e.S}$$

i_{ch} is assumed to have a roughly linear correlation to *u(t)-Vth* (*Vth* being a threshold voltage, under which no modification occurs, found experimentally to be around -4 V for a SET operation). Thus, i_{ch} can be written:

$$i_{ch} = K_2.[u(t) - Vth]$$

A relation between dx and the resistivity ρ of the film must now be found. From Ménétrier *et al.* [7], we can observe that ρ depends exponentially on x, thus we can write:

$$\rho = K_3.e^{K4.x}$$

K_3 and $K4$ being two parameters assumed constant. And, as the total resistance of the cell follows the same law as the resistivity, we thus obtain:

$$\frac{dR}{R} = \frac{d\rho}{\rho} = K_4.dx = K_4.\frac{-K_1.K_2.[u(t) - Vth].dt}{e.S}$$

This leads finally to the following expression, using only one K constant:

$$\frac{dR}{R} = \frac{-K.[u(t)-Vth].dt}{e.S} \tag{2}$$

If we use this latter equation and add the ones due to Ohm's law and Kirchhoff's law, we must consider the complete following system (i_{ch} is neglected):

$$\begin{cases} ir = \dfrac{u}{R} \\ i = \dfrac{Vs - u}{R0} \\ i = ir + icap \\ icap = -\dfrac{C.u}{dt} \\ \dfrac{dR}{R} = \dfrac{-K.u.dt}{e.S} \end{cases}$$

Using this latter system, a numerical simulation has been developed in order to obtain the time evolution of all variables by computing the successive values of u, R, ir, $icap$ and i step by step, after each incrementation of t by a small amount dt.

The initial values (at $t = 0$) have been taken as such: $u = 0$ (the capacitance is initially discharged), $R = R_{init} = 10^8 - 10^9\Omega$. The capacitance C (which depends on the dielectric permittivity ε, film thickness e and top electrode surface S) can be written as follows:

$$C = \varepsilon_0.\varepsilon_r.\frac{S}{e} \tag{3}$$

Given the shape of $V_s(t)$ and the previous parameters values, a MATHCAD program allows then to compute the time evolution of $u(t)$, $R(t)$, $i(t)$. An example of numerical result is given in **Fig. 4.7** hereafter, for consecutive pulses application: $V_s(t)$ is represented by negative pulses ($-8V$, duration $\tau = 100\text{ms}$, period $T = 200\text{ms}$). The threshold voltage has been taken $V_{th} = -4V$. The corresponding capacitance value of a 100x100µm² cell area is $C = 1.5 \times 10^{-9}$ F. Fig 3.16 represents *Vs(t), u(t)* and the *R* resistance time evolution using the above algorithm.

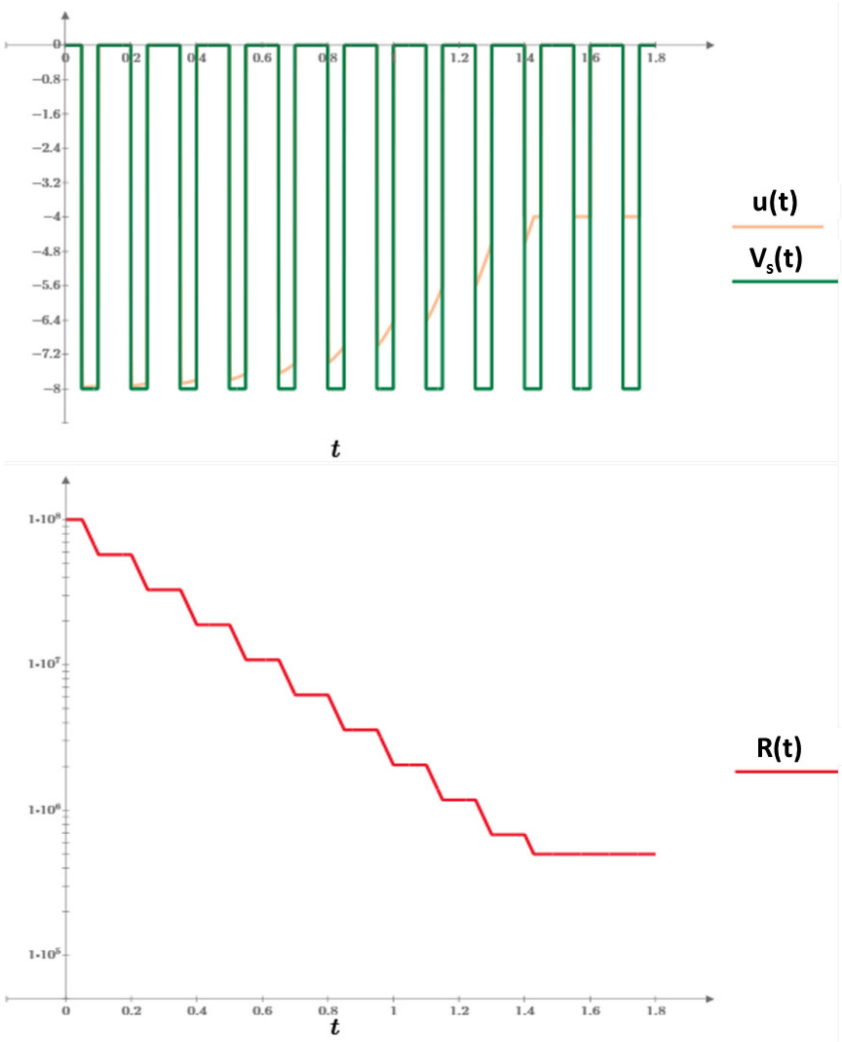

Figure 4.7: Example of numerical simulation: time evolution of **a)** $V_s(t)$ and u(t); **b)** R(t)

In **Fig. 4.7**, the simulation results show that $R(t)$ decreases progressively as a function of the pulses application. When the cell voltage $u(t)$ reaches the threshold voltage $V_{th} = -4V$, R will no longer be modified.

1.6 SET switching kinetics: experimental results vs. numerical simulation

Towards comparison between simulation and experimental results, the following parameters have been chosen for the simulation: film thickness $e = 100nm$, area of top electrodes : S = 10x10µm², 30x30µm² and 100x100µm². The capacitance C is calculated using formula (3) with the dielectric constant $\varepsilon_r \approx 4$. The resistance R_0 in series with the cell is set to $5.10^4\Omega$. The applied pulses are the following: $V_0 = -8V$, duration $\tau = 30ms$ and period $T = 100ms$. The threshold voltage for resistive switching is taken at $-4V$.

The K parameter (which is the same for all cells) has been adjusted to fit the experimental evolution of 100x100µm² cell resistance. **Fig. 4.8a** shows the comparison between experiment and simulation. We can observe that the simulated curves fit rather well the behavior of the 30x30µm² and 10x10µm² cell. Such results validate to some extent the assumption that the whole volume between a top electrode and the bottom substrate is involved in the switching process (equation 1 in previous section). Indeed, if a pure filamentary process were involved, there would be nearly no influence of the cell surface.

Using the numerical the model, we extrapolated the switching time (defined as a 2 decades resistance decrease) down to $20 \times 20nm^2$ cells as shown in **Fig. 4.8b**. The extrapolated switching time found (~100ns) for such cell size reaches the same order of magnitude as operation times of other kinds of fast ReRAM devices [8], considerably much faster than Flash memories (100µs).

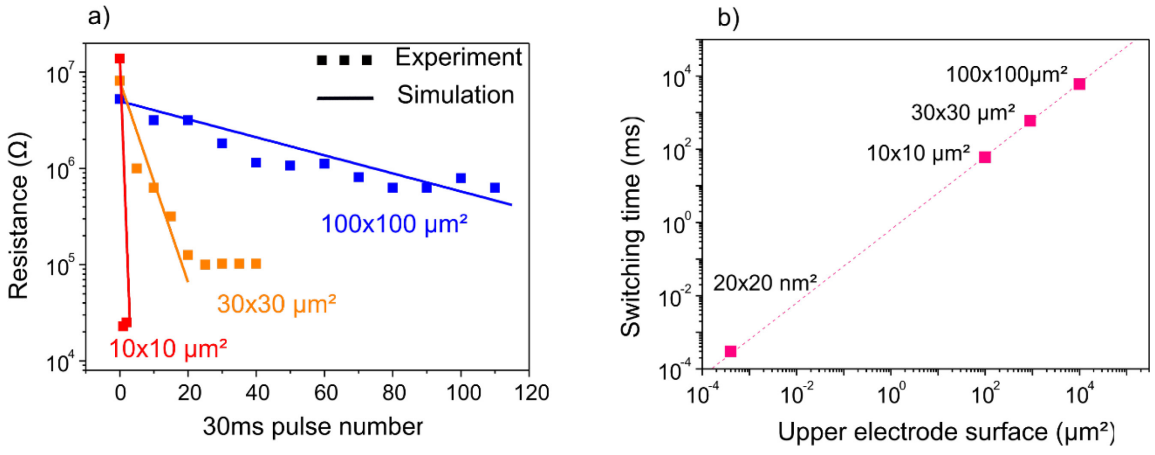

Figure 4.8: (a) Qualitative good agreement between the experimental results and the proposed kinetics model for Li_xCoO_2-based cells (b) Extrapolation of switching time down to 20x20µm² cells, using the numerical simulation.

It must however be kept in mind that our rough model disregards many contributions such as for example diffusion of Li^+ ions, and Joule effects (local heating of conducting paths in the film [9]).

1.7 Influence of the switching kinetics on current-voltage curves

Current-voltage curves have been recorded using different bias sweeping rates, to observe the cells behavior in these different conditions. Bias voltage ramps ($0 \rightarrow -6V \rightarrow +7V \rightarrow 0$) have been applied to $100 \times 100\mu m^2$ {Ti/film/Si} cells using $0.23\ V.s^{-1}$ to $23\ V.s^{-1}$ rates.

As we can see from **Fig. 4.9**, the sweeping voltage rate has an important influence on the cell behavior. For a fast sweeping rate ($23\ V.s^{-1}$), the current evolution (**Fig 4.9b** blue curve) could at first sight be attributed to capacitive effects (green arrows), whereas for a slow sweeping rate ($0.23\ V.s^{-1}$), the obtained curve (**Fig. 4.9b** red curve) exhibits a clear resistive switch from a high to a low resistance state for negative bias, and reversibly back a switch towards a high resistance state for positive bias.

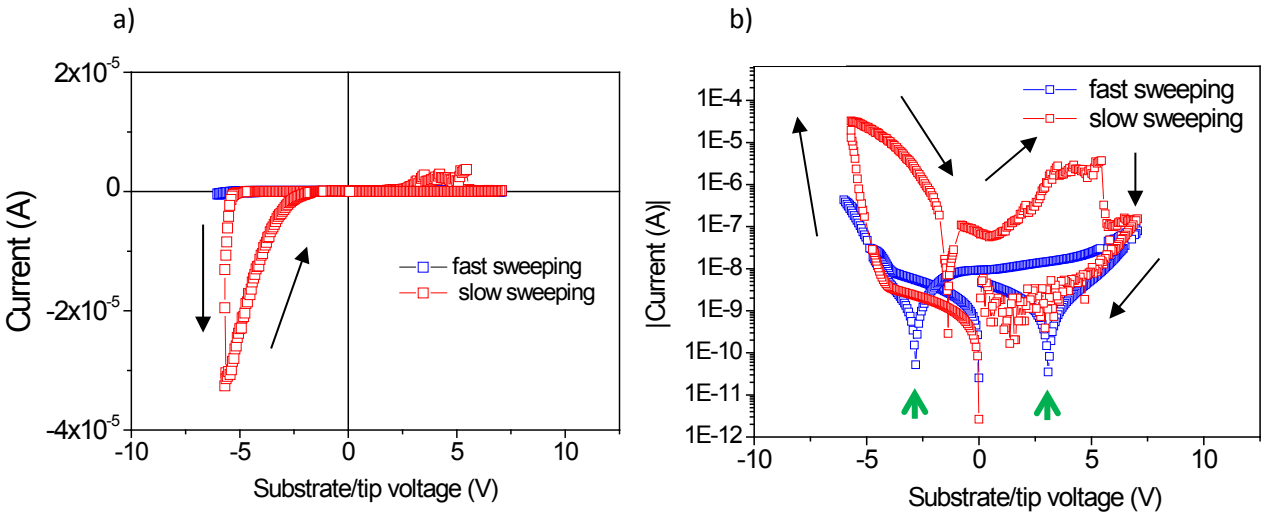

Figure 4.9: I-V characteristics of 100×100µm² {Au/Ti/Li_xCoO_2/Si} cell: **a)** in linear scale, **b)** in logarithmic scale. The I-V curve recorded in blue has been obtained using a fast sweeping rate ($23\ V.s^{-1}$), no resistive switching effect is observed (except possible capacitive effects, see green arrows); a slow sweeping rate ($0.23\ V.s^{-1}$) leads to a clear switching behavior (red curve).

Here, we try also to explain the overall shape of the experimental current-voltage curves obtained in **Fig. 4.9**. Towards this objective, the numerical model developed previously (section 1.5) has been modified: we basically use the same Mathcad program as already developed to study switching kinetics using pulses. Nevertheless, in order to obtain numerical I-V curves, the time evolution of the applied voltages $V_s(t)$ is no longer composed by square pulses, but bias ramps. Besides, 2 threshold voltages (V_{th1} = -4V, V_{th2} = +5V) are defined for both positive and negative polarities.

Fig. 4.10 exhibits numerical simulation of I-V characteristics of an MIM cell. For a fast sweeping rate ($>10\ V.s^{-1}$), no resistive switching occurs, and capacitive effects are clearly visible: the simulated curve reproduces qualitatively well the experimental blue curve of **Fig. 4.9**. For a slow sweeping rate ($0.4\ V.s^{-1}$), the simulated curve shows a well-defined resistive switching behavior, while the capacitive effects are much lower.

Hence, the experimental curves obtained are qualitatively well explained by the simulated curves.

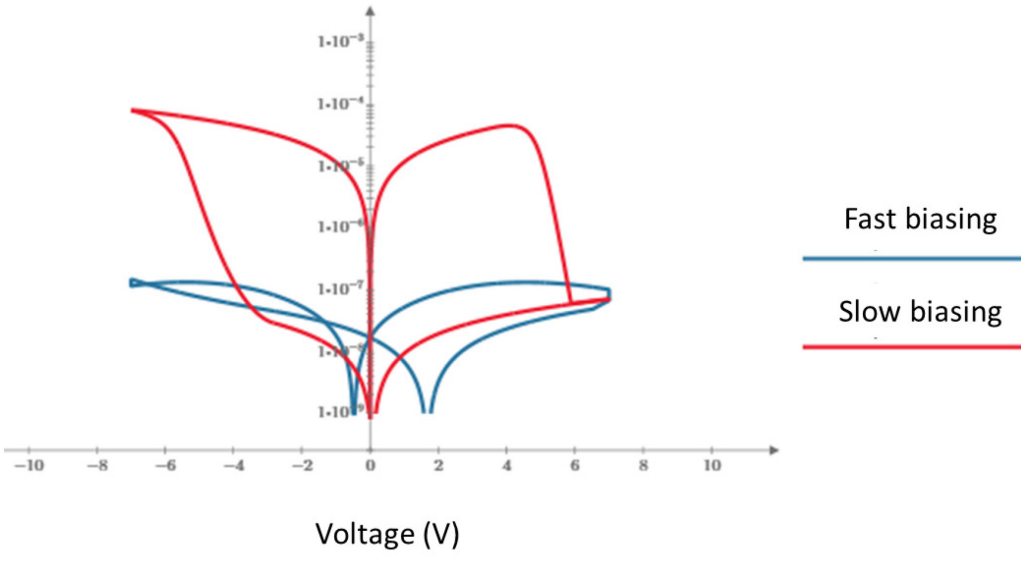

Figure 4.10: Simulation results of I-V characteristics of an 100x100 µm^2 MIM cell, using 2 different sweeping rates (ramped bias is swept 0→ -10V →+10V→0): **(a)** a fast sweeping rate: $23\ V.s^{-1}$and **(b)** a slow sweeping rate: $0.23\ V.s^{-1}$.

2 TIME STABILITY OF Li_xCoO_2 CELL RESISTANCE STATES

2.1 Stability of the initial resistance state as a function of time, using CP-AFM

2.1.1 Introduction: Method of study

An ideal device should keep data over an unlimited period of time. However, in a real device, the information (resistance state) may drift progressively. Hence, we investigated the evolution of the initial resistance state of Li_xCoO_2 MIM devices as a function of time using CP-AFM. This also helped us to better understand some conditions required to preserve the Li_xCoO_2 samples.

After an initial thermal annealing (1 hour) of the Li_xCoO_2 samples (to crystallize partly Li_xCoO_2 which is initially amorphous), top electrodes (made of Au or Au/Ti) of various sizes (from $5 \times 5\mu m^2$ to $200 \times 200\mu m^2$) have been deposited (using optical lithography and E-beam evaporation). The obtained MIM cells have then periodically been characterized (no switching operation done) using CP-AFM (as shown in **Fig. 4.11**).

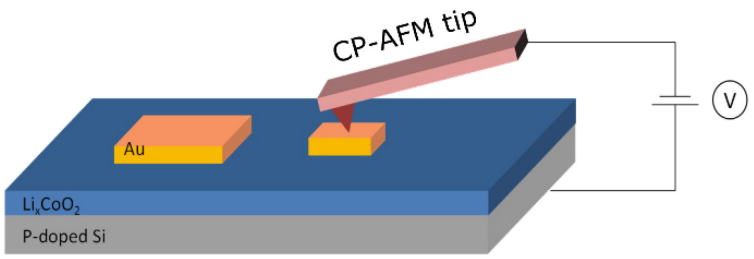

Figure 4.11: Schematic representation of Li_xCoO_2 MIM cells being scanned by CP-AFM: the cells resistance states are measured by using the electrical image recorded.

2.1.2 Time evolution of the initial resistance state of {Au/film/Si} cells

Fig. 4.12 shows the evolution, under ambient air, of the initial resistance state (not switched) of 10x10µm² and 100x100µm² Li_xCoO_2 cells, as a function of time. We can see that the cell resistance values significantly increase 3-4 orders of magnitude after 15 days

(from about 10^7 to over 10^{10} Ω). After 15 days, we carried out a fast annealing step (1min) to the samples: the resistance states went back to low values (below 10^7 Ω). Then the evolution of the cells has again been studied over 15 more days: the same phenomenon occurs again (resistance increase). A second fast annealing step is then carried out (the 30th experiment day), after which the samples were kept under high vacuum (< 10^{-9} Torr) for 35 days.

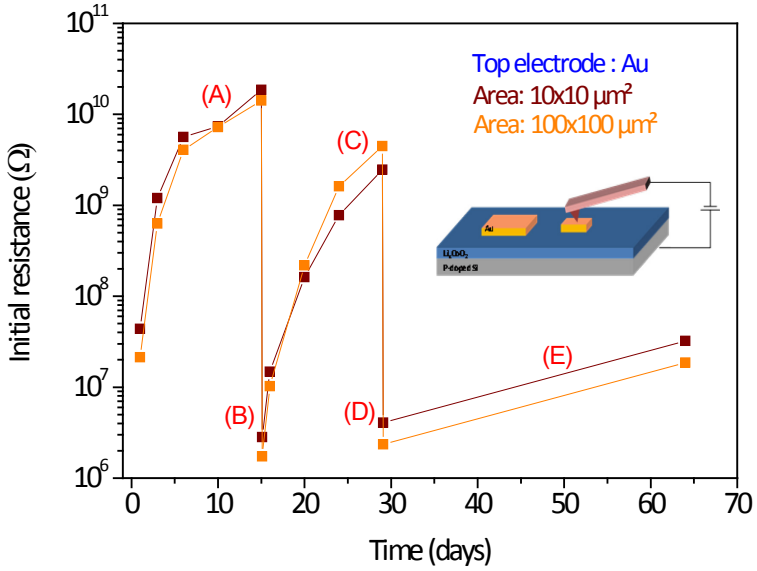

Figure 4.12: Evolution in ambient air, of the initial resistance state (no switching) of $10 \times 10\mu m^2$ and $100 \times 100\mu m^2$ (Au/film/Si) cells as a function of time **(A)** during 15 days after the first annealing step (580°C for 1 hour) **(B)** a fast annealing step (1min) is carried out during 1min **(C)** cells resistance evolution during 15 more days **(D)** a fast annealing step is again carried out during 1min **(E)** evolution of the cells resistance which are kept in high vacuum (10^{-9} Torr) for over 1 month.

We can see that when kept in ambient air, the cells resistance values increase very fast as a function of the number of days, whereas they are nearly stable under high vacuum. The CP-AFM images shown in **Fig 4.13** illustrate the cause of such a phenomenon. Just after an annealing step (**Fig 4.13B**, corresponding to B in **Fig 4.12**) the film surface seems nearly uniformly conducting, as well as the top electrode surface. But after only 5 days under ambient air, the same surface is already covered by insulating bumps (**Fig 4.13C**). A fast annealing step allows removing all the insulating domes (Fig 3.3D). If kept under high vacuum, the surface appears nearly stable (**Fig 4.13 D=>E**).

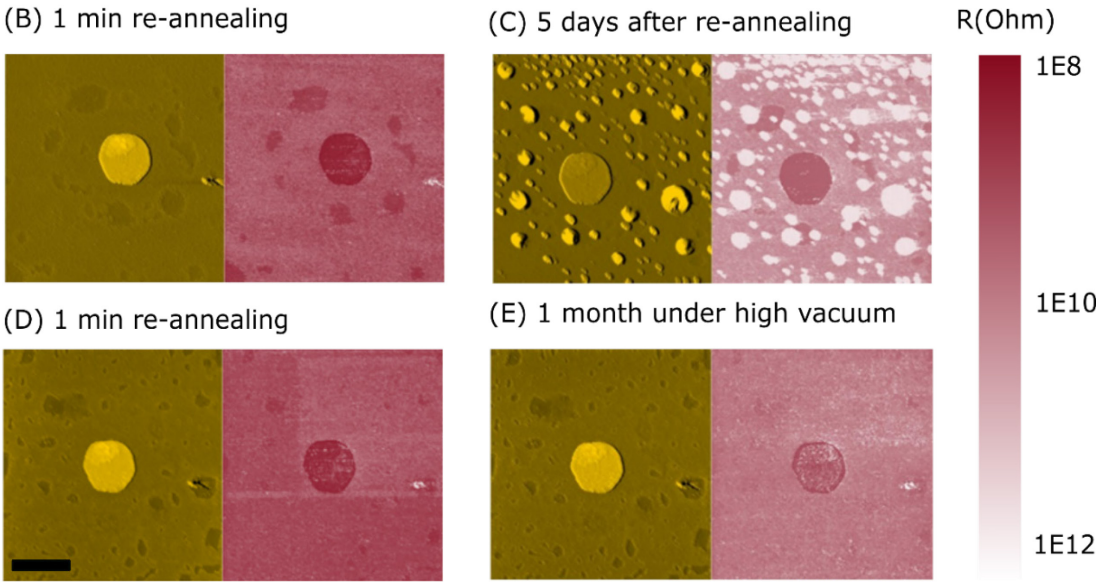

Figure 4.13: B) just after a fast annealing step : topographical and electrical CP-AFM images of a surface and a "5x5" µm² electrode (Au) at the center **C)** CP-AFM images of the same surface after 5 days in ambient air : the surface is covered by insulating bumps and the cell resistance is higher **D)** CP-AFM images of the same surface after a new fast annealing step : the insulating bumps have been removed and the cell resistance is much lower **E)** CP-AFM image of the same surface after 1 month sample conservation under high vacuum (10^{-9} Torr): no insulating bump has reappeared.

The reason for the cell resistance increase and the insulating bumps covering the surface can be explained by following consideration. At ambient air, the Li_xCoO_2 film surface is covered by a thin water layer, in which Li^+ ions exist. LiOH reacts then with CO_2, which corresponds to a carbonatation of the surface. It results in the formation of Li_2CO_3 according to the following chemical reaction:

$$2LiOH + CO_2 \Longrightarrow Li_2CO_3 \downarrow + H_2O$$

The precipitated Li_2CO_3 is insulating ($\sigma \leq 10^{-10} S.cm^{-1}$, derived from ref. [10]), can thus explain why the film surface resistivity significantly increases (not uniformly) as a function of time. However, not only the film surface becomes more insulating, but also the cell resistance increases. This means that the film volume under the top electrodes is also affected. O_2 and CO_2 may diffuse though the {top electrode/ film} interface.

We can also notice that a fast annealing step allows completely removing Li_2CO_3: this this material seems very volatile (it is known as being unstable to heat). Under high vacuum, there is nearly no O_2 and CO_2, thus the film surface and the cells remain stable. This shows that the ambient air environment has an important influence on the Li_xCoO_2 devices. Therefore, most of the samples in this thesis have been studied maximum one day after the

initial annealing process. Concerning applicability to memories, the evolution of resistance states due to the ambient air is not considered as a main drawback, since the cell could be normally covered by protecting insulating materials.

2.1.3 Influence of top electrode chemical nature on the cell resistance evolution

We tried to compare the time evolution of cells composed by different top electrodes materials (Au and Ti). The same experiment described in the previous section has been carried out. **Fig. 4.14** exhibits the evolution of resistance values of 100x100µm² cells as a function of time. We can clearly observe that the Ti/film/Si cells resistance value increases also, although not as fast as Au/film/Si cells.

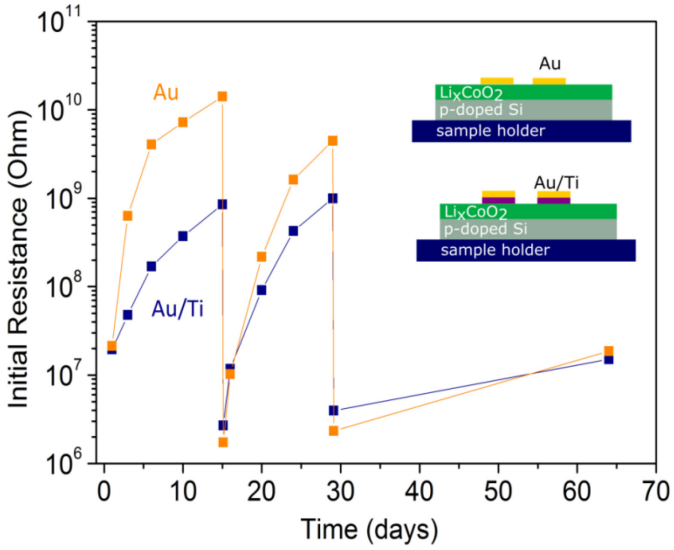

Figure 4.14: Evolution of initial resistance of MIM cells with different top electrodes: Au and Ti (Au/Ti).

The slower increase when using Ti as top electrode could be accounted for by the following hypothesis: at the Ti/Li_xCoO_2 interface, Ti reacts very easily with O_2 to form a stable TiO_x interface layer, which could further slowdown O_2 diffusion and reaction with Li_xCoO_2.

2.2 Time stability of the resistance states of devices, using two-probes method

2.2.1 Introduction : Method of study

To measure the retention time of Li_xCoO_2 MIM devices, two-probes method (described in chapter 2) has also been used, which allowed performing automatic measurements.

A LabVIEW program has been developed, allowing a periodic application of a small bias pulse to measure the cell resistance state (bias voltage in the 1V range to avoid resistive switching). The chosen pulse duration was chosen not longer than 100ms, in order to prevent joule heating which could potentially change the studied sample properties. The period between two consecutive pulses can vary from 15 min to 1 hour. In this way, we could study the resistance evolution as a function of time (hours).

The influence of environment conditions (ambient air and vacuum) has been studied, as well as the influence of several protecting layers, which will be discussed in the following sections.

2.2.2 Evolution of the resistance states in ambient air and vacuum

The time evolution of the initial resistance R_{init} of a 100x100µm² cell (Au top electrode) is measured during 14h (measurement carried out every hour). The same protocol is then used to record the evolution of the low resistance state (obtained after a single pulse: -9V 200ms). **Fig. 4.15** shows a significant difference in time evolution of the high resistance state (R_{OFF}) and the low resistance state (R_{ON}). R_{OFF} exhibits a good stability over a period of 14 hours. On the contrary, R_{ON} increases gradually, much faster than R_{OFF}.

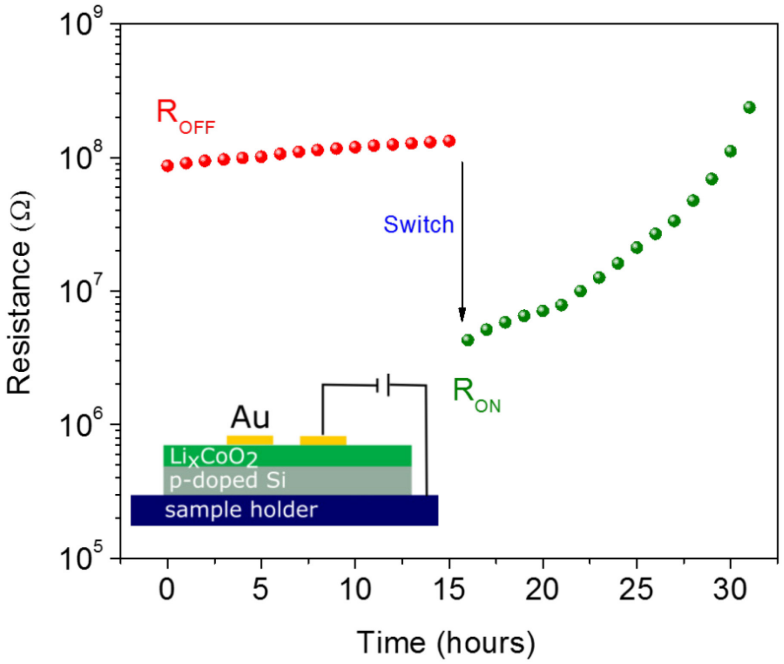

Figure 4.15: Time evolution of R_{OFF} and R_{ON} of a 100x100µm² {Au/film/Si} device, in ambient air

Hence, in the next experiments, we focused only on the R_{ON} state, and studied if vacuum has an influence on this time evolution. To do so, we switched cells from their initial state to R_{ON} (using -9V, 200ms) and recorded the time evolution of the R_{ON} state.

As illustrated in **Fig. 4.16**, in secondary vacuum (5.10^{-6} mbar) the R_{ON} state appears stable over 50hours, whereas in ambient air, the R_{ON} state has nearly drifted back to the initial resistance state in 10 hours. To confirm the high influence of ambient air, another experiment has been carried out: a cell was switched to its R_{ON} state, then kept under vacuum: this state remained stable. Air was then suddenly injected into the vacuum chamber: the R_{ON} value started to increase rapidly (See Appendix B).

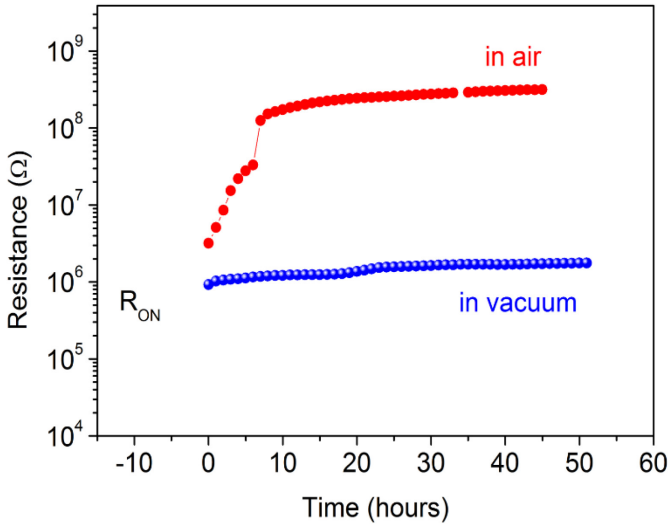

Figure 4.16: time evolution of the low resistance state R_{ON} of two {Au/Li_xCoO_2/Si} cells: in ambient air and in vacuum. The resistance state is measured at -1V (100ms) after each hour.

More detailed experiments should be performed in the future to understand what constituent of ambient air (O_2, H_2O …) has an effect on the low resistance state evolution. In the meanwhile, we studied two kinds of insulating layers to protect the cells and try to improve the time stability of the low resistance state.

2.2.3 Time stability in ambient air, using different kinds of protecting layers

Using protocol 3 (in Appendix A) for microfabrication in cleanroom, we deposited different materials on the Li_xCoO_2 thin film surfaces to act as protecting layers from ambient air. **Fig. 4.17** shows preliminary results obtained concerning the time stability of cells covered by Si_3N_4, and of cells covered by insulating photoresist AZ5214E.

We observe that unfortunately, these layers do not allow avoiding a drift of the low resistance state. Using Si_3N_4 did not lead to better results than in ambient air. Using AZ5214E photoresist led to a bizarre behavior (stable R_{ON} value, which suddenly increased beyond the initial resistance state value).

To account for the results, the Si_3N_4 layer (deposited using RF Magnetron sputtering) may not be uniform. Thus the Li_xCoO_2 films may not completely be covered by the Si_3N_4 layer. Concerning AZ5214E, more studies should be carried out.

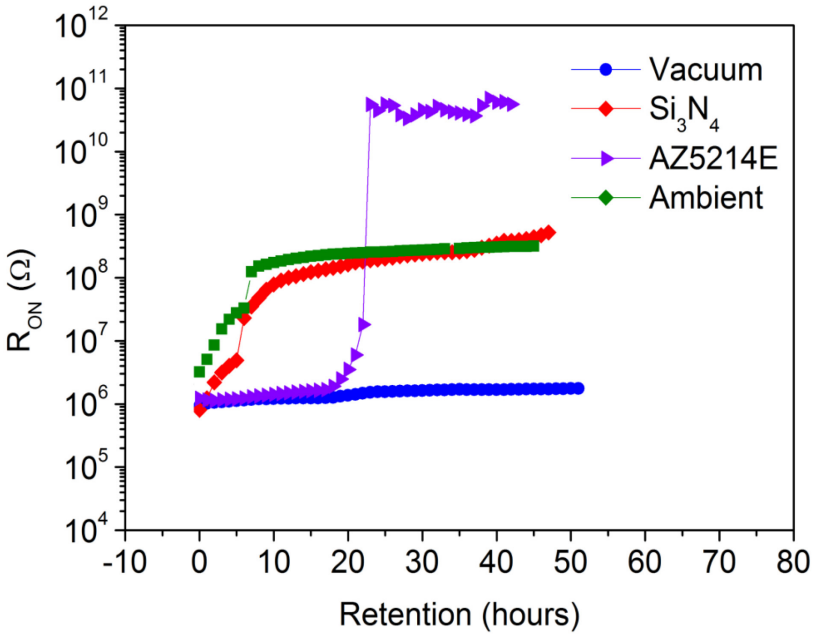

Figure 4.17: time evolution of the low resistance state R_{ON} of {Au/Li_xCoO_2/Si} cells: cell in ambient air (green), cell in vacuum (blue), and cells covered either by Si_3N_4 (red) or AZ5214E photoresist (violet).

3 CONCLUSION

In this chapter, we first investigated the switching kinetics of devices using consecutive voltage pulses. We observed that for negative (bottom/top electrodes) pulses, the cell resistance (initially at a high resistance state) progressively decreases. Such a decrease highly depends on the top electrode surface (which thus excludes a purely filamentary switching): the smaller the upper electrode, the faster the switching. The kinetics has also been observed to depend on the top electrode chemical nature: for Ti electrodes, the kinetics is slower, which has been attributed to the existence of a few nm thick TiO_x layer at the Ti/Li_xCoO_2 interface (confirmed by XPS analyses) which leads to a bias drop.

A numerical model has been developed using a mathematical software (MATHCAD) and has been proposed to account for the high dependence of the kinetics on the upper electrode surface. A qualitative good agreement between the numerical results and the experimental observation has been found. Besides, an extrapolation downto 20x20µm² small devices leads to a calculated switching time in the 100ns order of magnitude, which is 1000 times faster than Flash memories.

Concerning the stability of cell resistance states with time, we studied the drift (as a function of days) of the initial resistance states of cells, using CP-AFM. This drift is clearly attributed to the progressive carbonatation of Li_xCoO_2; under high vacuum, such a phenomenon does not occur. Such a film carbonatation can be completely removed by a fast annealing process (580°C - 1 minute). The resistance drift appears besides a little slower when Ti top electrodes are used (compared to Au electrodes). Furthermore, we observed that in air, the drift of the low resistance state is much faster (~ 10hours) compared to the high resistance state behavior (a few days). We tried several types of protecting films (Si_3N_4 and AZ5214E photoresist) to slow down such a drift, but the time stability was however not improved; other kinds of protecting layers will have to be studied in the future.

4 REFERENCES

[1] S. Menzel, U. Böttger, M. Wimmer, and M. Salinga, "Physics of the Switching Kinetics in Resistive Memories," *Adv. Funct. Mater.*, vol. 25, no. 40, pp. 6306–6325, 2015.

[2] S. Menzel, S. Tappertzhofen, R. Waser, and I. Valov, "Switching kinetics of electrochemical metallization memory cells.," *Phys. Chem. Chem. Phys.*, vol. 15, no. 18, pp. 6945–52, 2013.

[3] S. H. Jo, T. Chang, I. Ebong, B. B. Bhadviya, P. Mazumder, and W. Lu, "Nanoscale memristor device as synapse in neuromorphic systems," *Nano Lett.*, vol. 10, no. 4, pp. 1297–1301, 2010.

[4] O. S. Mendoza-Hernandez, H. Ishikawa, Y. Nishikawa, Y. Maruyama, Y. Sone, and M. Umeda, "Electrochemical impedance study of LiCoO2 cathode reactions in a lithium ion cell incorporating a reference electrode," *J. Solid State Electrochem.*, vol. 19, no. 4, pp. 1203–1210, 2015.

[5] S. Takeuchi *et al.*, "Epitaxial LiCoO<inf>2</inf> films as a model system for fundamental electrochemical studies of positive electrodes," *ACS Appl. Mater. Interfaces*, vol. 7, no. 15, pp. 7901–7911, 2015.

[6] K. Sivajee Ganesh, B. Purusottam Reddy, P. Jeevan Kumar, K. Jayanthbabu, P. Rosaiah, and O. M. Hussain, "Microstructural and electrochemical properties of LiTi yCo 1-yO2 film cathodes prepared by RF sputtering," *J. Solid State Electrochem.*, vol. 19, no. 12, pp. 3621–3627, 2015.

[7] S. L. and C. D. M. Menetrier, I. Saadoune, "The insulator – metal transition upon lithium deintercalation from," *J. Mater. Chem.*, vol. 9, pp. 1135–1140, 1999.

[8] R. Waser, R. Dittmann, C. Staikov, and K. Szot, "Redox-based resistive switching memories nanoionic mechanisms, prospects, and challenges," *Adv. Mater.*, vol. 21, no. 25–26, pp. 2632–2663, 2009.

[9] Y. Meng Lu, M. Noman, Y. N. Picard, J. A. Bain, P. A. Salvador, and M. Skowronski, "Impact of Joule heating on the microstructure of nanoscale TiO2 resistive switching devices," *J. Appl. Phys.*, vol. 113, no. 16, 2013.

[10] M. Sulaiman, a. a. Rahman, and N. S. Mohamed, "Li2CO3 – Al2O3 Composite Solid Electrolytes Prepared by Sol Gel Method," *Key Eng. Mater.*, vol. 471–472, pp. 379–384, 2011.

CHAPTER 5

POTENTIAL APPLICABILITY OF Li_xCoO_2-BASED DEVICES TO ReRAM MEMORIES: ENDURANCE MEASUREMENTS

TABLE OF CONTENTS

INTRODUCTION

Towards nonvolatile resistive memories (ReRAM) applicability, endurance (defined as the maximum number of write/erase cycles possible to achieve without degradation) is one of the critical key points to consider in the working performance of devices. This is why studies have been carried out on this point, presented in Chapter 5.

This chapter is divided into five parts. In the first part, we briefly study the influence of switching pulse characteristics (maximum pulse voltages and durations) on endurance in order to obtain the highest endurance possible. Furthermore, the cell configuration plays also an important role and has been examined in the second part: Au, Ti and Cr have been examined as possible upper electrode materials. We also compared cells whose film is well-delimited (same area as the upper electrode, done by Focused Ion Beam etching) to cells for which the sandwiched film is "unlimited" (the lateral film dimensions are much wider than the top electrode area).

In the third part, we observe the progressive degradation of cells during cycling, and try to account for this phenomenon by using X-ray Photoelectron Spectroscopy.

Preliminary results are then shown on the influence of temperature on endurance in a fourth part, and finally, we address downscaling potentialities by starting to study the influence of smaller cell sizes (10x10µm²).

1 INFLUENCE OF THE PULSES CHARACTERISTICS ON ENDURANCE

1.1 Recall: measurements of the resistance states during cycling

The diagram in **Fig. 5.1** recalls rapidly the principle used to study the endurance. A complete switching cycle consists of a SET process (high resistance state ⇨ low resistance state), followed by a read operation, then a RESET process (low resistance state ⇨ high resistance state), and followed by another read operation.

In the first cycle for example, the negative pulse V_{ON} (−8V, 200ms in **Fig 5.1** below) is applied to switch an MIM cell to a low resistance state (SET process). The current I_{ON} (thus R_{ON}) is measured by applying a small read voltage (−1V here). The positive bias V_{OFF} allows switching back the device to a high resistance state (RESET). The I_{OFF} current (thus R_{OFF}) is measured using the same read bias.

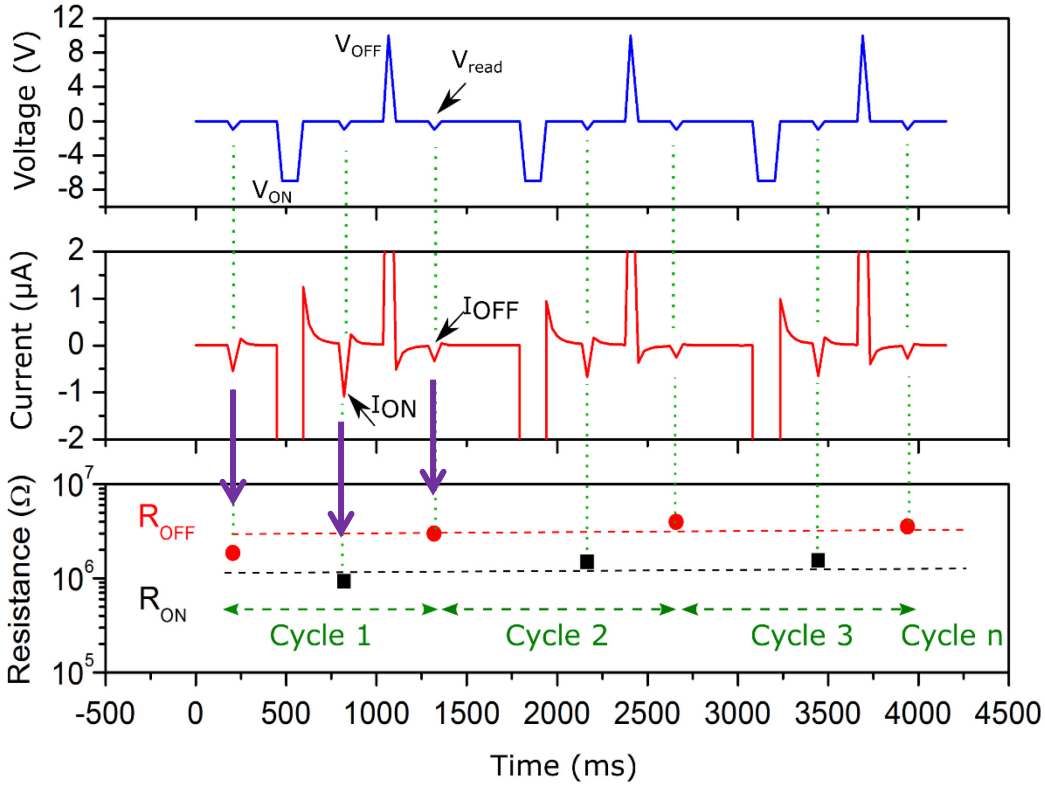

Figure 5.1: Voltage pulses shape used to record the endurance of MIM devices.

A LabVIEW program has been developed to apply the positive and negative pulses (V_{ON} and V_{OFF}) periodically. The repetitive measurements of the two states are carried out until failure of the device is considered as being reached (for example if R_{ON} and R_{OFF} values are both lower than 10^5 Ω, or if $R_{OFF}/ R_{ON} \approx 1$).

The aim is to obtain the highest achievable endurance i.e. the maximum number of cycles with a R_{OFF}/ R_{ON} ratio as high as possible. Hereafter, we report the observation of preliminary endurance measurements of Li_xCoO_2 MIM devices and point out the influence of some parameters on the endurance. Specifically, we try to achieve endurance beyond 1000 cycles, with a R_{OFF}/R_{ON} ratio ≥ 100 for 100x100µm² devices.

1.2 Influence of the SET and RESET voltages

We observed that the shape of the pulses applied to an MIM cell has a strong influence on endurance. First, from the initial state (or R_{INIT} state), a R_{INIT} => R_{LOW} switch can only occur by using *negative* voltage V_{ON}. Moreover, the absolute value of V_{ON} must be higher than a threshold voltage (around 4V), otherwise no switching occurs.

An application of V_{ON} = -6.4V (1000ms) and V_{OFF} = +6.4V (1000ms) yields an endurance reaching typically about 100 cycles with $R_{OFF}/R_{ON} \approx 100$ (**Fig. 5.2a**). The failure is characterized by a very low final resistance, which can be attributed to an irreversible breakdown.

An application of higher voltages (V_{ON} = -9.5V, V_{OFF} = +12V) during the same duration resulted in a straightforward breakdown. Even for shorter duration (V_{ON} = -9.5V 200ms and V_{OFF} = +12V 1ms) leads generally to a very short endurance (10-15 cycles, as shown in **Fig. 5.2b**): the devices seem then short-circuited: both HRS and LRS suddenly decrease to extremely low resistance and it is impossible to switch back again.

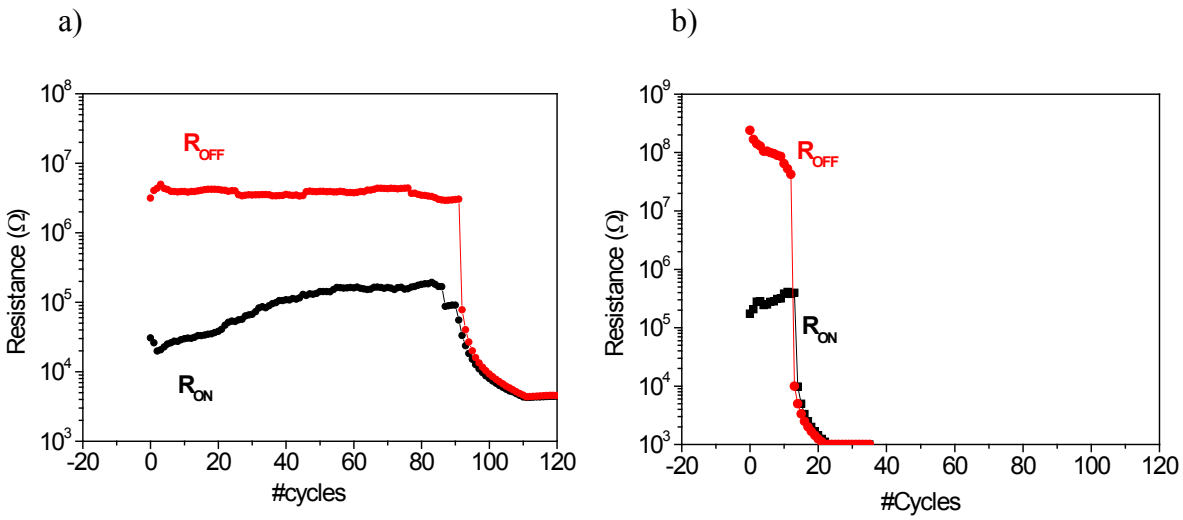

Figure 5.2: Examples of endurance of a {Au (50nm)/Li_xCoO_2/Si)} $100 \times 100\mu m^2$ device: **a)** with $V_{ON} = -6.4V$ (1000ms) and $V_{OFF} = +6.4V$ (1000ms). **b)** with $V_{ON} = -9.5V$ (200ms) and $V_{OFF} = +12V$ (1ms)

1.3 Influence of the pulse duration

A strong impact of pulse duration on the endurance can be observed in **Fig. 5.3**. In this experiment using CP-AFM, the application of a pulse $V_{ON} = -9V$ with for different pulse durations shows that the R_{ON} state depends directly on the duration. For such a voltage and 1x1µm² cell area, a 200ms pulse duration appears enough to obtain a R_{OFF}/R_{ON} ratio ≥ 100.

Such a pulse duration effect can be easily linked to the switching kinetics (already studied in chapter 4). This indicates that for a given pulse voltage value (and a given electrode area), the pulse must be applied long enough to allow switching in a complete way (resulting in a higher R_{OFF}/R_{ON} ratio). However, it must also not be too long (>1000ms), otherwise breakdown occurs easily after the first (or several) cycle(s).

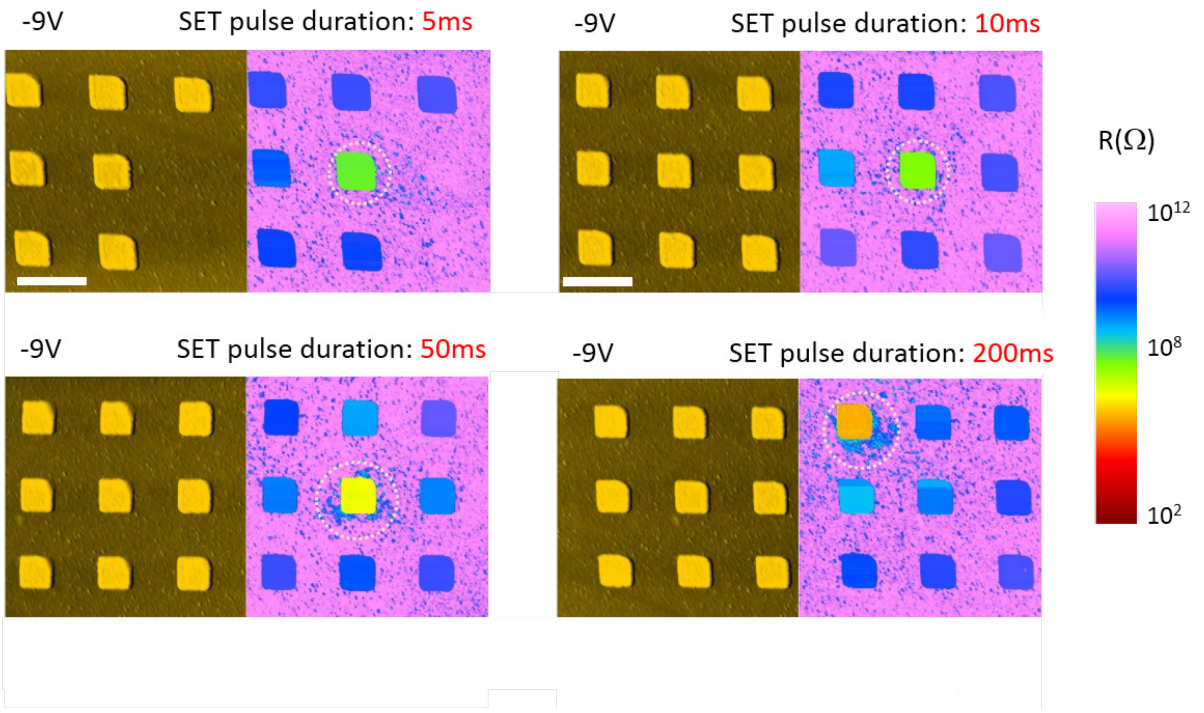

Figure 5.3: Effects of pulse width on the resistive switching of the MIM cell. Topological and electrical images of pads 10x10 µm² are obtained by scanning using CPAFM at +1V in nitrogen atmosphere. (In column) switching from R_{INIT} --> R_{LOW}--> R_{HIGH} and (in row) increasing pulse width applied to the cell.

To illustrate such a {endurance - R_{OFF}/R_{ON} ratio} compromise, a schematic representation is shown in **Fig. 5.4**. In this representation, cycling of 100x100µm² devices has been recorded using CP-AFM (SET pulses: -9V during Δt ms, and RESET pulses: +9V during 1000ms). The R_{OFF}/R_{ON} ratio increases if Δt increases, while endurance becomes shorter (<100) for Δt>1000ms. Hence, a "window" of device performance (pulse duration in the range [10ms - several 100ms]) can be deduced. This is however only valid for a given electrode area. Indeed, this window will shift to the left for smaller device areas (which switch faster, see section … from chapter 4).

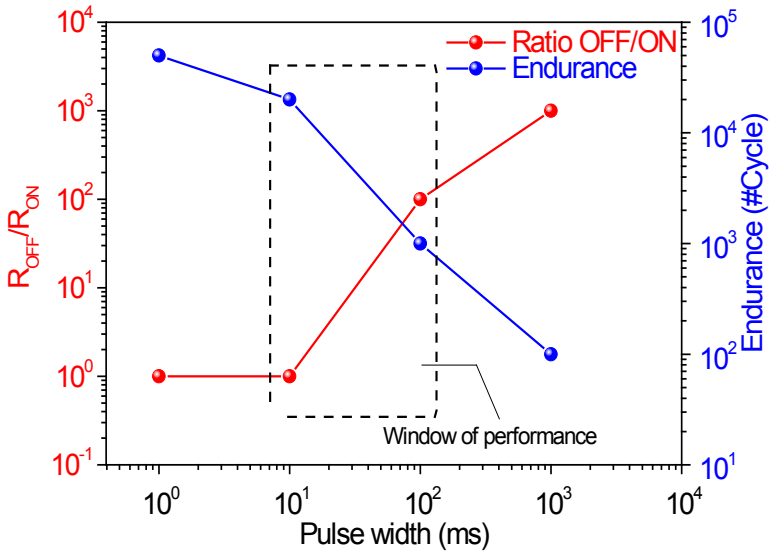

Figure 5.4: Schematic representation of the window of MIM based Li_xCoO_2 thin film device's performance (100x100 μm^2 cell): The R_{OFF}/R_{ON} ratios in red, the possible endurance in blue, the window of performance in the black-dashed rectangle.

1.4 Typical endurance obtained after "optimization" of pulse parameters

For 100x100µm² Au/film/Si devices, pulses characteristics (4 parameters: voltage value and duration of the SET pulse; voltage value and duration of the RESET pulse) play an important role on the achievable endurance.

Different combinations have been tried. After various tries, the maximum endurance obtained reached the [1000-2000] cycles range. A typical result of endurance is shown in **Fig. 5.5** hereafter.

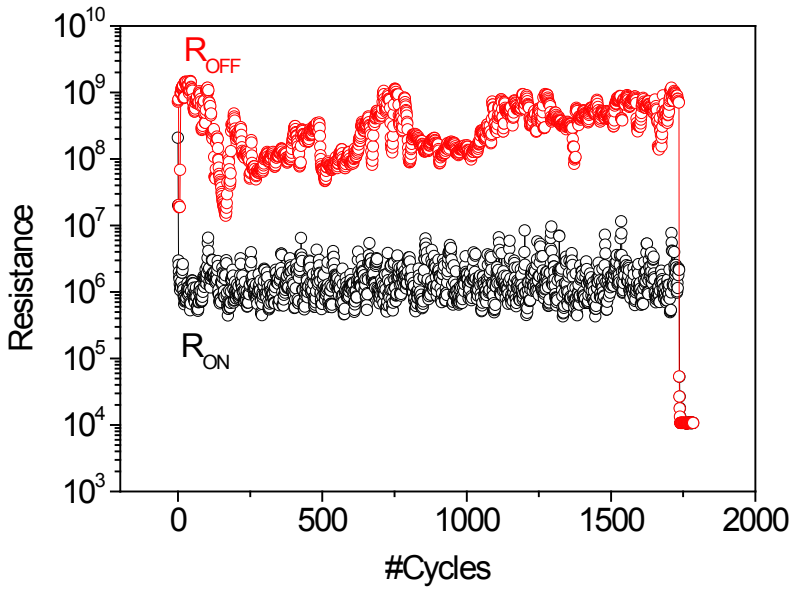

Figure 5.5: Typical example of endurance obtained on a 100x100 µm^2 Au/film/Si cell: the endurance reaches here 1700 cycles, with a R_{OFF}/R_{ON} ratio of about 300. (SET pulse : -7V, 100ms, RESET pulse : +10V, 50ms), using a 0.1mA current compliance.

1.5 Influence of the current compliance

The definition and objectives of current compliance (C.C.) has been presented in Chapter 2. The current compliance is employed to protect the sample from the electrical damages or breakdown. In this part, we compare the endurances of Li_xCoO_2 MIM device using two different compliance currents: 1mA and 0.1mA.

From **Fig. 5.6**, we observe that a typical endurance of 1800 cycles is obtained with a current compliance of 0.1mA. In case of a 1mA compliance, the endurance is however only 180 cycles. Thus, the C.C. is one of the key parameters to get a high endurance for Au/film/Si devices.

An hypothesis to explain such results is that a smaller current compliance limits the electrical power, which results in lower Joule effects. Hence it may limit the risk of thermal breakdown of the cells.

Current compliance smaller than 0.1mA has been tested, but led to much lower R_{OFF}/R_{ON} ratios, thus such compliance has not been considered further.

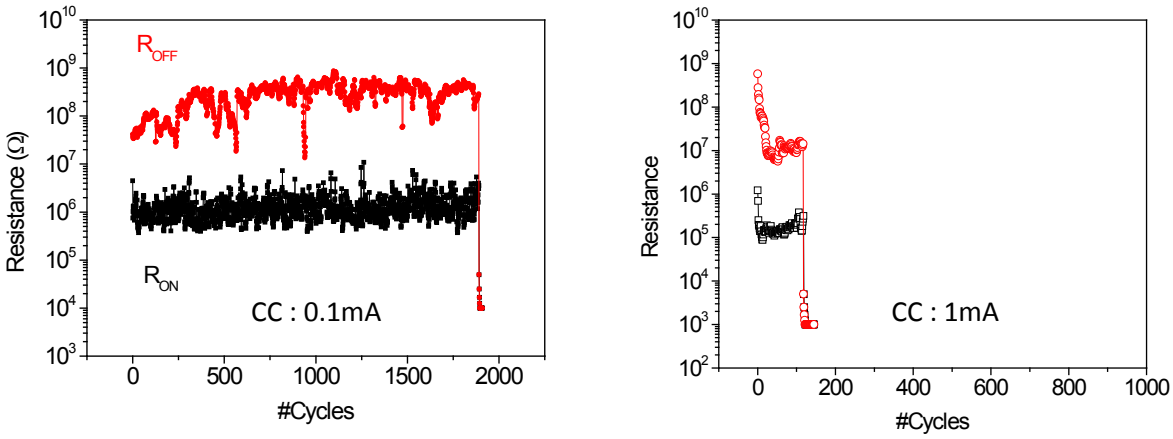

Figure 5.6: Influence of current compliance on the endurance of {Au/Li_xCoO_2/Si} MIM devices: typical results obtained for **a)** C.C. = 0.1mA: endurance = 1800 cycles and **b)** C.C. = 1mA : endurance < 200 cycles.

2 INFLUENCE OF CELL CONFIGURATION ON ENDURANCE

2.1 Influence of the chemical nature of the top electrode

We have previously seen that the current compliance has a strong influence on the endurance achievable on Au/film/Si devices. This could be attributed at first sight to Joule effects, which can degrade progressively the devices. This is the reason why the objective here, is to test other kinds of top electrodes, different from Au. The melting point of Au being 1064°C, we chose to study Ti, which melting point is higher (1668°C), as well as Cr (melting point : 1907°C).

2.1.1 Au electrode vs Ti electrode

For a same sample, some top electrodes deposited are only composed by Au (50nm thickness), and other electrodes are composed by 20nm thick Ti (covered by 50nm Au to ensure a good contact with the external probes). In this way, the post-annealing step of the Li_xCoO_2 film is strictly the same all over the whole film, allowing a better comparison between the cells composed by Au and those made of Ti.

Using a 0.1mA current compliance, we observed that Au/film/Si cells reach between 1000 and 2000 cycles, whereas Ti/film/Si cells reach between 1500 and 3000 cycles. **Fig. 5.7** shows an example of results obtained. Thus, endurance appears slightly better for Ti/film/Si devices. We can also notice that the low resistance state (R_{ON}) appears always less stable for Ti/film/Si cells.

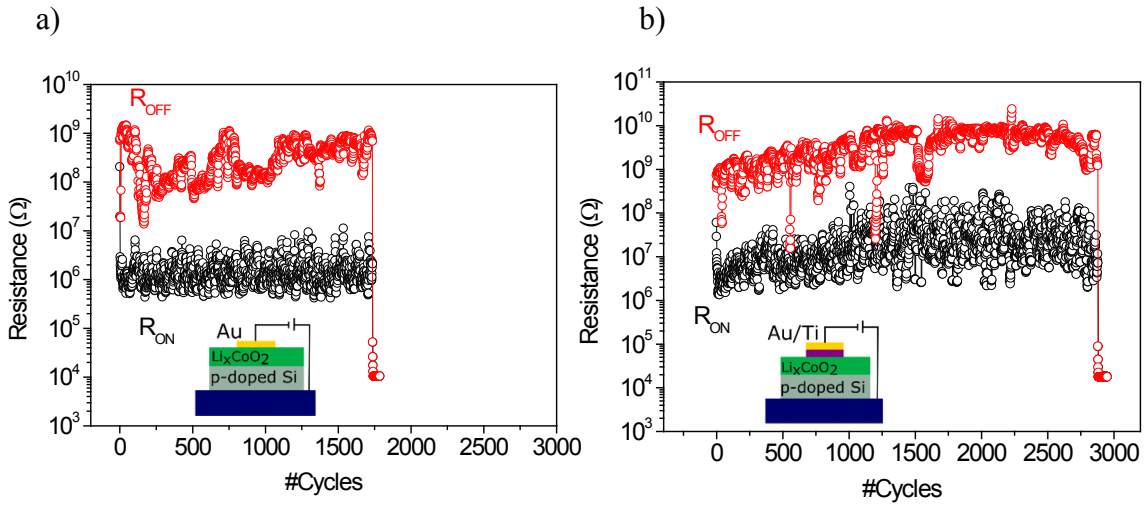

Figure 5.7: Current limitation is 0.1mA. The endurance (measured using two-probes method in ambient air) of two Li_xCoO_2 100x100 μm^2devices: **a)** with Au (50nm) top electrode and **b)** with Au(50nm)/Ti(20nm). For Au and Au/Ti: SET pulse: -7V, 100ms, RESET pulse: +10V, 50ms) , For Au/Ti: SET pulse : -7V, 100ms, RESET pulse : +10V, 50ms.

However, using a 1mA current compliance, we observed a completely different behavior. We had seen in the previous section that Au/film/Si cells reach always less than 200 cycles. However, in the case of Ti top electrodes, it is interesting to note that the endurance always exceeds 1200 cycles, as shown in Fig. **5.8b**. Moreover, the low resistance state (R_{ON}) appears more stable (**Fig 5.8b**) than in the case of 0.1mA current compliance (black points, **Fig 5.8a**, same as **Fig 5.7b**).

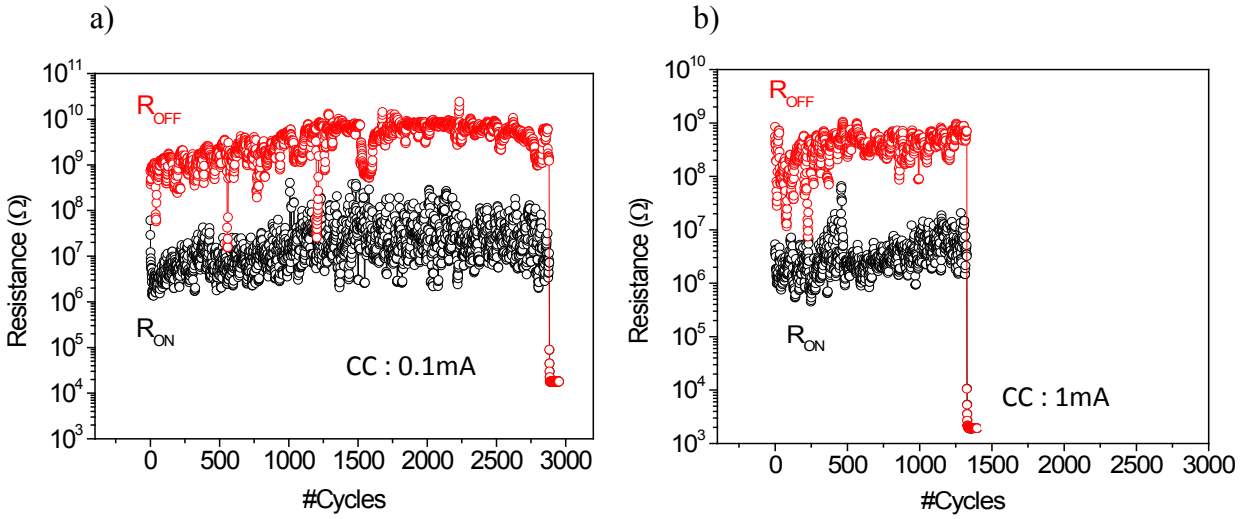

Figure 5.8: The endurance (measured using two-probes method in ambient air) of two Li_xCoO_2 100x100 µm^{2}devices with a Ti top electrode : **a)** left : with a 0.1mA current compliance **b)** right with a 1mA current compliance.

2.1.2 Cr electrode

We have previously observed that the cells with a Ti top electrode sustain longer endurance for a 1mA current compliance. We thus tried another kind of top electrode, composed by Cr (20nm Cr covered by 50nm Au). However, using Cr led to similar results (or even slightly less stable) compared to Ti. Hence Cr has not been considered further, and Ti has been privileged as a possible alternative to Au.

2.2 Endurance of area-restricted film configuration (by Focused Ion Beam)

Here, Focused Ion Beam (FIB) has been utilized (at LPS) to create area-delimitation of the Li_xCoO_2 films (See Chapter 2 section 1.4): the MIM structure including the film is limited to the volume beneath the top electrode. The aim is to avoid film modifications which can extend laterally far from the top electrode: this effect could potentially limit the reversibility (and thus the endurance) of the repetitive switching processes. Besides, the area-restricted film MIM configuration is similar to crossbar structure where the film is adequately sandwiched between two perpendicular bit lines. In such a configuration, we investigate the endurance for Au/film/Si and Ti/film/Si devices.

Before carrying out endurance, the switching behavior has been roughly tested. Typical results (by CP-AFM) have been obtained, shown in **Fig. 5.10**. Before switching, the cell resistance is high ($R \approx 10^9\Omega$, see electrical image in **Fig. 5.10a**. After application of a bias

pulse ($-8V$, $1000ms$), the cell appears much more conducting (cell resistance 3 orders of magnitude lower, see **Fig. 5.10b**. Finally, after another bias pulse (+8V 100ms), the cell resistance is higher again (R ≈ $10^8\Omega$**, Fig. 5.0c**). This result exhibits that switching the restricted-volume MIM cells is possible.

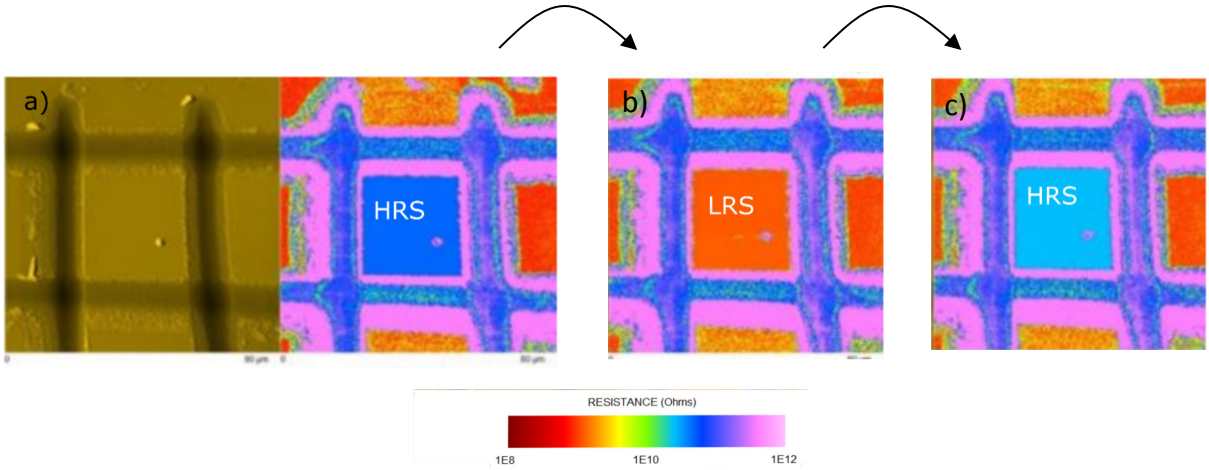

Figure 5.10: Switching test of an area-restricted Li_xCoO_2 cell of 30x30µm^2 using CP-AFM. Topological and electrical images were obtained by scanning (at +1V) over an area of 80x80µm^2 on the sample surface in N_2 atmosphere **a)** the cell is in an initial state ("HRS") in blue (R ≈ $10^9\Omega$), **b)** after a -8V pulse (τ=1000ms), the cell has become more conducting ("LRS", in orange, R≈$10^5\Omega$) **c)** after switching back to a high resistance state ("HRS", in cyan, R≈$10^8\Omega$) using a +8V pulse (τ=100ms).

2.2.1 Comparison between etched and non-etched cells (top electrode : Au)

Comparison between FIB-etched cells and non-etched cells has first been carried out, with a top electrode made of Au (prepared using e-beam evaporation). The endurances were measured (at -1V) on $100 \times 100\ \mu m^2$ cells using two-probes method. The pulses characteristics were the following: V_{ON} = -7V (100ms) and V_{OFF} = +10V (50ms). The resistances R_{ON} and R_{OFF}. The current compliance was set at 0.1mA. The RESET voltage is gradually increased up to +12 V to compensate the R_{OFF} degradation.

The endurances results are shown in **Fig. 5.11a,b**. The first thing to note is that the endurance of the etched sample is lower (around 800 cycles) compared to the non-etched cell (1700 cycles). This could be attributed to some defects coming from the FIB etching process, leading to faster degradation.

Apart from this effect, we can see that both R_{ON} and R_{OFF} appear more stable for the etched cells, compared the non-etched ones. In **Fig. 5.11c,d** the histograms of the two resistance states fluctuations ($\Delta R_{ON}/R_{ON}$ and $\Delta R_{OFF}/R_{OFF}$) illustrate this effect : for both states (R_{ON} and R_{OFF}), a smaller fluctuation of the etched cells is visible (narrower fitting blue curve, compared to wider fitting red curve).

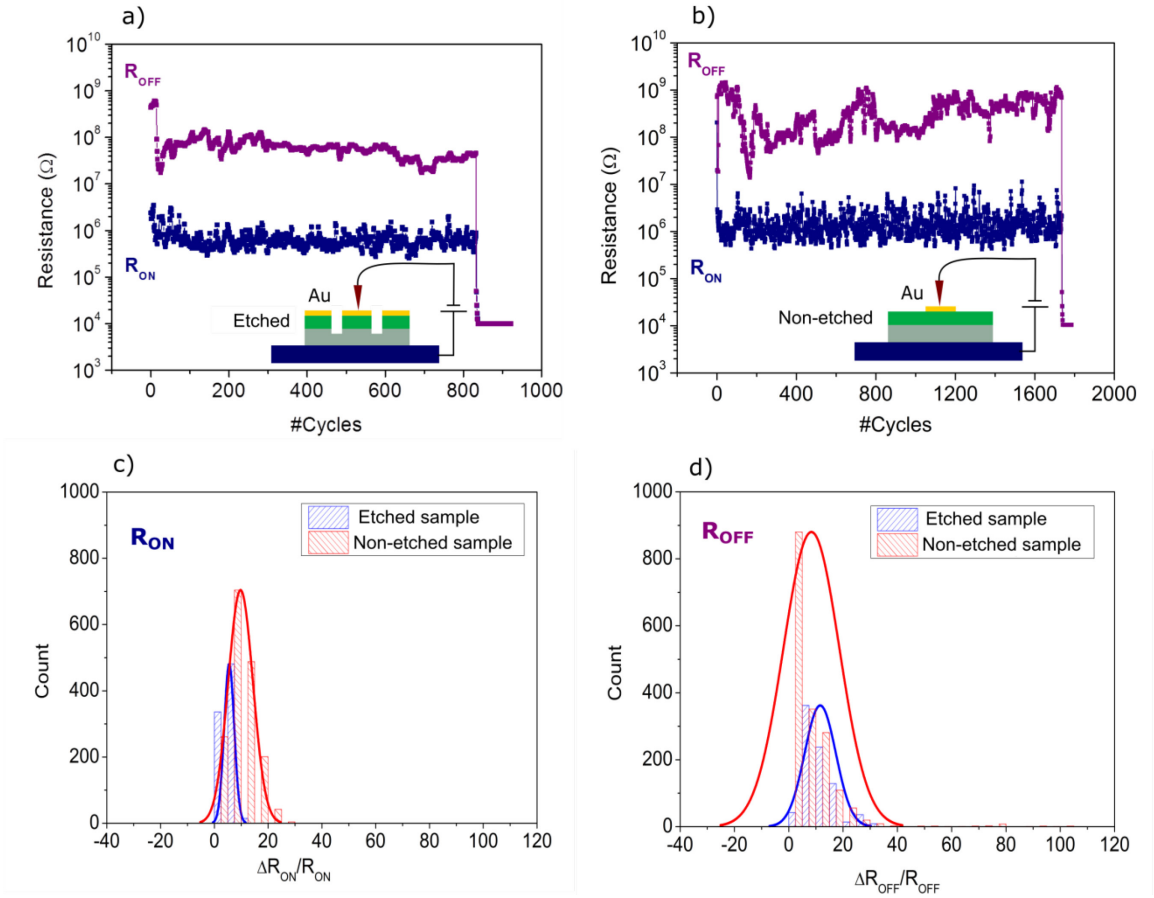

Figure 5.11: Endurance of two configurations (with 0.1mA current compliance) : (left) restricted-area Li_xCoO_2 film and (right) infinite-area Li_xCoO_2 film. The optimized pulse parameters applied are similar in both cases.

2.2.2 Comparison between etched and non-etched cells (top electrode : Ti)

The comparison between etched and non-etched cells has also been studied in the {Ti/Li_xCoO_2/Si} configuration (using a 1mA current compliance and V_{OFF} = +14V). An example of results is shown in **Fig. 5.12a,b**. The previous effect observed is also visible here: the fluctuations of R_{ON} and R_{OFF} are lower in the case of etched cells (see histograms in **Fig. 5.12c,d**). Such a phenomenon, which does not depend on the top electrode nature, can be accounted for by the FIB etching process.

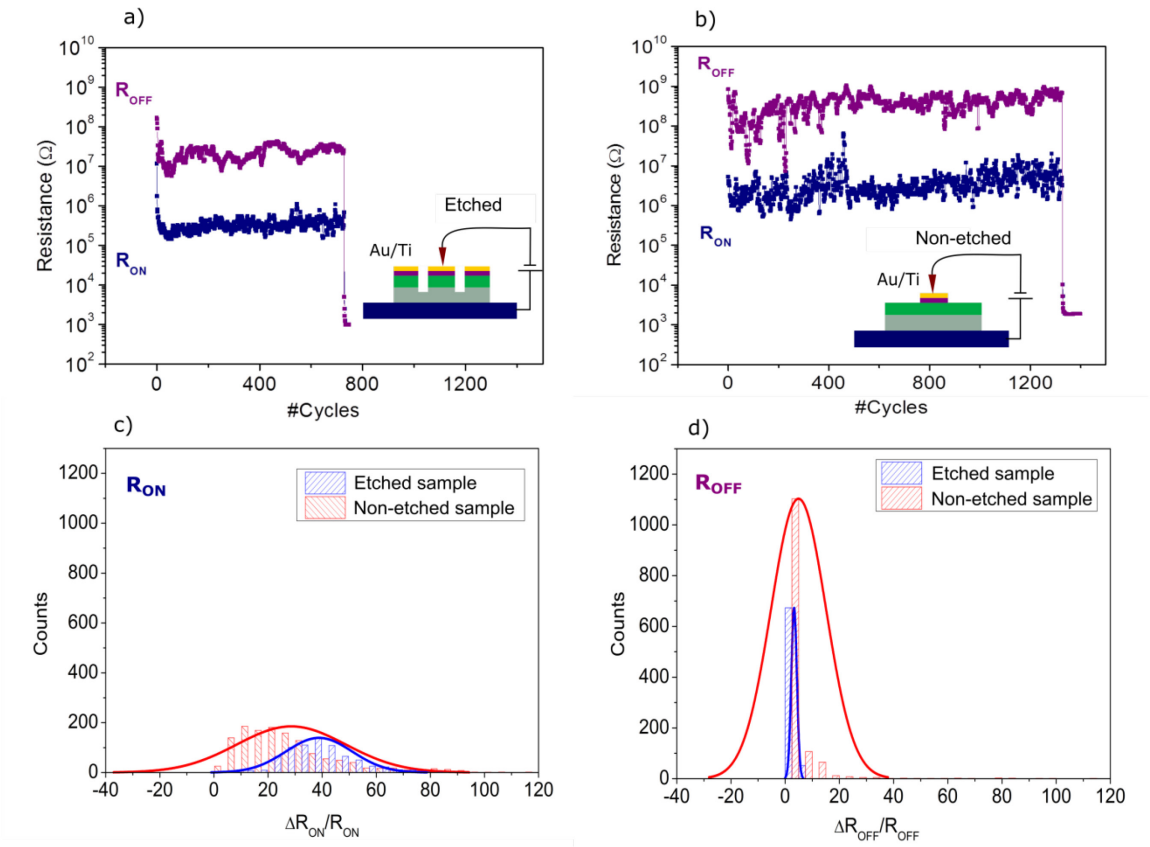

Figure 5.12: Endurance of two configurations: (left) restricted-area LixCoO2 film by FIB and (right) infinite-area Li_xCoO_2 film. The current compliance was set at 1mA.

Hence we tried to look for a possible cause for the smaller resistance fluctuations observed for etched cells. FIB has a well-known ability to amorphize various materials such as Si, Ga, *etc.* on the side-walls and bottom-wall of trenches [19]–[21]. Thus we made the following hypothesis: as sketched in **Fig. 5.13**, the film volume under the top electrode may be "protected" from the ambiant environment (in particular humidity) trough the vertical amorphous zones created by FIB. In addition, the film volume which contributes to switching is also limited (in the case of non-etched cells, the film modifications can extend laterally much further). This could also lead to a more stable switching. However, this remains an hypothesis to explore in a thoroughful way.

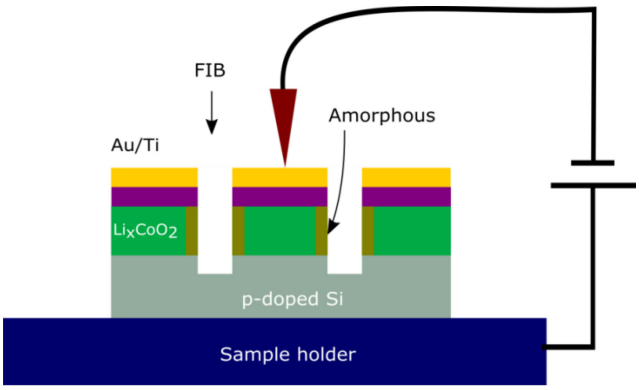

Figure 5.13: Schematic representation of amorphous zones (kaki colour) formed by FIB in a restricted-area cell. The film volume of the cell (green) may thus be isolated from ambiant humidity.

3 CELL DEGRADATION DURING CYCLING

3.1 Optical observations of top electrodes

During cycling, it has been observed by optical microscopy that the shape of the top electrodes changes progressively, as shown in **Fig. 5.14**. Dots on the surface of the top electrodes seem to grow. This is the case of Au top electrodes, but also of Ti electrodes.

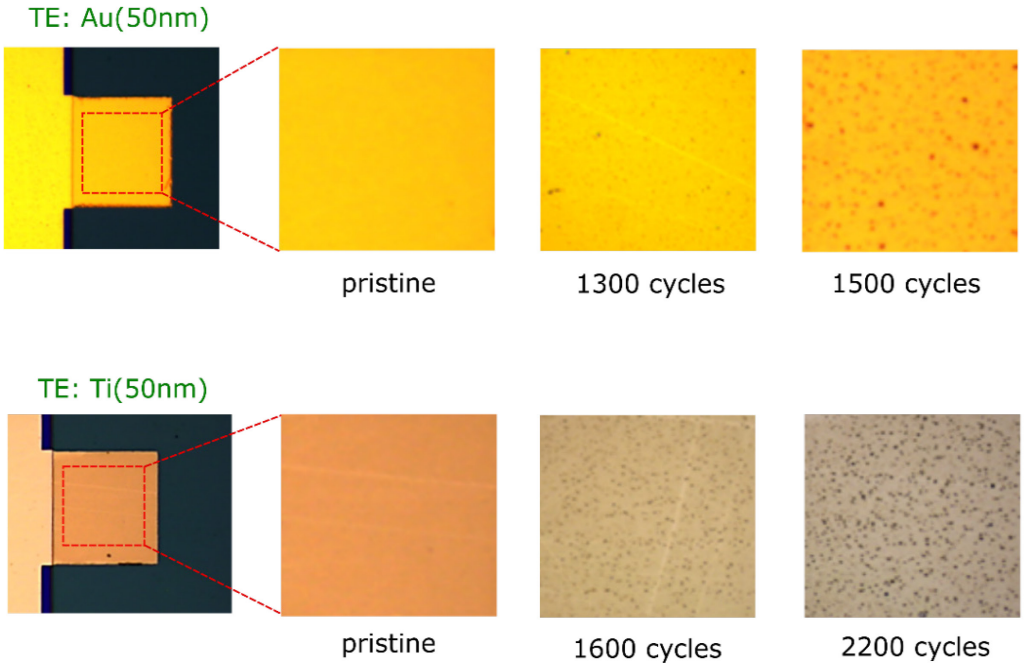

Figure 5.14: optical images of top electrodes after cycling

3.2 Observations by AFM of top electrodes

AFM has been used to carry out topographical images of top electrode surface before cycling, and after one cycle. After cycling, the electrode surface Au 50nm/Li_xCoO_2/ Si) appears covered by domes (**Fig. 5.15b**), which are not present on the pristine electrode surface (**Fig 5.15a**). One of these bumps is typically 1µm large laterally, and about 142 nm in height (**Fig. 5.15c,d**).

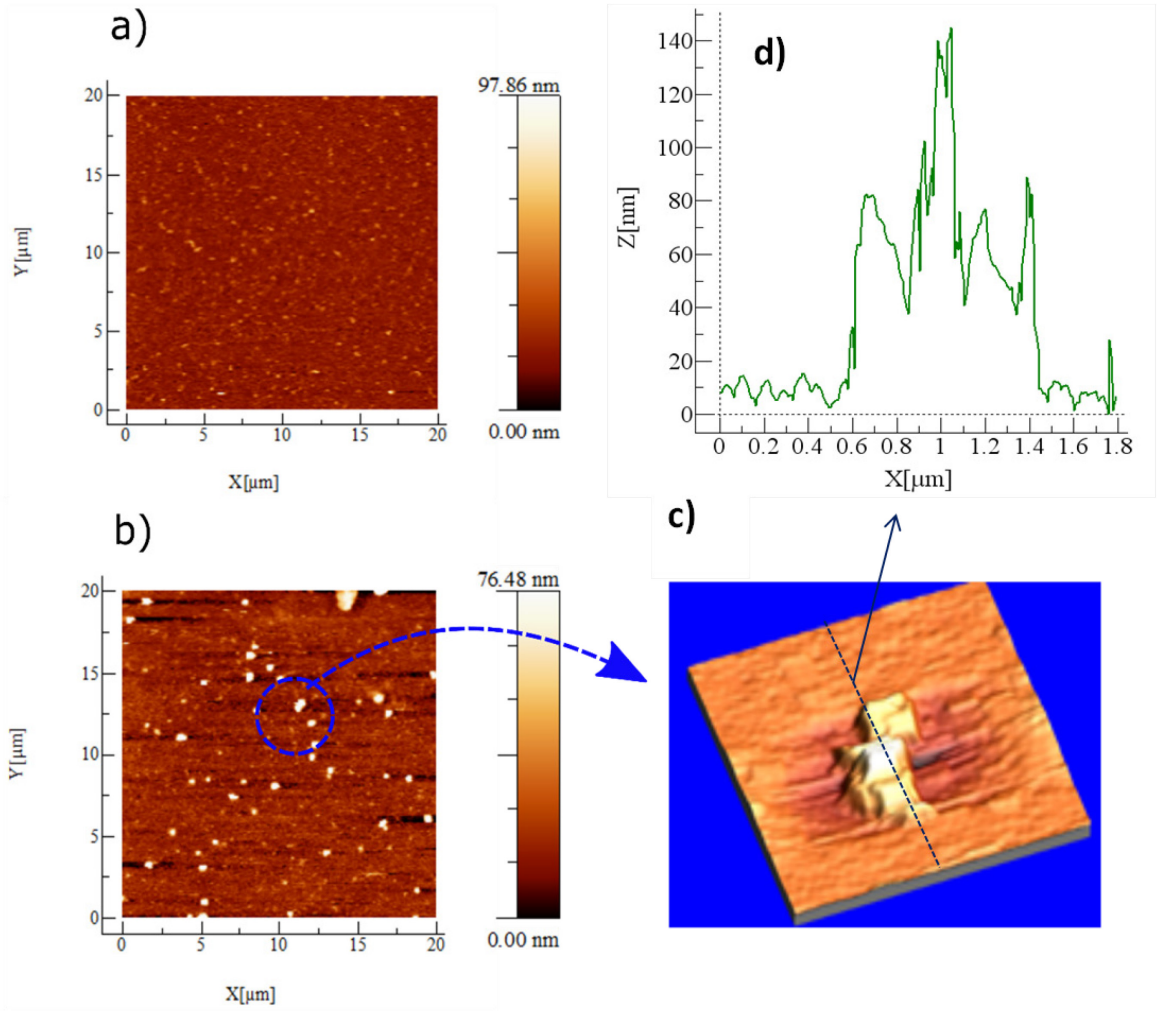

Figure 5.15: Topographical AFM images of an Au (50nm) top electrode surface: (a) pristine, (b) after switching; c) morphology of a dome-like dot scanned using AFM, d) height profile of the dot.

3.3 X-ray Photoelectron Spectroscopy (XPS) analyses of electrodes

XPS analyses have been carried out on 100x100µm² Au/Li_xCoO_2/Si cells which had previously undergone 1000 cycles. The objective is to try to identify the different elements present in the electrode and the film.

Fig 5.16 shows an atomic profile obtained. It is interesting to observe that a non-negligible concentration of Si is present inside the Li_xCoO_2 film, and that Co is present inside the gold top electrode (**Fig 5.16b**). In pristine films studied (**Fig 5.16a**), no Si was detected in the films. Thus cycling has led to a migration of Si coming from the bottom electrode towards inside the film. This could be one of reasons which could explain the final failure of devices (short-circuit). The cause of top electrode changes (domes observed by AFM) needs however more studies to identify precisely all the elements (except Co) present and conclude on the origin of the top electrodes degradation.

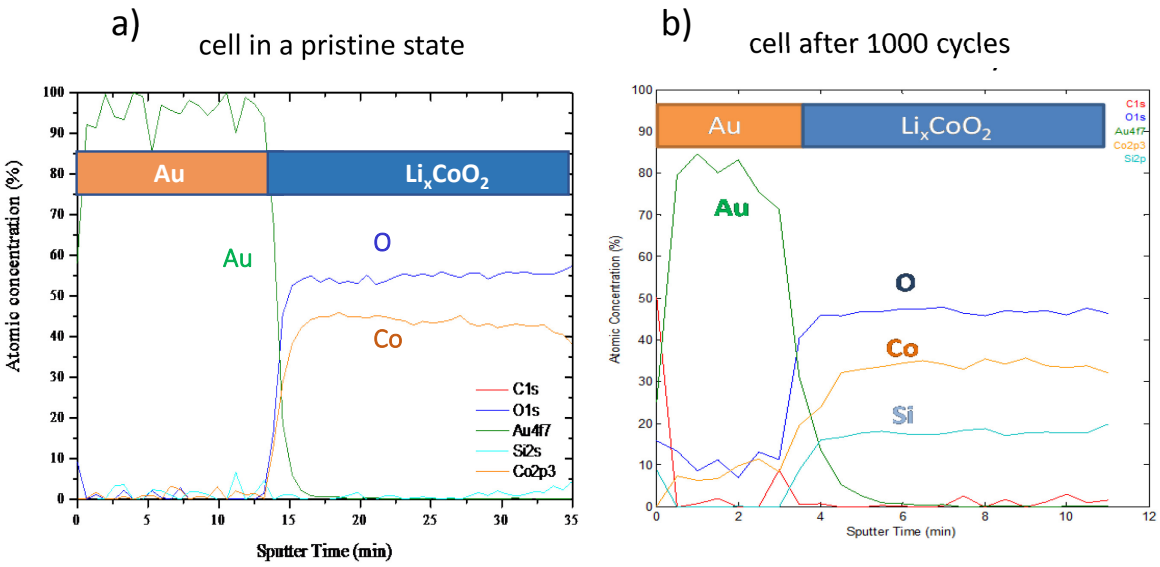

Figure 5.16: XPS depth profiles of Au, O, Co and Si elements of a Au/Li_xCoO_2/Si cells: **a)** cell in a pristine state (Au thickness: 120nm) **b)** cell which had previously undergone 1000 switching cycles (Au thickness: 50nm).

4 INFLUENCE OF TEMPERATURE ON ENDURANCE

4.1 Endurance at low temperature

Very preliminary results have been obtained concerning the influence of low temperature, using a setup allowing cooling down a small chamber downto 79K (using Liquid Nitrogen). In these experiments, we investigated the endurance of {Au(50nm)Ti20nm/Li_xCoO_2/ Si} cells at 79K (cells elaboration: Appendix A, protocol 2). At such a low temperature, it has been observed that higher pulse voltages are required to switch the devices (V_{ON}=-12V,τ=1000ms; V_{OFF}=+12V,τ=50ms). To connect the top electrodes to the outside measurement circuit (two-probes method), we bond a 20µm-in-diameter wire on the non-contact pads to a sample supporter.

Contrasted results have been obtained. As can be seen from **Fig. 5.17a**, the first example shows an endurance of 1000 cycles with a good stability of the high resistance state (R_{OFF}) and the low resistance state (R_{ON}), and a R_{OFF}/R_{ON} ratio of about 100. In the inset of **Fig 5.17a**, we can see the optical images of the top electrode's surface before and after cycling. The top electrode appears not destroyed after cycling. The second example however, shows a much shorter endurance: a breakdown occurred after only 400 cycles as shown in **Fig. 5.17b**. The top electrode appears locally damaged. A film defect might account for this ; further experiments are however needed to study in more detail the exact influence of low temperature on endurance.

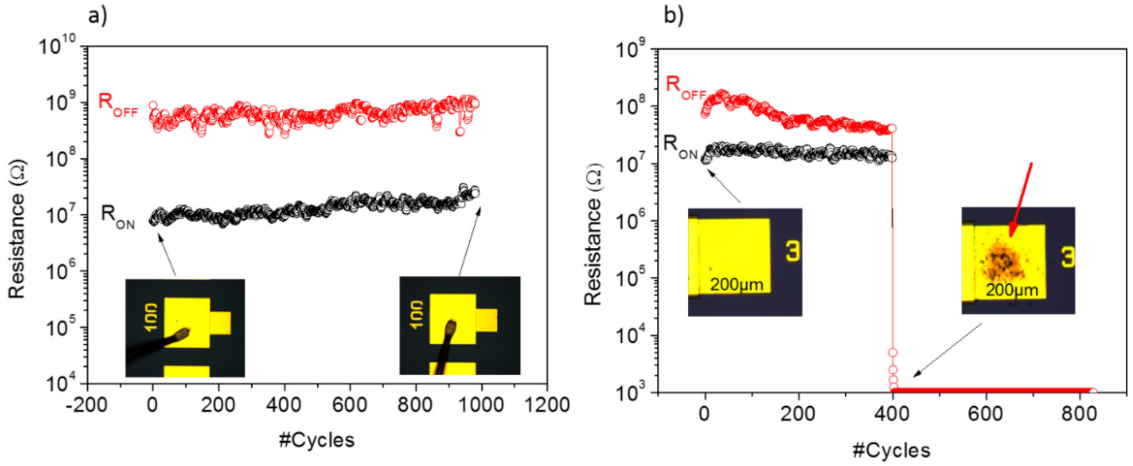

Figure 5.17: Endurance (measurements at -1V) at low temperature (79K): **(a)** cell #1: lateral size is 100x100 µm^2. **(b)** cell #2: lateral size is 200x200 µm^2. The optical images were taken before and after cycling. The current compliance was set at 1mA.

4.2 Endurance at higher temperature than room temperature

Very preliminary results have also been obtained (using Au(50nm)Ti(20nm)/film/Si cells), concerning the influence of high temperature. To carry out such experiments, the samples have been deposited on a hot plate, which temperature can vary from 27°C to 120°C (see **Fig. 5.18**).

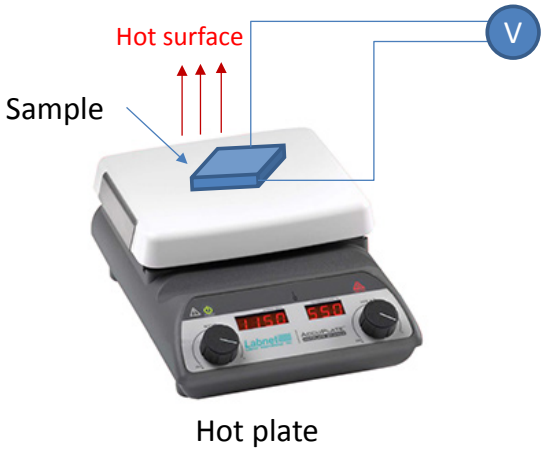

Figure 5.18: Setup used to heat the devices to a temperature in the [27°C-120°C] at ambient air. Cycling is carried out when the desired temperature is stable.

Results obtained are shown in **Fig. 5.19**. At 45°C, the R_{OFF}/R_{ON} ratio observed for a device is not good (cycling has been stopped at 1500 cycles). However at 90°C, after 6000 cycles, the studied device could still switch very well, with a R_{OFF}/R_{ON} ratio reaching 100 (without need to increase the V_{ON} pulse voltage). The same trend is observed at 120°C. Such an experiment has been carried out twice, and the same behavior has been observed. It would be very interesting to investigate even higher temperature, which will be carried out in the future with adequate setups.

According to literature, the endurance of devices such $Pt/HfO_x/TIN$ can reach 10^5 cycles, but the R_{OFF}/R_{ON} ratio fluctuates more than one order of magnitude at room temperature. These fluctuations reach 2 orders of magnitude at 150°C [17]. It is assumed in this case that higher temperature will enhance the possibility of defect formation [18]. In the case of Li_xCoO_2-based cells, the observed behavior appears completely different, and awaits further studies in this direction.

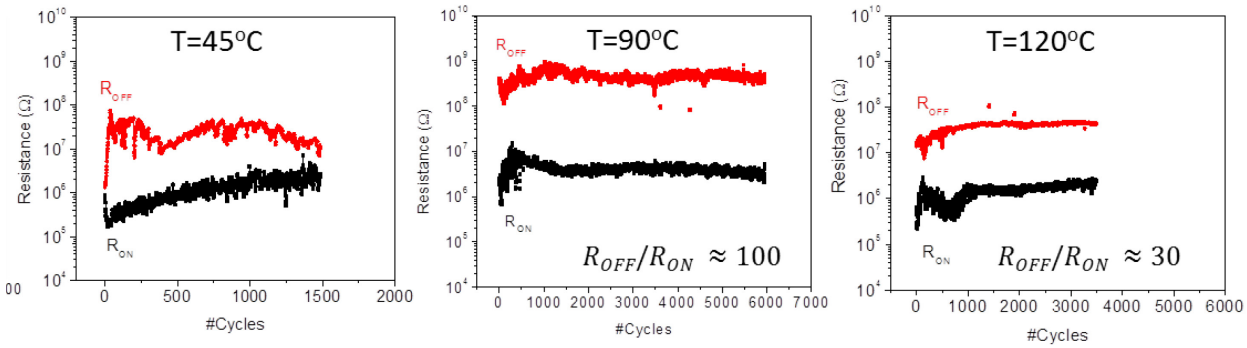

Figure 5.19: Endurance of MIM cells at high temperature ranging from 45°C to 120°C. The pulse voltage parameters are $V_{ON} = -7V, \tau = 50ms$; $V_{ON} = +10V, \tau = 50ms$. The resistances were measured at $V_{read} = -1V, \tau = 50ms$. The current compliance was set at 1mA.

5 PRELIMINARY RESULTS ON THE INFLUENCE OF DOWNSCALING ON DEVICE ENDURANCE

From chapter 3, both experimental results and model have shown that the switching kinetics is faster when using smaller cells. Thus kinetics appears to be better with downscaling. Hence we wondered what would be the effect of downscaling on endurance. This section tries to give a first insight on this subject.

5.1 Modified method to study the endurance of micrometric devices

Two-probes method is a simple and effective technique to characterize endurance (see Chapter 2, section 3.2). However, its macroscopic probes (about few tens of microns) can easily touch 100x100 µm² top electrodes, but it is difficult (if not impossible) to touch smaller ones. Moreover, the probes stiffness can cause a mechanical damage: indeed, the needles can go through the top electrodes and destroy the film, for long time cycling measurements (a few days).

To avoid such problems when studying small cells (< 100x100 µm²), a 200-300nm-thick Si_3N_4 layer was deposited on the films (using RF magnetron sputtering), before top electrode deposition (see Appendix A, protocol 2). A schematic view of this configuration is shown in **Fig. 5.20a**. This insulating Si_3N_4 layer is an intermediate layer which is hard enough to prevent the damage caused by the probes, and its lateral dimensions (area 200x200 µm², see

optical top view **Fig. 5.20b**) are wide enough to make easily a good electrical contact between the macroscopic probes and the top electrodes.

Using this deposition configuration, the endurance of 10x10µm² cells have begun to be studied, and the preliminary results are presented in the next section.

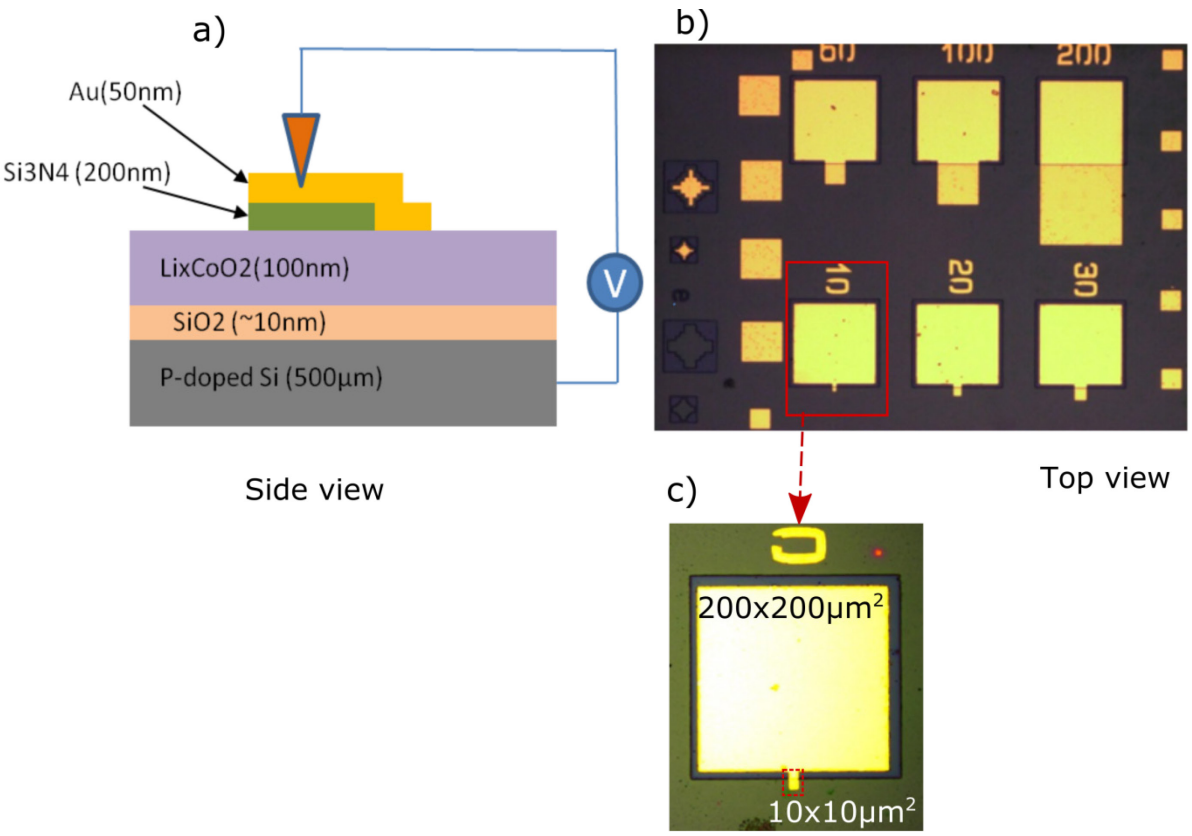

Figure 5.20: towards study of downscaling devices: (a) schematic cross-section of the devices, including an insulating Si_3N_4 intermediate layer, (b) top-view optical image of the devices of different top electrode sizes (200x200µm² down to 10x10µm²), (c) zoom of a 10x10µm² cell.

5.2 Preliminary results of endurance obtained on 10x10 µm² devices

5.2.1 First endurance results on 10x10µm² cells (Au top electrode)

The first result obtained on a 10x10µm² MIM cell is presented in **Fig. 5.21**. Interestingly, promising >6000-cycles endurance is obtained, with a R_{OFF}/R_{ON} > 100. The increased endurance could be accounted for by a lower number of film defects for such cell dimensions, but need more detailed studies in the future.

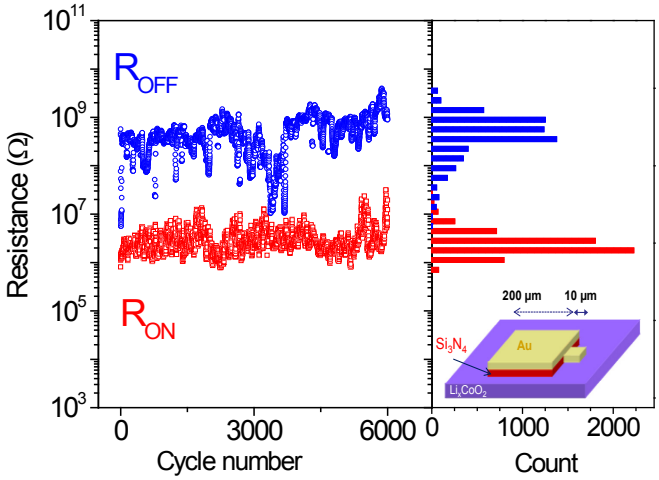

Figure 5.21: Endurance of >6000 cycles is obtained on a 10x10µm^2 cell at ambient air. The histograms on the right show the mean distribution of R_{OFF} and R_{ON}. The mean R_{OFF}/R_{ON} ratio is higher than 100. Pulse characteristics: V_{ON} = -7V, τ=100ms => 2000ms, V_{OFF} = +10V=>+12V, τ=50ms. The current compliance was set at 0.1mA.

5.2.2 First endurance results on 10x10µm² cells (Ti top electrode)

On {Au/Ti/film/Si} cells, promising results have also been obtained, by using adequate pulse voltages. Two examples of endurance are shown in **Fig. 5.22**, allowing endurance higher than 20.000 cycles, although the resistance states seem to be much more fluctuating. Future studies have to be carried out on smaller cells.

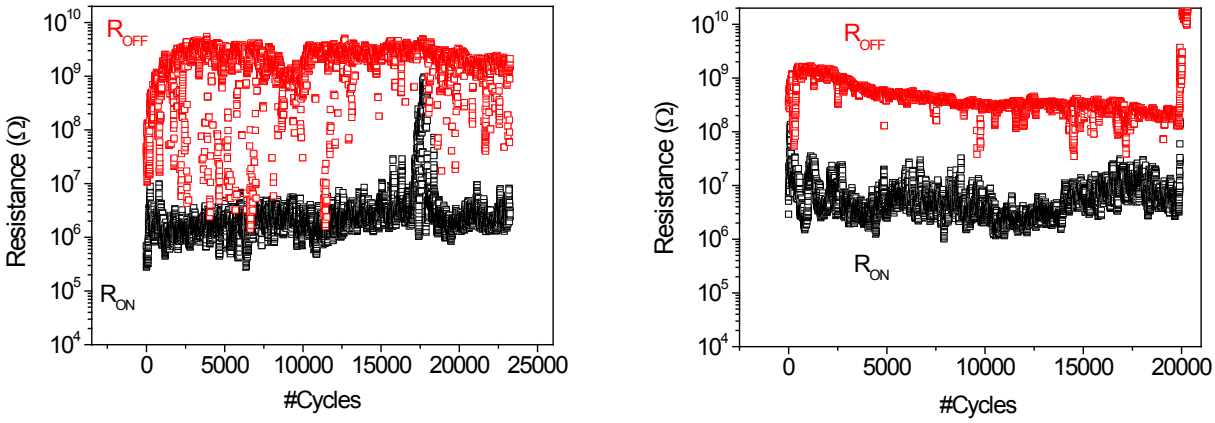

Figure 5.22: Cycling on 10x10µm^2 Ti/film/Si cells at ambient air. Pulse characteristics: V_{ON} = -7V, τ=100ms => 2000ms, V_{OFF} = +10V=>+12V, τ=50ms. Current compliance=1mA.

6 CONCLUSIONS

Endurance measurements have mainly been carried out on 100x100µm² cells, and the influences of several parameters have been considered. First, concerning the pulses characteristics, it is possible to define a performance window: indeed, for given pulse voltages, a long duration will increase the R_{OFF}/R_{ON} ratio, but decrease the endurance. Conversely, a low duration will not allow complete switching, and will lead to a lower R_{OFF}/R_{ON} ratio. Hence, attempts towards maximizing Au/film/Si cells endurance leads to a typical endurance in the [1500-2000 cycles] range (for a 0.1mA current compliance).

An important influence of the chemical nature of the top electrode has besides been observed: Ti/film/Si cells allow reaching higher endurance (2500-3000 cycles) for comparable current compliance (0.1mA). Besides, In the case of 1mA current compliance, using Ti as top electrode also allows endurance beyond 1000 cycles (compared to less than 200 cycles using Au). Joule effects seem here to be the main limiting parameter concerning Au.

Etched cells (delimited film to fit the top electrode lateral size) allowed to obtain more stable R_{OFF} and R_{ON} resistance states (endurance slightly decreases, probably due to defects introduction during FIB etching). As an hypothesis, etched cells (whose borders are "protected" by amorphous zones) may be less sensitive (than cells with "unlimited film" lateral extension) to ambient humidity, but the exact influence of humidity has still to be determined exactly, to confirm this hypothesis.

Furthermore, the progressive degradation of cells during repetitive cycling has been observed, using both Au and Ti top electrodes. Such a phenomenon appears correlated to Si migration from the bottom electrode towards the upper electrode, as seen by XPS analyses.

Moreover, preliminary studies show that temperatures of 90°C and over appear to improve the endurance beyond 6000 cycles. The origin of such phenomenon has however to be determined (linked or not to relative humidity?).

Finally, first results on smaller 10x10µm² cells show endurances over 6000 cycles (R_{OFF}/R_{ON} ratio ~ 100) ratio) using Au top electrodes, and even over 20.000 cycles using Ti top electrodes. Hence, downscaling seems to greatly improve endurance potentialities. Future studies have to be carried out on sub-micrometric cells.

7 REFERENCES

[1] R. Waser, R. Dittmann, C. Staikov, and K. Szot, "Redox-based resistive switching memories nanoionic mechanisms, prospects, and challenges," *Adv. Mater.*, vol. 21, no. 25–26, pp. 2632–2663, 2009.

[2] G. Bucci, S. P. V Nadimpalli, V. A. Sethuraman, A. F. Bower, and P. R. Guduru, "Measurement and modeling of the mechanical and electrochemical response of amorphous Si thin film electrodes during cyclic lithiation," *J. Mech. Phys. Solids*, vol. 62, pp. 276–294, 2014.

[3] H. Sitinamaluwa, J. Nerkar, M. Wang, S. Zhang, and C. Yan, "Deformation and failure mechanisms of electrochemically lithiated silicon thin films," *RSC Adv.*, vol. 7, no. 22, pp. 13487–13497, 2017.

[4] M. Green, E. Fielder, B. Scrosati, M. Wachtler, and J. S. Moreno, "Structured Silicon Anodes for Lithium Battery Applications," *Electrochem. Solid-State Lett.*, vol. 6, no. 5, p. A75, 2003.

[5] C. K. Chan, R. Ruffo, S. S. Hong, R. A. Huggins, and Y. Cui, "Structural and electrochemical study of the reaction of lithium with silicon nanowires," *J. Power Sources*, vol. 189, no. 1, pp. 34–39, 2009.

[6] Y. Zhang, Y. Li, Z. Wang, and K. Zhao, "Lithiation of SiO2 in Li-ion batteries: In situ transmission electron microscopy experiments and theoretical studies," *Nano Lett.*, vol. 14, no. 12, pp. 7161–7170, 2014.

[7] L. A. Berla, S. W. Lee, Y. Cui, and W. D. Nix, "Mechanical behavior of electrochemically lithiated silicon," *J. Power Sources*, vol. 273, pp. 41–51, 2015.

[8] A. A. Arie and J. K. Lee, "Electrochemical properties of P-doped silicon thin film anodes of lithium ion batteries," vol. 737, pp. 80–84, 2013.

[9] F. Shi, Z. Song, P. N. Ross, G. A. Somorjai, R. O. Ritchie, and K. Komvopoulos, "Failure mechanisms of single-crystal silicon electrodes in lithium-ion batteries," *Nat. Commun.*, vol. 7, no. May, p. 11886, 2016.

[10] A. Ostadhossein, S. Y. Kim, E. D. Cubuk, Y. Qi, and A. C. T. Van Duin, "Atomic Insight into the Lithium Storage and Diffusion Mechanism of SiO2/Al2O3 Electrodes of Lithium Ion Batteries: ReaxFF Reactive Force Field Modeling," *J. Mater. Chem. A*, vol. 120, no. 13, pp. 2114–2127, 2016.

[11] H. Jung, B. C. Yeo, K.-R. Lee, and S. S. Han, "Atomistics of the lithiation of oxidized silicon (SiOx) nanowires in reactive molecular dynamics simulations," *Phys. Chem. Chem. Phys.*, vol. 18, no. 47, pp. 32078–32086, 2016.

[12] Z. Zeng, W.-I. Liang, Y.-H. Chu, and H. Zheng, "In situ TEM study of the Li–Au reaction in an electrochemical liquid cell," *Faraday Discuss.*, vol. 176, no. July 2015, pp. 95–107, 2014.

[13] P. Bach, a. Seemayer, U. Rütt, O. Gutowski, and F. Renner, "In-situ Observation of Lithium Alloying with Gold - Structural details of lithium insertion/extraction in/from Au thin film electrodes for Lithium Ion Batteries," *Phot. Sci.*, no. 111, 2012.

[14] S. Sim, P. Oh, S. Park, and J. Cho, "Critical thickness of SiO2 coating layer on core@Shell bulk@nanowire Si anode materials for Li-ion batteries," *Adv. Mater.*, vol. 25, no. 32, pp. 4498–4503, 2013.

[15] V. H. Mai, "Etude de phenomenes de commutation de resistance de films minces de LixCoO2. Autre [cond-mat.other]. Universite Paris Sud - Paris XI, 2014. Fran ̧cais. < NNT : 2014PA112115 > . < tel-01164971 >," *Thesis Univ. Paris-Sud*, 2014.

[16] R. Waser and D. Lelmini, "Resistive Switching: From Fundamentals of Nanoionic Redox Processes to Memristive Device Applications," Wiley-VCH, Weinheim, 2016, pp. 231–233.

[17] B. Butcher *et al.*, "High endurance performance of 1T1R HfOx based RRAM at low (<20uA) operative current and elevated (150° C) temperature," *Int. Integr. Reliab. Work.*, pp. 146–150, 2011.

[18] Z. Fang, H. Y. Yu, W. J. Liu, N. Singh, and G. Q. Lo, "Resistive RAM Based on Hfox and its Temperature Instability Study," *World Acad. Sci. Eng. Technol.*, vol. 48, no. 12, pp. 905–907, 2010.

[19] L. a Giannuzzi, R. Geurts, and J. Ringnalda, "2 keV Ga+ FIB Milling for Reducing Amorphous Damage in Silicon," *Microsc. Microanal.*, vol. 11, no. S02, pp. 2004–2005, 2005.

[20] L. A. Giannuzzi and F. A. Stevie, "A review of focused ion beam milling techniques for TEM specimen preparation," *Micron*, vol. 30, no. 3, pp. 197–204, 1999.

[21] J. P. McCaffrey, M. W. Phaneuf, and L. D. Madsen, "Surface damage formation during ion-beam thinning of samples for transmission electron microscopy," *Ultramicroscopy*, vol. 87, no. 3, pp. 97–104, 2001.

CONCLUSIONS AND PERSPECTIVES

In order to cope with the present limits of Flash memory (e.g. low information density, low endurance and slow speed), many researches recently developed around various kinds of emergent memories, and especially around the concept of resistive memories based on the switching between different resistance levels The underlying mechanisms of memories whose resistance variations depend on electrochemical reactions (ReRAM) are often based on the formation/rupture of conducting filaments, involving migration of cations of metal elements or oxygen vacancies. This filamentary character makes it challenging to attain extreme downscaling towards the nanometric scale.

Hence, in order to overcome this latter limitation, the aim of this thesis was to investigate in more detail the origin of the switching processes observed in Li_xCoO_2 films, and to examine the potential applicability of Li_xCoO_2-based devices to ReRAM memories through the study of their performances in terms of kinetics, stability over time, and endurance.

We first characterized the structural and electrical properties of such films (elaborated by RF-sputtering at the LITEN-CEA, Grenoble), as well as the electrical behavior of the devices elaborated therefrom. Local TEM analyses (HAADF) show that the mean c-axis of the films is horizontally oriented, and that lithium is detected (by EELS) in the films, which also contains Co_3O_4 and CoO (located near the film surface). SIMS allows characterizing the 3D distribution of elements, and highlights the presence of the SiO_2 layer (~15nm thick) which exists at the Li_xCoO_2/Si interface.

In a further step, we investigated the electrochemical mechanisms which are at the origin of resistive switching, in the micrometric electrode/film/electrode configuration. The nanoionic migration of lithium (mechanism proposed before this thesis) has been observed, first indirectly (through the temperature dependence of the resistance states): from a semiconducting state (correlated to a high x stoichiometry), the Li_xCoO_2-cell character becomes metallic (after switching to a low resistance state), which has been correlated to a lower x stoichiometry. Besides, SIMS analyses allowed clear evidence of Li presence in the bottom electrode (Si), for cells which are in a low resistance state. These results confirmed directly, in the resistive switching process, the involvement of ionic migration outwards the films into the Si bottom electrode. The possible role of the SiO_2 interface layer has been discussed by examining current-voltage curves: SiO_2 allows Li^+ diffusion, but maybe also the growth of metallic conducting paths. Besides, preliminary EIS measurements show the resistance decrease phenomenon, but further studies are needed to detect by this mean the lithium diffusion at very low frequencies (<1Hz).

The kinetics of switching has then been studied. It has been observed that it highly depends on the top electrode surface (which thus excludes a purely filamentary switching). The kinetics also depends on the top electrode chemical nature (for Ti, the kinetics appears slower than for Au). A numerical model has been developed and proposed to account for the high dependence of the kinetics on the upper electrode surface. Using such a model, an extrapolation downto 20x20µm² small devices leads to a calculated switching time in the 100ns order of magnitude, which is 1000 times faster than Flash memories.

Concerning the stability of cell resistance states with time, the resistance drift in ambient air is clearly attributed to the progressive carbonatation of Li_xCoO_2 (under high vacuum, such a phenomenon does not occur). Furthermore, in air, the drift of the low resistance state is much faster (a few hours) compared to the high resistance state behavior. We tried several types of protecting films to slow down such a drift, but the time stability was however not improved.

Finally, we examined the potential applicability of Li_xCoO_2-based devices to Re-RAM memories through the study of their performances in terms of endurance. The influence of several parameters has been investigated. First, concerning pulses characteristics, it is possible to define a performance window. Besides, an important influence of the chemical nature of the top electrode has besides been observed: Ti/film/Si cells allow reaching higher endurance (2500-3000 cycles) than Au/film/Si cells. Using etched cells yields more stable R_{OFF} and R_{ON} resistance states, which origin has to be determined exactly. Moreover, the progressive degradation of cells during repetitive cycling has been observed, which appears correlated to Si migration from the bottom electrode towards the upper electrode (observed by XPS). And finally, preliminary downscaling studies (on 10x10 µm² cells) show very promising results (over 20.000 cycles using Ti top electrodes).

In conclusion, Li_xCoO_2-based devices can withstand high temperature over 100°C (concerning endurance), this is an outstanding advantage in electronics in which devices should withstand temperature over 80°C. Also, our results bring new promising insights in the field of rechargeable batteries.

Hence in the perspectives, it would be interesting to continue the current investigations, for example on the influence of elaboration (film thickness < 100nm, and improved film quality), and downscaling (cells size ≤ 200 nm) on switching kinetics, endurance and R_{OFF}/R_{ON} ratio. In the medium term, the research envisaged could focus on a better control of the interfaces (e.g. preformed channels in polymer interface layers, suitable lower electrodes made of nanorods…), and on the study of other types of films belonging to the class of intercalation materials.

APPENDIX A: METALLIZATION FOR FABRICATION OF AN MIM STRUCTURE (IN CLEANROOM)

Protocol 1: M/Li_xCoO_2/Si substrate (M=Au, Ti, Pt, Cr…)

The aim is to deposit a metal M as a top electrode on top of a Li_xCoO_2 film to obtain the MIM structure. The overall process is shown in **Fig. A.1**.

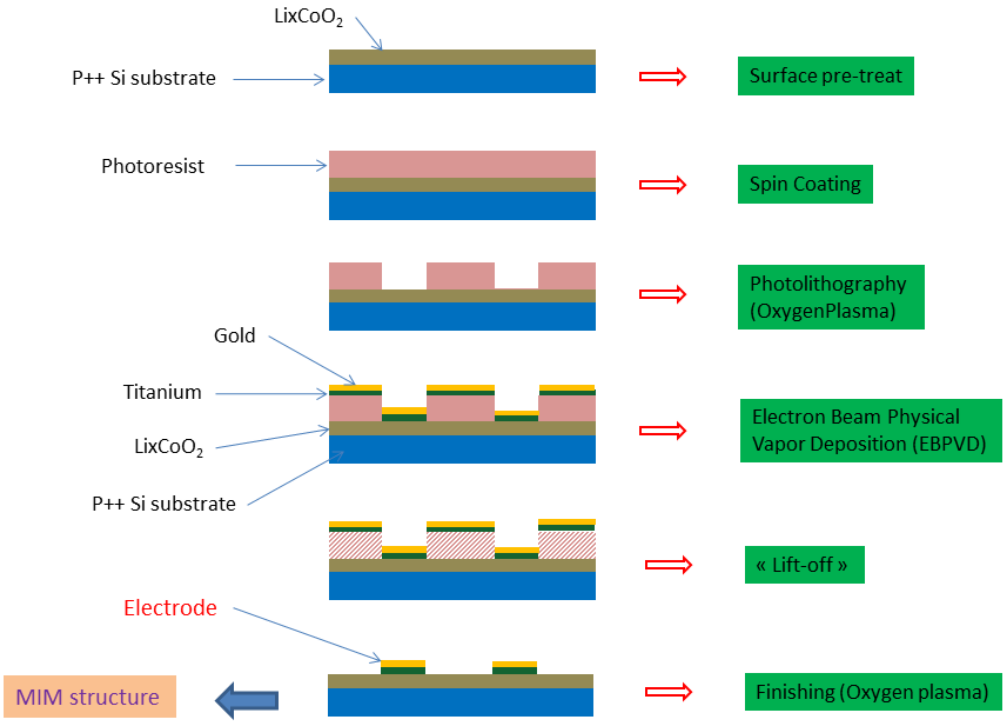

Figure A.1: Lift-off process

- ***Negative photolithography***

Step 1: Sample cleaning

- Cut a 5×5 mm^2 sample from a {Li_xCoO_2/p-doped Si} wafer. Then anneal the sample (for 1h at 580°C in air), clean gently the surface of the film using IPA and cotton tip then dried by Nitrogen air-jet.

Step 2: Spin coating

- Choose Mode SQR 5x5 MM. The spinning speed in this mode is set at 4000 rpm, which corresponds to 1.4 µm in thickness of photoresist layer. Spin coating time is set at 20 seconds to make photoresist homogeneously distributes on the surface of the film.
- Put the sample on the plate. Check vacuum P=0.6 – 0.8 mTorr by press START/ STOP.

- Using a pipette to withdraw and put a drop of positive photoresist **AZ 5214E** on the surface of sample.
- Press START

Step 3: Pre-bake (Soft-bake)

Using hot-plate, the sampled is solf-baked for 1min30" @ 110^0C.

Step 4: Edge bead removal

The edge bead causes the diffraction of the UV light illumination because of a not good contact between the mask and the photoresist layer. To remove the edge bead, it is necessary to use a special mask which covers the entire of photoresist layer except the edge beads. After that, the photolithography apparatus MJB4 is used to exposure the UV light on this mask. After the first development process, the edge beads are completely removed.

Step 5: Patterning (using MJB4 equipment)

- Place the mask on a mask holder.
- Open the contact lever
- WEC Setting value = 16 (safe distance far from the sample)
- Close the contact lever. Increase the WEC value until hearing a sound "beep". Stop and turn back slowly until a notification "WEC setting OK" is displayed on the screen.
- Open and close the contact lever again.
- Set parameters: Mode: Align + Exposure; Soft contact; Exposure time = 20 seconds
- Alignment: To place the sample and the mask precisely
- Exposure sample under UV for 4 seconds
- Open the contact lever, unload the sample.

Step 6: Post-bake (Hard-bake)

Using hot-plate, the sampled is post-baked for 2min @ 120^0C.

Step 7: Full (or flood) exposure (only for negative process)

Second exposure is to “reverse” the resist. This is a negative process. It is different to positive one because the masked resist parts will be removed in the development process. The description for chemical process is exhibited in **Fig. A.2**. We exposed the sample under UV for 60 seconds.

Step 8: Development

We used a formula for development as follows:

Solution= 1/5 developer AZ400K + 4/5 distilled water H_2O

Example: Solution= 15ml developer AZ400K + 60ml distilled water H_2O

Sink the sample in the solution for 20 seconds (time-dependent resolution). After that, sink the sample in distilled water for 20 seconds.

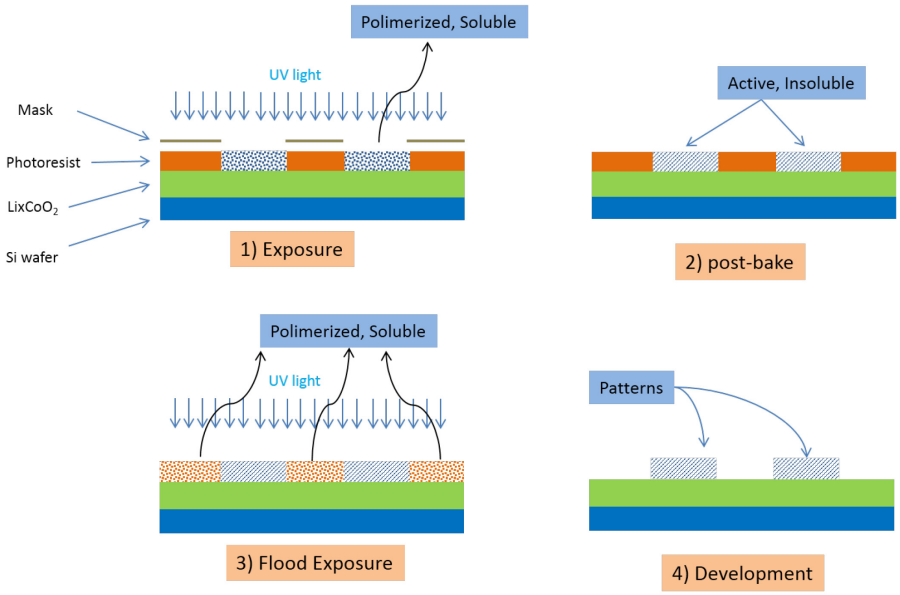

Figure A.2: Negative lithography process

- ***Oxygen plasma cleaning***

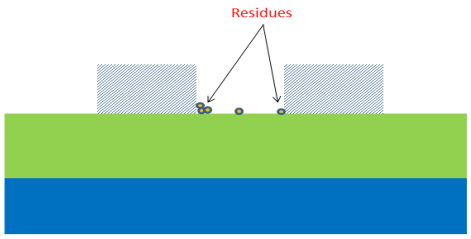

Figure A.3: Schematics of photoresist residues from the Lift-off

- Removal of residues, impurities and contaminants (as schematics in **Fig. A.3**) from the surface of the substrate after lift-off by creating high-pressure, energetic plasma from the gaseous species (here we use Oxygen)

- The vacuum for creating plasma is 0.6 mbar. The power is 160W (80% of max power). We cleaned for 3 min in the chamber.

- ***Electron Beam Physical Vapor Deposition (EBPVD)***

  Parameters:

  - Pressure of vacuum chamber: P = $3x10^{-6}$ Torr
  - For Ti: Current=0.17A, rate = 0.10 nm/s, thickness = 15 nm
  - For Au: Current=0.33A, rate = 0.25 nm/s, thickness = 50 nm

- ***Lift-off***

Place the sample into Acetone for at least 1 hour to lift the photoresist off. Result with a MIM stack . Gently clean the surface of sample using cotton tip and wash sample using IPA.

Protocol 2: M[Si_3N_4]/Li_xCoO_2/Si substrate (M=Au, Ti, Pt, Cr…)

This protocol allows depositing an insulating layer Si_3N_4 as an intermediate layer to measure endurance (chapter 5) of small lateral size (about 10µm) of Top electrode and to protect mechanical damages during electrical measurement.

- Use protocol 1 to deposit Si_3N_4 layer using sputtering systems (Lithography process is similar to protocol 1, like depositing M, but we use RF sputtering instead of e-beam evaporation). The working chamber of sputtering is pumped to P=2x10^6 mbar. Argon gas is introduced to chamber at the rate 52,7 sccm. The RF power is maintained at 200W, deposition time is about 50min for obtaining a 250nm-thick Si_3N_4 layer.
- Use protocol 1 again to deposit the top electrode M (in contact with film) by the mean of e-beam evaporation. In this case, the lithography step is similar to protocol 1. However we use layer 2 of mask for designing a small electrode on the side of Si_3N_4 pads with an electrical contact.

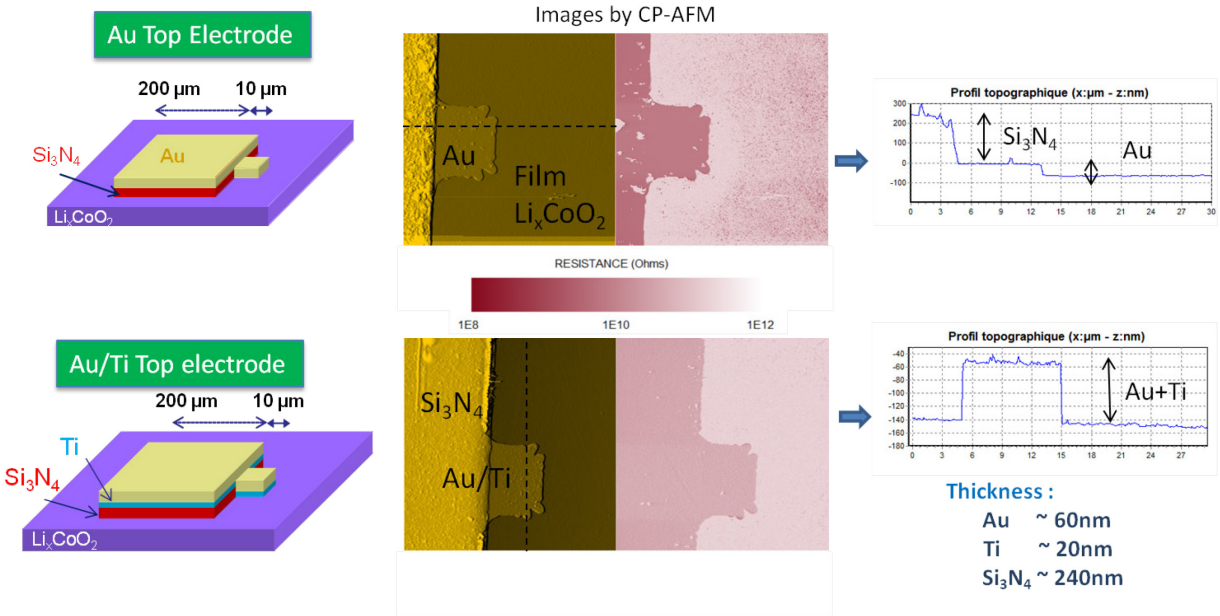

Figure A.4: Schematics of the cell configuration with an intermediate Si_3N_4 layer (lateral size: 200µm). The small pad on the side (lateral size: 10µm) is the top electrode. A corresponding electrical CP-AFM image shows an electrical connection between two levels. By taking the height profile: The thickness of Au and Ti is about 60nm and 20nm, respectively. The thickness of Si_3N_4 layer is about 240nm.

Protocol 3: M /[surrounded by a protecting layer]/LixCoO2/Si substrate (M=Au, Ti, …)

This protocol is used to deposit a protection layer on the Li_xCoO_2 film surface, to protect the humidity from the air when we measure retention of MIM stack.

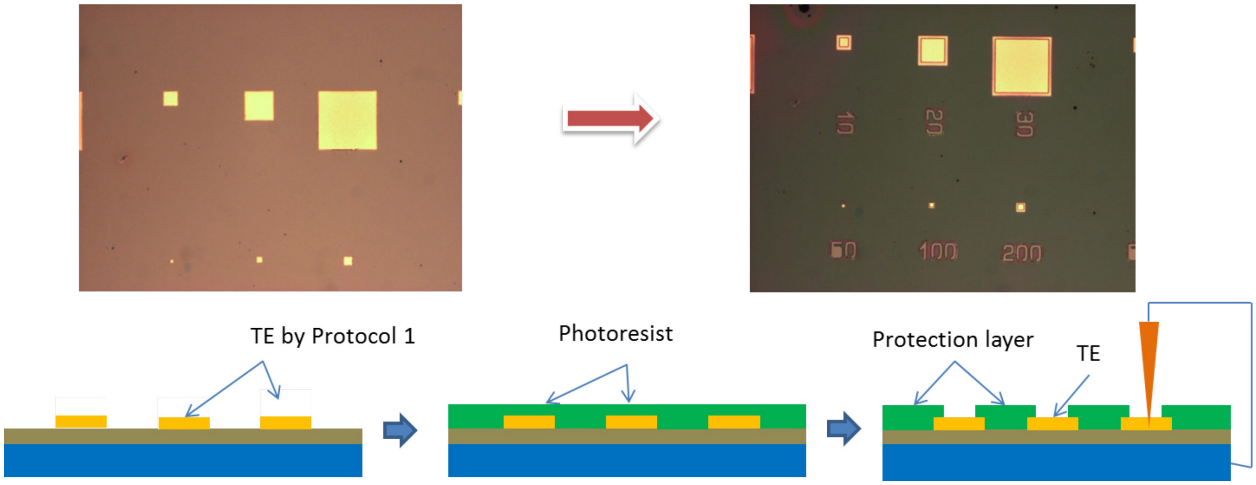

Figure A.5: Protocol is used to protect the film from the air. The top-view is shown on the top line. The schematics of side-view are in the bottom line.

- Step 1: Use protocol 1 to deposit the top electrodes (M=Au, Ti, Pt…) on the surface of Li_xCoO_2 film.
- Step 2: Use positive lithography. It has a similar process to negative lithography in protocol 1 and 2, however no hard bake and flood exposure processes are performed. The patterns on mask are smaller than the TE so that we cover fully the edge of TEs. The tip is then connected on top of TE, as shown in **Fig. A.5**.

APPENDIX B: SOME SUPPLEMENTARY INFORMATION CONCERNING TO THE RELIABILITY OF Li_xCoO_2 DEVICES:

Influence of vacuum on the retention of Li_xCoO_2 MIM device

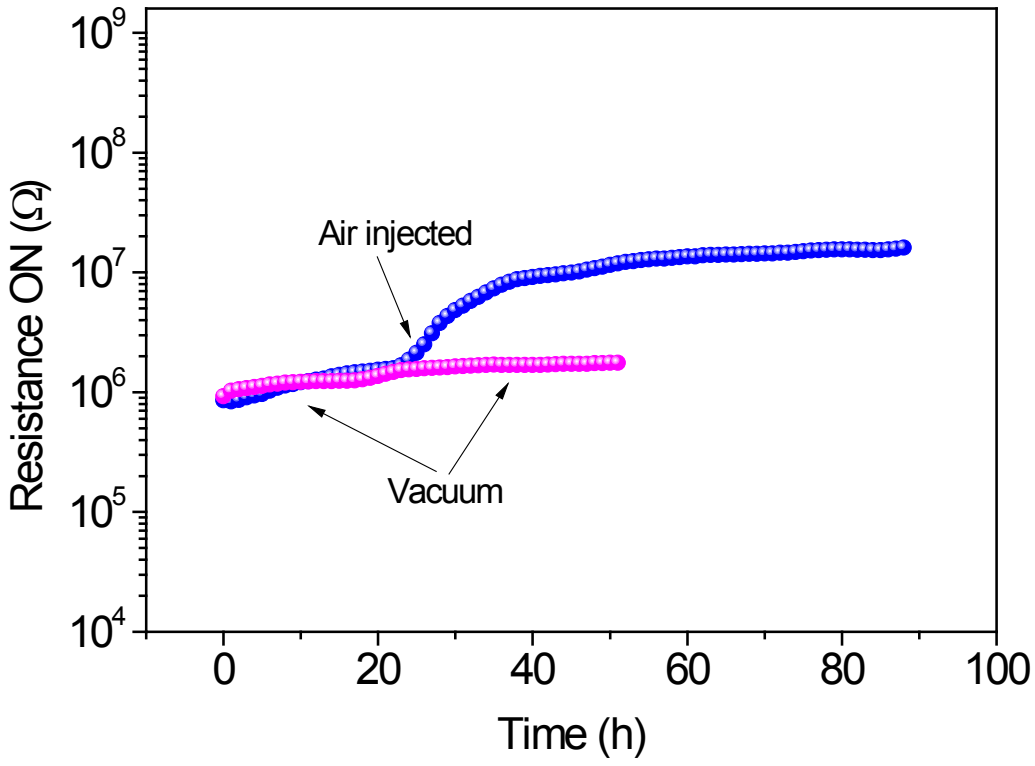

Figure B.1: Stability of R_{ON} state of MIM device under vacuum (pink) and under air (air has been injected into the vacuum chamber after 20 hours) (blue).

- We measured the retention of {Au/Li_xCoO_2/p-doped Si} sample using a small read voltage of -1V. The ON resistance state varies slightly under vacuum for about 20 hours. We then injected air into the vacuum chamber until the ambient atmosphere is reached. We observed that the resistance increases an order of magnitude from $10^6\Omega$ to 10^7 in ambient.

Résumé de la thèse (en français)

Introduction

Depuis son développement initial en 1988, la mémoire flash est extrêmement utilisée comme mémoire non volatile pour le stockage de données numériques dans la plupart des appareils électroniques mobiles (portable, téléphone portable, tablette ...). Cependant, avec le développement des technologies de l'information, les besoins en stockage de données (capacité et rapidité d'accès) augmente de manière exponentielle. De ce fait, les limites actuelles de la mémoire Flash (densité d'information, endurance et vitesse d'accès) constituent des verrous à lever.

Pour atteindre cet objectif, de nombreuses recherches se développent depuis le début des années 2000, notamment autour du concept de mémoire résistive basées sur la commutation entre différents niveaux de résistance via des impulsions de tension. En ce qui concerne les mémoires dont les variations de résistance dépendent de réactions électrochimiques (ReRAM), les mécanismes sous-jacents observés sont souvent basés sur la formation/rupture de filaments conducteurs, impliquant la migration de cations d'éléments métalliques (provenant des électrodes) ou de lacunes d'oxygène. Ce caractère filamentaire rend difficile la miniaturisation extrême vers l'échelle nanométrique.

Afin de surmonter cette limitation, une classe particulière de matériaux en couches - utilisés dans le domaine du stockage d'énergie - a commencé à être étudiée depuis 2010 à Orsay. Des résultats préliminaires intéressants ont déjà été obtenus sur des films minces de Li_xCoO_2, mais une meilleure compréhension est encore nécessaire concernant d'une part la nature des mécanismes sous-jacents, et d'autre part l'applicabilité potentielle de ces matériaux aux mémoires résistives non volatiles (ReRAM): c'est l'objectif de ma thèse. Mon travail a été réalisé au Laboratoire Génie Électrique et Électronique de Paris (GeePs) et au Centre de Nanosciences et de Nanotechnologies (C2N-Orsay), en collaboration avec le Laboratoire de Physique des Solides (LPS), l'Institut de Chimie Moléculaire et des Matériaux d'Orsay (ICMMO), le Groupe d'Étude de la Matière Condensée (GeMAC), le LITEN-CEA de Grenoble et l'Université de Chypre. Ce document est subdivisé en cinq chapitres, résumés ci-après.

Chapitre 1

Dans ce chapitre, l'état de l'art est présenté sur les principales caractéristiques de la mémoire Flash, ainsi que sur des mémoires dites émergentes, telles que les FeRAM, M-RAM, PC-RAM et ReRAM. Ces derniers types de mémoires (ReRAM) peuvent se répartir en trois classes principales, en fonction des mécanismes spécifiques impliqués dans les variations de résistance: Mémoires à métallisation électrochimique, Mémoires à Changement de Valence, et Mémoires Thermo-chimiques. Chaque classe est présentée ainsi que quelques exemples de matériaux appartenant à cette classe.

Nous abordons ensuite l'oxyde de cobalt et de lithium (Li_xCoO_2) qui a fait l'objet de cette thèse. Les propriétés structurelles et électriques de ce matériau (utiles pour les chapitres suivants) sont rappelées. En particulier, la conductivité électrique de Li_xCoO_2 peut varier de 4 à 5 ordres de grandeur, en fonction de la stœchiométrie (x).

Depuis 2013, plusieurs groupes de recherche internationaux ont commencé à étudier expérimentalement des dispositifs incluant des films de Li_xCoO_2, en vue d'applications potentielles au stockage d'information et au calcul bio-inspiré. En France à Orsay, des études commencées en 2010 ont permis d'observer un phénomène de commutation sur des cellules submillimétriques à base de Li_xCoO_2 avec un rapport {résistance élevée / résistance basse}

très important (5 ordres de grandeur).

Dans le cas d'un contact atomique {pointe AFM/surface d'un film de Li_xCoO_2}, le mécanisme a déjà été clarifié lors de la thèse précédente, de V.H. Mai (réaction redox de Co et de l'eau du ménisque pointe/échantillon). Cependant, dans la configuration d'électrodes dont la taille latérale est supérieure à l'épaisseur du film, le mécanisme apparaît cependant «inversé». Dans ce dernier cas, un mécanisme a été proposé, qui semble être conforme aux observations indirectes relevées. Cependant, la preuve directe de l'existence d'un tel mécanisme est restée jusqu'à présent sans réponse. L'objectif de ma thèse est de clarifier complètement le (s) phénomène (s) chimique (s) à l'origine de ces variations de résistance et d'évaluer les potentialités d'application de cette classe de matériaux aux mémoires Re-RAM.

Chapitre 2

Le chapitre 2 présente les méthodes d'élaboration et les techniques de caractérisation des films minces de Li_xCoO_2 et des dispositifs élaborés à partir de ces films. Il se compose de 3 parties. Dans la première partie, nous rappelons la méthode d'élaboration des films (par pulvérisation radiofréquence au LITEN-CEA et au C2N-Orsay). Les techniques de dépôt des électrodes supérieures (Au, Ti, Cr) sur les films sont également abordées: l'évaporation thermique a été utilisée au LPS, et j'ai effectué les dépôts par évaporation par faisceau électronique au C2N-Orsay.

Dans la deuxième partie, nous étudions les propriétés structurales des films minces de Li_xCoO_2 (provenant du LITEN-CEA), en utilisant diverses techniques de caractérisation. La technique de réflexion des rayons X (XRR) a permis de déterminer l'épaisseur moyenne (~ 100nm) des films étudiés. La diffraction des rayons X (XRD) a permis d'obtenir la valeur moyenne du paramètre c des films (environ 1,41 nm, ce qui correspond à une stœchiométrie de $x \approx 0,95$). Nous avons notamment observé que ce paramètre ne dépend pas du temps de post-recuit des films, et que la taille moyenne des grains (composant ces films) augmente en fonction du temps de post-recuit (atteignant environ 10 nm pour un recuit de 1 heure). Des analyses plus locales réalisées par Microscopie Electronique à Transmission ont montré que l'orientation de l'axe c de chaque grain est différente, l'axe c moyen étant orienté horizontalement. Ces analyses ont également permis de détecter qu'en dehors de Li_xCoO_2, les films contiennent également Co_3O_4 et CoO (au voisinage de la surface du film). Les analyses SIMS ont permis, après optimisation de plusieurs paramètres (nature de la source d'ions, énergie d'impact, et nature des ions détectés), d'obtenir des profils de profondeur et des cartographies en 3D de plusieurs éléments (Li, Co, O, Si).

Dans la troisième et dernière partie, nous présentons 3 techniques pour étudier les propriétés électriques des dispositifs. J'ai fréquemment utilisé la microscopie AFM à pointe conductrice (CP-AFM) lors de ma thèse au laboratoire GeePs; les images électriques obtenues présentent un contraste qui dépend du fait que le pointeur AFM est, soit directement en contact avec la surface du film, soit en contact avec la surface de l'électrode supérieure. Il s'agit également d'un outil très simple pour modifier l'état de résistance de cellules de toute dimension: ceci sera notamment utilisé pour étudier la cinétique de commutation de dispositifs au chapitre 4. La deuxième technique (méthode à deux sondes, réalisée au C2N-Orsay) est adéquate pour étudier des cellules de surface ≥ 100x100 µm: j'ai utilisé cette technique pour étudier l'endurance de dispositifs (au travers de programmes que j'ai développés durant ma thèse). Enfin, une technique de spectroscopie d'impédance électrochimique a été développée au C2N-Orsay afin d'essayer de mettre en évidence le phénomène de diffusion de lithium (discuté plus en détail dans le chapitre 3).

Chapitre 3

Dans ce chapitre, les cellules {$Au/Li_xCoO_2/Si$} ont été étudiées, en utilisant divers moyens, afin de mieux comprendre l'origine du phénomène de commutation résistive.

Ce chapitre est composé de trois parties. La migration nanoionique du lithium a été observée, d'abord indirectement à travers l'étude du caractère (métallique ou semi-conducteur) des cellules en fonction de leur état de résistance (par mesures de conductivité en fonction de la température). L'état de haute résistance d'une cellule est semi-conducteur, ce qui peut être corrélé à une stœchiométrie x élevée ($x \geq 0,95$), alors que l'état de faible résistance correspond à un comportement nettement plus métallique, qui peut être corrélé à une stœchiométrie x inférieure. De telles observations permettent déjà de souligner l'intercalation/désintercalation des ions lithium des films. En outre, la spectroscopie de masse à ionisation secondaire (SIMS) a permis de détecter la présence de Li dans l'électrode inférieure, pour des cellules qui se trouvent dans un état de faible résistance, alors qu'aucun lithium n'est détecté dans les cellules vierges (état de haute résistance). Ces résultats confirment directement l'importance de la migration ionique des films vers l'électrode inférieure, dans le processus de commutation de résistance.

Dans une deuxième partie, nous étudions le phénomène de commutation résistive, en utilisant une configuration développée au C2N-IEF : il s'agit de caractériser les cellules par spectroscopie d'impédance électrochimique (EIS). Les premiers résultats obtenus seront corrélés à la transition du métal semi-conducteur.

Enfin, dans la troisième partie, l'existence de mécanismes de conduction ionique et électronique est discutée plus en détail. En examinant les caractéristiques I-V de cellules, on peut proposer une hypothèse concernant le rôle possible de la couche mince de SiO_2 qui existe à l'interface Li_xCoO_2 / Si. La conduction électronique est également discutée et comparée à un modèle d'émission d'électrons (effet Poole-Frenkel).

Chapitre 4

Dans ce chapitre, nous avons d'abord étudié la cinétique de commutation des dispositifs par application d'impulsions de tension répétitives. Nous avons observé que pour des impulsions de polarité négative (l'électrode inférieure est polarisée négativement), la résistance des cellules (initialement à un état de résistance élevée) diminue progressivement. Une telle diminution dépend fortement de la surface supérieure de l'électrode (ce qui exclut une commutation de nature purement filamentaire): plus la dimension de l'électrode supérieure est faible, plus la commutation est rapide. La cinétique de commutation dépend également de la nature chimique de l'électrode supérieure: pour des électrodes en Ti, la cinétique est plus lente qu'avec des électrodes en Au, ce qui a été attribué à l'existence d'une couche de TiO_x de quelques nm d'épaisseur à l'interface Ti/ Li_xCoO_2 (confirmée par des analyses XPS) ce qui entraîne une chute de tension à cette interface.

Un modèle numérique, développé à l'aide d'un logiciel mathématique (MATHCAD), a été proposé pour expliquer la forte dépendance de la cinétique en fonction de la surface de l'électrode supérieure. Un bon accord qualitatif entre les résultats numériques et l'observation expérimentale a été trouvé. De plus, une extrapolation vers des dispositifs de dimension $20x20\mu m^2$ conduit à un temps de commutation calculé de l'ordre de grandeur de 100ns, ce qui est 1000 fois plus rapide que pour des mémoires Flash classiques.

En ce qui concerne la stabilité des états de résistance des dispositifs dans le temps, nous avons étudié la dérive (en fonction des jours) de l'état initial de résistance des cellules, par microscopie AFM à pointe conductrice. Cette dérive est clairement attribuée à la carbonatation progressive de Li_xCoO_2; sous vide poussé (10^{-9} T), un tel phénomène ne se produit pas. La carbonatation des films peut être complètement éliminée par un procédé de recuit rapide (580 ° C pendant 1 minute). De plus, la dérive de la résistance apparaît plus lente pour des électrodes en Ti (par rapport à des électrodes en Au). En outre, nous avons observé que dans l'air, la dérive de l'état de résistance faible est beaucoup plus rapide (~ 10 heures) que celle de l'état de résistance élevée (quelques jours). Nous avons essayé plusieurs types de films protecteurs (Si_3N_4 et résine AZ5214E) pour espérer ralentir une telle dérive, mais la stabilité du temps n'a cependant pas été améliorée; d'autres types de couches protectrices devront être étudiées à l'avenir.

Chapitre 5

Des mesures d'endurance ont été réalisées principalement sur des cellules de 100x100 µm², et l'influence de plusieurs paramètres a été étudiée. Tout d'abord, en ce qui concerne les caractéristiques des impulsions (durée et valeur maximale), il est possible de définir une fenêtre de performance: en effet, pour une tension donnée, une plus longue durée d'impulsion augmentera le rapport {résistance élevée/résistance basse}, mais diminuera l'endurance. À l'inverse, une faible durée ne permettra pas une commutation complète et entraînera un rapport {résistance élevée/résistance basse} plus faible. Par conséquent, les essais visant à maximiser l'endurance des cellules {Au / film / Si} conduisent à une endurance typique dans l'intervalle [1500-2000 cycles] (pour une limitation de courant de 0.1mA).

Une influence importante de la nature chimique de l'électrode supérieure a par ailleurs été observée: les cellules {Ti / film / Si} permettent d'atteindre une endurance plus élevée (2500-3000 cycles) pour une limitation de courant comparable (0,1 mA). De plus, pour une limitation de 1 mA, les électrodes supérieures en Ti conduisent à des endurances supérieures à 1000 cycles (contre moins de 200 cycles avec Au). Les phénomènes d'échauffement semblent être le principal paramètre limitant concernant Au.

Les cellules gravées par faisceau d'ions focalisés (le film ainsi délimité a la même surface que l'électrode supérieure) conduisent à des états de résistance plus stables (l'endurance diminue légèrement, probablement en raison de l'introduction de défauts lors de la gravure). Nous avons émis l'hypothèse que les cellules gravées (dont les frontières sont "protégées" par des zones amorphes) sont moins sensibles (que les cellules non gravées) à l'humidité ambiante, mais l'influence exacte de l'humidité doit être examinée de manière précise.

Par ailleurs, la dégradation progressive des cellules pendant les cycles répétitifs a été observée, quelle que soit la nature des électrodes supérieures (Au ou Ti). Un tel phénomène apparaît corrélé à la migration de Si de l'électrode inférieure vers l'électrode supérieure, comme le montrent des analyses XPS.

De plus, des études préliminaires montrent que l'endurance est nettement améliorée pour des températures élevées (au-delà de 6 000 cycles à 90 ° C). L'origine d'un tel phénomène reste à déterminer (liée ou non à l'humidité relative?).

Enfin, de premiers résultats sur des cellules de surface inférieure (10x10µm²) montrent des endurances supérieures à 6000 cycles pour des cellules dont l'électrode supérieure est en Au, et même supérieurs à 20.000 cycles dans le cas d'électrodes supérieures en Ti. La miniaturisation semble ainsi améliorer considérablement les performances en termes d'endurance. Des études futures seront à réaliser sur des cellules sub-micrométriques.

Conclusion et perspectives

En conclusion, en termes d'applicabilité, l'un des résultats les plus frappants est que les dispositifs à base de films de Li_xCoO_2 affichent d'excellentes performances pour des températures élevées supérieures à 100°C, ce qui constitue un avantage exceptionnel par rapport à d'autres types de mémoires dans l'électronique. De plus, nos résultats apportent de nouvelles idées prometteuses dans le domaine des batteries rechargeables.

Dans les perspectives, il serait intéressant de poursuivre les recherches actuelles, d'une part sur l'élaboration (épaisseur des films <100nm, et amélioration de la qualité des films) et d'autre part sur la miniaturisation des dispositifs (≤ 200x200 nm²), afin d'améliorer encore la cinétique de commutation, l'endurance et rapport {résistance élevée/résistance basse}. À moyen terme, les recherches envisagées pourraient porter sur un meilleur contrôle des interfaces (en utilisant par exemple des interfaces {film/électrode inférieure} constituées de canaux préformés, ou encore des électrodes inférieures composées de nanofils ...), ainsi que sur l'étude d'autres types de films appartenant à la classe des matériaux d'intercalation.

université PARIS-SACLAY

ÉCOLE DOCTORALE
Physique et ingénierie : électrons, photons, sciences du vivant (EOBE)

SHORT SUMMARIES OF THE THESIS

Titre : Films minces et dispositifs à base de Li_xCoO_2 pour application potentielle aux mémoires résistives non volatiles ....

Mots clés : nanoélectronique, stockage de l'information à haute densité, mémoires résistives non volatiles, films minces, ReRAM

Résumé : La mémoire Flash est actuellement extrêmement utilisée en tant que mémoire non volatile pour le stockage des données numériques dans presque tout type d'appareil électronique nomade (ordinateur portable, téléphone mobile, tablette, …). Pour dépasser ses limites actuelles (densité d'informations, endurance, rapidité), un grand nombre de recherches se développent notamment autour du concept de mémoires résistives qui repose sur la commutation entre différents niveaux de résistance, via l'application d'une tension.

Les mémoires dont la variation de résistance dépend de réactions électrochimiques (ReRAM) sont potentiellement de bonnes candidates pour les mémoires non volatiles de prochaine génération; les mécanismes d'oxydo-réduction impliqués sont cependant souvent de type filamentaire, mettant notamment en jeu des migrations de cations d'éléments métalliques (provenant des électrodes), ou de lacunes d'oxygène. Ce caractère filamentaire rend difficilement atteignable la miniaturisation extrême, à l'échelle nanométrique.

Dans cette thèse, une classe de matériaux particulière -utilisée dans le domaine du stockage d'énergie- est étudiée. L'objectif est d'approfondir l'origine des processus de commutation de résistance observés sur des films de Li_xCoO_2.Nous caractérisons d'abord les propriétés structurales et électriques de tels films, ainsi que le comportement électrique des dispositifs élaborés à partir de ces films. Nous étudions ensuite les mécanismes électrochimiques qui sont à l'origine des commutations résistives, dans la configuration d'un contact micrométrique électrode/film/électrode. Nous cherchons à déterminer la validité d'un mécanisme qui avait été proposé auparavant, mais non démontré. Nous étudions également la cinétique de commutation des dispositifs, et proposons un modèle numérique permettant d'expliquer les résultats expérimentaux observés. Enfin, nous étudions l'applicabilité potentielle des dispositifs (intégrant les films de Li_xCoO_2) aux mémoires Re-RAM au travers de leurs performances en termes d'endurance (nombre maximum de cycles d'écriture/ effaçage), et de stabilité. En particulier, nous étudions l'influence de plusieurs paramètres (impulsions de tension, nature des électrodes, température et c…) sur ces performances.

Université Paris-Saclay
Espace Technologique / Immeuble Discovery
Route de l'Orme aux Merisiers RD 128 / 91190 Saint-Aubin, France

ÉCOLE DOCTORALE
Physique et ingénierie : électrons, photons, sciences du vivant (EOBE)

Title : Li_xCoO_2-based thin films and devices for potential application to nonvolatile resistive memories..... ....

Keywords : nanoelectronics, high density information storage, nonvolatile resistive memories, ReRAM

Abstract : Flash memory is now extensively used as non-volatile memory for digital data storage in most mobile electronic devices (laptop, mobile phone, tablet...). To overcome its current limits (e.g. low information density, low endurance and slow speed), many researches recently developed around the concept of resistive memories based on the switching between different resistance levels by applying appropriate bias voltages.
Memories whose resistance variations depend on electrochemical reactions (ReRAM) are potentially good candidates towards next-generation non-volatile memories. The underlying redox mechanisms observed are however often of the filamentary type, involving in particular migration of cations of metal elements (coming from the electrodes), or oxygen vacancies. This filamentary character makes it challenging to attain extreme downscaling towards the nanometric scale.
In this thesis, a particular class of materials - used in the field of energy storage - is studied. The aim is to investigate the origin of the resistance switching processes observed in Li_xCoO_2 films.
We first characterize the structural and electrical properties of such films, as well as the electrical behaviors of the devices elaborated therefrom. We then investigate the electrochemical mechanisms which are at the origin of resistive switching, in the micrometric electrode/film/electrode configuration. We try to determine the validity of a formerly proposed mechanism which was however not yet demonstrated. Furthermore, we study the experimental switching kinetics of devices, and propose a numerical model to explain the results observed. Finally, we examine the potential applicability of Li_xCoO_2-based devices to Re-RAM memories through the study of their performances in terms of endurance (*i.e.* maximum number of write/erase cycles) and retention. Specifically, the influence of several parameters (such as voltage pulses, chemical nature of the electrodes, temperature *etc.)* on these performances is investigated.

Université Paris-Saclay
Espace Technologique / Immeuble Discovery
Route de l'Orme aux Merisiers RD 128 / 91190 Saint-Aubin, France